

**A Study of Turbulent Jet Ignition Combustion in an Optical
Research Engine with Alternative Fuels**

Khalifa Bureshaid



**Department of Mechanical and Aerospace Engineering
College of Engineering, Design and Physical Sciences
Brunel University London**

**Dissertation submitted to Brunel University London in accordance with the
requirements of the degree of Doctor of Philosophy**

May 2019

I. Abstract

Turbulent Jet Ignition (TJI) is an advanced ignition process where ultra-lean mixtures can ignite in standard gasoline spark ignition engine. In this research, a TJI unit by Mahle Powertrain USA was adopted and studied in a bespoke single-cylinder engine with optical access. The TJI device features a very small pre-chamber that is connected to the main chamber by multiple small orifices and can be separately fuelled by a direct fuel injector. The spark plug shifts from the main chamber to the pre-chamber to ignite the pre-chamber mixture. A new cylinder head was designed and manufactured to accommodate the TJI unit and optical windows on the top and sides of the cylinder head block. A new direct injector (DI) fuel supply system was set up for direct fuel injection in the pre-chamber. A new engine control and a data system were commissioned and used for engine experiments and heat release analysis. High-speed combustion imaging and spectroscopic techniques were developed to study the ignition and combustion in the main chamber through high-speed cameras and spectrographic equipment.

Thermodynamic studies on TJI combustion in a single-cylinder engine demonstrate the ability of TJI to extend the lean-burn limit of gasoline operation at different engine speeds and loads. Similar effects are also observed with engine operations fuelled with ethanol and wet-ethanol. TJI exerts the greatest effect in extending the lean-burn limit of ethanol fuel and leads to near-zero NO_x emissions near the lean-burn limit. In addition, the TJI ethanol engine operation has higher thermal efficiency as well as lower HC and CO emissions than the gasoline operation.

Spectroscopic results reveal that ethanol combustion produces higher chemiluminescent emissions than gasoline during the normal spark ignition combustion in the main chamber. The OH spectral peak at 310 nm is the highest throughout the ignition and combustion, followed by CH emission at 430 nm and HCO at 330 nm. Their intensities peak before the maximum heat release rates measured by the in-cylinder pressure.

Emission spectra produced by the pre-chamber ignition are stronger than the normal spark ignition in the main chamber. The highest emission intensities are observed with the fuelled pre-chamber ignition even with leaner air–fuel mixture in the main chamber. As pre-chamber fuel is increased, the pre-chamber pressure rises faster to a higher peak value, producing greater pressure differential between the pre-chamber and main

chamber and faster turbulent jets of partially burned products at higher temperature. The increase in the pre-chamber pressure causes the jets to travel deeper into the main chamber and enlarges the ignition sites. In addition, the ignition delay of the main chamber combustion is shortened due to the higher temperature of turbulent jets, as indicated by the stonger emission spectra. The turbulent ignition jets of ethanol are characterised with greater momentum than gasoline due to the faster combustion speed of ethanol and higher energy input. When the pre-chamber spark timing is advanced, the OH and CH emission intensities increase due to higher pressure and temperature in the pre-chamber, causing the pre-chamber products to travel deeper to ignite most of the main chamber charge. In comparison, the pre-chamber fuel injection timing has minimal effect.

Finally, the spectroscopic investigation at different air–fuel ratios with fuelled pre-chamber ignition shows that the peaks of OH, CH and HCO drop towards the lean-burn limits for both fuels. The intensity of the emission spectra is dependent on the ignition type, fuel properties and air–fuel ratios.

II. Acknowledgements

First and foremost, I would like to thank God for the opportunity and the talents to complete this dissertation. The journey has been long, and many people have supported me to achieve this goal.

My heartfelt thanks to my principal supervisor, Prof. Hua Zhao, for his invaluable guidance and help during this work. His supervision and encouragement refined my knowledge in the field of combustion. I am very proud and honoured to be under his guidance. He is not only a boss but also a leader and a role model for me. He always show concern towards his students and treats us like a family member.

Prof. Zhao, thank you so much for all the support, wise guidance as well as prompt communications either via numerous email exchange or meetings. Your reassurance during difficult conditions will forever be in my mind. I learned a great deal from you. I could not ask for a better supervisor.

I would like to express my deepest gratitude to Prof. Alasdair Cairns. He was my principal supervisor before he moved to Nottingham University. I am fortunate to have known him and to have spend almost a year under his supervision. He is a supportive man, and I will not forget his kindness.

I am extremely grateful to the Bahrain Defence Force for the financial support that made my study and stay in UK possible. I would like to acknowledge Mahle Powertrain USA for all the support provided to this work. Particularly, I am grateful to Mr. Mike Bunce of Mahle Powertrain for his technical support to the Mahle TJI unit and for his patience. Without their support and assistance and donation of numerous engine components and instrumentation, this project would not be completed.

I would like to extend my appreciation to the personnel of Brunel University, Chris Alan, John Wenn, Paul Yates, Kevin Robinson, Varinder Sandhu and Guillermo Schkzamian, who provided guidance, advice and support on many occasions. My gratitude also goes to the engine lab technicians Andy Selway and Eamon Wyse, with special thanks to Eamon who has greatly helped me over the last four years.

I would like to thank my best friends and colleagues, Mr. Nasser Alnoaimi, Dr. Fuhaid Alshammeri, Dr. Dengquan Feng, Dr. Milad Arrir, Ray Shimura and Mullah Dr. Hassan. I am also grateful towards my colleagues, Dr. Apostolos Karvountzis, Dr. Thompson

Lanzanova, Dr. Wei Guan, Dr. Reza Golzari, Dr. Jack Justus, Dr. Mazan Al-Kheetan, Ismaeel, Saud, Basam, Dr. Faras, Abdulla, Jamal and Mamdouh.

A special thanks to my parents and my family. Words cannot describe how grateful I am to my parents for their unwavering and unconditional love and support throughout my entire life. Finally, thanks to my wonderful wife, Um Khaled, who has supported me and put up with long distance and stressful days whilst I have been working on this dissertation.

III. Dedication

To my late father who passed away four months ago. My father is a man like no other. He gave me life, nurtured me, taught me, dressed me, fought for me, kissed me and, most importantly, loved me unconditionally.

No words can describe the importance of my father to me. He was and continues to be a powerful influence.

I love you, Dad. I will always love and miss you. Until we meet again.

IV. Author's Declaration

I declare that the work in this dissertation was carried out following the requirements of the university's regulations for PhD and that it has not been submitted for any other academic award. Except where indicated by specific reference in the text, this work is my work. Work performed in collaboration with, or with the assistance of others, is indicated as such. I identified all materials in this dissertation that is not my work through appropriate referencing and acknowledgement. Where I quoted or otherwise incorporated a material, which is the work of others, I included the source in the references. Any views expressed in this dissertation, other than referenced materials, are mine.

SIGNED.....

DATE:

(Signature of student)

V. Publication and Conference from this Work

The work detailed in this dissertation has resulted in the following refereed publications:

Journal papers

1. **Bureshaid, K.**, Feng, D., Zhao, H., & Bunce, M. (2019). Combustion and emissions of gasoline, anhydrous ethanol, and wet-ethanol in an optical engine with a turbulent jet ignition system. Proceedings of the Institution of Mechanical Engineers, Part D: *Journal of Automobile Engineering*. <https://doi.org/10.1177/0954407019825999>.
2. **Bureshaid, K.**, Shimura, R., Zhao, H., & Bunce, M. (2019). "Spectroscopic comparison of in-cylinder combustion between normal spark ignition and jet ignition system in an optical engine fuelled with gasoline and ethanol" (*International Journal of Engine Research, Under review*).
3. **Bureshaid, K.**, Shimura, R., Zhao, H., & Bunce, M. (2019). Experimental Studies of the Effect of Ethanol Auxiliary Fuelled in Turbulent Jet Igniter in an Optical Engine (SAE, *Under review*).

Conference papers

1. **Bureshaid, K.**, Feng, D., Vafamehr, H., and Zhao, H. "In-Cylinder Study of Combustion and Knocking Tendency of Gasoline, Anhydrous Ethanol and Wet Ethanol in an Optical Engine," SAE Technical Paper 2018-01-0655, 2018, <https://doi.org/10.4271/2018-01-0655>.
2. Feng, D., **Buresheid, K.**, Zhao, H., Wei, H. and Chen, C. (2018). "Investigation of lubricant induced pre-ignition and knocking combustion in an optical spark ignition engine." Proceedings of the Combustion Institute, 37 (4). pp. 4901–4910. ISSN: 1540-7489
3. **Bureshaid, K.**, Shimura, R., Feng, D., Zhao, H., & Bunce, M. (2019). "Investigation on knock resistance with turbulent jet ignition at different engine load in an optical engine." JSAE Technical Paper Number: 20199006
4. **Bureshaid, K.**, Feng, D., Zhao, H., & Bunce, M. "Experimental Studies of Gasoline Auxiliary Fuelled Turbulent Jet Igniter at Different Speeds in Single Cylinder Engine." NSAE Technical Paper Number: 19ICENA-00

VI. Table of Contents

I. Abstract.....	I
II. Acknowledgements	III
III. Dedication.....	V
IV. Author’s Declaration.....	VI
V. Publication and Conference from this Work	VII
VI. Table of Contents.....	VIII
VII. List of Figures	XII
VIII. List of Tables	XIX
IX. List of Equations.....	XX
X. Acronyms and Abbreviations.....	XXI
Chapter 1 Introduction.....	1
1.1 General Background	2
1.2 Aims and Objectives	4
1.3 Structure of Thesis	4
Chapter 2 Literature Review	7
2.1 Chapter Outline	8
2.2 Four-stroke SI Engine Operation	8
2.3 Gasoline Engine Developments	12
2.3.1 Catalytic Converter	12
2.3.2 Downsizing and Turbocharging	13
2.3.3 Exhaust Gas Recirculation (EGR)	14
2.3.4 SI Direct-Injected (SIDI) Engines	14
2.3.5 Lean Combustion.....	15
2.3.6 HCCI Combustion.....	16
2.4 Pre-chamber Ignition System	17

2.4.1	Overview of Pre-chamber Ignition Systems	17
2.4.2	Mahle TJI.....	25
2.5	Alternative Fuels for SI Engines	31
2.6	Combustion Imaging and Spectroscopic Measurement of Combustion Radicals	34
2.7	Detection of Combustion Radicals Through Spectroscopy	36
2.7.1	OH Chemiluminescence	38
2.7.2	H ₂ O, CH, C ₂ and HCO Chemiluminescence	39
2.8	Summary of Reviewed Literature	39
Chapter 3	Engine Design and Experiment Setup	41
3.1	Introduction	42
3.2	Engine Setup	42
3.2.1	Valve Selection	44
3.3	Fuel Supply.....	45
3.4	Engine Control and Instrumentation	47
3.4.1	Electric Control Unit (ECU)	47
3.4.2	Ignition Control.....	51
3.4.3	Engine Instrumentation.....	52
3.5	Cylinder Head Design.....	52
3.5.1	Cylinder Head Design and Mahle TJI Unit Installation	52
3.5.2	Optical Access and Top Window Design	56
3.5.3	Finite Element Analysis (FEA)	60
3.6	Experimental Procedure	62
3.7	Emission Analyser	64
3.8	Summary.....	66
Chapter 4	Data Analysis and Flame Imaging Techniques	67
4.1	Introduction	68

4.2	Heat Release Analysis	68
4.2.1	Heat Release Analysis	70
4.2.2	Knocking Combustion Analysis	71
4.3	High-speed Flame Imaging through the Top Window.....	72
4.4	Imaging of Turbulent Jets and Ignition Process through the Side Window	78
4.5	Spectroscopic Measurement	79
4.6	Summary	81
Chapter 5	Gasoline TJI Engine Operations	82
5.1	Introduction	83
5.2	Preliminary Engine Testing with Unfuelled Pre-chamber Ignition	83
5.3	Effect of Pre-chamber Ignition on the Lean-burn Limit at WOT	91
5.4	TJI at Different Intake Pressures	96
5.5	Jet Ignition at Different Engine Speeds	102
5.6	Summary	110
Chapter 6	TJI Combustion and Emissions of Gasoline, Anhydrous Ethanol and Wet-Ethanol in an Optical Engine	112
6.1	Introduction	113
6.2	Experimental Test Conditions.....	114
6.3	Results and Discussions	116
6.3.1	Effect of Fuel on IMEP and Lean-burn Limit.....	116
6.3.2	Effect of Fuel on Exhaust Emissions	119
6.3.3	Comparison of the Combustion and Heat Release Processes	122
6.3.4	Imaging Results.....	125
6.4	Summary	128
Chapter 7	Spectroscopic Studies on Ignition and Combustion by SI and Jet Ignition 129	
7.1	Introduction	130

7.2	Experimental Test Conditions.....	130
7.3	Results and Discussion.....	131
7.3.1	Spectroscopic Investigation of Initial Combustion Fuelled by Ethanol and Gasoline with Normal SI System	131
7.3.2	Spectroscopic Investigation of Initial Combustion Fuelled by Ethanol and Gasoline with Unfuelled Pre-Chamber Ignition System	138
7.3.3	Spectroscopic Investigation of Initial Combustion Fuelled by Ethanol and Gasoline with Ignition in the Fuelled Pre-Chamber.....	143
7.3.4	Ignition and Combustion Studies by ICCD Imaging.....	149
7.3.5	Spectroscopic Investigation of Initial Combustion Fuelled by Ethanol and Gasoline at Different Lambdas with Fuelled Pre-Chamber Ignition System 162	
7.4	Conclusions	167
Chapter 8	Conclusions and Suggestions for Future Work	169
8.1	Conclusions of Research	170
8.1.1	Effect of TJI on Gasoline Combustion and Emissions at Different Loads 170	
8.1.2	Effect of TJI on Gasoline Combustion and Emissions at Different Speeds 170	
8.1.3	Effect of TJI on Combustion and Emissions of Gasoline, Ethanol and Wet-ethanol Engine Operations	171
8.1.4	Spectroscopic Analysis of In-cylinder Combustion Between Normal SI and Jet Ignition System in an Optical Engine Fuelled with Gasoline and Ethanol 171	
8.2	Recommendations for Future Work.....	172
XI.	References	173
XII.	Appendix.....	185

VII. List of Figures

Figure 1.1 Comparison of global regulations for passenger cars [3]	3
Figure 2.1 Extension of lean limit by increasing turbulence intensity, 1200 r/min, homogeneous [19]	11
Figure 2.2 BSFC map for a typical turbocharged gasoline direct fuel injection engine [20]	11
Figure 2.3 Three-way catalyst: Simultaneous conversion of CO, HC and NO _x [21].....	13
Figure 2.4 NO _x emissions for different inlet temperatures T ₂ [37]	16
Figure 2.5 Combustion differences between the three modes of IC operation [41]	17
Figure 2.6 Chain of research on ignition improvement [42].....	18
Figure 2.7 Ricardo cylinder head of a stratified charge engine [44].....	19
Figure 2.8 Torch ignition with the turbulence-generating cell [46].....	20
Figure 2.9 Engine out emissions [73]	22
Figure 2.10 Sectioned view of the jet ignition unit installed in the CFR engine	23
Figure 2.11 Comparison between COV _{IMEP} < 5% (left) and < 10% (right) of the pre-chamber and main chamber fuel combinations with varying lambdas and MAP (1200 rev/min, CR = 11 and MBT spark timing) [74]	23
Figure 2.12 TJI pre-chamber and nozzle	26
Figure 2.13 Timeline of TJI Sequence[77]	27
Figure 2.14 Rapid compression machine and optical and TJI igniters used with the RCM piston at TDC.....	29
Figure 2.15 Combustion visualisation of TJI in the main chamber of the RCM for a stoichiometric air–fuel ratio $\lambda = 1$	30
Figure 2.16 SI and TJI combustion operating maps with varying fuel octane and combustion phasing. 1500 rev/min, 98 kPa MAP (~WOT) and stoichiometric conditions.....	31
Figure 2.17 Global ethanol production by country/region and year (adapted from [91][92])	32

Figure 2.18 Comparison of net energy balance for anhydrous and wet ethanol (E65W35) considering all ethanol production steps [99]	33
Figure 2.19 Electrons excited by exothermic reactions to a higher energy level and photons produced during the subsequent decay of electrons to a lower energy level	35
Figure 3.1 Modified cylinder head	42
Figure 3.2 Current engine with modified cylinder head on top (left), original Lister Petter TS-1 engine (right).....	43
Figure 3.3 Cylinder head with cross-section through ports.....	44
Figure 3.4 Selected valve timing	45
Figure 3.5 PFI fuel supply system.....	46
Figure 3.6 Average mass fraction burned (MFB) data for pre-chamber and normal SI ..	47
Figure 3.7 Screenshot of the data acquisition software	47
Figure 3.8 Injector current and voltage waveform for single-pulse mod.....	48
Figure 3.9 Schematic of the TJI's fuelling and engine control systems	49
Figure 3.10 NI driver.....	50
Figure 3.11 Screenshot of the data acquisition software	50
Figure 3.12 Actual trace waveform.....	51
Figure 3.13 Section view of the final cylinder head assembly. 1) Exhaust valve, 2) spark plug, 3) overhead, optical window, 4) intake cam lobe	53
Figure 3.14 Adapter that holds the TJI unit and top window	54
Figure 3.15 TJI unit in the horizontal direction	54
Figure 3.16 Images of the adapter, cutting part, side window and top window	55
Figure 3.17 Schematic of optical access.....	56
Figure 3.18 Top schematic of the cylinder head concept at Brunel University.....	57
Figure 3.19 Groove in glass and tone in the aluminium part	58

Figure 3.20 a) Damage to the window highlighted, b) original glass received from supplier by the red circle, c) upper and lower aluminium jackets	59
Figure 3.21 CAD image of the installed window and jacket assembly	59
Figure 3.22 Fine mesh	61
Figure 3.23 Distributions of von Mises stress (left) and displacement (right) using ANSYS	62
Figure 3.24 Photo of MEXA-584L gas analyser	65
Figure 4.1 99% confidence interval for the measurement of the average IMEPnet against sample size	70
Figure 4.2 Energy released in terms of MFB and cumulative heat released against crank angle (data averaged over 1200 cycles)	71
Figure 4.3 Calculated knock pressure signal and definition of knock intensity.....	72
Figure 4.4 Images showing the experimental engine control, image capture and data acquisition systems	73
Figure 4.5 Selected perimeter around the image at first image.....	74
Figure 4.6 Raw combustion image (right) and binary image following the mask filter (left).....	75
Figure 4.7 Computed values of the shape factor for the four-base fuels against the flame radius [107]	77
Figure 4.8 MATLAB image processing sequence and output	77
Figure 4.9 High-speed camera (<i>FastCam</i> mini) with Endoscope	78
Figure 4.10 ICCD camera (Pimax 4, Princeton) coupled with endoscope.....	79
Figure 4.11 Combustion chamber location.....	80
Figure 4.12 Pictures and sketches of the experimental apparatus for optical investigations	80
Figure 5.1 Modified cylinder head (left) and original cylinder head (right)	83
Figure 5.2 Motored in-cylinder pressure against crank angle for both ignition systems	84
Figure 5.3 Copper top window gasket (left) and paper gasket (right).....	84

Figure 5.4 LogP/LogV graph of motored in-cylinder pressure against cylinder volume at 1200 rpm.....	85
Figure 5.5 Flow diagram of test procedure.....	86
Figure 5.6 In-cylinder pressure and HRR for both ignition systems at fixed spark timing of 22° CA bTDC.....	87
Figure 5.7 Schematic view of the optical engine and high-speed imaging system	88
Figure 5.8 In-cylinder pressure and HRR of the normal SI and TJI.....	89
Figure 5.9 Combustion phase of normal SI and TJI.....	90
Figure 5.10 Image sequence of normal SI and TJI at 1200 rpm, 1 bar, MBT spark timing	91
Figure 5.11 Sectioned view showing the interaction between the main chamber and the pre-chamber.....	92
Figure 5.12 Maximum lean-burn limit of pre-chamber ignition (with and without auxiliary fuel) and normal SI	94
Figure 5.13 IMEP results at MBT for pre-chamber (with and without auxiliary fuel) and normal SI	95
Figure 5.14 Lean-burn limit with TJI under different inlet pressures	97
Figure 5.15 IMEP under stoichiometric ratio and lean-burn limit at different inlet pressures.....	98
Figure 5.16 NO _x emission at the lean-burn limit of different intake pressures (1200 rev/min, maximum lean and MBT spark timing).....	99
Figure 5.17 HC emission at the lean-burn limit at different loads (1200 rev/min, maximum lean and MBT spark timing).....	100
Figure 5.18 CO and CO ₂ emissions at the lean-burn limit at different inlet pressures (1200 rev/min, maximum lean and MBT spark timing).....	101
Figure 5.19 Comparison of lean-burn limits between pre-chamber and normal SI systems at different speeds (800, 1000 and 1200 rpm)	103
Figure 5.20 Effect of engine speed on IMEP by using pre-chamber ignition and gasoline fuel at inlet pressure 1 bar and MBT spark timing	104
Figure 5.21 Effect of engine speed on COV _{IMEP} by using pre-chamber and normal SI system and gasoline fuel.....	105

Figure 5.22 Effect of engine speed on 0%–10% MFB by using pre-chamber ignition and gasoline fuel at inlet pressure 1 bar and MBT spark timing	106
Figure 5.23 Effect of engine speed on 10%–90% MFB by using pre-chamber ignition and gasoline fuel at inlet pressure 1 bar and MBT spark timing	106
Figure 5.24 Effect of engine speed on MBT spark timing by using pre-chamber ignition and gasoline fuel	107
Figure 5.25 Effect of engine speed on NO _x emissions by using pre-chamber ignition and gasoline fuel	108
Figure 5.26 Effect of engine speed on HC emissions by using pre-chamber ignition and gasoline fuel at inlet pressure 1 bar and MBT spark timing	109
Figure 5.27 Effect of engine speed on CO emissions by using pre-chamber ignition and gasoline fuel at inlet pressure 1 bar and MBT spark timing	110
Figure 6.1 Comparison of lean-burn limits between normal SI and pre-chamber ignition (with and without auxiliary fuel) combustion systems for gasoline, ethanol and wet-ethanol.....	117
Figure 6.2 Effect of air–fuel ratio of each fuel on IMEP variation with pre-chamber fuel injection	118
Figure 6.3 Effect of air–fuel ratio of each fuel on combustion stability at 1200 rpm, inlet pressure 1 bar	119
Figure 6.4 Effect of air–fuel ratio on NO _x emissions at inlet pressures 1 bar, 1200 rpm maximum lean and MBT spark timing with fuel pre-chamber.....	120
Figure 6.5 Effect of air–fuel ratio of each fuel on HC emissions at inlet pressures 1 bar, 1200 rpm maximum lean and MBT spark timing with fuel pre-chamber	121
Figure 6.6 Effect of air–fuel ratio of each fuel on CO emissions at inlet pressures 1 bar, 1200 rpm maximum lean and MBT spark timing with fuel pre-chamber	121
Figure 6.7 Effect of fuel on 0%–10% MFB at inlet pressure 1 bar, 1200 rpm and MBT spark timing	122
Figure 6.8 Effect of pre-chamber fuel on 10%–90% MFB at inlet pressure 1 bar, 1200 rpm and MBT spark timing	123
Figure 6.9 In-cylinder pressure and HRR at different lambdas: (a) gasoline, (b) wet-ethanol, (c) anhydrous ethanol.....	125
Figure 6.10 Images of the flame propagation of different fuels at lambda 1.3 and spark timing 22° CA bTDC.....	126

Figure 6.11 Stages of image processing (from left to right, the original natural light image, the selected parameter and binarised image).....	126
Figure 6.12 Effect of fuel on mean flame radius development	127
Figure 6.13 Effect of fuel on the flame speed.....	127
Figure 7.1 In-cylinder pressure and HRR curves for the main chamber spark ignition at 22° CA bTDC	133
Figure 7.2 IMEP at different relative air–fuel ratios (λ)	133
Figure 7.3 UV-visible emission spectrum of combustion of ethanol and gasoline at 22° CA bTDC.....	136
Figure 7.4 Light emission intensities for gasoline and ethanol at different air–fuel ratios	137
Figure 7.5 Emission intensity OH @ 309 nm, HCO @ 330 nm and CH @ 430 nm vs crank angle for ethanol (left) and gasoline (right).....	138
Figure 7.6 In-cylinder pressure and HRR at fixed spark timing 10° CA bTDC	139
Figure 7.7 Effect of fuel on IMEP variation with lambda with unfuelled pre-chamber.....	140
Figure 7.8 UV-visible emission spectrum of ethanol and gasoline combustion at 10° CA bTDC.....	142
Figure 7.9 Emission intensity OH @ 309 nm, HCO@ 330 nm and CH @ 430 nm vs crank angle for ethanol (left) and gasoline (right).....	142
Figure 7.10 Comparison between normal SI and jet ignition system	143
Figure 7.11 Emission intensity OH @ 309 nm, HCO@ 330 nm and CH @ 430 nm vs crank angle for ethanol (left) and gasoline (right).....	144
Figure 7.12 Effect of fuel on 0%–10%, 10%–90% MFB and CA50 at inlet pressure 1 bar and 1200 rpm under different ignition systems.....	145
Figure 7.13 Spectra emissions of ethanol at lambda 1.4, spark timing 10° CA bTDC and injection timing 50° CA bTDC with different injection durations (0.3, 0.5 and 0.7 mg/pulse)	146
Figure 7.14 Spectra emissions of gasoline at lambda 1.4, spark timing 10° CA bTDC and injection timing 50° CA bTDC with different injection durations (0.3, 0.5 and 0.7 mg/pulse)	147

Figure 7.15 Effect of pre-chamber fuel injection timing for ethanol (left) and gasoline (right)	148
Figure 7.16 Spectral emission intensity at injection timing 30°, 50° and 70° CA bTDC for ethanol (left) and gasoline fuel (right).....	149
Figure 7.17 Pre-chamber and main chamber pressure and ICCD images of ignition sites in the main chamber at fixed injection timing of 50° CA bTDC and spark timing of 10° CA bTDC fuelled by ethanol under fuel injection duration of 0.3, 0.5 and 0.7 mg/pulse	153
Figure 7.18 Pre-chamber and main chamber pressures and ICCD images of ignition sites in the main chamber at fixed injection timing of 50° CA bTDC and spark timing of 10° CA bTDC fuelled by gasoline under fuel injection duration of 0.3, 0.5 and 0.7 mg/pulse	156
Figure 7.19 Jet travel distance and ignition delay for both fuels at different fuel injections (0.3, 0.5 and 0.7 mg/pulse).	157
Figure 7.20 Pre-chamber and main chamber pressures and ICCD images of ignition sites in the main chamber at fixed spark timing of 10° CA bTDC and $\lambda = 1.0$	160
Figure 7.21 Pre-chamber and main chamber pressures and ICCD images of ignition sites in the main chamber at fixed spark timing of 10° CA bTDC and $\lambda = 1.2$	162
Figure 7.22 Temporal profiles of radical emission intensities at different relative gasoline to air ratios with a constant spark timing of 10° CA bTDC and 0.3 mg/pulse fuel injection at 50° CA bTDC.....	164
Figure 7.23 Temporal profiles of the radical emission intensities at different relative ethanol to air ratios with a constant spark timing of 10° CA bTDC and 0.3 mg/pulse fuel injection at 50° CA bTDC.....	166
Figure 7.24 Variation of emission spectrum intensity for different ignition systems under different air–fuel conditions	167
Figure 8.1 Cylinder head design: (a, b) cylinder head drawing, (c) multi-hole dimensions, (d) cylinder head, (e) cylinder head and adapter, (f) cylinder head during machining	186
Figure 8.2 Image of the engine showing the belt and pulley arrangement with the intake cam (a), belt is driven off a pulley connected to the crankshaft via a toothed gear (b).....	187
Figure 8.3 Cross-sectional view of the engine showing the inlet and exhaust port geometry.....	188
Figure 8.4 Pre-chamber dimension.....	188

Figure 8.5 Top window dimension.....	189
Figure 8.6 Side window dimension	189
Figure 8.7 Modified side window dimension.....	190
Figure 8.8 Comparison between the required and existing waveform.....	191
Figure 8.9 Schematic of the experimental engine control and data acquisition systems	191
Figure 8.10 High-speed images with intensifier	192
Figure 8.11 High-speed images without intensifier	193
Figure 8.12 Top view images with full circle window	195
Figure 8.13 Top view images with modified half window	196
Figure 8.14 <i>FastCam</i> mini with telescope.....	196
Figure 8.15 <i>FastCam</i> mini with Lambert intensifier.....	197

VIII. List of Tables

Table 2.1 Literature review of jet ignition research with small pre-chamber volumes (<3% clearance volume).....	21
Table 2.2 Comparison between different ignition technologies (SI, HCCI and jet ignition) [41][42][43][75][76][77][78].....	24
Table 2.3 Different TJI designs	28
Table 2.4 Strong emission peaks of major combustion [111]	38
Table 3.1 Engine geometric parameters	44
Table 3.2 Mechanical and thermal properties of aluminium	60
Table 3.3 Status LED indicators	63
Table 3.4 Resolutions of the gas analyser	65
Table 4.1 Outlining of interdependence between image resolution, frame rate and maximum exposure time	73
Table 5.1 Test condition	86

Table 5.2 Test condition	96
Table 5.3 Test condition	102
Table 6.1 Physical–chemical characteristics for gasoline, ethanol and hydrous ethanol [107][138]	114
Table 6.2 Test condition	115
Table 6.3 Test condition	124

IX. List of Equations

Equation 2.1	15
Equation 4.1:	68
Equation 4.2:	69
Equation 4.3	69
Equation 4.4	69
Equation 4.5	69
Equation 4.6	75
Equation 4.7:	75
Equation 4.8	76
Equation 4.9	76
Equation 4.10	76

X. Acronyms and Abbreviations

AFR	air–fuel ratio
aTDC	after top dead centre
API	American Petroleum Institute
BDC	bottom dead centre
BLD	borderline detonation
BMEP	brake mean effective pressure
BSFC	brake-specific fuel consumption
bTDC	before top dead centre
C	carbon
C ₂	carbon-carbon
CA0	crank angle at the start of combustion
CA10	crank angle at 10% MFB
CA50	crank angle at 50% MFB
CA90	crank angle at 90% MFB
CAD	computer-aided design
CA Pmax	crank angle location of maximum in-cylinder pressure

CCV	cycle-by-cycle variations
CFD	computational fluid dynamics
CO ₂	carbon dioxide
COV	coefficient of variation
DAQ	data acquisition
DI	direct injection/injector
ECU	engine control unit
EGR	exhaust gas recirculation
EGT	exhaust gas temperature
EMOP	exhaust valve maximum open position
EU	European Union
EVC	exhaust valve close
EVO	exhaust valve open
fps	frame per second
GDI	gasoline direct injection
HC	hydro-carbon
IMEP	indicated mean effective pressure
IMEPnet	net-indicated mean effective pressure

IMOP	inlet valve maximum open position
IQT	ignition quality test
IVC	inlet valve close
IVO	inlet valve open
KI	knock intensity
MBT	maximum brake torque
MEP	mean effective pressure
MFB	mass fraction burned
NEDC	new European drive cycle
PAO	polyalphaolefins
PC	personal computer
PFI	port fuel injection
Pmax	maximum in-cylinder pressure
PRF85	primary reference fuel with research octane number of 85
ROHR	rate of heat release
RON	research octane number
rpm	revolutions per minute

SI	spark ignition
SOI	start of injection
TDC	top dead centre
UEGO	universal exhaust gas oxygen (sensor)
UHC	unburned hydrocarbons
ULG	unleaded gasoline
USB	universal serial bus

Chapter 1 Introduction

1.1 General Background

The global growth in oil prices and increasing awareness about the environmental impact of rising carbon dioxide (CO₂) emissions induce governments and automotive manufacturers to minimize tailpipe CO₂ emissions and other pollutant emissions. Emissions affect air quality, which in turn greatly affects people's lives, so producing clean air is essential. A large proportion of emissions come from vehicles. Andrews [1] stated that motor vehicles, on average, contribute 69% carbon monoxide (CO), 47% unburned hydrocarbons (HC) and 63% oxides of nitrogen (NO_x) to the total airborne pollution in western cities. Motor vehicle emissions contribute to global warming with carbon dioxide (CO₂) and NO_x greenhouse gases. The World Health Organization (WHO) reported that due to vehicle emissions, including particulate matter, approximately 40,000 people die in Austria, Switzerland and France annually and roughly 2.7 million people die around the world each year [2]. As a result, reducing engine emissions and developing engine efficiency are high market demands.

Figure 1.1 shows the regulation trends of vehicle CO₂ emissions worldwide. The data have been converted to be consistent with EU standards. The data indicate that the CO₂ emission regulations become progressively restricted. Improvement of engine efficiency is driving a strong demand for increasing thermal efficiency and reducing fuel consumption [3]. For example, the UK markets sell a growing number of small cars to improve fuel economy. Considerable research and technologies focus on the fuel economy of the spark ignition (SI) engine. European fleets indicate that substantial work is still required in the field of gasoline SI engines [4].

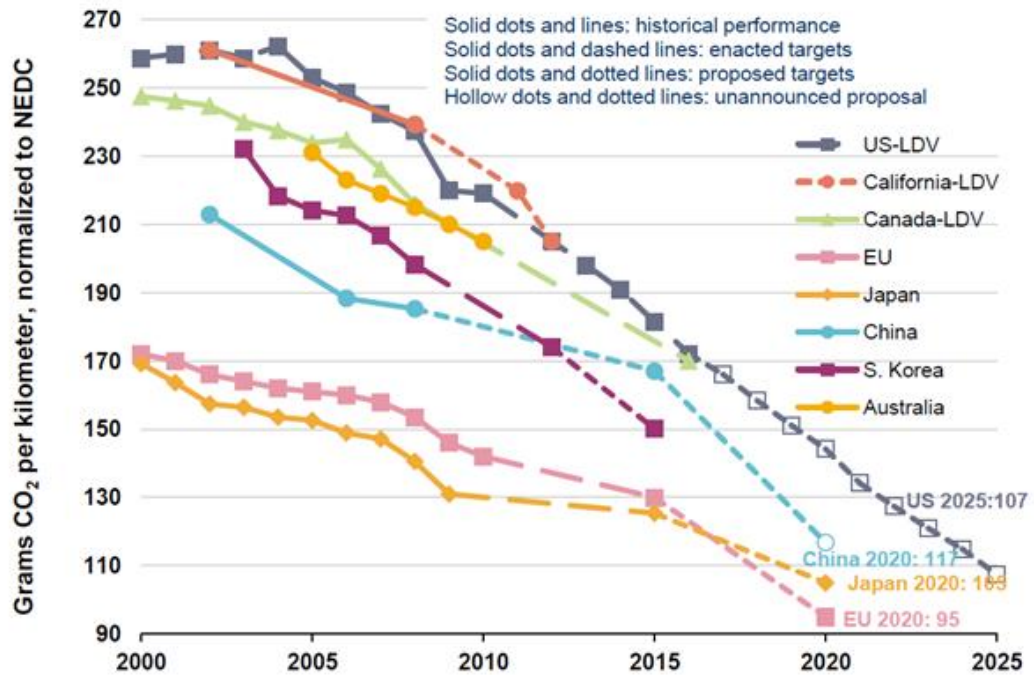


Figure 1.1 Comparison of global regulations for passenger cars [5]

At present, operating SI combustion engines under lean condition attracts renewed interest due to its ability to reduce engine emissions and fuel consumption. A key challenge for successful combustion of a premixed charge with high dilution of exhaust gas or air (lean burn) is stable ignition, slow flame speed and poor combustion stability. Amongst several technologies studied and developed is the pre-chamber ignition combustion, such as the turbulent jet ignition (TJI) which is discussed in detail in Chapter 2.

Parrallel to increasing the engine thermal efficiency, using low carbon or renewable fuels can largely contribute to the reduction in the GHG and pollutant emissions. Ethanol is increasingly used as an automotive fuel on its own or blended with gasoline in an SI engine. Ethanol can be produced from different natural sources, such as crops and sugar cane. In addition, ethanol has higher latent heat of vaporization (HOV) than gasoline per unit of mass and higher latent heat of vaporization for a stoichiometric mixture [6]. This attribute reduces the charge temperature and the knocking combustion at WOT and increases the volumetric efficiency.

1.2 Aims and Objectives

This research aims to study the combustion processes involved when utilising the Mahle TJI combustion system through in-cylinder heat release analysis and high-speed optical techniques. The primary goal is to enhance understanding of how TJI can ignite and speed up the combustion of lean mixtures at different engine operating conditions and the synergy between TJI and ethanol-based fuels to extend the lean-burn limit of such engines. The specific objectives are as follows:

- (1) To design and commission a new cylinder head with the Mahle TJI unit in a single-cylinder engine with optical access
- (2) To set up engine control, data acquisition system and high-speed optical measurement techniques for in-cylinder heat release and combustion analysis
- (3) To demonstrate the ability of TJI in extending the lean-burn limit of SI engine through heat release and exhaust measurement
- (4) To clarify the synergy between TJI and ethanol/wet ethanol fuels for improved thermal efficiency and reduced emissions
- (5) To investigate how pre-chamber ignition parameters affect multiple ignition sites and the main combustion process through high-speed imaging and spectroscopic studies
- (6) To study the ignition and combustion characteristics of gasoline and ethanol fuels

1.3 Structure of Thesis

Chapter 1

This chapter introduces the background of IC engines and sets out the aim and objectives of the research.

Chapter 2

This chapter reviews literature related to this research. The chapter starts with a brief introduction to SI engine operation followed by an overview of SI engine developments. Pre-chamber ignition systems are then extensively reviewed, with a specific section on the TJI system. Finally, ethanol fuel combustion is discussed.

Chapter 3

This chapter describes the engine and engine test bed equipment used in this research. The design details of a newly modified cylinder head and related engine modifications are included.

Chapter 4

Details of the thermodynamic data collection techniques are provided together with the heat release analysis used in the current research. Following an overview of the flame imaging techniques, the setups for the optical and spectroscopic measurement of ignition and combustion processes are presented.

Chapter 5

The engine testing procedure and the basic engine performance are introduced. Engine performances with normal SI and TJI when fuelled with gasoline are then compared, initially at different loads and then at different engine speeds. The capability of TJI to extend the lean-burn limit and improve the combustion stability of lean-burn combustion is demonstrated.

Chapter 6

This chapter focuses on the effectiveness of the TJI system on combustion stability, lean-burn limit and emissions in a single-cylinder optical engine fuelled with gasoline, anhydrous and wet-ethanol. The combustion and emissions of gasoline, anhydrous ethanol and wet-ethanol in an optical engine with TJI system are analysed and compared. The synergy between the TJI and ethanol/wet ethanol fuel is reflected by the improved thermal efficiency and reduced NO_x emissions.

Chapter 7

This chapter presents the spectroscopic measurements of radicals and their relative intensities through the endoscopic and high-speed spectrograph system described in Chapter 4. The temporal evolution and relative intensities of OH, CH and HCO radicals are recorded and compared between normal spark ignition and jet ignition system in an optical engine fuelled with gasoline and ethanol. Moreover, the effects of pre-chamber

control parameters on the multiple jet ignition sites and combustion processes in the main chamber are presented and discussed.

Chapter 8

Based on the results in Chapters 5 to 7, the main findings and conclusions are summarised in this chapter followed by recommendations for future work.

Chapter 2 Literature Review

2.1 Chapter Outline

This chapter aims to review the literature on SI combustion engine, particularly the pre-chamber ignition combustion systems. Following a brief description of the four-stroke SI engine operation, an overview on various engine combustion and control technologies is presented. These technologies can lead to improved thermal efficiencies and reduced CO₂ and pollutant emissions of the gasoline engines. Specifically, the fundamentals and technologies pertinent to the pre-chamber ignition combustion system are reviewed and discussed. Finally, the use of ethanol and wet-ethanol in SI engines is reviewed.

2.2 Four-stroke SI Engine Operation

The SI engines have been extensively studied in terms of ignition, fluid flow, combustion phenomena and fuel effects since the idea of combustion was realised. The four-stroke engine operation principle can be defined according to four stages: intake, compression, expansion (power stroke) and exhaust. All of these phases represent one crank revolution of 360 crank angle degrees (CAD). Regarding the instantaneous valve movements, the intake valve opens at the top dead centre (TDC) and an air–fuel mixture is induced into the cylinder as the piston moves downwards. The intake valve closes as the piston moves to the bottom dead centre (BDC), with the air–fuel mixture being carried near the polytropical compression as the piston travels upward. The combustion occurs instantaneously and adiabatically at TDC. The pressure increases rapidly due to the exothermic chemical reactions between the combustion contents. Moreover, these reactions increase charge temperature. In the case of the expansion stroke, the burned gases are isotropically expanded. During the exhaust stroke, the exhaust valve opens around BDC, and the burned gases are exhausted out from the cylinder when the piston moves upward to replace the fresh charge. This step is known as scavaging.

Combustion occurs in a very short period, starting some degrees prior to TDC and completing effectively after TDC, with combustion duration and phasing directly influencing engine output. Through the expansion of burned gas, the chemical energy of fuel is converted into mechanical power output at the crankshaft. Spark-ignited combustion can be divided into four phases according to [7].

Phase 1 - Spark and flame initiation: Owing to a rise in the voltage between the spark plug electrodes, an electrical breakdown creates an electrical arc. An initial flame kernel between the electrodes then starts to form.

Phase 2 - Initial flame development: The duration of this stage is approximately 30% of the total combustion time [8]. The surrounding in-cylinder flow affects the flame kernel between the electrodes, and it takes a spherical form after the spark breakdown. The progressive convection effects increase the wrinkling of the flame front as the scales of the turbulence are encroached [9]. The flame development angle (FDA) occurs from the timing of the spark to approximately 5% MFB to 10% MFB due to cycle-to-cycle variation [10].

Phase 3 - Turbulent flame propagation: This stage corresponds to the period when the mass fraction between 10% and 90% is burned. Many parameters, such as flame front area, spark plug location, mixture composition and turbulence intensity, can affect this stage. The rate of unburned mass is controlled by the turbulence intensity and distribution as well as the local charge mixture composition. The flame front size is increased during this stage by retaining the same shape until it is quenched close to the wall [10].

Phase 4 - Flame termination: The flame front hits the cylinder wall, and the flame is quenched. However, some fuel mass can be entrained although still burning behind the front and continues to do so during the power stroke/ expansion in case of the temperature is adequate to support the chemical mechanisms.

The flame kernel growth and propagation are important to support stable combustion by reducing the cyclic variability of the engine performance [10][8]. The cyclic variability in the first and second combustion stages is responsible for the differences in the combustion phasing due to the turbulent flame propagation is roughly constant, leading to an increase in cylinder pressure variability. Increasing the early flame kernel development reduces cyclic variability while increasing the maximum charge dilution limit. In addition, the cycle-by-cycle air variability of the intake process influences the in-cylinder charge and flow structures, directly affecting the first stages of flame kernel growth and resulting in IMEP variability.

The in-cylinder flow structure largely affects the engine gas exchange, air–fuel mixing, combustion and output performance [11][12]. Combustion processes are controlled by flow motion that increases flame propagation and improves scavenging. Large scale flow

structures, such as swirl or tumble, are used in conventional engines to maintain the flow's kinetic energy until the end of the compression stroke, where they break down into very small scale turbulence, supporting early flame kernel growth and increased flame speed [13]. This phenomenon increases knocking resistance, thereby permitting the use of increased compression ratios and resulting in increased fuel efficiency and reduced CO₂ emissions. In addition, a higher flame speed allows burning of a leaner air–fuel mixture to improve fuel economy. Moreover, the effect of an in-cylinder flow system in a uniflow two-stroke engine is efficient in engine performance. In-cylinder flow should be investigated to obtain information for optimising its flow structure.

Turbulent motion occurs when the inlet jet flow interacts with cylinder contents [14]. Internal combustion requires turbulent motion to improve engine efficiency and fuel economy. Turbulent flow exists by inducing air or air–fuel mixture into the engine cylinder. Li et al. [13] deduced that the bulk motion is a small scale of turbulent recirculation due to the dissipation of kinetic energy present in the flow field produced in the cylinder. Turbulence can cause unsteady flow and raise the combustion rate due to flame quenching. Turbulence and other flow motion affect flame propagation by 10 times [15]. Checkel and Ting [16] analysed the turbulence effects on burning velocities in a constant volume combustion chamber and deduced a linear correlation between turbulent burning velocity and turbulence intensity. However, turbulence enhancement must be controlled as it can be detrimental to thermal efficiency because of increasing heat transfer to the walls and increasing unburned HCs [17]. Figure 2.1 depicts the relationship between lean-burn limit and mean turbulence intensity. The mean turbulence intensity increases with the lean limit. However, any increase in turbulence intensity above 2 m/s cannot further increase the lean limit because of the reduced flame kernel growth rate caused by negative flame stretch, which is produced in lean mixtures exposed to high levels of turbulence [18].

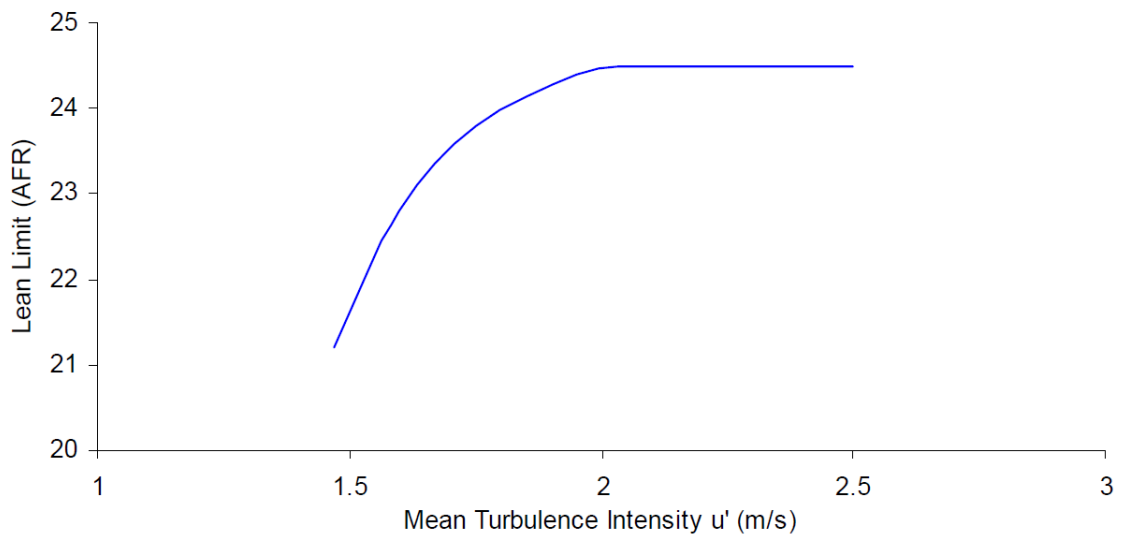


Figure 2.1 Extension of lean limit by increasing turbulence intensity, 1200 r/min, homogeneous [19]

Figure 2.2 presents the brake-specific fuel consumption (BSFC) map for a modern turbocharged gasoline direct injection (GDI) engine. The minimum BSFC is typically located near the mid-speed and load. In the case of high engine speed operation, the BSFC increases as the friction losses increase with the engine speed. Reducing the pressure and load within the intake manifold increases the engine pumping loss. At the top left hand corner and at a low speed and high load, the BSFC increases due to knocking combustion, which results in the retarded spark timing from the optimal.

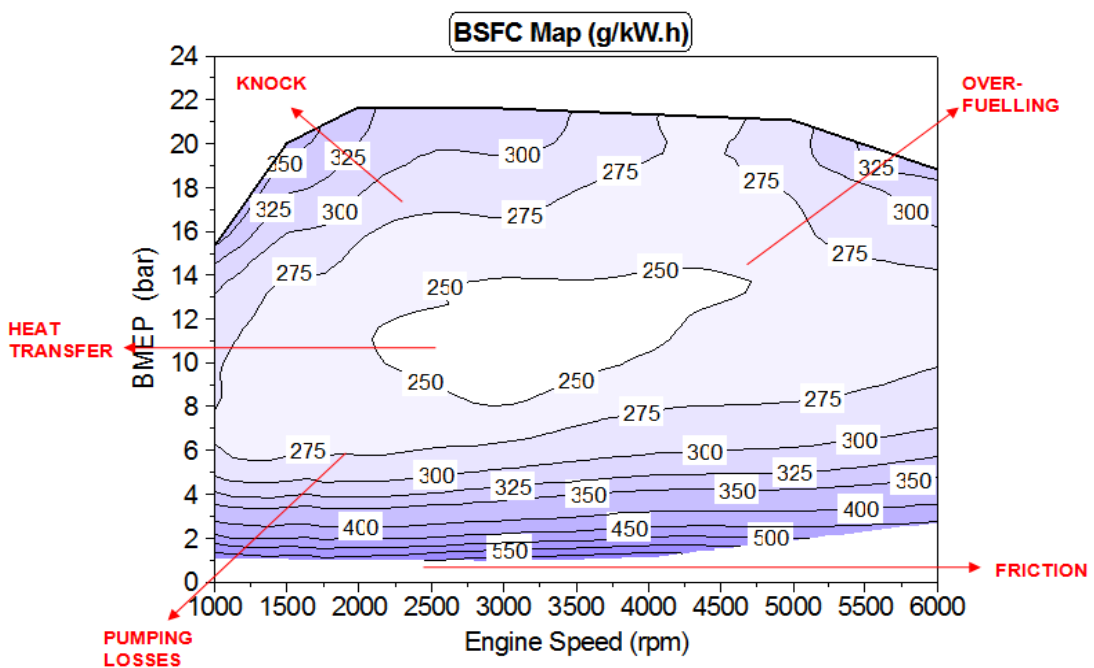


Figure 2.2 BSFC map for a typical turbocharged gasoline direct fuel injection engine [20]

2.3 Gasoline Engine Developments

Spark combustion engines face two main challenges as for reducing fuel consumption and developing strict emissions standards become high priority. These challenges are increasing thermal efficiency and reducing exhaust emissions. Increased efficiency in any combustion engine reduces the amount of fuel burnt, thus producing less carbon dioxide (CO₂) emissions for a given number of kilometres travelled. In previous years, improvements in fuel economy and exhaust emissions for SI engines have been achieved through the following mechanisms.

2.3.1 Catalytic Converter

In the 1970s, a two-way catalytic converter, which used platinum and palladium metals as catalysts to oxidise HCs and CO to create water and CO₂, was proposed to reduce exhaust emissions. With the introduction of more stringent emission legislation, three-way catalytic (TWC) converter becomes mandatory for SI gasoline engines because it can simultaneously reduce CO, HC and NO_x, as shown in Figure 2.3. However, SI engine must operate with the stoichiometric air–fuel ratio having a deviation of less than 0.1 for the three-way catalyst to work effectively. SI engine must be operated with leaner mixtures and extended relative air–fuel ratio (λ) that can produce ultra-low NO_x emissions to improve thermal efficiency and reduce CO₂ emission. This approach has renewed interest in the research and development of new ignition and combustion technologies for lean-burn combustion engines.

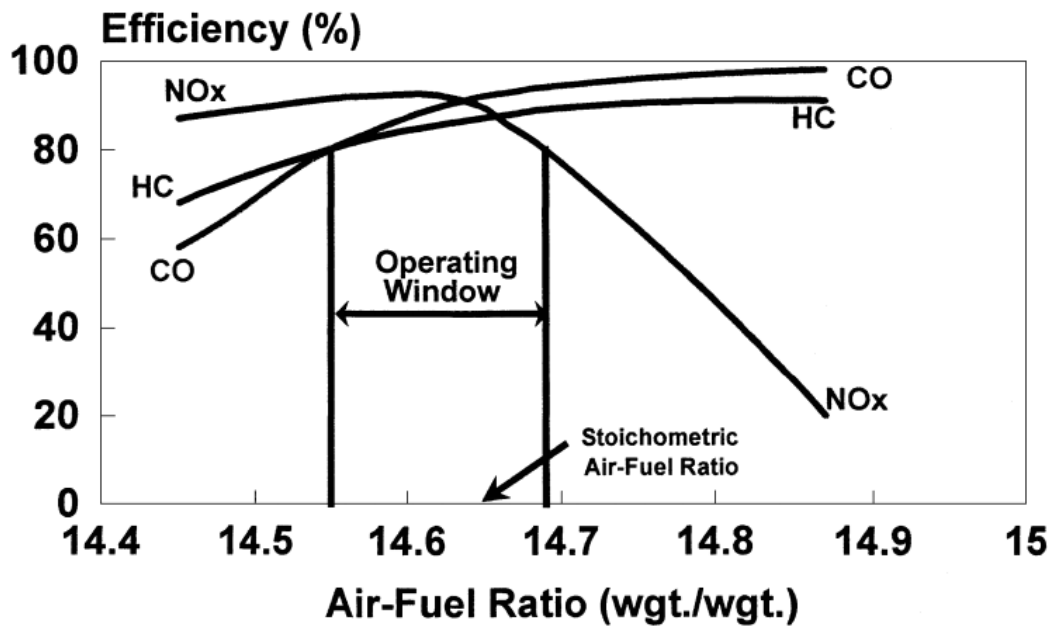


Figure 2.3 Three-way catalyst: Simultaneous conversion of CO, HC and NOx [21]

2.3.2 Downsizing and Turbocharging

Engine downsizing is one of the most efficient methods to reduce fuel consumption and exhaust emission of SI engine-powered vehicles. A smaller engine with less number of cylinders reduces CO₂ emissions and fuel consumption [22][23] because of the reduced friction, less weight and optimised engine operation near the minimum BSFC region during normal vehicle operation. Boosting is applied to downsized engine to maintain engine and vehicle performance. Boosting technology was originally used to improve engine performance, and its main purpose is to supply pressurised air to the engine. This increases output power and improves brake engine efficiency due to the relative decrease in engine mechanical losses. Boosting is typically implemented by a single turbocharger that recovers part of the exhaust energy to drive a radial compressor. Higher boost can be achieved by a two-stage system using a combination of small and large turbochargers or a supercharger and turbocharger in series or in parallel. For example, Fraser et al. [22] used a Mahle 1.2 l downsized engine to investigate effects of several different boosting systems on combustion. The results reveal that a twincharger system provides maximum low-speed load, whereas a turbocharger with electric supercharger system offers the best transient response. However, downsizing of four-stroke SI gasoline engine is constrained by knocking combustion, thermal and mechanical limits as well as boost limit.

2.3.3 Exhaust Gas Recirculation (EGR)

EGR can effectively reduce NO_x formation in the cylinder. In SI engines, using EGR increases the heat capacity of the cylinder charge, which reduces the peak combustion temperatures and consequently the production of NO_x. Adding EGR at part load reduces throttling losses and, thus, improves brake thermal efficiency. For example, Egnell [24] demonstrated the effect of EGR in reducing NO_x emission by changing the heat release. Pulkrabek [25] studied effects of EGR in terms of diluting the intake gas mixture for combustion and showed that temperature and nitrogen oxide are reduced. In addition, cooled EGR has been used under high load wide open throttle (WOT) conditions to suppress knocking combustion. Neame et al. [26] tested different fuels in an automotive V6 engine that utilised EGR and demonstrated that methanol at 40% EGR delivered the best fuel economy improvement.

2.3.4 SI Direct-Injected (SIDI) Engines

SIDI works by injecting fuel directly into the combustion chamber, as opposed to the intake port fuel injection (typically on a closed valve) in the conventional PFI system. Bosch [27] believed that by 2007, every new SI engine will have direct injection. SIDI reduces fuel consumption by as much as 15% over PFI. However, the stratification of the charge creates similar emission problems to diesel. In excess of 50% load and engine speed, the engine must switch to homogeneous mode to avoid further degradation in emission and combustion stability. Injecting fuel directly into the chamber has the following advantages over PFI injections.

- better transient response
- improved fuel economy
- no fuel pooling phenomena in intake ports
- less emissions, especially at start-up
- the desire to stratify the air–fuel mixture using fuel spray and interacting gas dynamics

The disadvantages are as follows:

- difficulty in controlling the system due to short time available for preparing the mixture prior to combustion
- additional calibration required
- difficult NO_x after treatment by operating the system under lean combustion

- potential to produce smoke and particulate emissions
- increased unit price of engine

The SIDI engine was originally developed to improve the performance of the engines in the 1930s when the SI gasoline engine was used in combat aircraft prior to the invention of jet engines [28]. Recent efforts have been focused on the potential of improved fuel economy of SIDI engines initially through the stratified charge lean-burn operations in the 1990s [29]. However, since 2000, the SIDI engine has been designed to operate with a turbocharger as downsized engine to take advantage of the charge cooling effect of direct fuel injection, which suppresses the knocking combustion due to increased boost [30][31][32].

2.3.5 Lean Combustion

Lean combustion and ignition enhancement have been the subject of intensive research over the past few years [33][34][35]. Lean burn occurs when the combustion engine operates with excess air in the air–fuel mixture as measured by the relative air–fuel ratio or lambda value (λ) that is equal to the actual AFR divided by the stoichiometric AFR. As more air is present in the mixture, the specific heat ratio of the cylinder charge increases. The ideal Otto cycle efficiency in Equation 2.1 indicates that thermal efficiency increases with the specific ratio.

$$\eta_{th} = 1 - \frac{1}{CR^{\gamma-1}},$$

Equation 2.1

where CR is the compression ratio (maximum cylinder volume/clearance volume), and γ is the specific heat ratio.

Lean-burn combustion at part-load operation results in reduced pumping losses, which improve brake thermal efficiency and reduce fuel consumption. Moreover, the low temperature of lean-burn combustion reduces heat loss and NO formation, as shown in Figure 2.4. Honda CVCC [36] lean-burn engine was produced in the 1970s but subsequently withdrawn from the market due to higher emissions. The three-way catalyst could not be effectively used with such lean-burn engines.

Two drawbacks exist though. High energy is required to obtain reliable ignition of very lean mixtures, and the slow flame speed of lean combustion can lead to less stable combustion and, ultimately, misfiring.

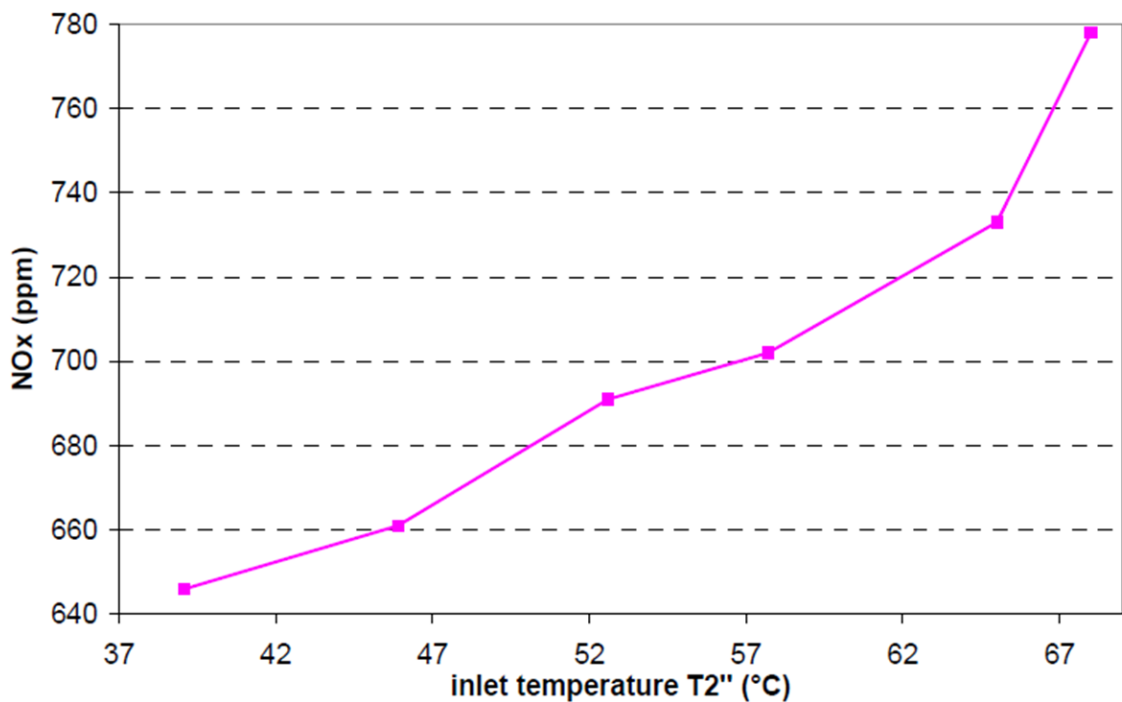


Figure 2.4 NOx emissions for different inlet temperatures T2 [37]

2.3.6 HCCI Combustion

Figure 2.5 presents the differences between the three modes of internal combustion operation. Controlled auto ignition/homogenous charge compression ignition (CAI/HCCI) technology is an alternative approach to combusting a lean homogeneous charge. This technology was first identified as a combustion phenomenon when the SI engine continued running even when the ignition was turned off [38][39]. This method allows for combustion to occur within ultra-lean or diluted mixtures, resulting in low temperature that leads to reduced engine NOx emissions. Autoignition occurs in a number of sites in the cylinder simultaneously, thereby burning the air–fuel mixture immediately. It increases the temperature and density of the air–fuel mixture to the level wherein the reaction of the whole mixture occurs at the same time in CAI/HCCI. Oakley, Zhao and Ladommatos [40] reported an experimental study of CAI/HCCI combustion in a four-stroke engine. Their results show that with EGR dilution, this form of combustion improves fuel economy by 20% at a moderate engine load. However, the ignition timing and heat release rate (HRR) are indirectly controlled during CAI/HCCI

combustion. Applying CAI/HCCI at high load operation is also difficult due to extremely high rate of pressure rise and peak cylinder pressure.

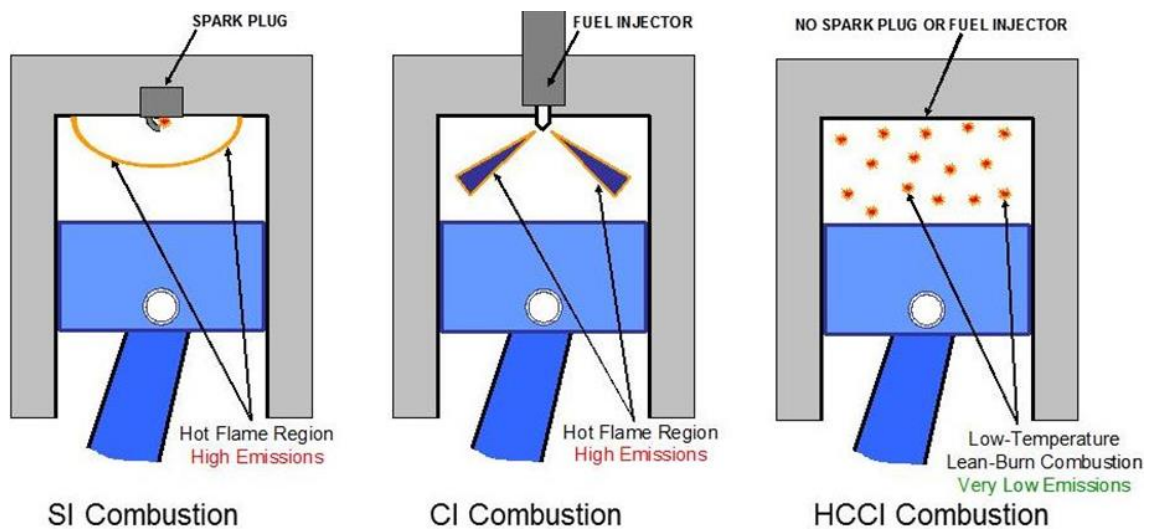


Figure 2.5 Combustion differences between the three modes of IC operation [41]

2.4 Pre-chamber Ignition System

2.4.1 Overview of Pre-chamber Ignition Systems

Lean combustion requires high ignition energy and flame speed. One of the solutions is to increase the energy of the ignition system. Dale et al. [42] reviewed the ignition and combustion enhancement systems for homogeneously fuelled internal combustion engines to identify the differences between ignition systems, such as plasma jet and pre-chamber torch cells, as shown in Figure 2.6.

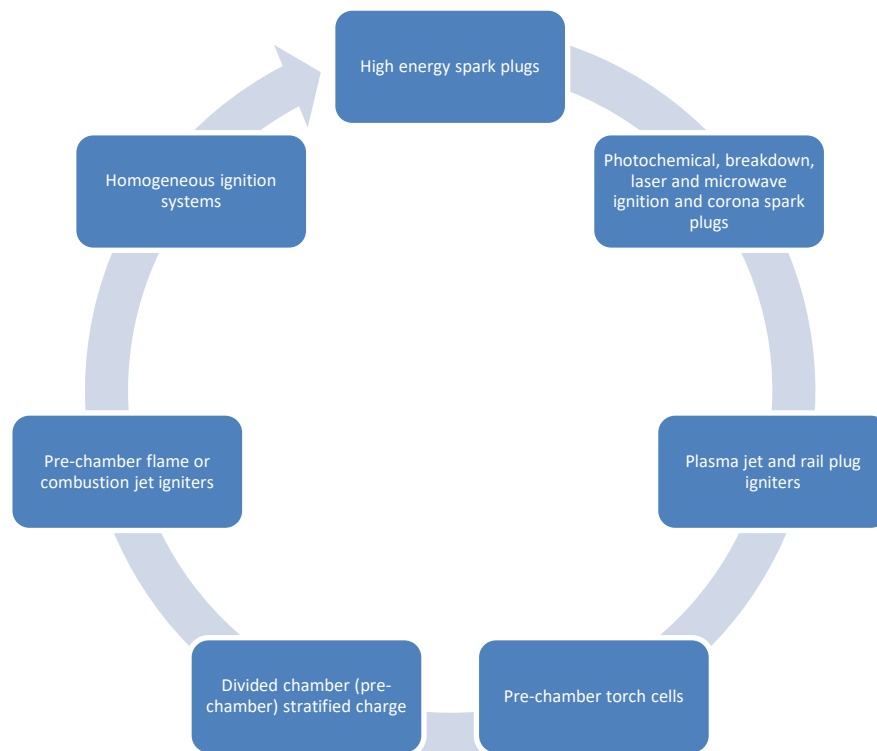


Figure 2.6 Chain of research on ignition improvement [42]

In addition, Elisa et al. [43] reviewed the historical background of pre-chamber application and reported how ignition enhancement contributes to running the combustion engine with excess air.

The pre-chamber idea was born at the beginning of the twentieth century when a two-stroke Ricardo Dolphin engine was developed (Figure 2.7). With this engine, a passive auxiliary intake valve was utilised to supply the pre-chamber with a rich mixture, which could ignite a leaner main chamber mixture. Since this outset, various forms of pre-chamber combustion systems have been developed to increase the lean-burn limit of SI engine.

The pre-chamber is categorised by having one of the following:

- large/small pre-chamber volumes
- auxiliary pre-chamber fuelling (active)/no auxiliary pre-chamber fuelling (passive)
- large or small orifice/multi-orifices connecting the pre-chamber to the main chamber

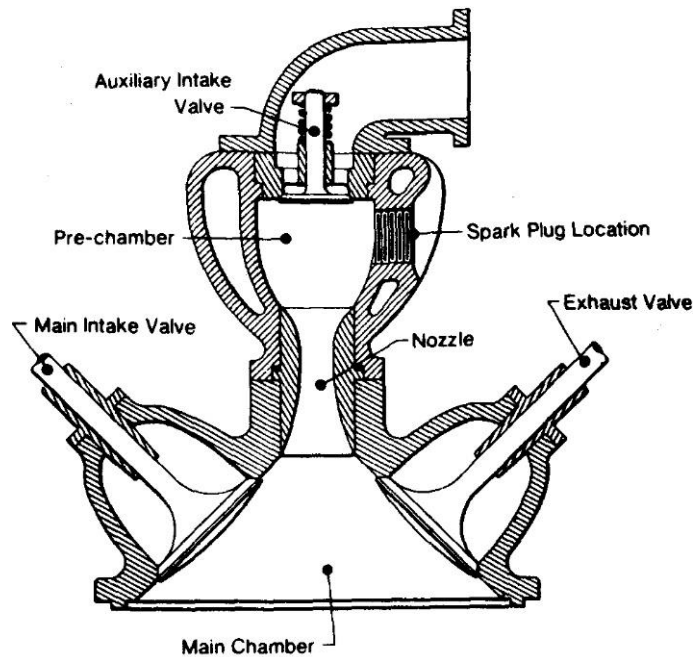


Figure 2.7 Ricardo cylinder head of a stratified charge engine [44]

A torch cell (Figure 2.8) is an example of a passive pre-chamber ignition system. The pre-chamber is filled with the premixed mixture from the main chamber charge during compression wherein the ignition of the mixture is initiated by a spark plug. The combustion jet from the pre-chamber then ignites the main chamber charge. The system creates more turbulence and high ignition energy to ignite a leaner air–fuel mixture, thereby reducing exhaust emissions. The pre-chamber volume was tested from 1% to 20% of the main chamber to reach the maximum lean-burn limit and reduce emissions [45].

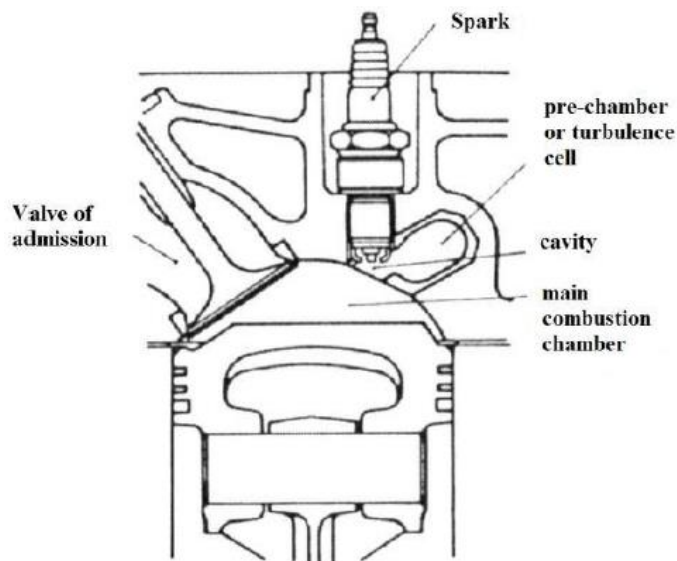


Figure 2.8 Torch ignition with the turbulence-generating cell [46]

At the end of the 1950s, the concept of jet ignition was proposed by Nikolai Semenov and developed by Gussak as the Lavinia Aktivatsia Gorenia [47]. Jet igniters are a part of the divided chamber stratified charge. Jet igniters contain smaller orifice(s) connecting the combustion cavities of the main chamber and pre-chamber. The smaller orifices create multiple flame jets that penetrate deeper into the main charge, which in turn ignites the main cylinder charge by injecting high temperature reactive radicals. The LAG system is characterised by a smaller pre-chamber with a clearance volume of 2%–3%, smaller orifices of $0.03\text{--}0.04\text{ cm}^2/1\text{ cm}$ pre-chamber volume with an orifice length to diameter ratio of $\frac{1}{2}$ [43].

More studies on jet ignition and the importance of active radicals were conducted, and the following section explains the novelty of the jet ignition system. Since this idea was proposed, considerable research has been published on pre-chamber size, location and the fuelling system to achieve extended lean-burn limit with increased thermal efficiency and reduced emissions. Table 2.1 summarises the development of the jet ignition system with small pre-chambers.

Table 2.1 Literature review of jet ignition research with small pre-chamber volumes (<3% clearance volume).

Date	Jet Ignition Systems	Publications
1950s	LAG – Avalanche Activated Combustion	L.A. Gussak and colleagues [48][49]
1970s	Jet Plume Injection and Combustion (JPIC)	Oppenheim et al. [50][51]
1984	Swirl Chamber Spark Plug	Reinhard Latsh [52]
1992	Hydrogen-assisted Jet Ignition (HAJI)	H.C. Watson et al. [53][54]
1993	Pulsed Jet Combustion	Warsaw [55][56]
1993	Hydrogen Flame Jet Ignition (HFJI)	Toyota College [57][58]
1999	Self-ignition Triggered by Radical Injection (APIR)	University of Orleans [59]
1999	Scavenged and Unscavenged Swirl Chamber Spark Plugs	Pischinger et al. at Aachen University of Technology [60]
1999	Bowl Pre-Chamber Ignition (BPI)	University of karlsruhe and Multitorch [61][62]
2003	Pulse Jet Igniter (PJI)	Najt et al. [63]
2005	Homogenous Combustion Jet Ignition (HCJI)	Robert Bosch. [64][65]
2007	IAV Pre-Chamber Spark Plug with Pilot Injection	IAV GmbH and Multitorch [66]
2009	Turbulent Jet Ignition (TJI)	Mahle Powertrain [3][67][68][69]

For example, the hydrogen-assisted jet ignition (HAJI) system was developed by Watson et al. at the University of Melbourne in the 1990s. It utilises hydrogen (H₂) for approximately 2% of the main fuel energy as a pre-chamber fuel [70][71][72]. A spark plug is used to ignite the H₂ inside the pre-chamber cavity, which then injects very high reactive radicals into the main chamber [54]. The usage of HAJI demonstrates the ability to reduce exhaust emissions and increase combustion burning rate, which improves engine efficiency. Lawrence and Watson [73] used flame imaging technique to study HC

emissions in a four-valve single-cylinder engine. A fast flame ionisation detector was utilised to collect real-time hydrocarbon concentration data from the exhaust valves, inside the HAJI pre-chamber and near the main chamber wall. Flame images were also obtained. Figure 2.9 shows the engine out emissions at different air–fuel ratios. The results indicate that as the lambda value increases, the NOx emission decreases. Contrary to NOx emission, a higher HC emission amount is obtained at greater lambda value. Moreover, wall quenching increases in engine out HC emissions.

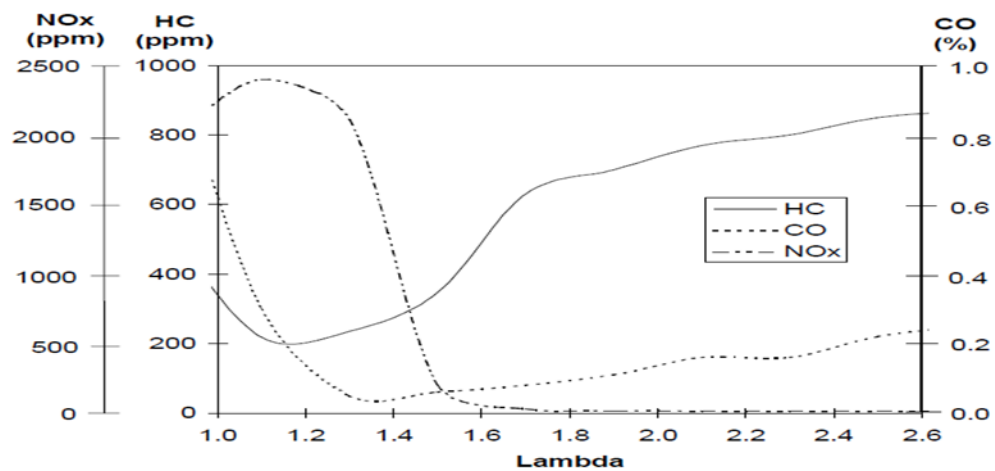


Figure 2.9 Engine out emissions [73]

To study the influence of fuel on mixture lean limit, emissions levels and combustion characteristics, Toulson et al. [34] used a HAJI system with different fuels for the main chamber (LPG or gasoline) and the pre-chamber (H₂ or LPG), as shown in Figure 2.10. Figure 2.11 demonstrates the lean limits for different fuel combinations. The highest lean limit was for an LPG–H₂ combination, followed by an H₂–gasoline combination. Lean limit variations were higher at low manifold absolute pressures (MAPs) than at high MAPs in all fuel combinations.

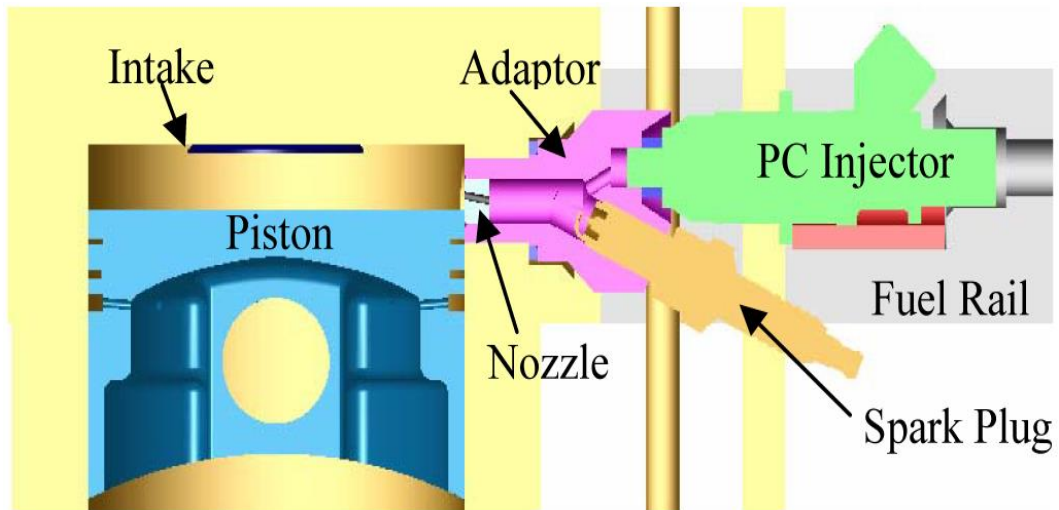


Figure 2.10 Sectioned view of the jet ignition unit installed in the CFR engine

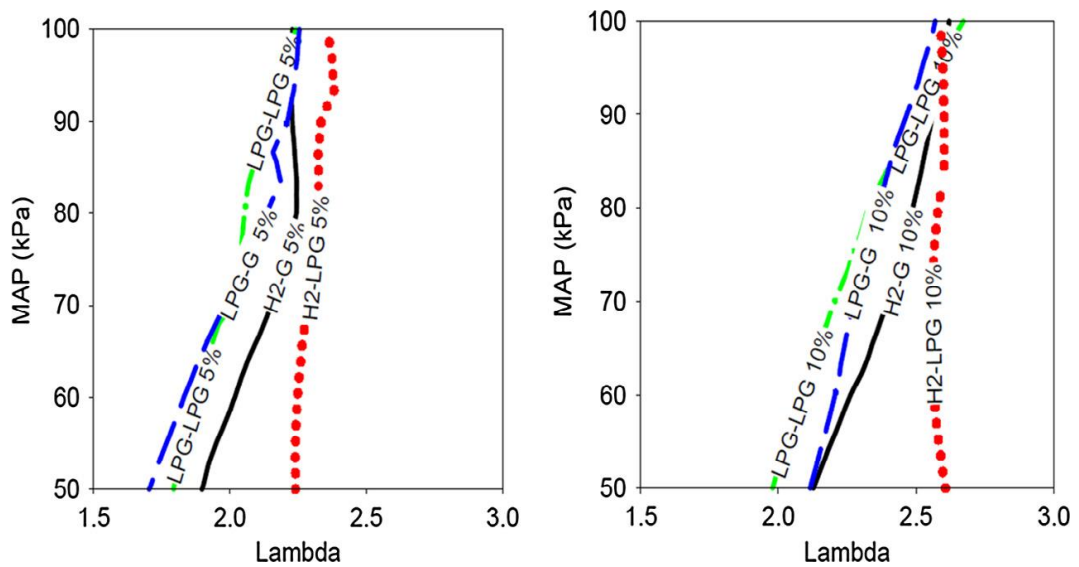


Figure 2.11 Comparison between $COV_{IMEP} < 5\%$ (left) and $< 10\%$ (right) of the pre-chamber and main chamber fuel combinations with varying lambdas and MAP (1200 rev/min, CR = 11 and MBT spark timing) [74]

Table 2.2 lists the relevant differences between gasoline SI, HCCI and jet ignition. The comparison focuses on jet ignition concept with a small pre-chamber volume (<3% of clearance volume).

Table 2.2 Comparison between different ignition technologies (SI, HCCI and jet ignition)
 [41][42][43][75][76][77][78]

Ignition system	Spark Ignition	HCCI	Jet Ignition
Special technology and parts required for operation	Spark plug, PI or DI injector, three-way catalytic converter	Spark plug, PI or DI injector, three-way catalytic converter (or a lean NOx trap, NSC), variable valve lift and phasing, DI injector, advanced control system with closed loop combustion control	Spark plug, PI or DI injector for the main chamber and DI injector for the pre-chamber
Control	Least complicated control strategy	Most complicated control strategy	Similar to SIDI with multiple pulse injections
Engine structure	Least expensive and maintenance	High-rate pressure rise add cost and weight due to structure concern	Similar to but more expensive than SI engine
Fuel economy over drive cycle	Lowest drive-cycle fuel economy	Up to 10%–15% improvement compared with SI engine	Up to 18% improvement compared with SI engine
Emissions	Very low emissions using three-way catalyst	Low NOx emission	Low NOx emission, requiring three-way catalyst
Peak efficiency	Lowest efficiency	High efficiency compared with SI engine	High efficiency compared with SI engine

2.4.2 Mahle TJI

The Mahle TJI unit has been developed and designed to achieve a more realisable system in modern SI production engine. The system has also been developed to operate on readily available commercial fuels (e.g. gasoline, propane and natural gas), overcoming previous jet ignition hurdles of using biofuel, such as ethanol and wet-ethanol as the pre-chamber fuel. Other pre-chamber applications have exhibited capabilities of burning a lean mixture, improving combustion efficiency and reducing exhaust emission. By contrast, Mahle TJI has been designed to obtain the following characteristics (Figure 2.12):

- extremely small pre-chamber volume (~2% of the clearance volume)
- pre-chamber connected to main chamber by small orifice/multi-orifices (~1.25 mm diameter) that supports flame quenching and penetration into the main chamber
- separately fuelled pre-chamber allowing a rich mixture to be contained in the prechamber whilst the main chamber is heavily diluted
- separately fuelled main chamber
- spark discharge initiating pre-chamber combustion (flush mounted electronically controlled spark plug)
- research targets using readily available commercial fuels for the main chamber and pre-chamber

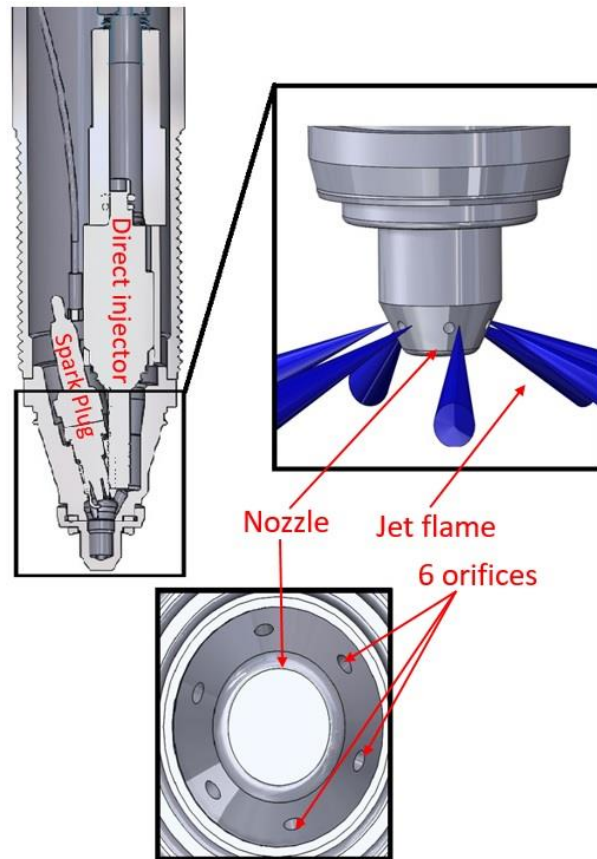


Figure 2.12 TJI pre-chamber and nozzle

Figure 2.13 shows the TJI sequence over one complete engine cycle. The main difference between conventional SI and pre-chamber ignition system is the added small quantities of pre-chamber fuel ($\sim 2\%$ of total energy). Generally, the pre-chamber fuelling event is timed to end at approximately 50° prior to spark discharge [67]. This approach guarantees that a rich plentiful mixture can be contained in the pre-chamber before the spark discharge, which has been proven to chemically enhance combustion through the formation of active radicals [79].

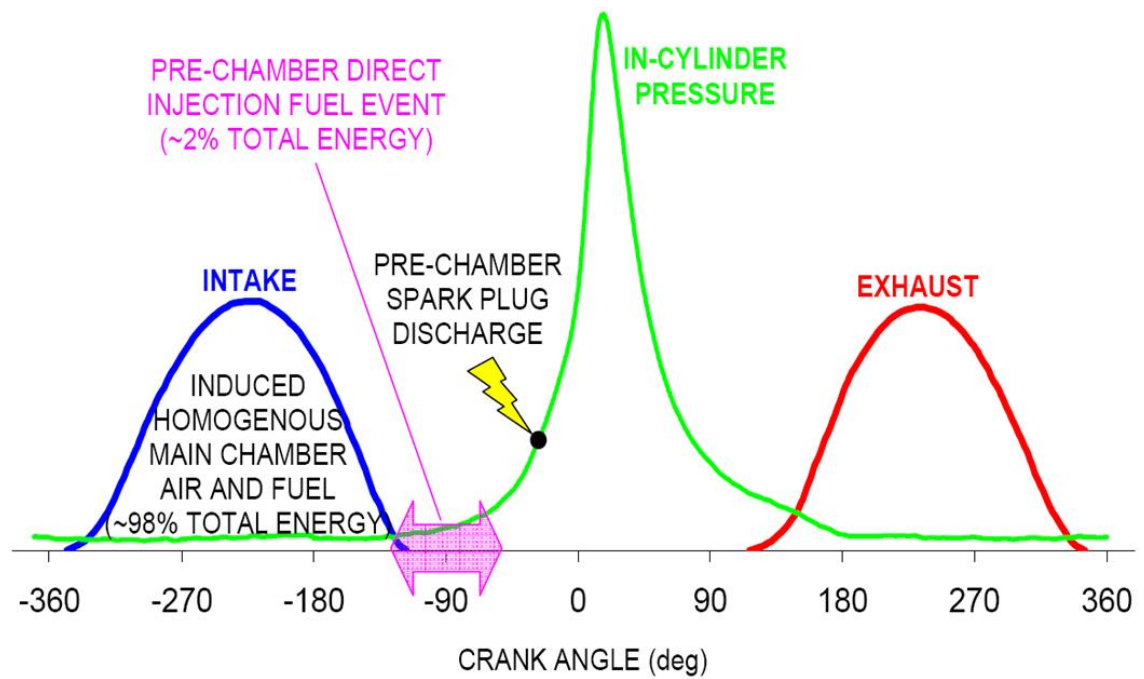


Figure 2.13 Timeline of TJI Sequence[77]

Most of the published studies on the Mahle TJI unit focus on pre-chamber systems' orifice nozzle diameter and/or pre-chamber volume. The effect of the pre-chamber nozzle orifice diameter and the total cross-sectional area of the nozzle orifices have been studied in several works [80][81]. For instance, Ashish et al. [82] evaluated the influence of the pre-chamber volume and nozzle diameter on a large bore natural gas single-cylinder engine. The results show that the pre-chamber volume and nozzle diameter affect combustion by enhancing efficiency and reducing engine emissions. Kawabata et al. [83] optically investigated the influence of different nozzle orifice diameters by observing the flame jets emerging from the pre-chamber and the dependencies of the number of orifices on the flame jet distribution. Bunce et al. [3] also studied the effect of nozzle design on engine efficiency and performance by testing different orifice diameters and varying numbers in an optical engine. They revealed that the main chamber ignition is sensitive to the diameter of the orifices' nozzle. They compared the diameters of small and large orifices' nozzle to observe their effects on combustion, and they found that a small orifice generates choked flow jets that are limited in their energy density. To the contrary, a large orifice produces jets that contain a substantial flame from the pre-chamber combustion.

Baumgartner et al. [84] carried out further work on TJI design. They tested the effect of pre-chamber orifices with variations of their orientation and number at different

operating conditions of engine speed and load. The results conclude that orifice diameter controls the operating conditions of pre-chamber ignition systems. Reduced orifice diameters accelerate the jets emerging into the main chamber. Moreover, orifice direction must be perpendicular to the surface to obtain impingement and enhanced entrainment in the back flow.

Bunce and Blaxill [67] aimed to enhance understanding of TJI combustion, specifically in terms of the ignition of the main chamber and the dynamics of the interaction between the pre-chamber and main chamber. A single-cylinder engine and an optical engine were used to conduct experiments and compare the results. The pre-chamber volume was <5% v/v of the main combustion chamber volume. The pre-chamber and main chamber were fuelled with liquid indolene for both engines. Different TJI designs were used, as shown in Table 2.3. The results reveal that for all the different designs, visible jets appear from the pre-chamber within 1° CA of the point, at which its pressure peaks during combustion. The metal engine results indicate a delay of 5° CA after spark. At this crank angle, the pre-chamber pressure evidently increases above that of the main chamber.

Table 2.3 Different TJI designs

Nozzle Design	Number of nozzle orifices	Nozzle orifice diameter (norm.)	Nozzle orifice area (norm.)	Nozzle orifice L/D ratio (norm.)
1	4	0.64	0.27	0.73
2	8	0.64	0.54	0.73
3 (base)	6	1	1	1
4	4	1.36	1.24	1.22
5	8	1.36	2.48	1.22

Gentz et al. [85] studied the auto-ignition of the unburned mixture, effect of nozzle geometry and performance of combustion. They used a rapid compression machine, liquid iso-octane and a low flow fuel injector (Figure 2.14). The results indicate that using auxiliary fuel and increasing the number of orifices can control combustion stability. Gentz et al. [85] also used a high-speed imaging technique to study the auto-ignition phenomenon. The image shows that increasing the injector pulse width leads to acceleration of the auto-ignition.

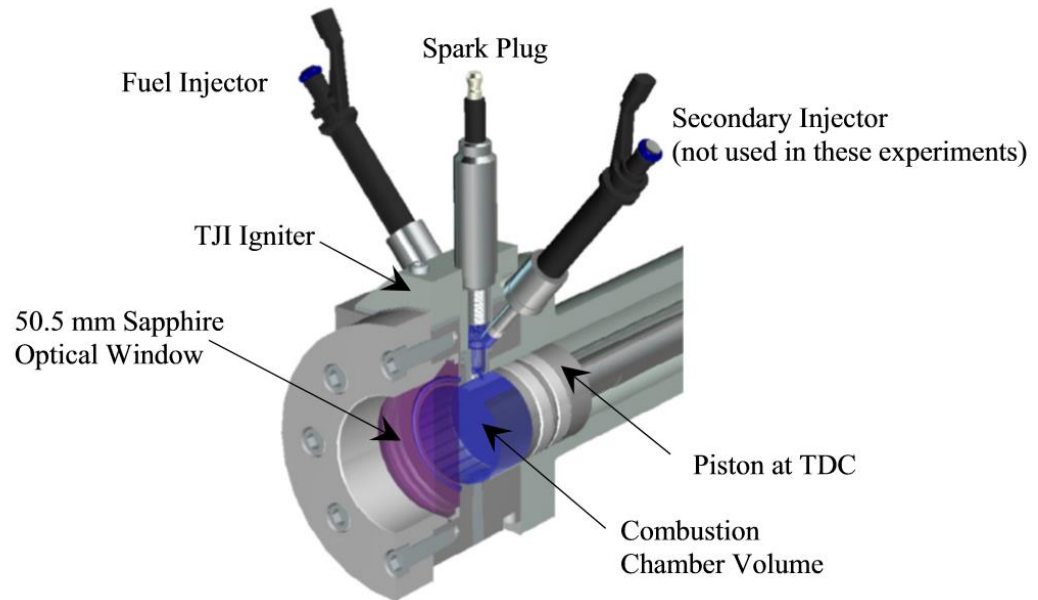


Figure 2.14 Rapid compression machine and optical and TJI igniters used with the RCM piston at TDC

In another research, Gentz et al. [86] used three different single orifice nozzles with diameters of 1.5, 2 and 3 mm to test a TJI pre-chamber fixed at optical RCM over a range of air–fuel ratios. Additional experiments were also undertaken using CFD modelling to simulate TJI in the RCM. The results illustrate that the smallest orifice diameter of 1.5 mm provides the shortest burn duration of 0%–10%, which corresponds to the fastest flame initiation. Figure 2.15 shows the combustion visualisation of TJI in the main chamber of the RCM for a stoichiometric air–fuel ratio $\lambda = 1$, as captured by a high-speed camera.

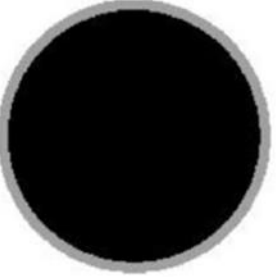
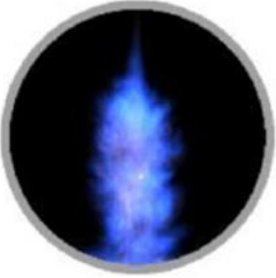
Time (ms)	D=1x1.5 (mm)	D= 1x 2.0 (mm)	D=1x 3.0 (mm)
1.0			
1.1			
1.2			
1.3			

Figure 2.15 Combustion visualisation of TJI in the main chamber of the RCM for a stoichiometric air–fuel ratio $\lambda = 1$

Attard et al. [30] used a modern PFI engine fuelled with seven PRF blends ranging from 93 to 60 octane number to determine the knock limit extension with an unfuelled pre-chamber jet igniter. All the test conditions were applied experimentally in a stoichiometric normally aspirated single-cylinder research engine at a fixed speed of 1500 rev/min and MBT spark timing. Figure 2.16 summarises the results from the first phase of experiments. An improvement of 10 octane number was recorded with the unfuelled pre-chamber when compared with the conventional SI combustion because

of burn rate enhancement. Moreover, the results show that the unfuelled pre-chamber jet igniter can operate on 65 octane fuel compared with normal spark plug due to the increased ignition delay and rapid combustion. Through pre-chamber auxiliary addition, the results indicate significant lean limit extension and successfully operating engine with 60 octane fuel.

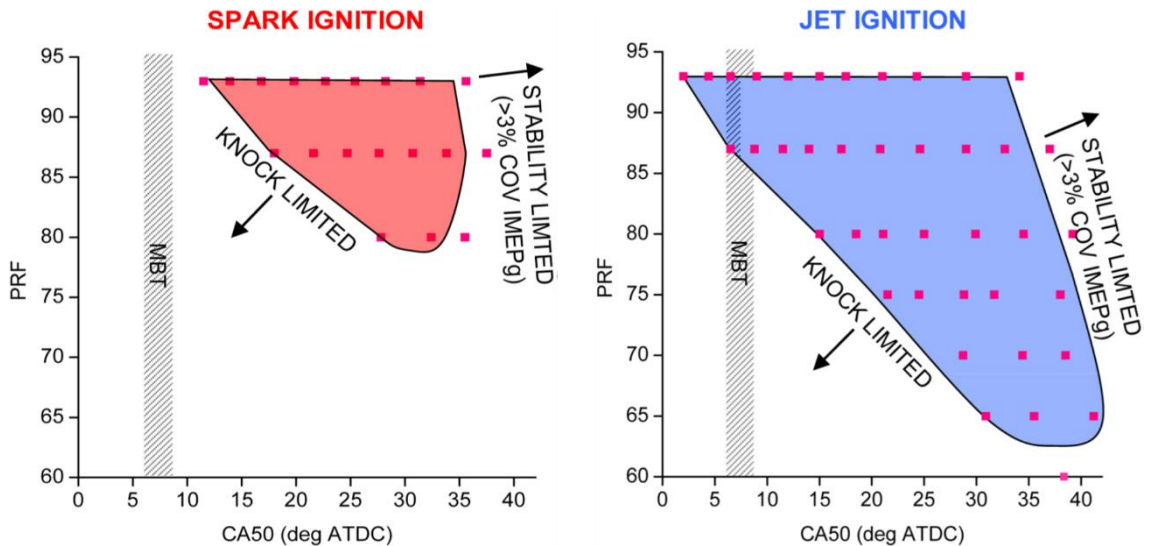


Figure 2.16 SI and TJI combustion operating maps with varying fuel octane and combustion phasing. 1500 rev/min, 98 kPa MAP (~WOT) and stoichiometric conditions.

Attard et al. [87] analysed natural gas combustion in an optically accessible engine ignited by a pre-chamber at several different air–fuel ratios, speed and load. All the pre-chamber results were compared with baseline SI. The results highlight reductions in flame propagation rates at further lean due to poor combustion. The pre-chamber ignition system actually reach ultra-lean ($\lambda = 1.8$) because of the enhancement, which leads to faster burning rate. By contrast, Kontakiotis et al. [88] showed how maximum lean can be reached by normal SI. Lambda equals to 1.21, with a speed of 4000 rpm and an 80% throttle position. The identical ignition timing is 38° CA bTDC, and the lean limit is controlled by cycle-to-cycle combustion variability.

2.5 Alternative Fuels for SI Engines

Alternative fuels, such as alcohols, have been used in different types of combustion engines. Their usage can be either as neat fuels, blended with base fuels (diesel or gasoline) or even as an additive. The uses of ethanol have been remarkably expanded in the SI engine due to its economic viability and less exhaust emissions than fossil fuels.

Ethanol is considered a suitable candidate to replace fossil fuel as a renewable fuel [89][90]. The higher octane number of ethanol also enables a higher compression ratio to be used for better thermal efficiency. Figure 2.17 shows the global ethanol production from 2007 until 2016. In 2016, the global ethanol production doubled compared with that in 2007. Ethanol is often blended with gasoline, for instance E10 or E5, and used widely in many countries.

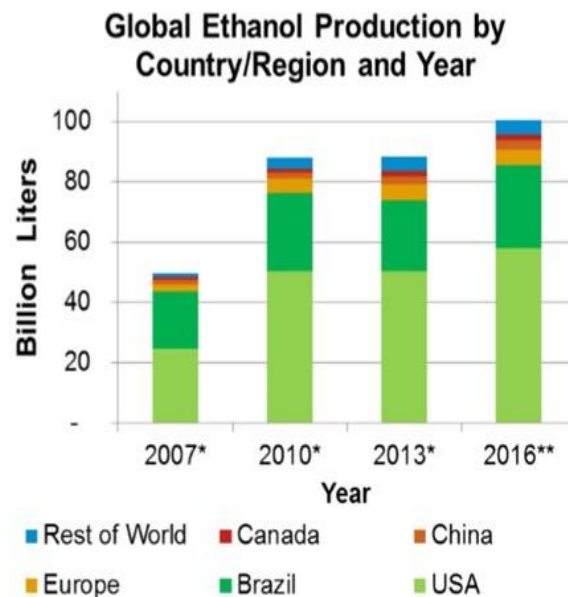


Figure 2.17 Global ethanol production by country/region and year (adapted from [91][92])

Ethanol can be produced using many sources, including fermenting sugars from wheat, corn, triticale, rye, barley, sweet sorghum, sugarcane, sugar beet or cassava. The raw material is initially milled and then passes through different stages to produce ethanol. The subsequent processes are saccharification, fermentation, distillation and dehydration. In the late 1970s, the U.S. implemented tax credits for ethanol production to support the corn agricultural sector because of the growing environmental concerns regarding gasoline anti-knock additives and, hence, the need to find an alternative fuel source [93]. At the beginning of 2006, the U.S. government supported ethanol production [94]. Similarly, since the 1970s, Brazil has implemented a programme promoting the production of sugarcane by connecting the agricultural and industrial sectors to its market [95].

The second source is from wood industry waste, corn and rice straw which are converted into sugar. Producing ethanol from industrial waste is more beneficial for the environment; however, it is more expensive than the first source [94]. A proposed third source is algae, and the latest technology to produce ethanol is to sequester CO₂ from the air and transform it to alcohol with renewable hydrogen [96].

The final stage in producing ethanol is separation and dehydration due to water content. Generally, the ethanol output contains 6% to 12% water [97], and removing water from ethanol consumes additional energy [98]. Figure 2.18 illustrates the steps and energy consumption for producing ethanol from corn in the U.S. Anhydrous ethanol requires more energy to dry the ethanol/water mixture. Between anhydrous and wet-ethanol, the latter is preferred as it can be used directly in the engine.

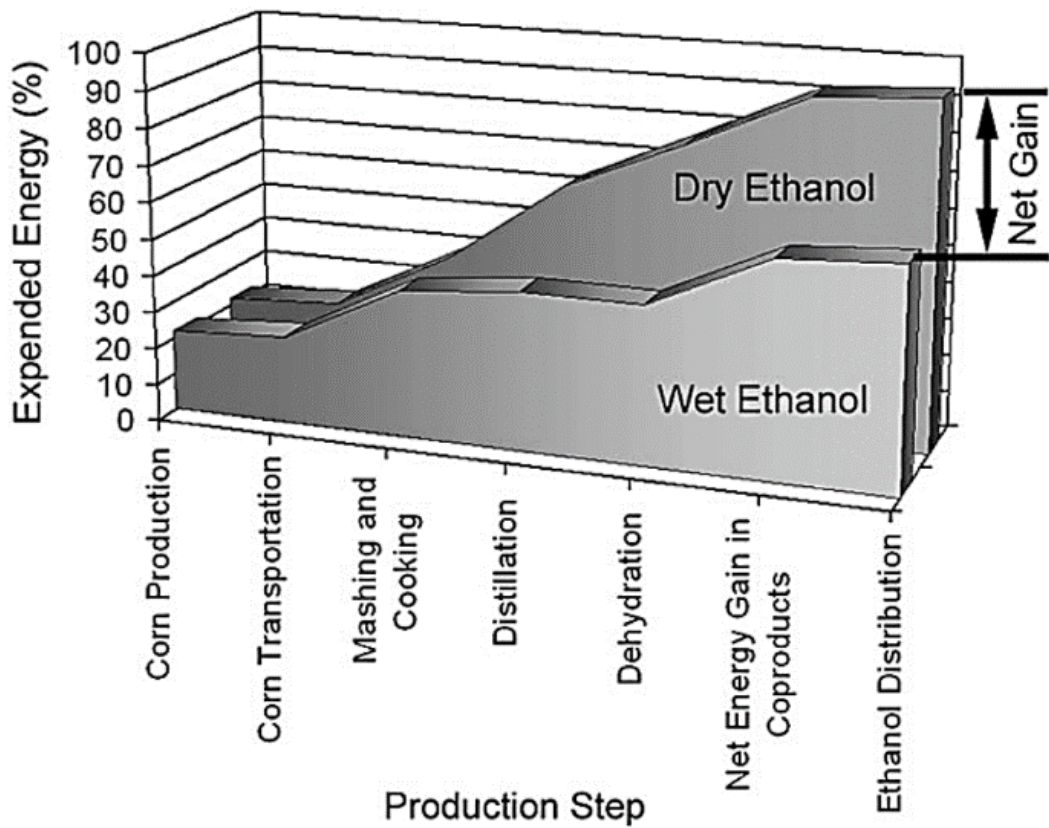


Figure 2.18 Comparison of net energy balance for anhydrous and wet ethanol (E65W35) considering all ethanol production steps [99]

In 1949, Wiebe and Porter [100] reported the first application of wet-ethanol in IC engines by injecting it into the intake system of aircraft engines. This method aimed to decrease the charge temperature and reduce knock tendency. The results show that an

alcohol–water mixture increases fuel economy and power output because the engine runs with advanced spark timing and high engine compression ratio. Brewster [101] used a four-cylinder air-assisted direct injection turbo-charged engine at high loads to study combustion when using wet-ethanol with up to 20% of water on a mass basis. Wet-ethanol requires advanced spark timing because it produces a high exhaust gas temperature when delayed. Wet-ethanol also reduces NO_x. The problem is that the presence of water reduces flame speed and extends combustion duration [47].

2.6 Combustion Imaging and Spectroscopic Measurement of Combustion Radicals

The light emission of flame in an SI engine is dominated by the chemiluminescence occurring in the flame front and burned gas region. Chemiluminescence is a light emission resulting from chemical reactions of hydrocarbon fuel and oxygen through combustion [102], as depicted in Figure 2.19. Chemiluminescences can occur across UV and visible spectral range, depending on the type of molecules involved in the chemical reactions. When flame images are obtained, they effectively record the chemiluminescence integrated over the broad range of spectrum depending on the camera's spectral response region.

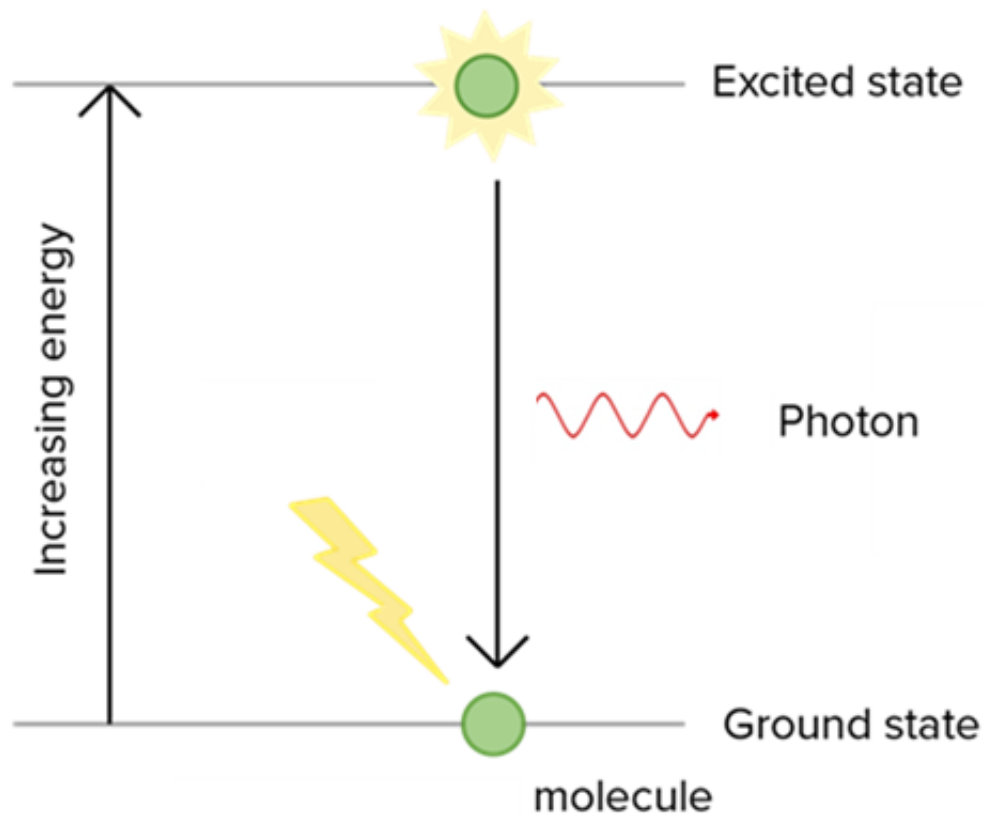


Figure 2.19 Electrons excited by exothermic reactions to a higher energy level and photons produced during the subsequent decay of electrons to a lower energy level

The optical engine has been regularly used to observe the ignition and combustion of conventional SI and compression ignition combustion operations since the 1930s when the first flame imaging was recorded through optical windows [103]. Glyde utilised six miniature windows in the cylinder head to withstand the high combustion pressure due to the mechanical limitation of the optical windows available at the time. In the 1930s, Rassweiler and Withrow [104][105] used a high-speed film camera to record up to 5000 frames per second (fps) at speed 2000 rpm, equivalent to 2.4 crank angle degrees for every image, to capture the flame as it progressed across the cylinder. They established a method to calculate the mass fraction burnt that is still used at present for its simplicity, which is suitable for rapid online calculations.

With the advances in optical engine design and windows, larger optical access through the piston crown or cylinder head has been installed to provide better and larger view of combustion in the optical engine. Augoye and Aleiferis [106] studied flame behaviour

of different fuels and fuel injectors in an optical engine through high-speed flame chemiluminescence imaging. Ben et al. [107] used high-speed flame imaging to study the fundamental of ethanol turbulent flame development and found that pure ethanol is characterised with the highest initial laminar-like burning velocity compared with other fuels, such as gasoline, iso-octane, pure ethanol and an E10 fuel consisting of ethanol and iso-octane.

Several optical studies on TJI system have been performed in different optical engine setups and rapid compression machines. Bunce et al. [3] and Bunce and Blaxill [67] studied the effects of nozzle design on the turbulent jet characteristics and combustion in the main chamber by using high-speed flame imaging technique. They gained central insights into how TJI ignites the charge in the main chamber by comparing the simultaneously recorded in-cylinder pressure measurements in the pre-chamber and the main chamber. The speed of turbulent jets was calculated by measuring the distance travelled from the nozzle orifice and time interval between frames. The result confirms that smaller orifice area produces turbulent jets that are of high velocity and penetrate deeply into the main chamber.

Gerald and Elisa [69] studied the TJI combustion by using a coloured high-speed camera in an optical accessible RCM. They studied the effect of TJI with and without auxiliary fuel (propane) injection into the pre-chamber volume. The results show that, with auxiliary injection fuel, combustion is faster, and the jet emerges into the main chamber of the RCM faster than in the unfuelled case. They also compared the pre-chamber ignition system with small nozzles and a large connection channel to illustrate the important effect of the nozzle geometry. By installing a nozzle, the hot radicals from the pre-chamber penetrates deeper into the main chamber, and the effect is much faster than without the nozzle. Attard et al. [87] compared the combustion visualisation between conventional spark plug ignition and TJI in an optical signal cylinder engine with different air–fuel ratios at different speeds. A significant reduction in flame propagation rates is found owing to the TJI as excess air dilution increases across all test points.

2.7 Detection of Combustion Radicals Through Spectroscopy

In addition to the overall chemiluminescence flame images, individual combustion radicals, such as OH, CH and C₂, can be detected through spectroscopic analysis of the

emission spectra [108]. Using spectroscopy to investigate the quality and quantity of light emitted by flames during combustion is important to the study on combustion processes. Spectrophotometry is utilised to conduct a chemical analysis of combustion flame due to the importance of assessing trace elements, in which each flame has its own properties of spectrum. For instance, flames of hydrogen show very little visible light but provide strong bands in the near ultra-violet (UV), whereas the flames of carbon monoxide illustrate blue burning flame, particularly a continuous spectrum from green to the near UV with a large number of faint bands.

In one of the earliest spectroscopic studies on SI combustion, Rassweiler and Withrow [105] found that a flame front through the knocking cycle-emitted photons are associated with the existence of C_2 , methane and hydroxide. Recently, Augoye and Aleiferis et al. [106] have used high-speed chemiluminescence imaging to observe flame growth and OH planar laser-induced fluorescence images to introduce the local flame front structure of all tested fuels (hydrous ethanol, anhydrous ethanol, iso-octane and gasoline) in a single-cylinder SI research engine with 1000 rpm load and 0.5 bar intake plenum pressure. Through spectroscopic analysis, Augusta et al. [109] found that CHO, CH_2O , CH and OH are the major spectra during combustion. Kawahara et al. [104] confirmed the previous relationship by using a Cassegrain optic sensor. This sensor was adapted to measure local chemiluminescence spectra and the local chemiluminescence intensities of OH, CH and C_2 in a four-stroke SI engine. Fissenewert et al. [110] used an optical engine fuelled with iso-octane fuel under spray-guided DI to observe soot formation in cycle-to-cycle variation by using laser-induced fluorescence imaging and UV chemiluminescence at exhaust and late 'homogeneous vs. stratified' injection conditions. Schlatter et al. compared a pre-chamber TJI (spark plug) and pilot injection of a little amount of liquid diesel fuel (auto-ignition) in rapid compression expansion machine adopted with optical system to investigate the emission of OH, CH and C_2 radicals. Table 2.4 presents the prominent spectral peaks of intermediates and products of auto-ignition and combustion in UV and visible regions.

Table 2.4 Strong emission peaks of major combustion [111]

Methane	Hydroxide	Formaldehyde	CO ₂	C ₂	Aldehyde
CH (nm)	OH (nm)	CH ₂ O (nm)	CO ₂ (μm)	(nm)	CHO (nm)
314–387	302–309	368–384	2.69–2.77	470–474	320–330
389–431		395–412	4.25–4.3	516–558	340–355
		457		563	360–3801
					385

2.7.1 OH Chemiluminescence

Using OH radical to identify the flame front marker is challenging with natural light imaging. Finding the accurate front of the flame depends on identifying the UV light released from the hydroxide elements. Generally, this marker is not visible via cool flame combustion. Srinivasan and Saravanan [112] demonstrated that ethanol gains lower light intensity because of cooler combustion temperatures. Many studies observe OH radical during hydrocarbon combustion. Tracing the OH radical through combustion has many benefits. The main advantage is that OH radical provides extensive information about flame propagation, chemical structure and combustion flame through ignition. The chemiluminescence of OH is produced from the electronically excited hydroxyl radical. Tanaka and Tabata [113] used planar laser-intensified fluorescence (PLIF) device to investigate the OH radical in the combustion chamber of an SI engine fuelled by gasoline. Moreover, the device was used to analyse the chemical structure of different combustion processes and reaction mechanisms of combustion. Lu et al. [114] conducted an experiment through spectrum chemiluminescence imaging and found that the OH radical begins from the premix combustion period until the early diffusion combustion period. A relationship between OH emission and EGR concentration and equivalence ratio is noted due to the amount of the existing oxygen during combustion. Lu et al. [114] also demonstrated the advantage of OH radical, that is, it can be used to burn part of the soot formed early in the combustion process. Through spectrometer and intensified camera (ICCD) analysis adopted on truck-sized optical engine and fuelled by the combination of n-heptane and iso-octane used to study homogeneous charge

compression ignition (HCCI) during combustion, Hultqvist et al. [115] found that the OH radicals formed at peak temperature provide an impression that a combustion reaction occurs in the hydrocarbon flames and speeds up the main heat release.

2.7.2 H₂O, CH, C₂ and HCO Chemiluminescence

H₂O, OH, C₂, NO and CO result from a chemical reaction between hydrocarbon fuel and oxygen. They are used to analyse flame combustion and spark kernel growth during combustion. Experimental works prove that H₂O, OH, C₂, NO and CO radicals form at high temperature at the reaction zone and decrease after the burning zone [115]. Moreover, all these radicals form in the SI and compression ignition engines. Many techniques are used to detect the chemiluminescence of radical emission during combustion, including spectroscopy, PLIF and intensified CCD camera [116][117][118]. Currently, global warming is a major concern due to its effects on the environment and humans. One of the main causes of this phenomenon is exhaust emission from combustion especially from transportation modes (road and off-road cars, airplanes). John and Robert [119] used PLIF imaging technique to measure the NO formation during DI diesel combustion. Moreover, many studies use chemiluminescence to develop combustion engines and facilitate emission improvements [118][120].

2.8 Summary of Reviewed Literature

The SI gasoline engine has been the subject of extensive and continued research and development over the recent years to improve thermal efficiency and reduce CO₂ emissions. A range of combustion and engine technologies have been developed and applied to modern SI engines which are typically operated with stoichiometric air–fuel mixture. Lean-burn combustion is identified as a key enabler for developing future high-efficiency gasoline engines. The pre-chamber ignition can effectively extend the lean-burn limit of an SI engine to overcome the problems of unstable ignition and slow flame propagation speed of the lean-burn mixtures. In particular, the TJI technology is well suited for modern gasoline engines, and the Mahle TJI unit can improve the lean-burn combustion of gasoline engine.

In the current research, further investigation is carried out to enhance understanding of the effect of Mahle TJI on engine operations fuelled with gasoline and ethanol or wet-

ethanol. The pre-chamber charge preparation during ignition and combustion is investigated through in-cylinder high-speed imaging and spectroscopic measurements as well as heat release analysis in the pre-chamber and main chamber.

Chapter 3 Engine Design and Experiment Setup

3.1 Introduction

In any experimental work, the development of a testing setup that can deliver reliable results is a prerequisite. In this dissertation, a Lister Petter TS-1 engine was used to investigate combustion processes with a fully redesigned cylinder head. The original full-bore overhead optical engine was modified to replace the normal spark plug with Mahle TJI unit, as shown in Figure 3.1. The modified cylinder head with half-bore optical access allowed direct visual observation of the combustion events in the main chamber after initiating the pre-chamber ignition in the TJI unit. In this chapter, the engine setup is presented, and the design and installation of the new cylinder head are described in detail.

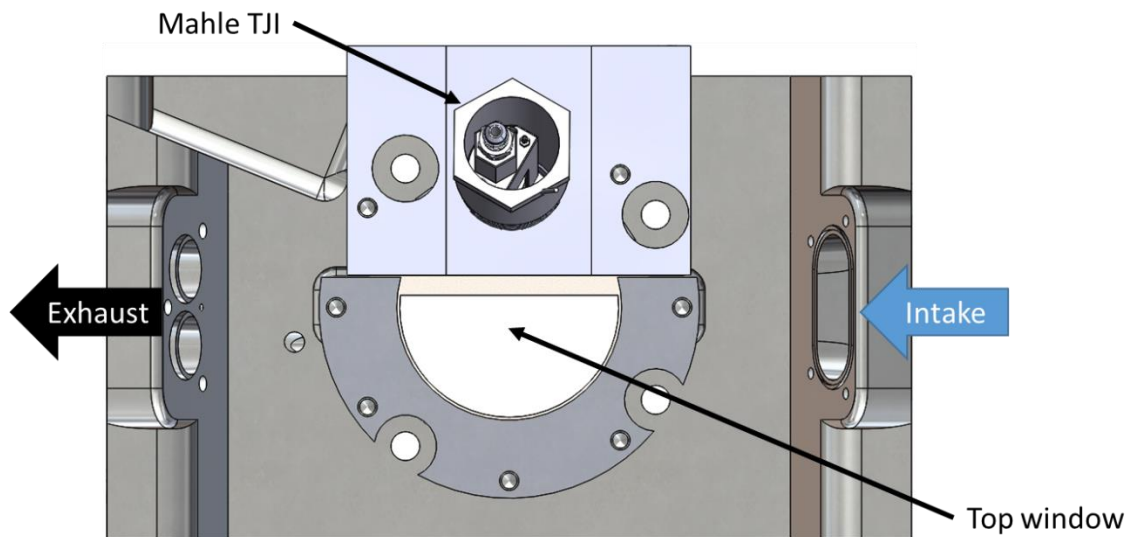


Figure 3.1 Modified cylinder head

3.2 Engine Setup

The original single-cylinder engine was designed as an air-cooled DI single-cylinder diesel engine with overhead valves. It has a bore of 95 mm and stroke of 89 mm. In previous projects, an optical cylinder head was designed to provide a full view of the combustion chamber from the top by placing the valves on the sides [107][121][122]. The optical window was sufficiently strong to withstand peak cylinder pressure up to 150 bar, enabling the study of knocking combustion.

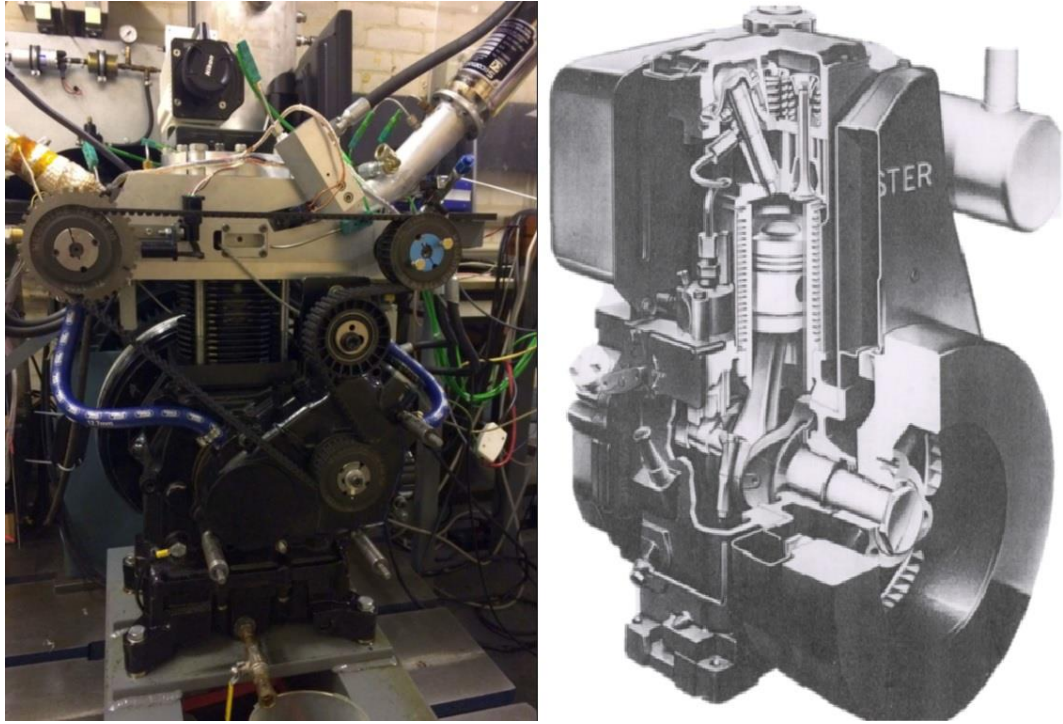


Figure 3.2 Current engine with modified cylinder head on top (left), original Lister Petter TS-1 engine (right).

In addition to the top window, two side windows allow the observation of the combustion process from the sides. Further details of the cylinder and window design are discussed in the subsequent section. The inlet and exhaust poppet valves are actuated by the two camshafts fitted on the opposite sides of the cylinder head. The two camshafts are connected to the crankshaft by belts.

The optical engine contains a flat-roofed combustion chamber with flat crown piston. In the current work, the conventional spark ignition was replaced with the pre-chamber ignition (detailed in the subsequent section), but an additional spark plug was mounted on the side of the cylinder head in case of misfire. The clearance height at TDC is 9 mm. Table 3.1 presents the engine geometry. The engine was connected to a 10-kW electric motor for motored and fired operations.

Table 3.1 Engine geometric parameters

Parameter	Value
Bore	95 mm
Stroke	89 mm
Geometric Compression Ratio	8.45:1
Displacement	631 cc
Number of Cylinders	1
Number of Valves per Cylinder	4
Inlet Duration (end of ramp)	230° CA
Exhaust Duration (end of ramp)	230° CA
Clash limited IMOP	100° aTDC
Clash limited EMOP	100° aTDC

3.2.1 Valve Selection

The 22 mm diameter valve was selected as the optimal size for this engine because of the relationship between the diameter of the valve head, choked engine speed and geometric compression ratio. Four valves were used on the side of the cylinder head to provide the required air for sufficient breathing (Figure 3.3). Each of the valve seats required a counter-bore to be machined into the cylinder head to control the placement. The cylinder head was sent to RST Company for spark erosion to open the inlet and outlet valves.

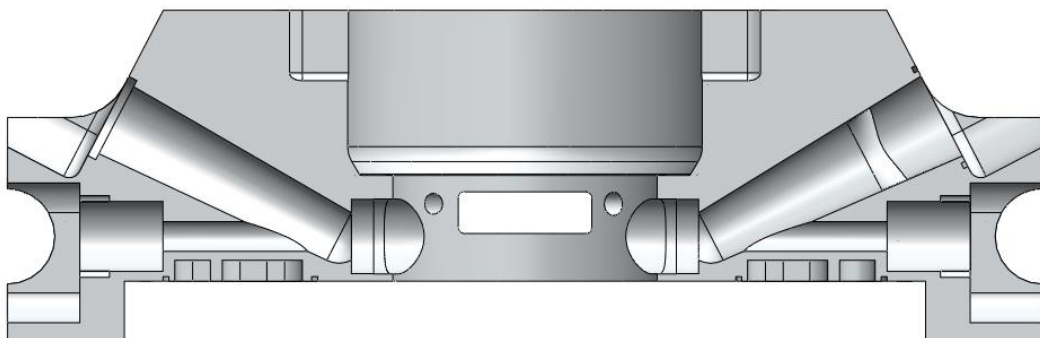


Figure 3.3 Cylinder head with cross-section through ports

The inlet camshaft has an Encoder Technology EB58 shaft encoder linked to the DAQ data system to provide the clock and TDC signals. The inlet and exhaust valve profiles

were selected to provide satisfactory scavenging and air induction at 1500 RPM at timing 230° duration (ramp end to ramp end) with a maximum lift of 5 mm, and the overlap was set to 20° (Figure 3.4). The two cylinder head camshafts were connected to the crankshaft by using a 30-mm wide simple pulley and 28-tooth taper-lock.

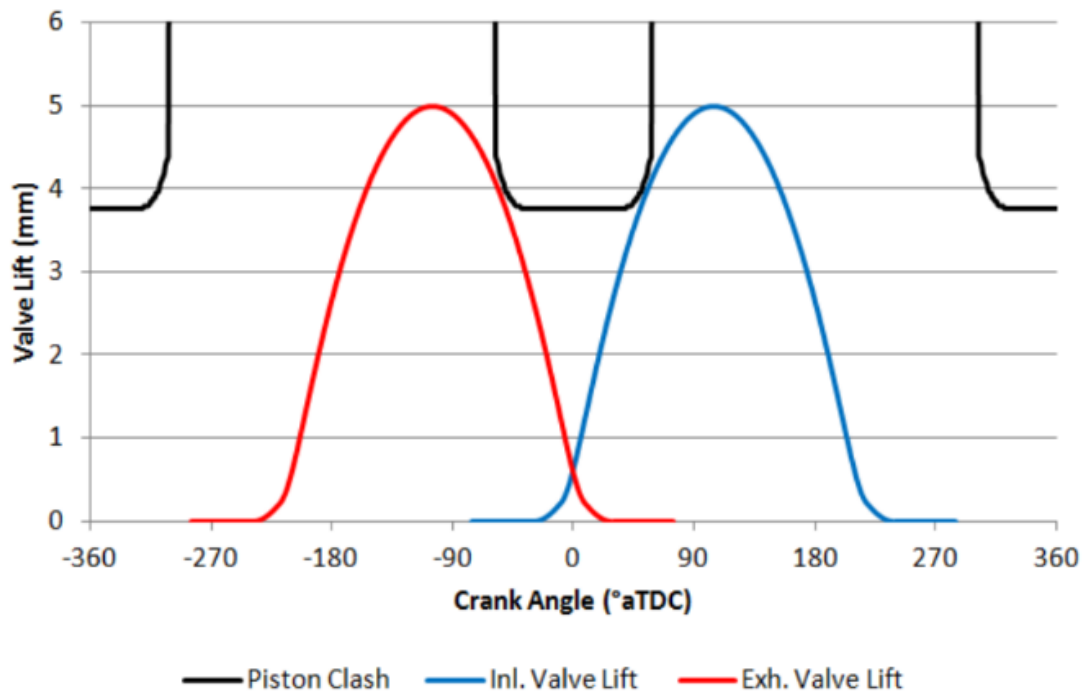


Figure 3.4 Selected valve timing

3.3 Fuel Supply

The fuel can be supplied to the cylinder either by a PFI or a DI injector. In this research the PFI was used for the main chamber and a bespoke DI injector for the pre-chamber. The main chamber used a separate fuelling rig. The fuel was delivered from a five-litre tank using an electric fuel pump to pressurise the fuel rail to three-bar gauge and a mechanical regulator to control the fuel pressure. A filter was installed downstream of the pump to clean the fuel from particles before it was injected to the engine, as shown in Figure 3.5.

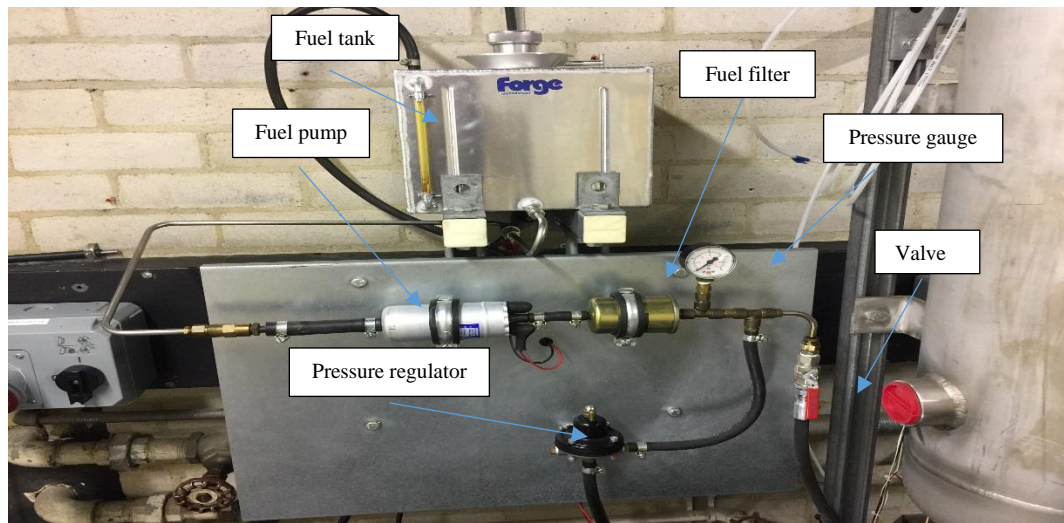


Figure 3.5 PFI fuel supply system

The pre-chamber was fuelled with a separate high-pressure fuel supply system comprising a two litre tank and a pneumatic driven diaphragm pump. The DI injector was assembled inside the Mahle TJI unit to inject the fuel into the pre-chamber volume. The pump was used to pressurise the fuel rail up to 70 bars. To filter the pre-chamber fuel, a filter was fitted between the fuel pump and fuel rail.

Both chambers could be supplied with different fuels including gasoline/alcohol blends, such as E90W5 and E100. The stainless steel lines and pumps were monitored to spot any corrosion or failure.

The DI injector in the pre-chamber was specially designed to inject a very small quantity of liquid fuel (~3% of total engine fuel) with small penetration. The injection was calibrated by measuring the injected fuel mass as a function of the pulse width, as illustrated in Figure 3.6. This finding is consistent with the original data provided by Mahle Powertrain.

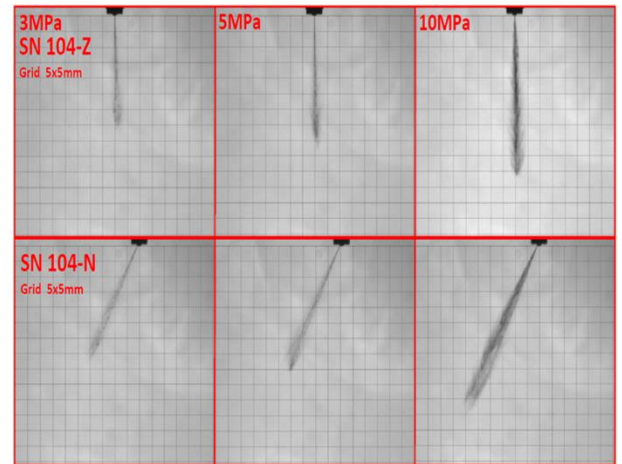
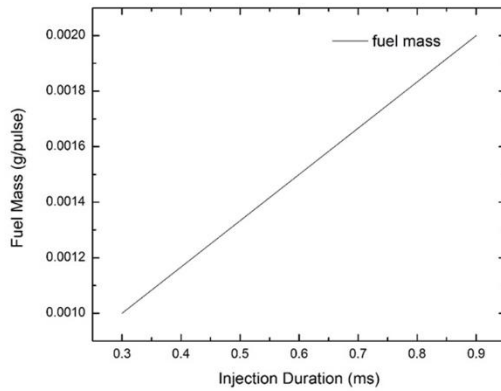


Figure 3.6 Average mass fraction burned (MFB) data for pre-chamber and normal SI

3.4 Engine Control and Instrumentation

3.4.1 Electric Control Unit (ECU)

An MBE 959 ECU was used for the control of normal engine operation with PFI and main chamber SI (Figure 3.7). Two trigger discs were fitted to the engine, one on the crankshaft and the other on the exhaust camshaft. Each disc has a 36:1 tooth pattern. The ECU used the trigger disc on the crank shaft to measure the engine speed and TDC timing. The trigger disc on the camshaft was used to synchronise the ECU with the exact phase of the engine.

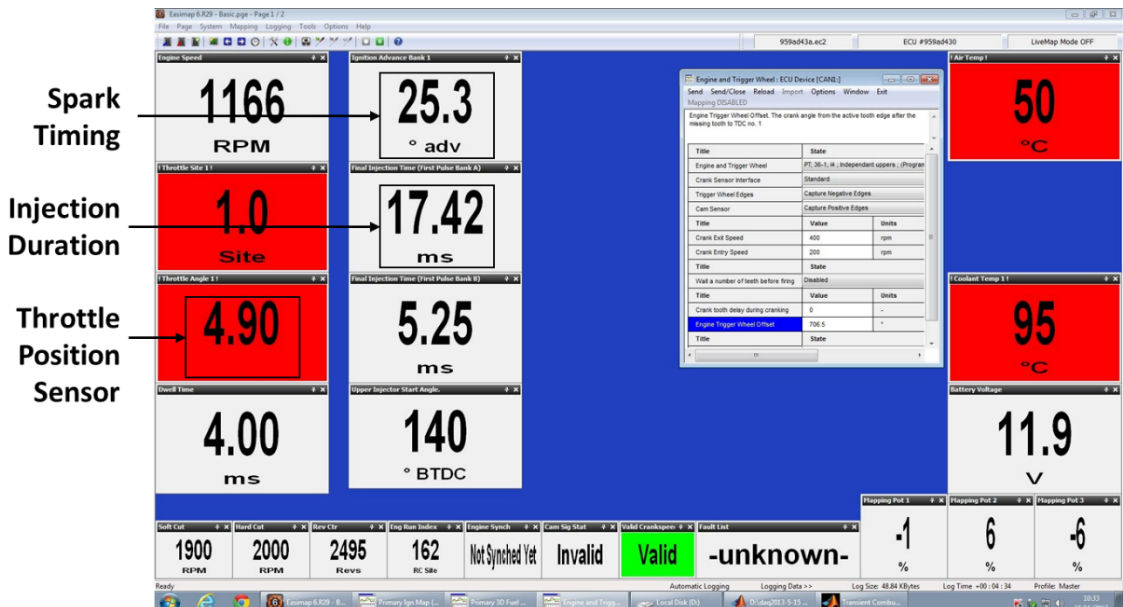


Figure 3.7 Screenshot of the data acquisition software

The DI injector was operated by a bespoke Delphi ECU that was especially manufactured for the Mahle TJI system when it was used in Mahle USA. In the current research, the

initial plan was to use the same MBE unit and recalibrate it to operate the DI injector and the spark plug in the pre-chamber. However, the MBE unit could not reproduce the DI injector voltage and current profiles, as presented in Figure 3.8.

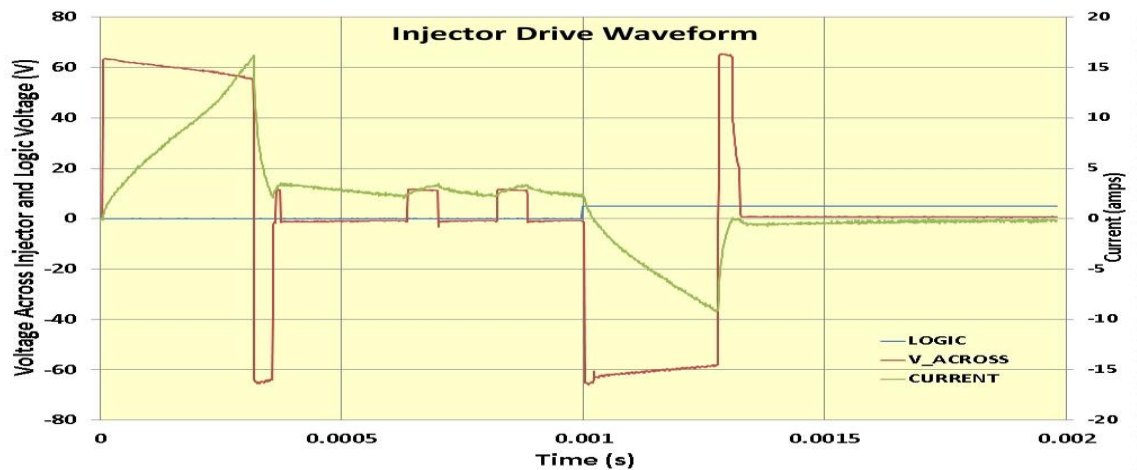


Figure 3.8 Injector current and voltage waveform for single-pulse mod

Finally, an NI DI driver system comprising an NI CompactRIO controller 9066, NI 9751 output module and NI 9760 input module was set up. The cRIO-9066 was connected to a host computer by using the RJ-45 Gigabit Ethernet port. The NI system provides a digital input per injector channel for directly commanding each injector. After testing, additional sensors had to be installed to provide the timing signals for the NI system to avoid the noise and interference problems, whereas the existing Hall effect and variable reluctance sensors on the timing discs were only used for the MBE unit. The two Hall effect sensors (1GT101DC) were sourced from RS online, whereas the two variable reluctance crank sensors were bought from a 2004 Ford Focus ST170. Each variable reluctance crank sensor needed two connections for signal and ground, and both Hall effect sensors required three connections of signal, 5A power and ground.

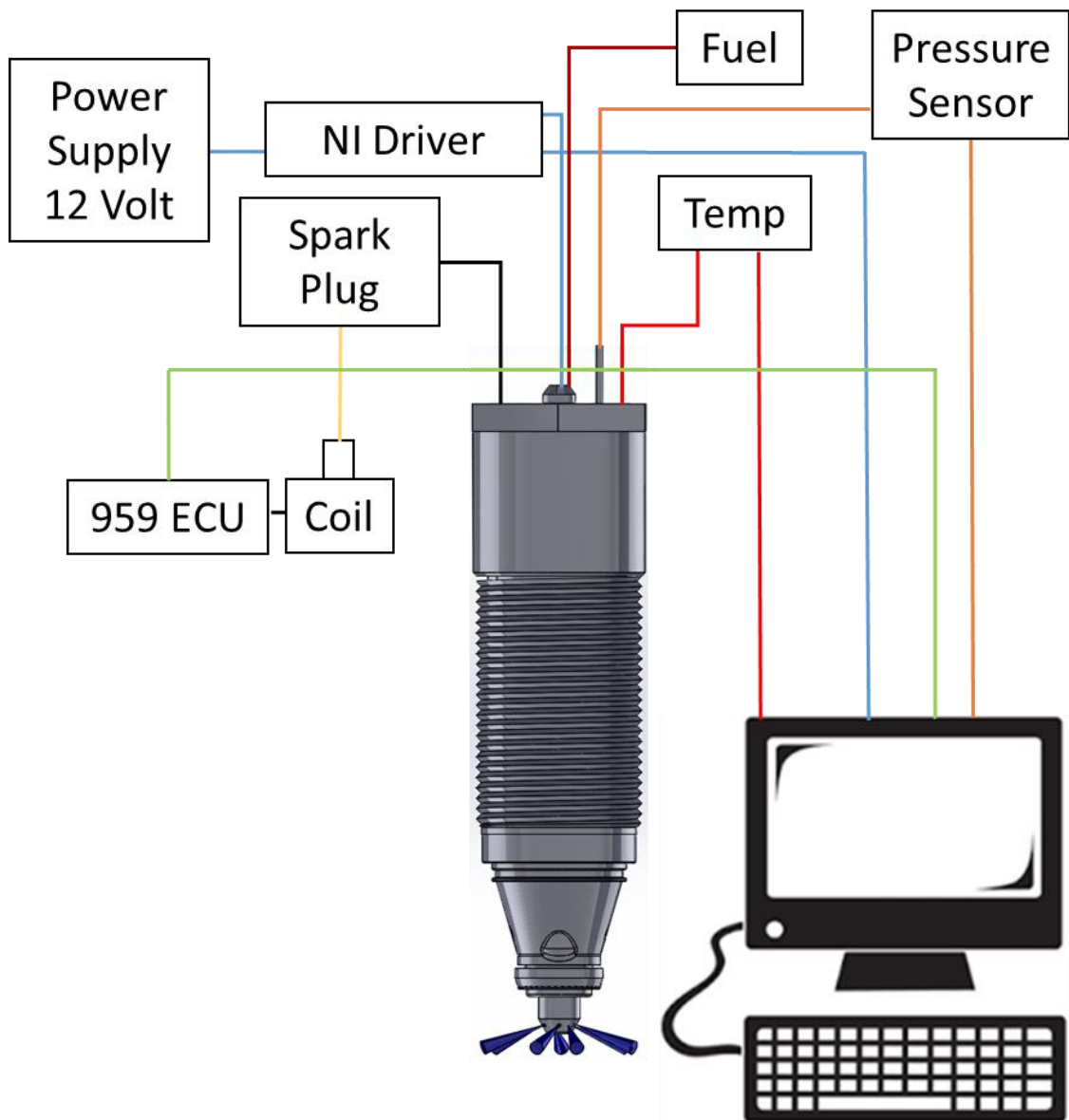


Figure 3.9 Schematic of the TJI's fuelling and engine control systems

To power the NI driver, 12 volt external power supply is required, as shown in Figures 3.9 and 3.10. The NI 9751 module was powered from cRIO driver, whereas the NI 9760 module could be operated with the existing external 12 voltage power supply. The maximum required power values for cRIO 9066, NI 9751 and NI 9760 were 25, 75 and 2 watts, respectively. The NI unit requires powering and grounding for each module in the system in a star-wiring configuration. Wire polarity is critical and highly recommended by NI. The NI 9751 driver module provided the input power to operate the DI injector inside the TJI unit whilst the NI 9760 module acted as a timing unit with inputs from the

Hall effect and variable reluctance sensors. To secure wire connections, the NI 9923 connector kit was used to connect to the NI 9760.

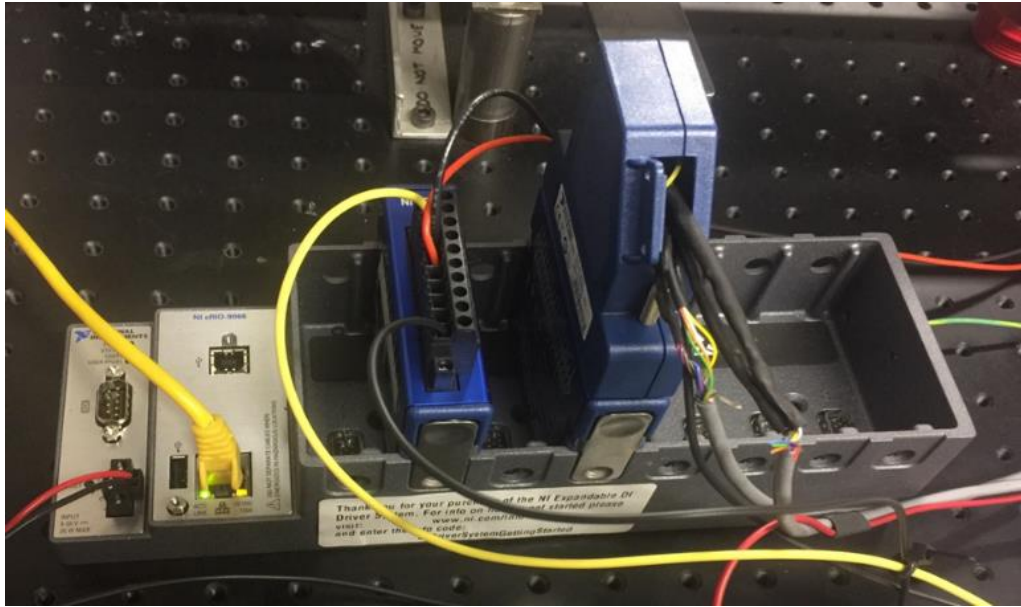


Figure 3.10 NI driver

The Labview-based NI Software Calibration Management (SCM) Toolkit version 2015 (Figure 3.11) was used to operate the NI DI injector driver unit.



Figure 3.11 Screenshot of the data acquisition software

The SCM software allowed the user to change the end of injection (EOI), duration of injection and start of injection. The NI driver could read the TDC by using cam and crank sensors. The sensor signals were configured via the engine position tracking (EPT) mode

tab of the pulse generation setup window. EPT parameters are configured via the EPT tab of the EPT setup window for a variety of crank and cam signal patterns. Tracing the current and voltage waves is possible by pressing on the DIX_Scope icon, as shown in Figure 3.12.

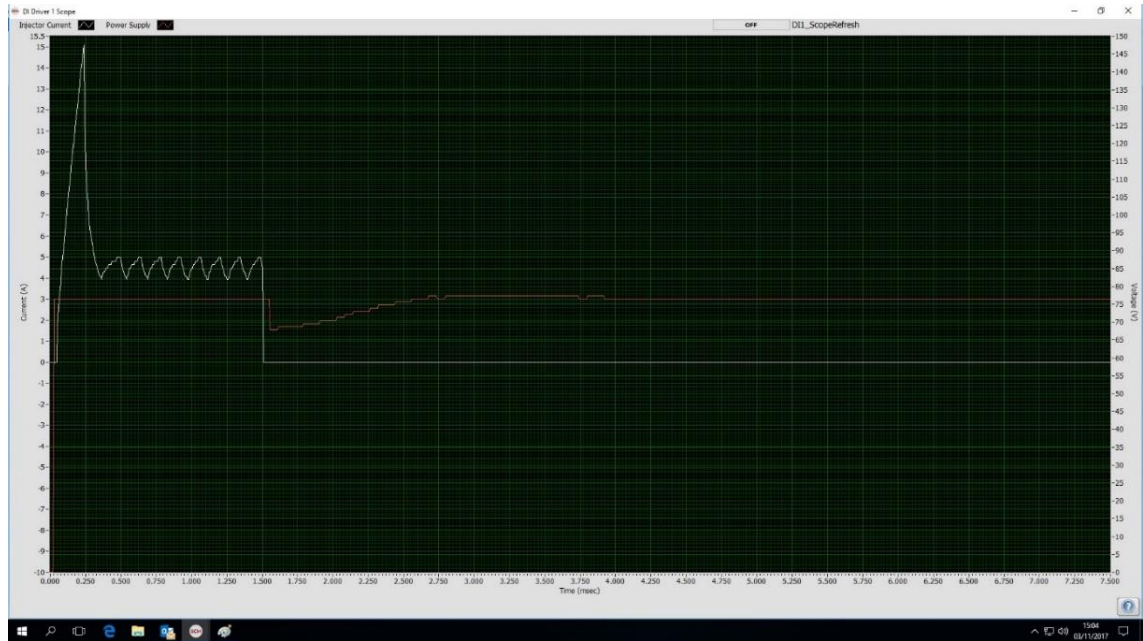


Figure 3.12 Actual trace waveform

3.4.2 Ignition Control

In this research, the spark plug was used to ignite the charge in the pre-chamber. An additional spark plug was installed in the cylinder head between the uppermost exhaust valve and the top side window, and it was only used during the test to compare with the pre-chamber ignition systems. Both ignition systems used NGK ER9EH 8-mm spark plug and an ignition coil (Bosch P100-T) that was modified to incorporate a longer high-tension lead with additional external electro-magnetic shielding. This is because the spark plug was slightly difficult to access once the pre-chamber was installed. The modified coil had a maximum ignition energy value of 100 mJ and a maximum ignition frequency of 133 Hz. The coil extender snaked down into the pre-chamber assembly with a rubber boot that suited at the top of the spark plug. A switch box was installed to switch the ignition on and off manually.

3.4.3 Engine Instrumentation

A 50 litre plenum was installed in the engine's intake system downstream of the intake throttle to reduce any pressure waves. The temperature and pressure of the air flow inside the plenum were recorded. A drain valve was used to remove any water that was present in the compressed air supply. The plenum flowed through a steel pipe and could be heated to a required temperature by a 2 kW Secomak 571/4 Process Heater via a closed loop temperature regulator attached to the heater. The temperature was measured via a k-type thermocouple.

The air–fuel ratio was measured by a Bosch LSU 4.9 UEGO (Universal Exhaust Gas Oxygen) lambda sensor in the exhaust tract linked to an ETAS LA4 lambda meter. The output of the lambda meter was logged onto the data acquisition system (DAQ). The air–fuel ratio inside the pre-chamber could be estimated after determining the overall lambda as well as the fuel in the main chamber. To control the mass flow rate of air and engine load, a 24-mm manual throttle was used. The throttle body was connected to two throttle position sensors to measure the throttle position to the ECU.

The inlet air pressure was measured by a Gems 1200 series piezoresistive pressure transducer and used to peg the dynamic pressure transducer in the cylinder at BDC. The temperature in the intake port between 0 °C and 1100 °C with a sensitivity of 41 $\mu\text{V}/^\circ\text{C}$ was measured by a k-type thermocouple. The k-type thermocouple used was susceptible to electromagnetic interference due to the low voltage created by the measured temperature. Consequently, every effort was exerted to route the wires away from the possible sources of electromagnetic noise.

3.5 Cylinder Head Design

3.5.1 Cylinder Head Design and Mahle TJI Unit Installation

The cylinder head was designed to be closer to a commercial automotive engine as possible and with optical access, so the poppet valves were fixed on the side of the combustion chamber. In addition, due to the requirement of sufficient breathing, four valves (two intakes and two exhausts) were used. The two camshafts were required to operate all four ports because of the limited space available, as shown in Figure 3.13.

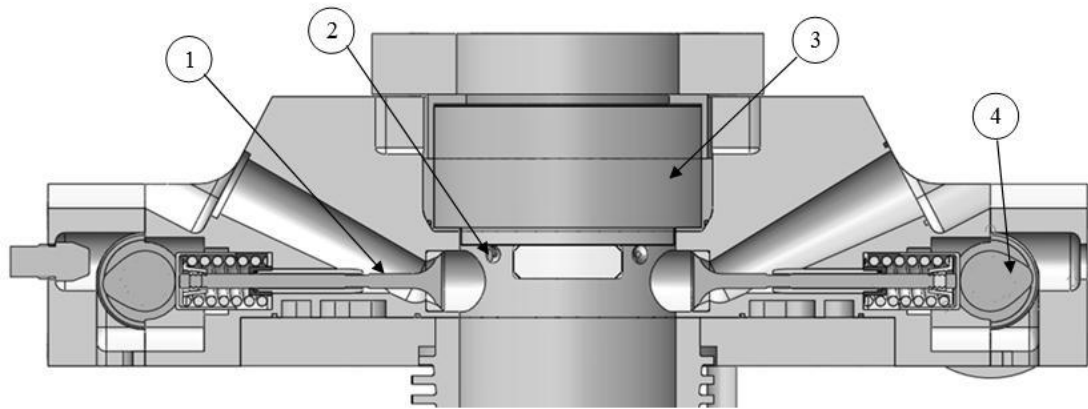


Figure 3.13 Section view of the final cylinder head assembly. 1) Exhaust valve, 2) spark plug, 3) overhead, optical window, 4) intake cam lobe

Sandia National Laboratories used a concept similar to Brunel University optical research engine [123], but the exhaust and intake valves were designed to pass the cylinder liner wall, which would increase the possibility of valve–piston collision. This design reduced the maximum achievable compression ratio up to 5.3:1. In the Brunel optical engine, the compression ratio is higher because the valve seats recessed into the side wall, making the valve timing more realistic.

The University of Leeds used a feature similar to the engine presented in this dissertation [124]. The university used the engine for the laser sheet investigations and modified the version of simple single-cylinder JLO L372 ported two-stroke engine. The original JLO engine cylinder arrangement was replaced with a modified cylinder to maximise the optical access to the combustion chamber.

Different designs for the cylinder head were devised to find a suitable location to install a TJI unit. The first option considered fitting the TJI unit perpendicular to the top window by making a hole to match the pre-chamber outer diameter, as shown in Figure 3.14. An adapter could then be used to hold the TJI unit in place. However, this option faced difficulty in terms of studying the flame structure because only a very small area of optical access remained after installing the TJI unit.

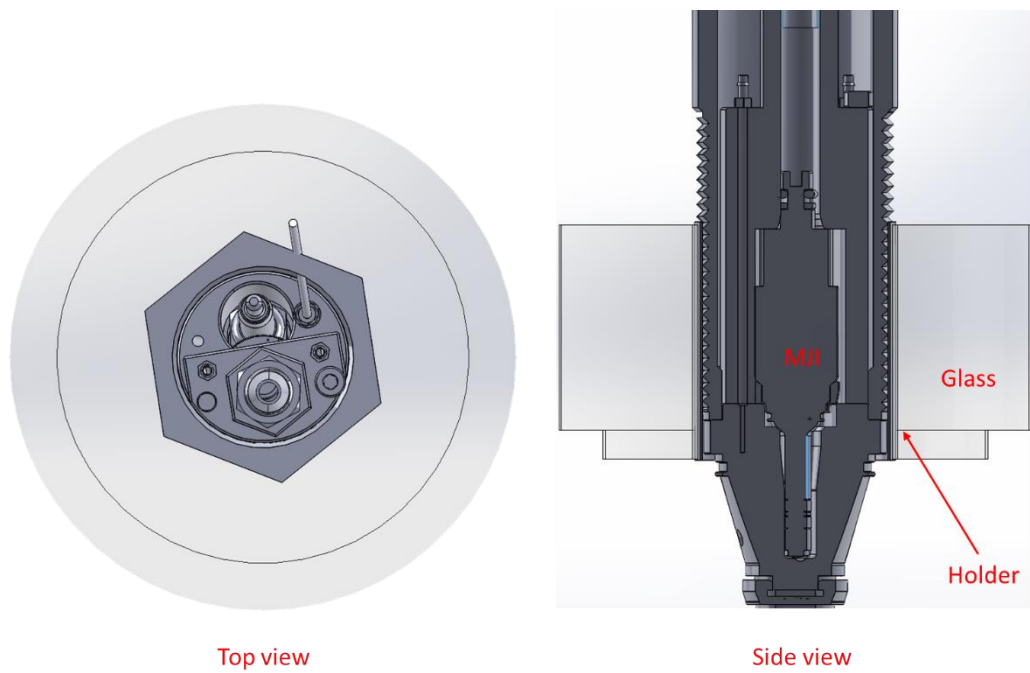


Figure 3.14 Adapter that holds the TJI unit and top window

The second option considered fitting the TJI unit in a horizontal direction with increased chamber height to avoid a clash between the cylinder head and the TJI unit. In this case, the inlet pressure must be increased to compensate for the drop in the compression ratio. This option provided full optical access but ran the risk of the jet flow hitting the top window and breaking the glass, as shown in Figure 3.15. The jet travel distance is between 15 mm and 25 mm from the pre-chamber surface to main chamber [3].

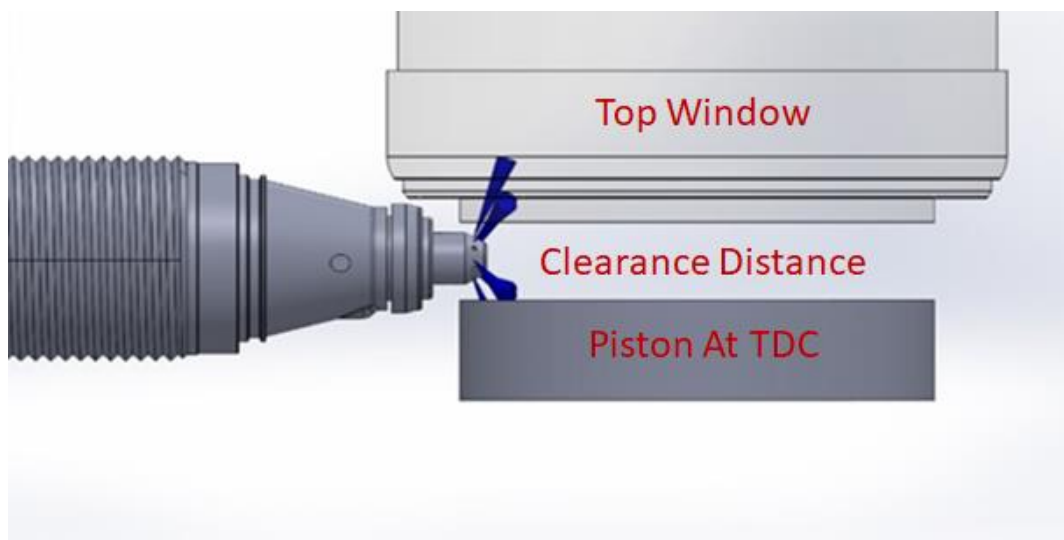


Figure 3.15 TJI unit in the horizontal direction

Moreover, to fit the TJI unit in a horizontal direction, closing the side window and making multi-holes to fit the TJI unit were necessary. Subsequently, the main combustion chamber had to be supplied with inlet pressurised air up to 2.6 bar.

Finally, the TJI unit was installed on top of the cylinder head (at 13 deg incline), and a new semi-circular window must be made. As illustrated in Figure 3.16, the Mahle TJI unit has a diameter 47.5 mm and a height of 182.5 mm, so it could only be fitted into the cylinder head by reducing the size of the top window by half. The cylinder head thickness was increased to accommodate the TJI unit and the half circular window. An adapter was used to hold the TJI unit in place. Fitting a central TJI into the cylinder head allowed even distribution of the multiple jets in the main chamber. An aluminium part was machined in the L edge shape to prevent gas leakage, and it was in the same level as the chamber height. A gasket and sealant were used between the cylinder head and top window.

Two fittings exist on either side of the fuel injector clamp inside the pre-chamber, allowing the coolant to flow down into a water jacket around the pre-chamber body in the TJI unit. Generally, the coolant runs from a separate circuit to the remaining parts of the engine. To drain the coolant, the coolant lines were disconnected from the pre-chamber. A compressed air was then used to remove the coolant in the pre-chamber from the engine. In the present work, using the coolant around the pre-chamber is unnecessary because the engine was ran in a short time with the pre-chamber.

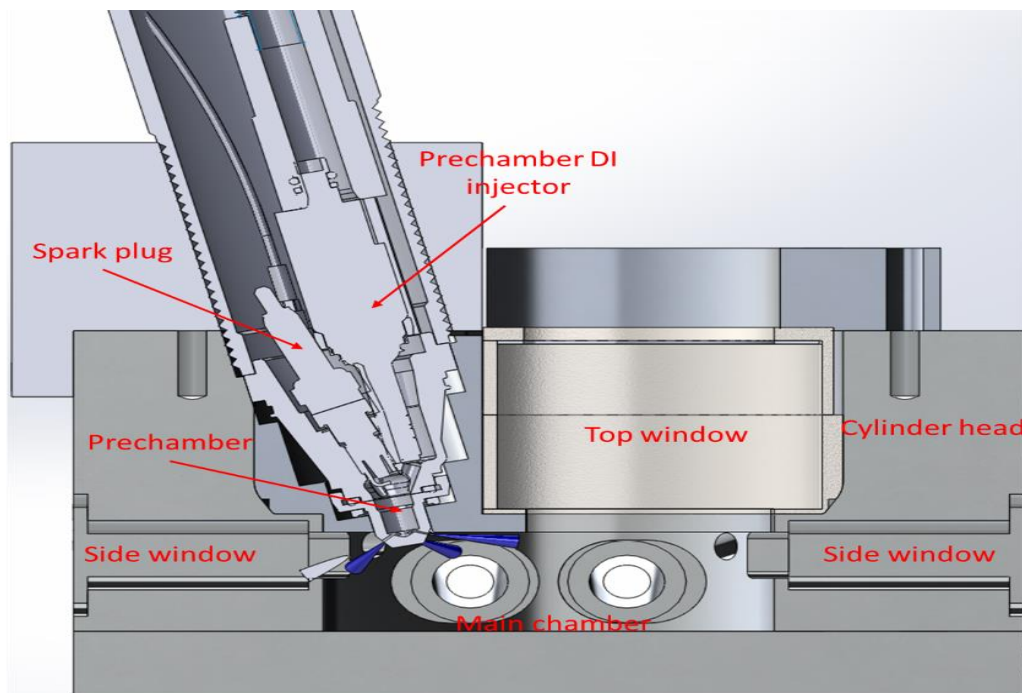


Figure 3.16 Images of the adapter, cutting part, side window and top window

3.5.2 Optical Access and Top Window Design

Using an optical engine to visualise combustion facilitates to deepen the understanding of flame–turbulence interaction and study the flame behaviour [3]. In the current study, using an optical engine allows to observe how the high temperature turbulent jets lead to ignition and combustion in the main chamber through the side windows in the cylinder head, as shown in Figures 3.17 and 3.18.

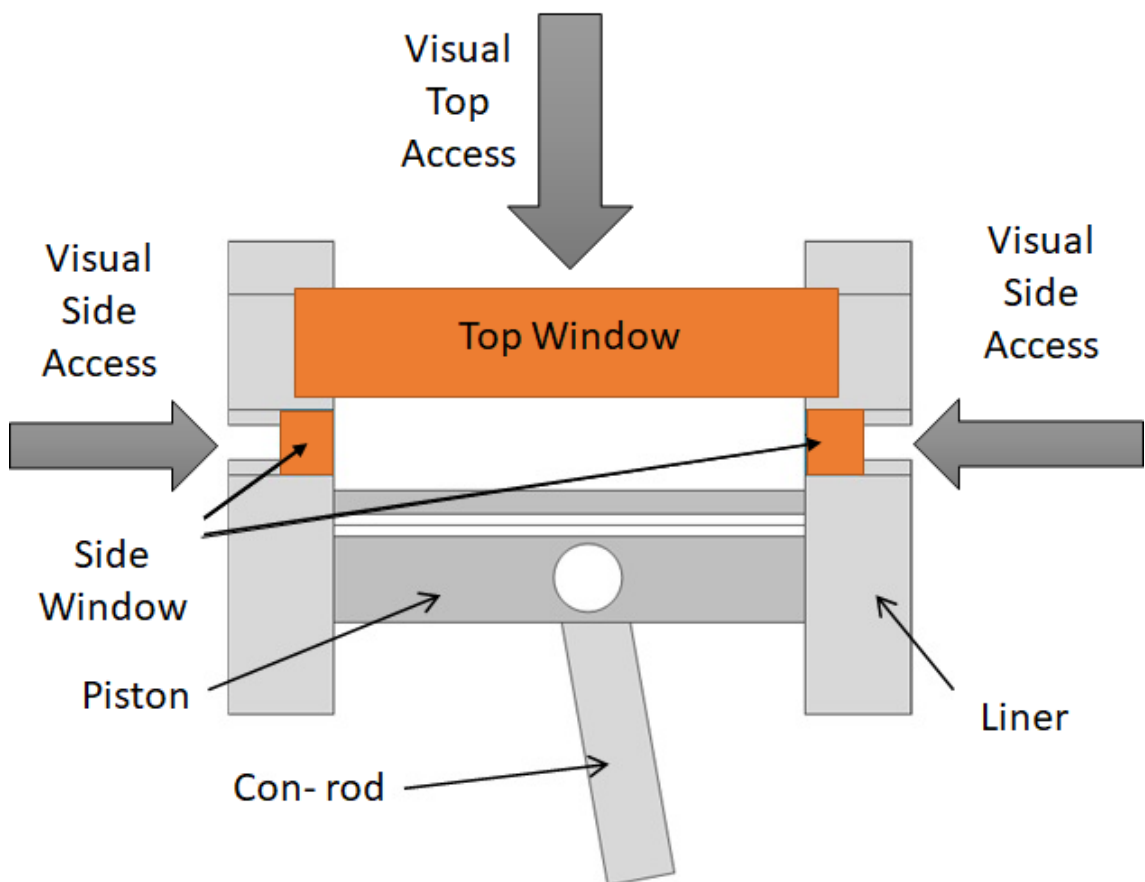


Figure 3.17 Schematic of optical access

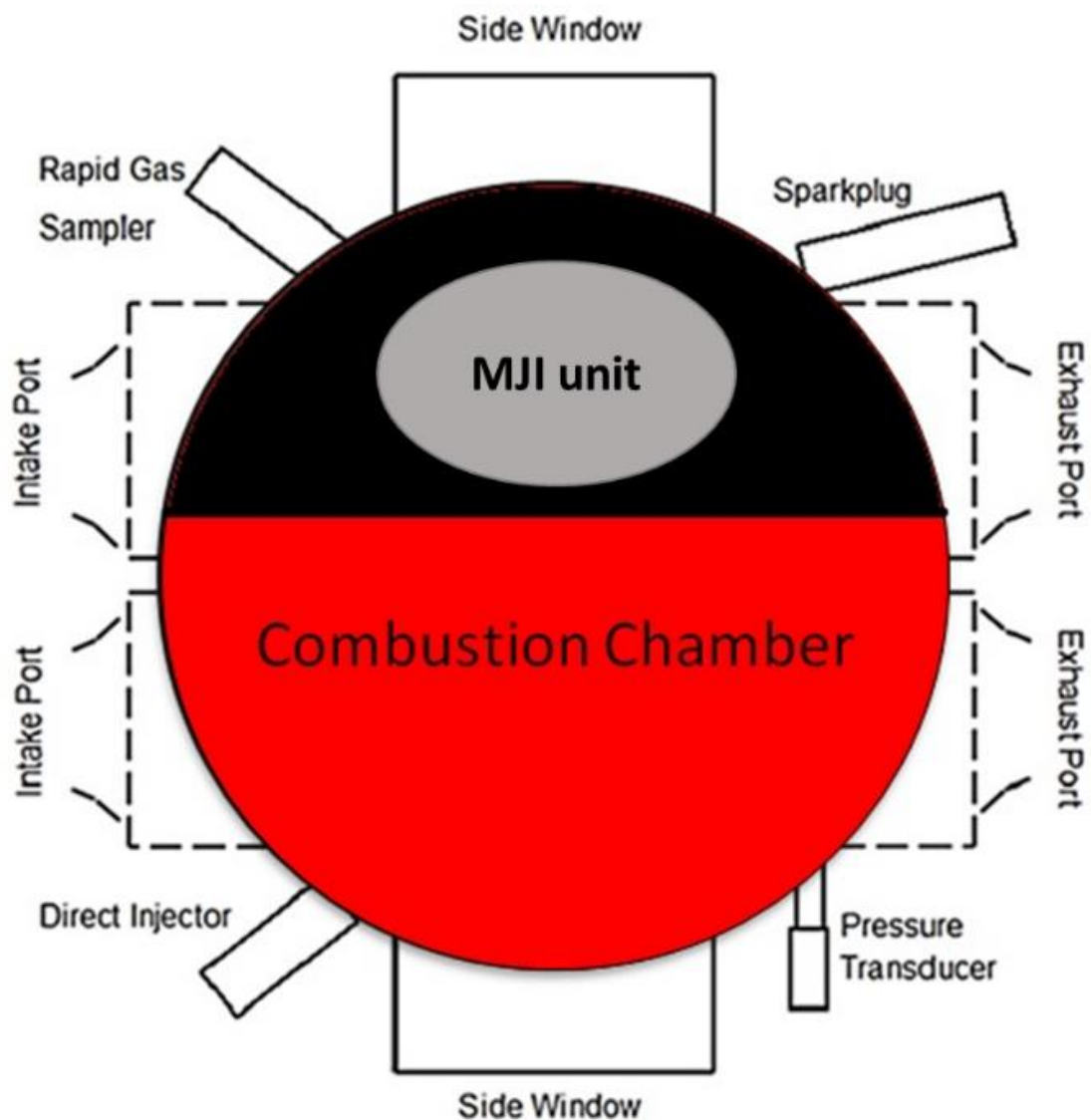


Figure 3.18 Top schematic of the cylinder head concept at Brunel University

To seal in any gas leak, a groove must be built on the top window and the aluminium part must be toned, as shown in Figure 3.19. However, this approach is discouraged because of the complexity of machining the window with groove. Alternatively, an edge with an L shape on the mating metal blank to prevent the gas leakage and support the mating glass was the best solution. This edge with the same level as the combustion chamber top sealed any gas leakage and maintained the same compression value.

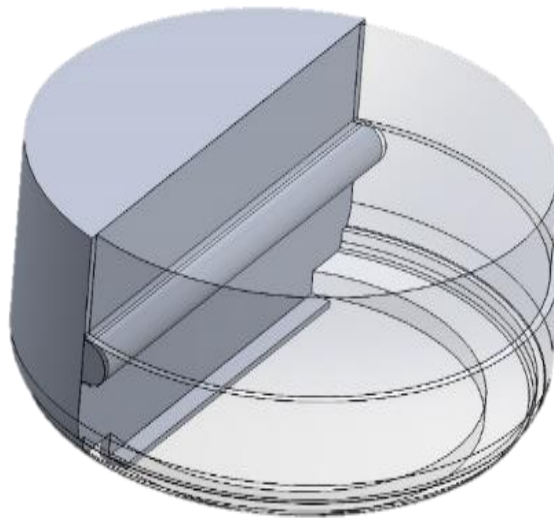


Figure 3.19 Groove in glass and tone in the aluminium part

Fused silica quartz was used to manufacture all the windows, and it was characterised by low heat transfer coefficient and string mechanical strength. The window was designed to withstand a peak cylinder pressure of 15 MPa and force of 106 kN.

A Klingersil gasket C4400 and high-temperature silicone-based sealant were used between the top window and the upper window jacket to avoid metal to glass contact and reduce heat losses. Relevant photos of the damage glass, original glass and aluminium gasket are presented in Figure 3.20. The top window was fixed by a clamping method, whereby a clamping ring was screwed on top of the cylinder head (Figure 3.21).

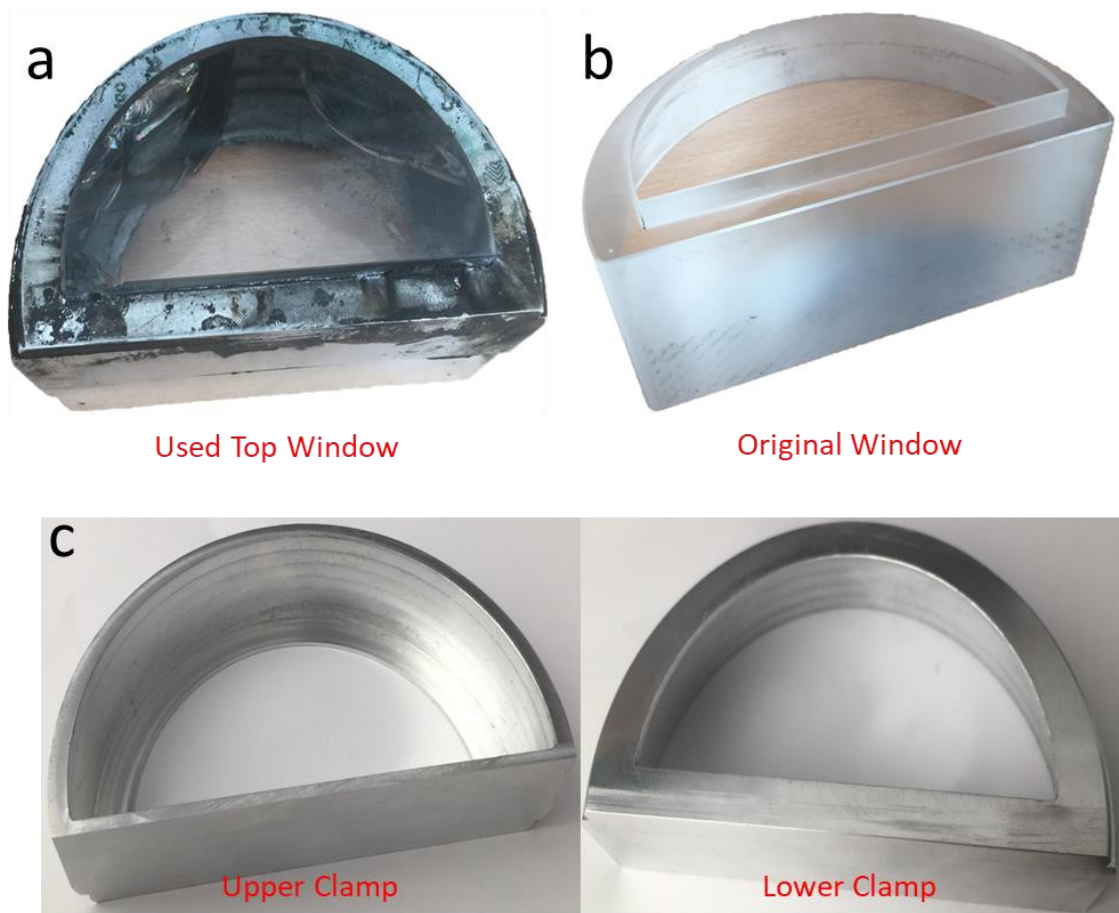


Figure 3.20 a) Damage to the window highlighted, b) original glass received from supplier by the red circle, c) upper and lower aluminium jackets

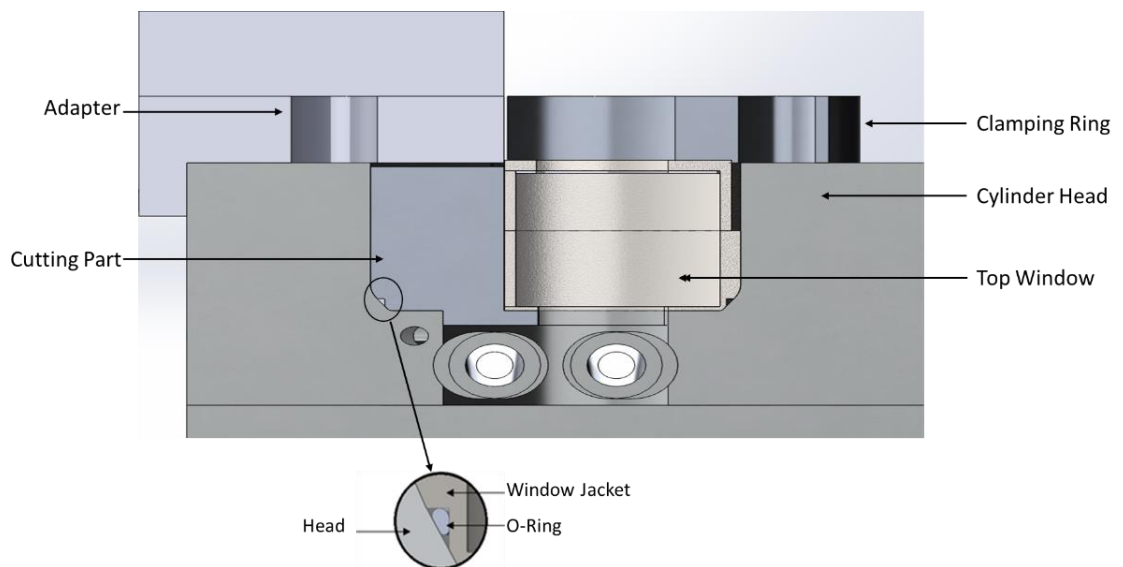


Figure 3.21 CAD image of the installed window and jacket assembly

3.5.3 Finite Element Analysis (FEA)

FEA was performed using ANYAS to investigate the mechanical integrity of the semi-circular aluminar head. The stock properties of the aluminium bar are listed in Table 3.2. The failure of the aluminium occurs when the predicted stresses are greater than the tensile stress of the material.

Table 3.2 Mechanical and thermal properties of aluminium

Parameter (Unit)	Value
Density (g/c2)	2.7
Tensile strength, Ultimate (MPa)	310
Tensile strength, Yield (MPa)	276
Modulus of elasticity (GPa)	68.9
Shear modulus (GPa)	26
Shear Strength (MPa)	207
Thermal conductivity (W/mK)	167
Specific heat capacity (j/gco)	0.896

The aluminium part was modelled as one component. The mesh of the aluminium part was generated with mapped face/tetrahadron mesh type in ANSYS, in which the physical preference was mechanical. Figure 3.22 presents the fine mesh (Node # 175775, Elements # 113678).

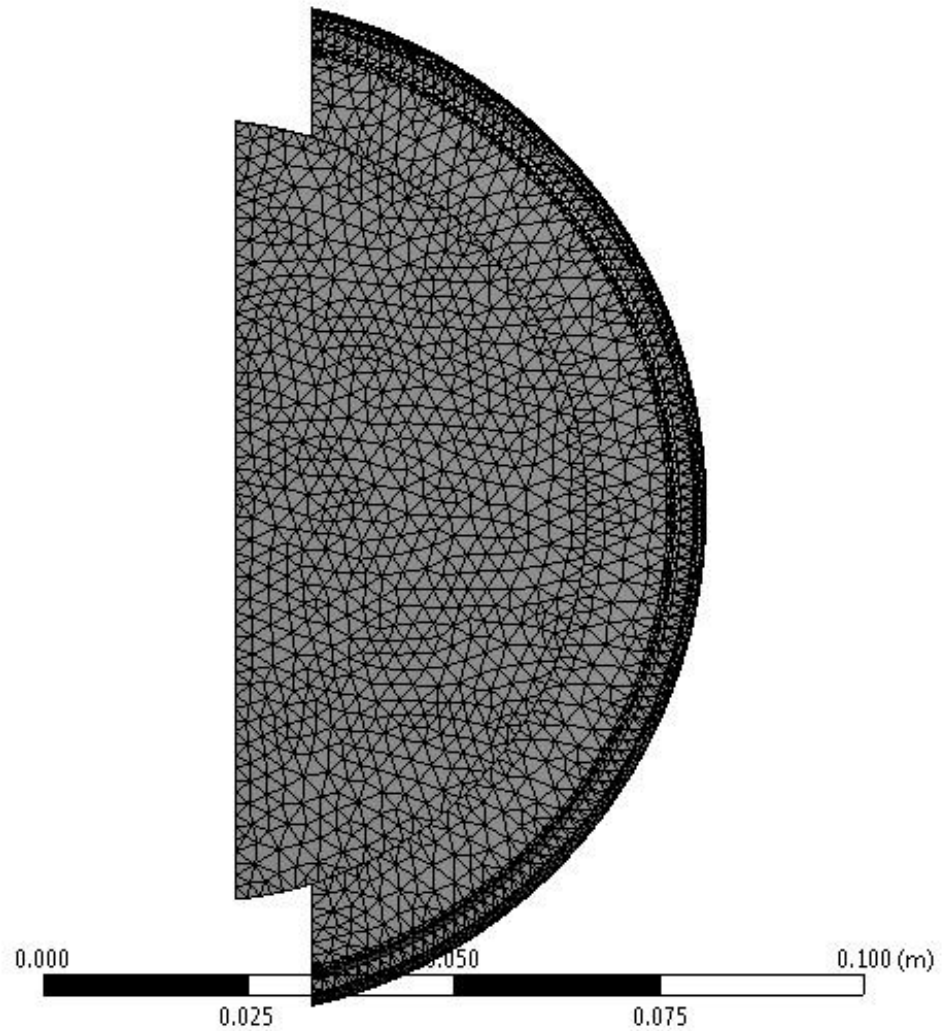


Figure 3.22 Fine mesh

The figure depicts that the maximum stress and displacement in ANSYS were below the material tensile strength at 6.8344×10^7 Pa and 3.0549×10^{-5} , respectively. The maximum stress occurred at the hub and the maximum displacement at the middle of the hub, as shown in Figure 3.23. These results confirm the mechanical integrity of the investigated part and are considered sufficient for the current work.

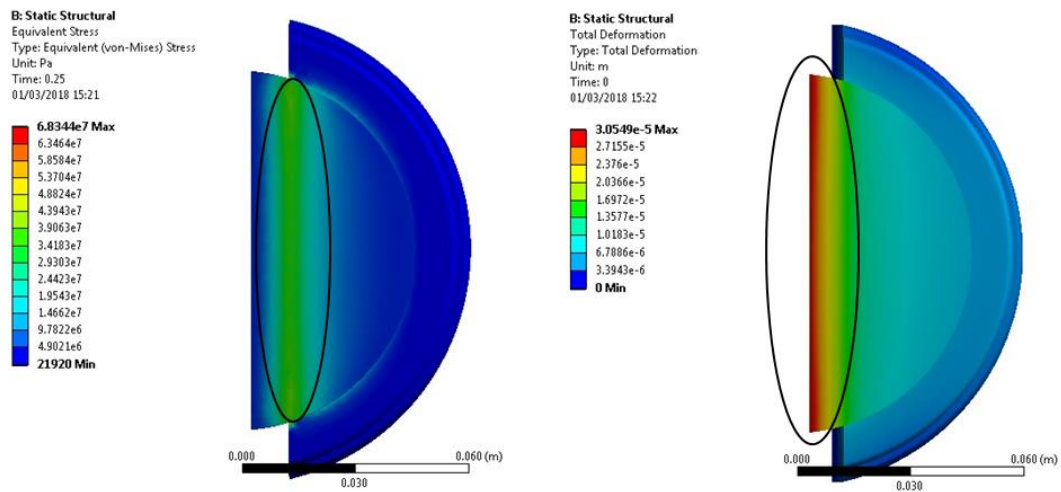


Figure 3.23 Distributions of von Mises stress (left) and displacement (right) using ANSYS

3.6 Experimental Procedure

Gasoline fuel was used for all the baseline reference tests, which allowed for comparison with the alcohol fuels. Prior to each test, the fuel lines were visually checked to ensure that no fuel leakages occur. The oil and fuel levels were checked to ensure that they were sufficient for testing. When the visual checks were completed, the dynamometer power supply and ECU power supply were turned on. In addition, checking all seals, such as oil and air, was necessary especially around the cylinder head during motoring. All checks were undertaken visually. At the same time, the Easimap software was initiated, the in-cylinder pressure charge amplifier was switched and the DAQ, PSU and lambda sensor were powered up. Then, the engine was initially monitored to check the in-pressure cylinder, where the required pressure range to warm up was between 12 and 15 bar.

When oil leak was detected occasionally, the top window was opened and the piston rings and gasket were replaced. Once completed, the cylinder head and all the connections, such as sensors and fuel lines, were placed back. Furthermore, the valve timing was adjusted again because the timing belt had been moved using a clock device. The fuel injection, engine speed and ignition timing were entered into the ECU by the Easimap software. Subsequently, the engine was ran by gradually increasing the power to warm up and to avoid any damage. During this time, a dummy pre-chamber was used to avoid any damage to its DI injector due to overheating. Recording the temperature, humidity and pressure for each test was necessary because these parameters affected

the output results. The engine was warmed up from ambient temperature until that of the cylinder head reached 90 °C. This method was performed by running the engine until the exhaust temperature reached 95 °C. Then, it was turned off to cool down. After the cylinder head had been warmed up, the dummy pre-chamber was replaced by the TJI unit, and then the cRIO-9066 was turned on. Whilst the NI driver was powered, the status LED indicators shown in cRIO-9066 must be observed, as discussed in Table 3.3.

Table 3.3 Status LED indicators

LED Pattern	Indication
Blinks twice and pauses	The cRIO-9066 is in safe mode. Software is uninstalled, which is the factory default state, or software has been inappropriately installed on the cRIO-9066. An error can occur when an attempt to upgrade the software is interrupted.
Blinks three times and pauses	The cRIO-9066 is in user-directed safe mode, or the cRIO-9066 is in install mode, indicating that software is currently being installed.
Blinks four times and pauses	The cRIO-9066 is in safe mode. The software has crashed twice without rebooting or cycling power between crashes.
Continuously blinks	The cRIO-9066 either booted into an unsupported operating system, was interrupted during the boot process or detected an unrecoverable software error.
On momentary	The cRIO-9066 is booting. No action required.
Off	The cRIO-9066 is in run mode.

The SCM software was ran after the cRIO-9066 had been powered up. The EOI was set between 50° and 70° CA bTDC, and the injection duration was varied between 0.3 and 1.5 ms. In this research, a fixed TDC offset at 25° CA was selected after calculating and comparing the new and old sensors. To reach the maximum lean limit for each fuel, the engine was ran to determine MBT at $\lambda = 1$. Afterward, the fuel amount was reduced, and the injection duration and EOI were varied to reach the lean limit, whereas the inlet air and speed were fixed at 1 bar and 1200 rpm, respectively. Finally, the main chamber lambda was swept to reach the lean limit and varied spark timing to maintain CA50 = 8–10 °CA aTDC and CoV of IMEP \leq 5%. All tests started at the cylinder head temperature from 90 °C to 95 °C maximum, and the results were saved upon completion. They were repeated with different spark timing, fuels, load and lambda. After all the tests had been completed and the data recorded, the fuel valve, spark, engine and fuel pumps were turned off, followed by the ECU switch and power.

3.7 Emission Analyser

The engine exhaust was connected to a Horiba MEXA-584L automotive emission analyser that can measure CO, HC and NOx emissions, as shown in Figure 3.24. The Horiba MEXA-584L automotive emission analyser was calibrated before each measurement, according to the international slandered ISO 3930/ OIML R99 (2000) class 0. The exhaust gas was collected in the middle of the exhaust gas pipe and delivered via a silicon rubber sample line, a water trap and a combined concentrate and particulate removal filter. A non-dispersive infrared (NDIR) absorption cell measured CO and CO₂, and a galvanic cell measured the oxygen content of the exhaust gas to determine the AFR. The NDIR absorption cell also measured the concentration of HC. This method consists of the emission of infrared light of the same wavelength, which is absorbed by a specific molecule. Thus, the difference between the emitted light and received light after passing through the sampled mean is proportional to the molecular concentration. The output of HC provided by the gas analyser was on a Carbon 6 (C6) basis, where the HC results were converted to C1. The resolutions of the gas analyser are listed in Table 3.4. A separate automotive NO sensor was purchased and used to measure the NO in the exhaust gas.

Table 3.4 Resolutions of the gas analyser

CO	0.01 %vol
HC	1 ppmvol (within the range of 0 ppmvol to 2000 ppmvol), 10 ppmvol (within the range of 2000 ppmvol to 10000 ppmvol)
CO ₂	0.02 %vol
AFR	0.1
Lambda	0.001
O ₂	0.02 %vol
NO	0 ppm vol to 5000 ppm vol



Figure 3.24 Photo of MEXA-584L gas analyser

3.8 Summary

This chapter described the single-cylinder engine and engine experimental setup. A full description of the optical engine cylinder head design, the installation of the Mahle TJI unit and the optical window was provided. The SI and fuel injection systems and their controls were also described. The experimental test procedure used to complete the experimental testing was discussed.

Chapter 4 Data Analysis and Flame Imaging Techniques

4.1 Introduction

In-cylinder pressure measurements and combustion visualisation techniques were applied to the single-cylinder engine with optical access to study the effect of pre-chamber ignition and fuel properties on the ignition, combustion and heat release processes. In this chapter, the high-speed data acquisition setup and the data processing methods used to calculate the IMEP, MFB and knock intensity are presented. The second part describes the high-speed combustion imaging set up and the image post-processing technique for determining the mean flame radius and apparent flame speed. Finally, the spectroscopic technique and its experimental setup used to measure the temporal evolution of emission spectra of the radicals are discussed.

4.2 Heat Release Analysis

The in-cylinder pressure in the main chamber was measured by a piezoresistive pressure transducer (GH14DK), whereas the pre-chamber pressure was measured by another piezoresistive pressure transducer GH14D. A NI DAQ system was set up to record the in-cylinder pressure at a high sampling rate of four samples/CA (0.25 CA) by a USB-6353 card and temperature and lambda values at a low sampling rate of 3 Hz by the USB-6210 card. Both cards were controlled over a USB by an in-house MATLAB-based program called 'YanTech', which is developed by Dr. Yan Zhang.

The condition results were saved three times to add up to 300 cycles. To analyse the cyclic variations, Brunt and Emtage [125] recommended that 150 cycles should be the minimum number. Lancaster et al. [126] concluded that a sample size of 300 cycles would be required to minimise the measurement error.

The 99% confidence interval of the measurements can be calculated by Equation 4.1.

$$99\% \text{ Confidence Interval} = \frac{2.5\sigma}{\sqrt{n}}$$

Equation 4.1:

where σ is the standard deviation of the data, and n is the sample size.

The IMEP was calculated by the following formula:

$$\text{IMEP}_{\text{net}} = \frac{\oint p dV}{D}$$

Equation 4.2:

where p is the in-cylinder pressure, V is the cylinder volume, and D is the displacement of the engine.

The coefficient of variation (COV) of IMEP is used to quantify the stability or repeatability of the combustion for a given condition. COV_{IMEP} is calculated by the following formula:

$$\text{COV}_{\text{IMEP}} = \frac{(\text{Standard Deviation of IMEP of 300 cycles})}{(\text{average IMEP of 300cycles}) * 100}$$

Equation 4.3

The standard deviation is calculated by the following equation:

$$s = \sqrt{\sum_{i=1}^N |A_i - \mu|}$$

Equation 4.4

where μ is the mean of A :

$$\mu = \frac{1}{N} \sum_{i=1}^N A_i$$

Equation 4.5

Figure 4.1 represents the 99% confidence measurement of IMEP net calculation for data sets up to 600 cycles. The 99% confidence interval was reduced to 1.1% with 300 cycles. The sample size was typically reduced to 50 cycles as the optical measurement required much greater storage [127], thereby slightly increasing the 99 percent confidence interval to 2.5%.

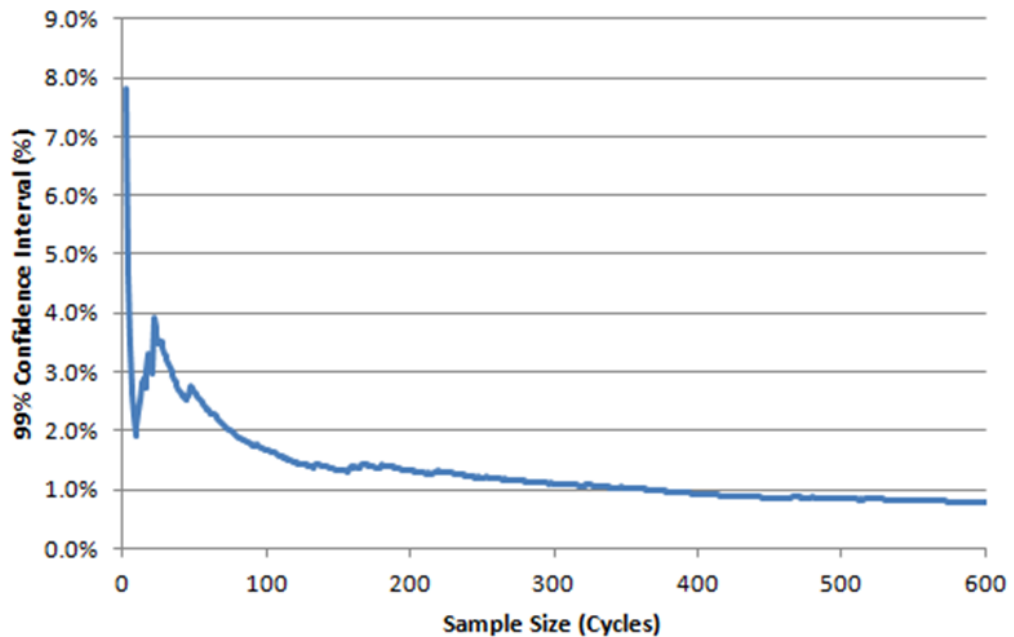


Figure 4.1 99% confidence interval for the measurement of the average IMEPnet against sample size

4.2.1 Heat Release Analysis

The realtime heat release analysis was based on the Rassweiler and Withrow method [128][129], which was developed to compare the change rate in the pressure of a fired cycle to that predicted by polytropic compression and expansion.

Measuring the values of the polytropic exponent from the log P-V diagram at the same engine operating condition as the fired engine operation was necessary because this exponent depends on the heat transfer and in-cylinder gas mixture.

Once the heat release was calculated as a function of crank angle, the MFB could be determined. Figure 4.2 shows the averaged rate of heat release and average MFB against crank angle for a total of 1200 combustion cycles. The combustion is measured by the following on the basis of fuel–air mixture burned:

- CA0, the crank angle location of the start of combustion.
- CA10, the crank angle location of 10% MFB.
- CA50, the crank angle location of 50% MFB.
- CA90, the crank angle location of 90% MFB.
- CA0–CA10, the flame development period, and the number of crank angles for the first 10% of fuel mass burned.

- CA10–90, the combustion duration, and the number of crank angles for the central 80% of fuel mass burned.
- The CA50 at the minimum spark advance for best torque (MBT) is typically located at approximately 10° aTDC ($\pm 2^\circ$ CA) [129][130].

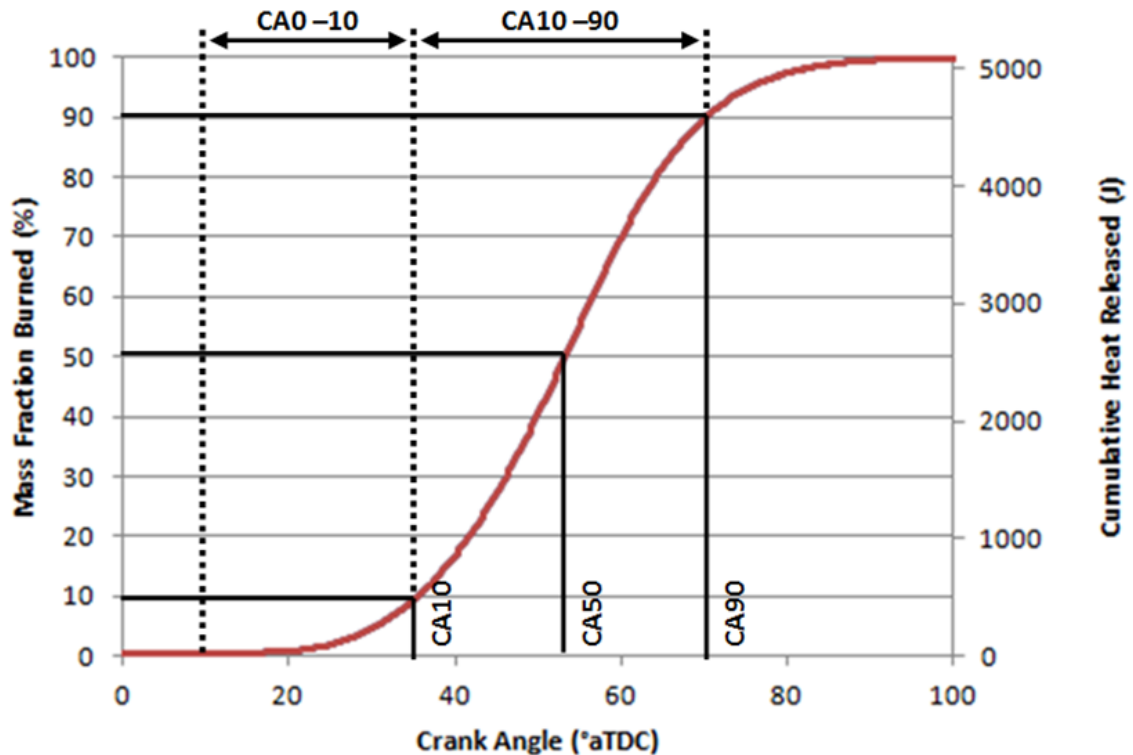


Figure 4.2 Energy released in terms of MFB and cumulative heat released against crank angle (data averaged over 1200 cycles)

4.2.2 Knocking Combustion Analysis

The knocking combustion was detected and the knocking intensity was calculated by subtracting the filtered pressure signal from the original pressure signal, as shown in Figure 4.3. The filtered pressure was obtained by applying a simple box filter to the raw pressure signal to filter out the high frequency. Knocking combustion is defined here when the filtered pressure signal exceeded 0.25 bar.

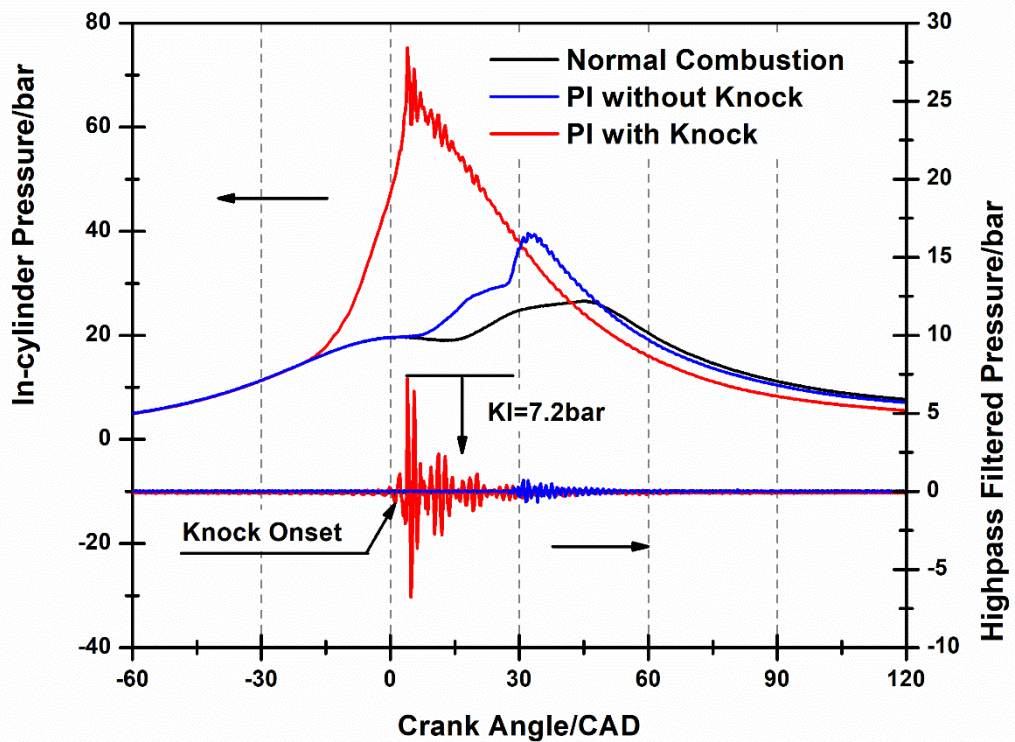


Figure 4.3 Calculated knock pressure signal and definition of knock intensity

4.3 High-speed Flame Imaging through the Top Window

The flame images in the main chamber were captured by a high-speed camera through the top window via a 45° mirror (Figure 4.4). A Memrecam fx6000 high-speed camera with the maximum resolution of 512 x 512 pixels was used. Table 4.1 shows the link between frame rate, exposure and resolution based on the engine speed and imaging setup. As a trade-off between the spatial and temporal resolutions, combustion images were captured at 6000 frames per second (fps) with a resolution of 512 x 384 pixels and one frame every 1.2° crank angle. The high-speed camera was controlled by the GXLink software sourced from the NAC Image Technology. GXLink software was used to control the trigger and to save images. The high-speed video camera was triggered at the same time as the DAQ to save images simultaneously with the pressure and temperature data. The gamma and gain of the camera were adjusted for each test to improve the clarity of the images. Images over five cycles were recorded because of data storage capacity. Thus, each data point could result in up to 15000 images.

Table 4.1 Outlining of interdependence between image resolution, frame rate and maximum exposure time

Frame Rate (fps)	Resolution (pixels)	Exposure Time (μ s)
240,000	512 x 8	4
120,000	512 x 16	8
60,000	512 x 36	17
10,000	512 x 248	100
8,000	512 x 308	125
6,000	512 x 384	167
3,000	512 x 512	333

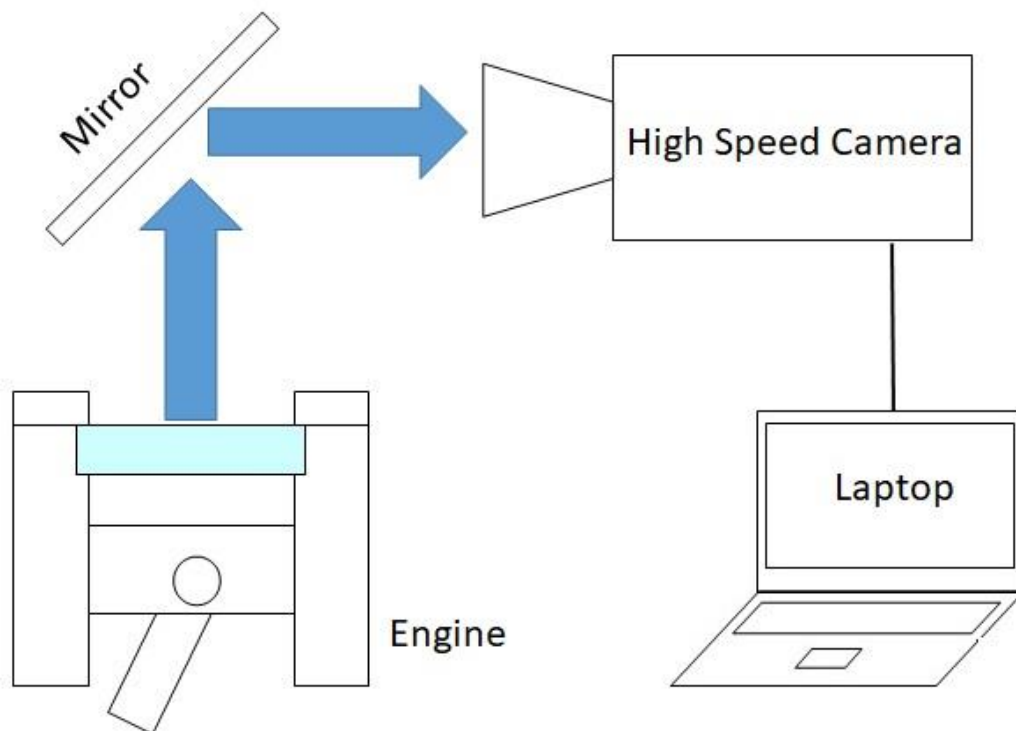


Figure 4.4 Images showing the experimental engine control, image capture and data acquisition systems

The image processing was carried out through automated batch operation in MATLAB. The 'imread' function of the MATLAB allows the user to open the first image and draw the perimeter around the image. Once completed, the next image is imported and processed until the last image. All processed images were stored in the MATLAB workspace in matrix format.

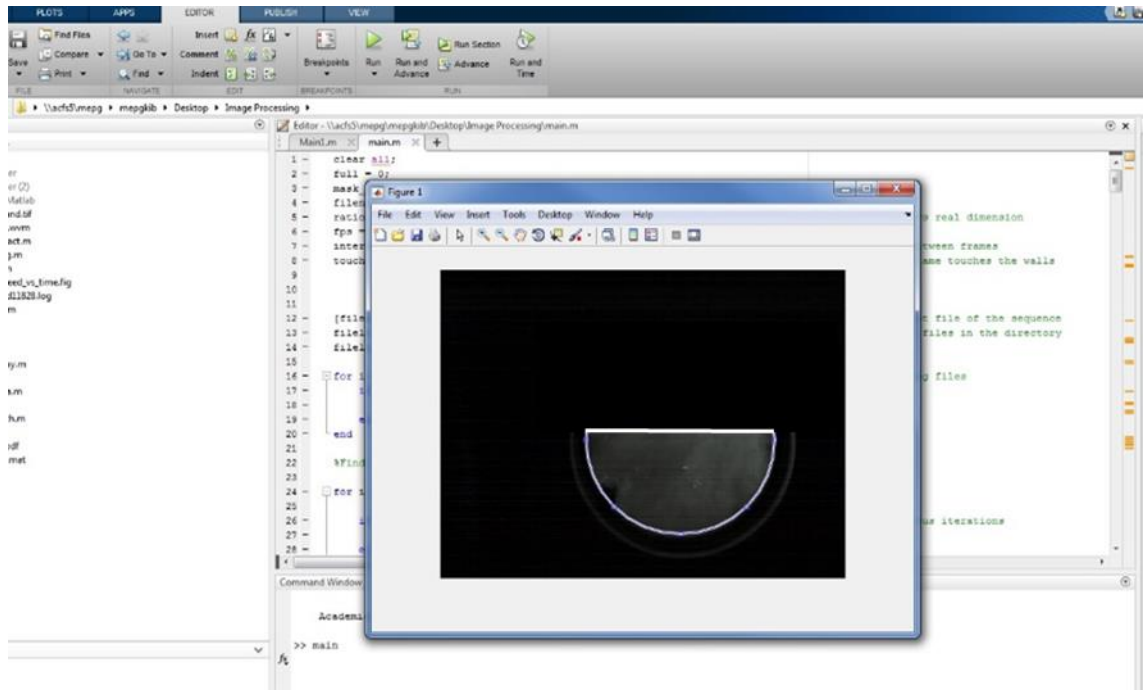


Figure 4.5 Selected perimeter around the image at first image

Owing to noise and any reflection from outside of the combustion chamber, each image analysed had a 'background image' subtracted from it to remove the background noise. Then, a mask was applied to crop out the cylinder wall noise 'halo', and only the flame was retained for analysis, as shown in Figure 4.5. The MATLAB code analysed the pixel density of the image and assigned each image with a value between 0 and 1 as set by a pre-defined threshold value. The images were converted into binary black and white regions, where the white regions were the 'pixels under that assigned value', and the black regions were the 'pixels over that assigned value'. The flame edge was identified by the interface between the two regions, as shown in Figure 4.6, from which the area of the flame, the perimeter length of the 'flame front', the 'shape factor' of the flame and the level of 'wrinkle' could be determined.



Figure 4.6 Raw combustion image (right) and binary image following the mask filter (left)

The centroid was found by locating the point at which a centre of mass would be situated. It is computed as follows:

$$C = \frac{\sum P_x}{K},$$

Equation 4.6

where K is the number of pixels selected in the image, and $P_x = (x_i, y_i)$ represents the Euclidean coordinates of the pixels.

Upon locating the flame centre, the code calculates the flame radius using the best-fit circle method [124][131][132]. This method searches the flame's centre and radius by affixing a circle to the image. This search is completed to obtain an equal amount of unburnt charge involved by the circle and burnt charge. The best-fit circle can be calculated by solving the non-linear Equation 4.7 to minimise the sum of the squares of the distances.

$$d_i^2 = (\|z - x_i\| - r)^2$$

Equation 4.7:

where d_i is the distance between a point (x_i) and the centre of the best-fit circle (z) , which possesses a radius of r .

In the case of $u = (z_1, z_2, r)^T$, \tilde{u} must be determined as follows:

$$\sum_{i=1}^m d_i(u)^2 = \min$$

Equation 4.8

Jacobian, defined by the partial derivatives $\frac{\partial d_i(u)}{\partial u_j}$, is given by the following:

$$\begin{pmatrix} \frac{u_1 - x_{11}}{\sqrt{(u_1 - x_{11})^2 + (u_2 - x_{12})^2}} & \frac{u_2 - x_{12}}{\sqrt{(u_1 - x_{11})^2 + (u_2 - x_{12})^2}} - 1 \\ \vdots & \vdots \\ \frac{u_1 - x_{m1}}{\sqrt{(u_1 - x_{m1})^2 + (u_2 - x_{m2})^2}} & \frac{u_2 - x_{m2}}{\sqrt{(u_1 - x_{m1})^2 + (u_2 - x_{m2})^2}} - 1 \end{pmatrix}$$

Equation 4.9

The best-fit circle could be iteratively calculated around a set of given points by using the Gauss–Newton method [133]. Assuming those points are the flame front data, the calculated circle would equal one with a radius equal to that of the flame radius. The flame speed was calculated by differentiating the mean flame radius in each frame.

$$\text{Flame speed} = \frac{\text{flame radius}}{\text{time}}$$

Equation 4.10

The shape factor (SF) of the flame represents the development of the flame front's distortion. It equals to the ratio between the perimeter of the flame contour (Pc) and circle (Pr), as shown in Figure 4.7 [134][135][136]. The calculated mean shape factor can determine the burning rate, where the large scales of shape factor are normally

associated with slow burning. The shape factor is also used to observe the knock-on effect of faster initial laminar burning velocity of different fuels [107].

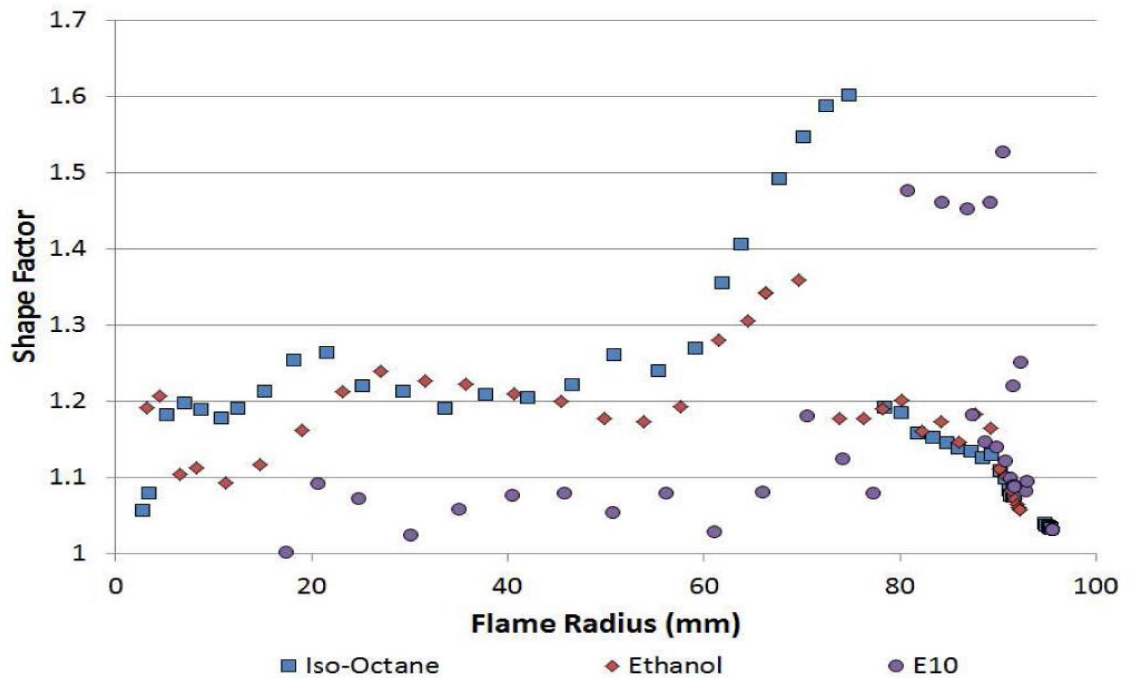


Figure 4.7 Computed values of the shape factor for the four-base fuels against the flame radius [107]

Figure 4.8 illustrates the sequence of the image processing, including the binarisation and determination of the flame radius, flame speed and shape factor.

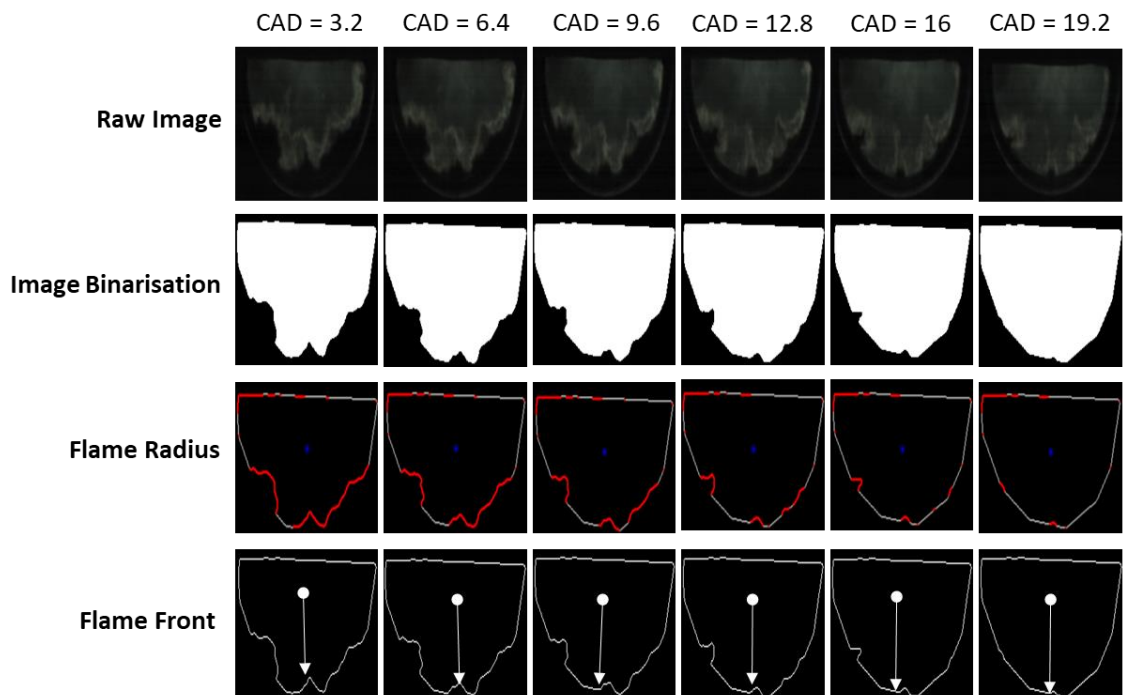


Figure 4.8 MATLAB image processing sequence and output

4.4 Imaging of Turbulent Jets and Ignition Process through the Side Window

A *FastCam* mini AX100 type 540K-M-8GB was used with an endoscope through one side window to study the re-ignition sites of the jets coming out of the pre-chamber and their temporal changes, as shown in Figure 4.9. The *FastCam* was set at 4500 frames per second (fps) with a resolution of 1024 x 992 pixels and one frame every 1.6° crank angle at the engine speed of 1200 rpm. PFV software was used to control the *FastCam* camera and save the images. The gain and gamma of the camera were adjusted for each test to increase the clarity of the images. For one complete cycle, only 100 frames were measured due to data storage capacity.

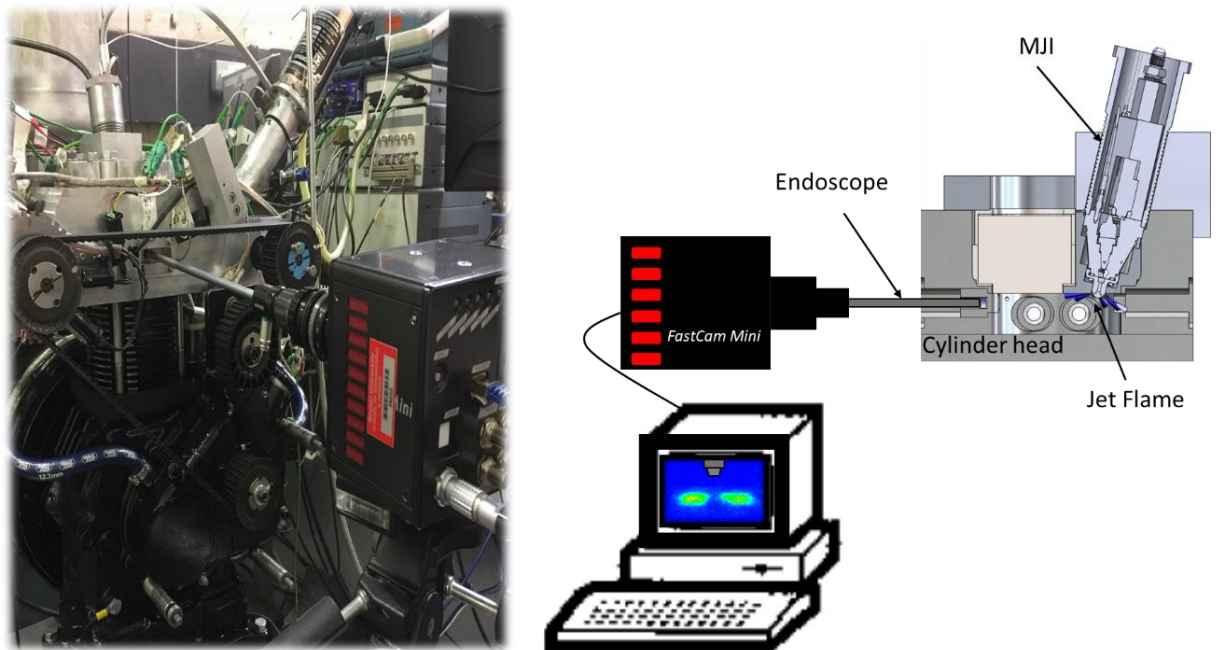


Figure 4.9 High-speed camera (*FastCam* mini) with Endoscope

As the air–fuel ratio was increased to higher values, the *FastCam* camera was unable to capture the combustion due to the lower light emission of the lean-burn combustion. Therefore, a *Plmax4* intensified CCD camera was used to record one combustion image per cycle with endoscope, as shown in Figure 4.10. The camera used a micro channel plate image intensifier coupled to a CCD array of 512 by 512 pixels, and the fastest intensifiers can be gated in less than 3 ns. The camera was operated by LightField software. The gain and gate delays were adjusted for each measurement condition. The frame rate was set at 134 fps to save 25 frames.

The synchronisation of the ICCD and high-speed camera with engine was driven by the trigger signal through the delay unit. The trigger signal was connected to the control box, and then the output signal was connected directly to the camera to control and record a certain crank angle [108].

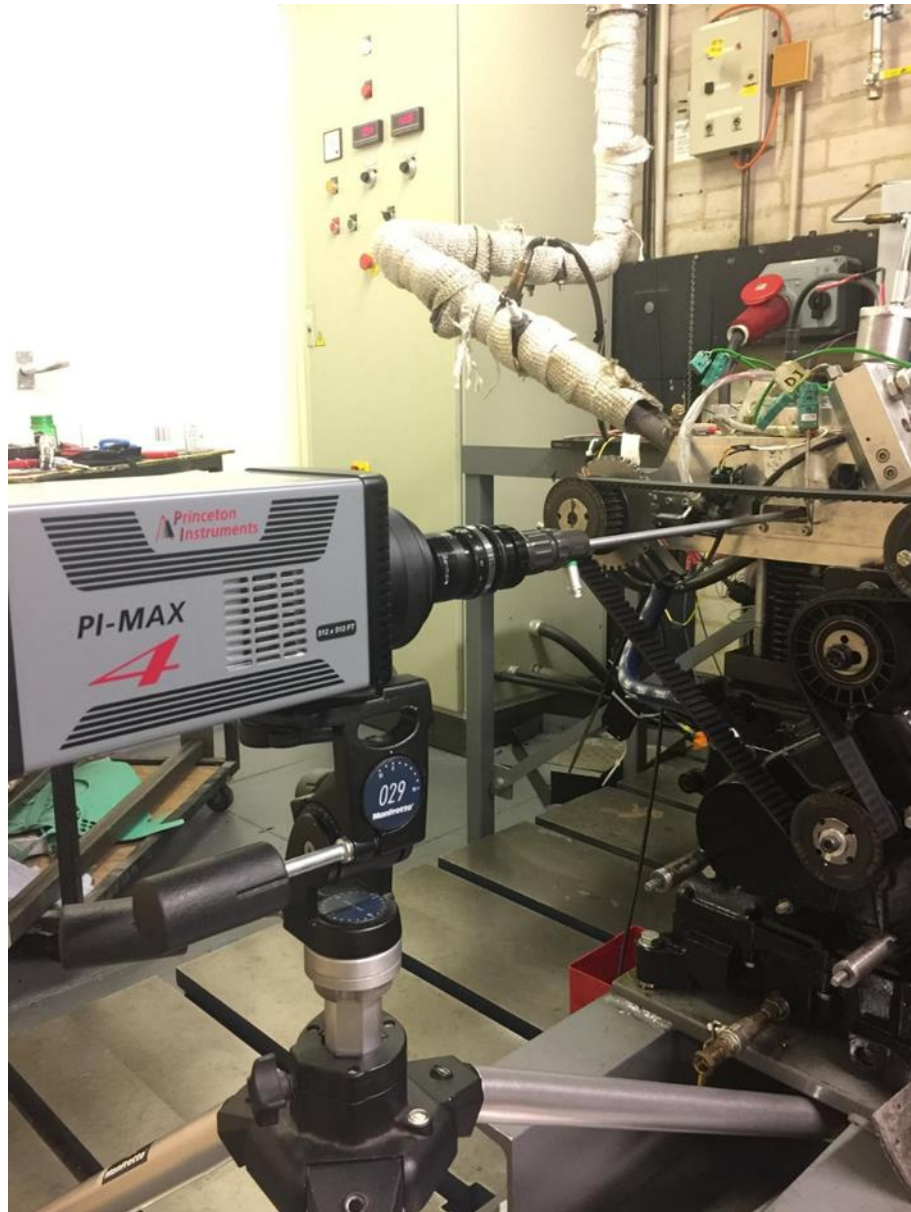


Figure 4.10 ICCD camera (Pimax 4, Princeton) coupled with endoscope

4.5 Spectroscopic Measurement

High-speed UV-visible spectroscopic techniques were used in this research. A single-leg fibre optics was used to collect the chemiluminescence of combustion, as shown in Figure 4.11. The fibre optics contain nineteen 200- μm fibres, an SMA connector at the illumination end and a 10 mm ferrule at the slit end to be connected to a spectrometer.

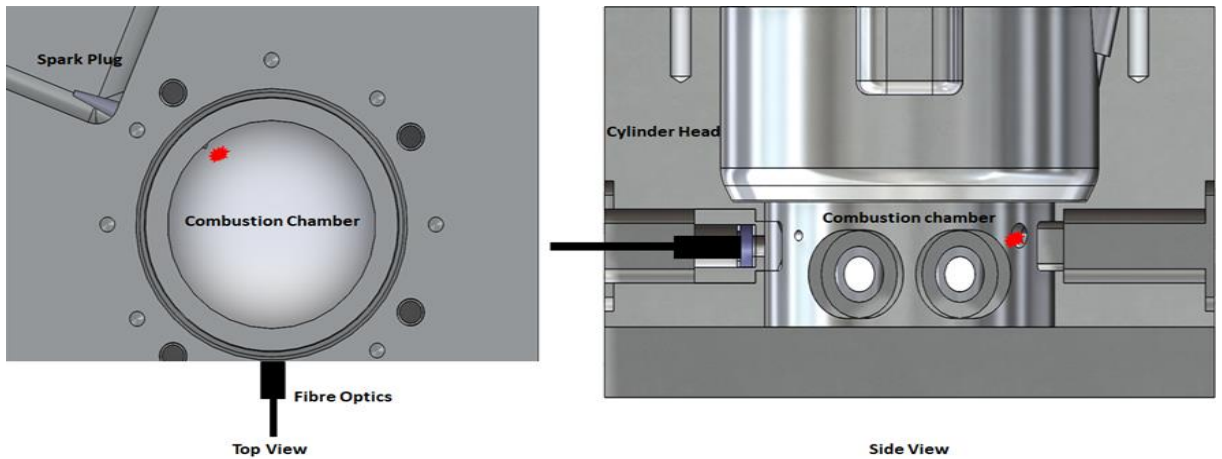


Figure 4.11 Combustion chamber location

The fibre bundle was placed inside the small channel and drilled through a dummy aluminium window block, as shown in Figure 4.12. It was protected from the combustion gas by a sapphire window fixed in front of the channel. The fibre bundle had a field of view covering in the central region of the combustion chamber.

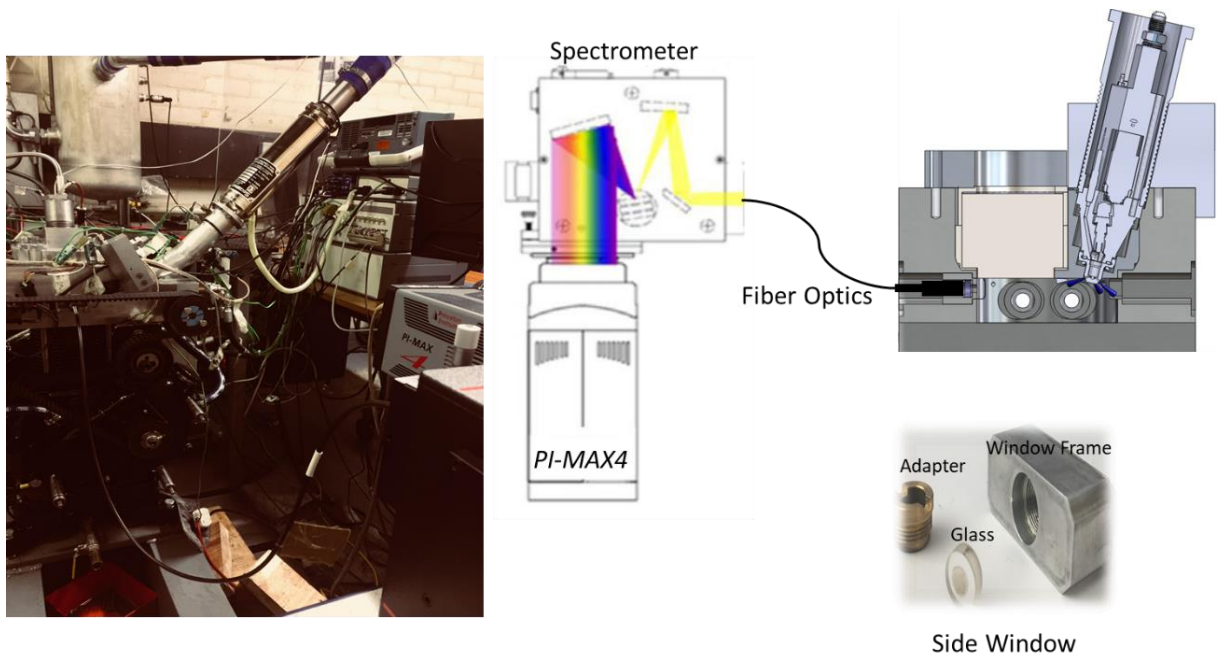


Figure 4.12 Pictures and sketches of the experimental apparatus for optical investigations

The chemiluminescence signals were collected and focused on the entrance slit of a SpectraPro HRS-500 spectrometer. The spectrograph has a focal length of 500 mm, f/6.5 aperture ratio, scan range from 0 nm to 1500 nm and wavelength accuracy of +/-0.2 nm. The main feature of the SpectraPro HRS-500 spectrometer is the grating change

reproducibility that allows as many as three gratings to be mounted on a turret and selected when required for an application. The spectral image formed on the spectrograph exit plane was matched with the PImax4 intensified CCD camera. The camera had an array size of 1024 x 1024 pixels with a pixel size of 13 x 13 μm and 16-bit dynamic range digitisation at 10 MHz. The width of the slit was fixed at 180 μm . Data were detected with the spectrograph placed at three central wavelengths, namely, 310, 330 and 430 nm to investigate a wider spectral range, whereas the grating was fixed at groove density of 600 g/mm (blaze wavelength 150 nm). The spectra were calibrated for the optical set up efficiency using IntelliCal calibration light. The intensifier–gate delay was set at 31 ns, and the gatewidth was 0.81 μs .

4.6 Summary

In-cylinder studies of ignition and combustion were realised by in-cylinder high-speed pressure measurement and optical imaging techniques. The methods used to calculate the heat release data were presented. The sample size and the acceptable minimum sample for each test condition were discussed. Then, the methods to calculate IMEP, HRR, MFB and knocking combustion were presented. Following, the high-speed combustion imaging systems and setups for the visualisation of flame propagation through the top window and for the observation of multiple jet ignition and combustion in the main chamber were introduced. In addition, the methods to calculate the flame radius, speed and shape factor were described in detail. Finally, the spectroscopic system and set up to identify the presence of radicals and species based on the spectral peaks present were presented.

Chapter 5 Gasoline TJI Engine Operations

5.1 Introduction

This chapter presents and compares the performance and emission characteristics of the single-cylinder engine under normal SI and jet ignition combustion operations. The use of Mahle TJI at different loads is then considered. Finally, its usage at different speeds is evaluated.

5.2 Preliminary Engine Testing with Unfuelled Pre-chamber Ignition

Substantial effort was exerted to design a modified cylinder head to adapt the Mahle TJI unit and to maintain sufficient optical access through the cylinder head, as shown in Figure 5.1.

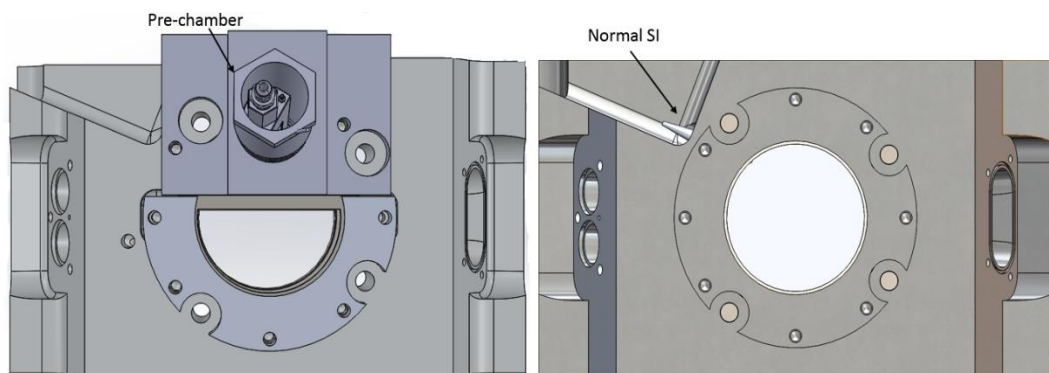


Figure 5.1 Modified cylinder head (left) and original cylinder head (right)

After completing the design and installation of the new cylinder head, various engine tests with both ignition systems were performed. They were undertaken to ensure robust mechanical operation and to check the performance characteristics of the combustion engine with a pre-chamber and normal SI system prior to any advanced thermodynamic and optical testing.

Figure 5.2 presents the motored ensemble averaged in-cylinder pressure trace over 100 motored cycles at 1200 rpm and 1 bar intake pressure. The analysis result of the in-cylinder pressure data during motoring clearly shows that the in-cylinder pressure for both setups was similar, with a difference in the maximum in-cylinder pressure (P_{max}) between the two motored tests due to the combustion chamber leakage. Initially, a paper gasket (Klingersil, C-4400) was used between the top window and cylinder head. However, it was burned in every test due to high temperature and pressure, which consumed considerable time in replacing the gasket. This problem was solved by replacing the paper gasket with a copper, as shown in Figure 5.3.

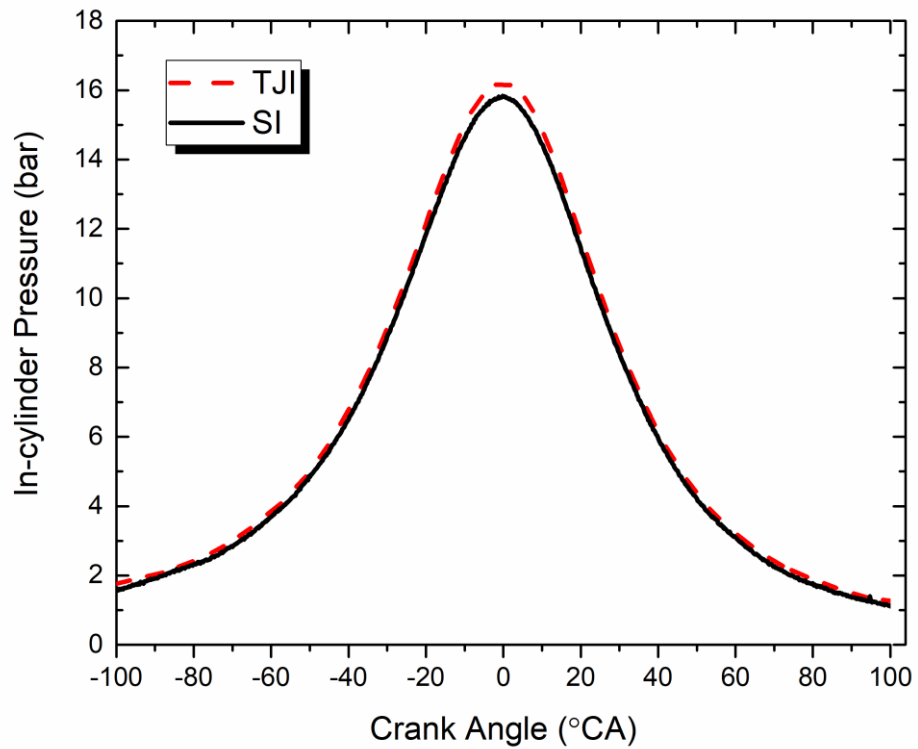


Figure 5.2 Motored in-cylinder pressure against crank angle for both ignition systems



Figure 5.3 Copper top window gasket (left) and paper gasket (right)

Figure 5.4 shows the log P-V line with the copper gasket, which had a straight line of gradient of 1.30 during the compression stroke. Haywood and Brunt et al. [129][125] suggested that a slope of 1.3 for the compression stroke indicates that no unexpected

chamber leakage occurred during compression, and the absolute pressure pegging was sufficiently accurate. The line graph shows that the expansion stroke line does not return to the exact same line as the compression stroke due to the irreversibility of the compression or expansion.

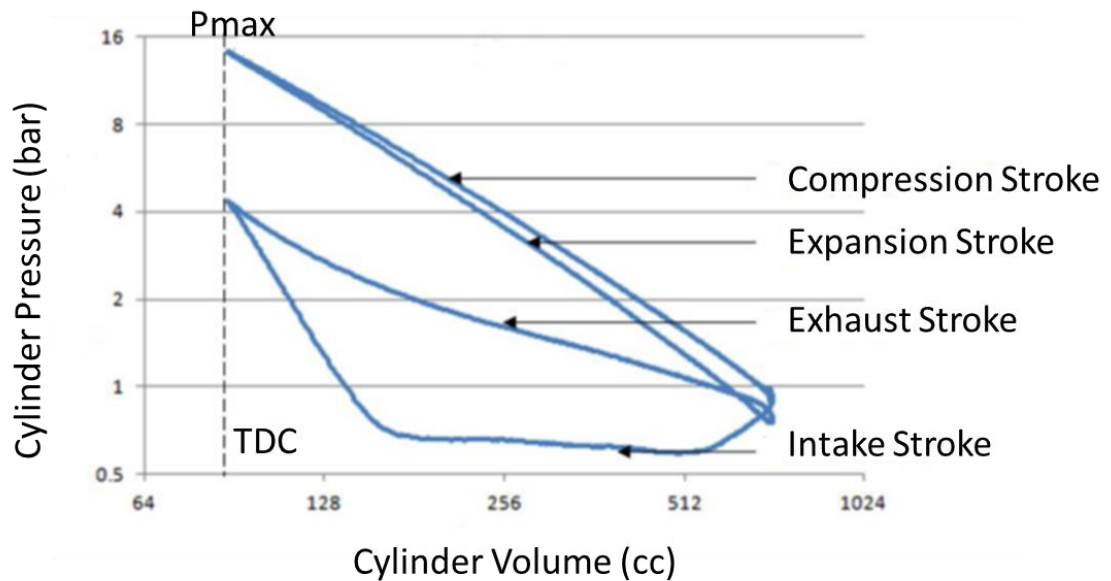


Figure 5.4 LogP/LogV graph of motored in-cylinder pressure against cylinder volume at 1200 rpm

After the motoring tests, both ignition systems were tested under the same conditions, as shown in Table 5.1. All tests were conducted using a metal blank to avoid any damage to the top window. In stoichiometric operation, the pre-chamber was not fuelled with auxiliary fuel, and only the main chamber was fuelled with gasoline by a PFI injector. The pre-chamber ignition and main chamber ignition were compared at the fixed spark timing 22° CA bTDC, at 90°C head temperature and at 1200 rpm. To ensure that the combustion engine reached this temperature, the engine was ran at approximately 95°C for approximately 10 min and then allowed to cool naturally to 90°C . Once the engine had cooled to this temperature, the test results were recorded, as shown in the flow diagram of the test procedure in Figure 5.5.

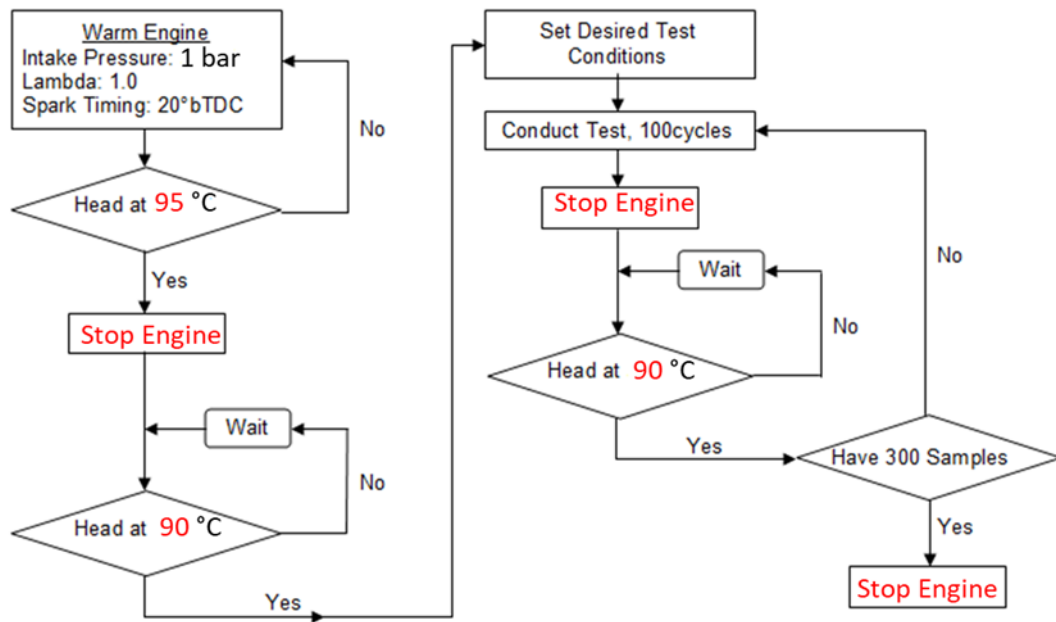


Figure 5.5 Flow diagram of test procedure

An unfuelled pre-chamber cavity (without auxiliary fuel) was used during the stoichiometric condition, which was achieved by using a dummy direct fuel injector in the pre-chamber volume. With this concept, the pre-chamber was filled with a pre-mixed stoichiometric mixture from the main chamber due to the piston motion owing to the interaction between both combustion cavities. The pre-mixed stoichiometric mixture was then ignited by a spark plug that was placed in the pre-chamber volume. Following, the pre-chamber combustion products were transferred to the main chamber through orifices, thereby igniting the main chamber charge. That is, the pre-chamber products travelled to the main chamber due to the combustion produced that increased the pre-chamber pressure, thereby forcing the pre-chamber contents into the main chamber via the orifices in the nozzle.

Table 5.1 Test condition

Parameter/unit	
Speed (rpm)	1200
Relative air–fuel ratio	1
Fuel	gasoline
Fuel amount (mg/pulse)	25
Spark timing	fixed spark timing 22° CA bTDC
Inlet air pressure (bar)	1

Figure 5.6 presents the in-cylinder pressure data for both operations averaged over 100 cycles. The maximum in-cylinder pressure with the pre-chamber was higher than the normal SI due to the rapid burning of the multiple ignition and combustion sites caused by the multiple high-temperature turbulent jets from the pre-chamber. The HRR graph shows that the start of combustion (SOC) of TJI occurred subsequently despite having the same spark timing as the main chamber SI operation. The faster and earlier heat release of the pre-chamber ignition caused the IMEP to be increased from 6.8 bar to 7.3 bar.

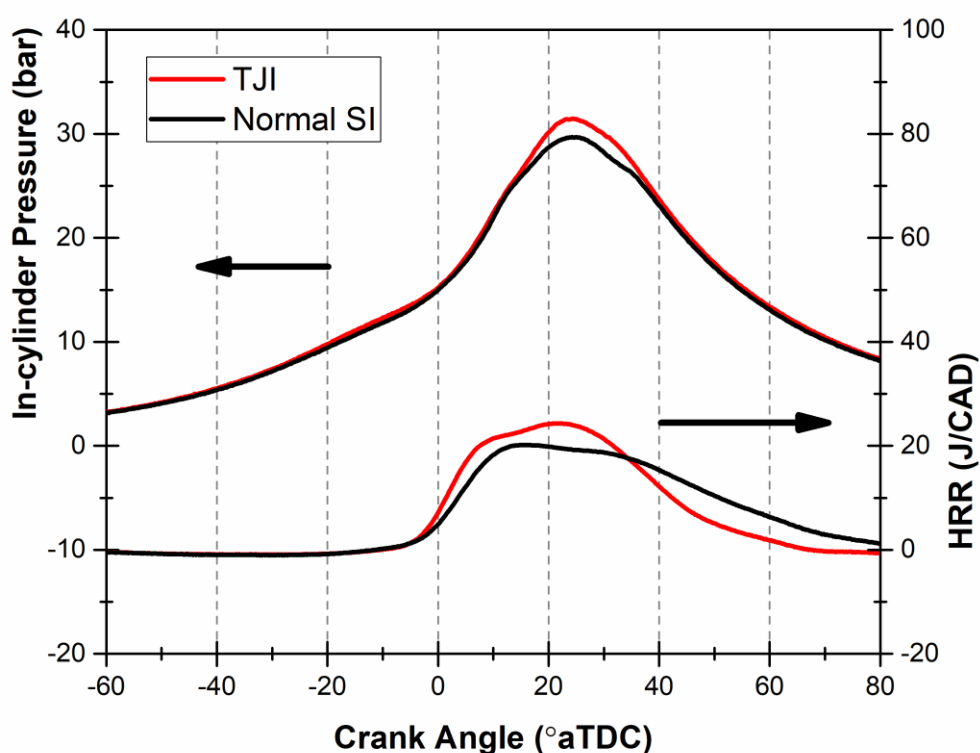


Figure 5.6 In-cylinder pressure and HRR for both ignition systems at fixed spark timing of 22° CA bTDC

Finally, tests were carried out with a glass window at the same engine speed of 1200 rpm and inlet pressure of 1 bar. The MBT spark timings of SI and TJI were 24° CA bTDC and 26° CA bTDC, respectively. Combustion images were captured through the top window via a 45° mirror by a MEMRECAM fx6000 high-speed video camera at 6,000 frames per second (fps), with a resolution of 512 x 384 pixels, as shown in Figure 5.7.

The camera was triggered at the same time as the DAQ to save the images simultaneously with the pressure and temperature data. The gamma and gain of the camera were adjusted for each test to improve the clarity of the images. The combustion images were saved as TIFF files, where each image represents a frozen snapshot over an exposure time of 125 μ s. As presented in Chapter 4, the coloured images were converted into binary black and white images using the built-in MATLAB function 'im2bw'. A mask filter was applied to reduce noise or reflections from outside the combustion chamber. The inflamed area was calculated by assuming that the combustion chamber contained only two areas, namely, the inflamed and unburned areas.

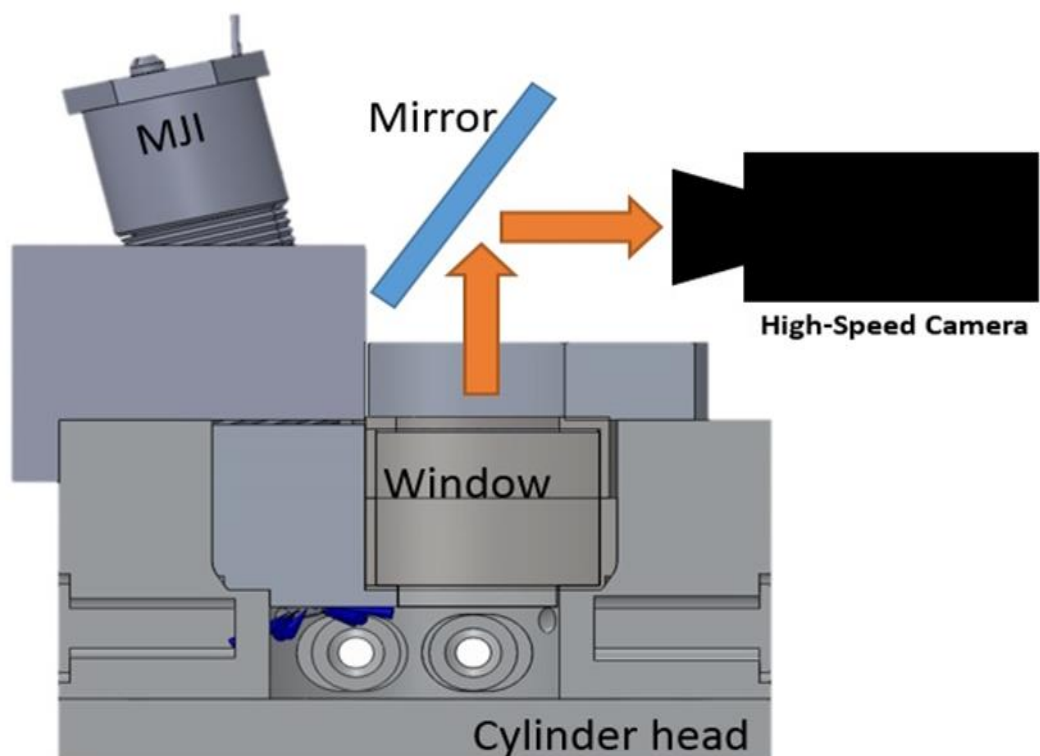


Figure 5.7 Schematic view of the optical engine and high-speed imaging system

Figure 5.8 presents the cylinder pressure and the HRR of the normal SI and TJI. The cylinder pressure data were averaged for 100 continuous cycles. Compared with the normal SI combustion, the start of combustion (SOC) induced by TJI occurred slightly later, despite its slight earlier spark timing. The earlier elevation of the in-cylinder pressure of the normal SI around the end of the compression stroke. Other evidence was provided in the HRR profiles, which revealed that the SOC of TJI was slightly retarded compared with the normal SI. A pre-chamber was used for TJI, and the spark plug did not directly ignite the main chamber contents. Once the spark was discharged in the

pre-chamber, ignition initially began inside it, and then the flame proceeded down towards the nozzle. Then, the main chamber was ignited by the jets as the gases generated by the pre-chamber combustion were expelled. Hence, an ignition delay occurred between the SI in the pre-chamber and the ignition in the main chamber by the turbulent radical jets. By defining the crank angle of SOC as the moment of the ROHR exceeded 1J/CA, the ignition delay was approximately 17° CA. As the main chamber was ignited by the radical jets, the main cylinder pressure increased rapidly and subsequently, and became greater than the cylinder pressure of SI at approximately 5° CA aTDC. The cylinder pressure of the TJI operation peaked at approximately 34 bar at 18° CA aTDC, whereas that of SI reached approximately 31 bar at 20° CA aTDC. This finding is due primarily to the distributed nature of TJI combustion, which enabled multiple ignition sites throughout the main chamber, resulting in more rapid burn rates compared with the normal SI.

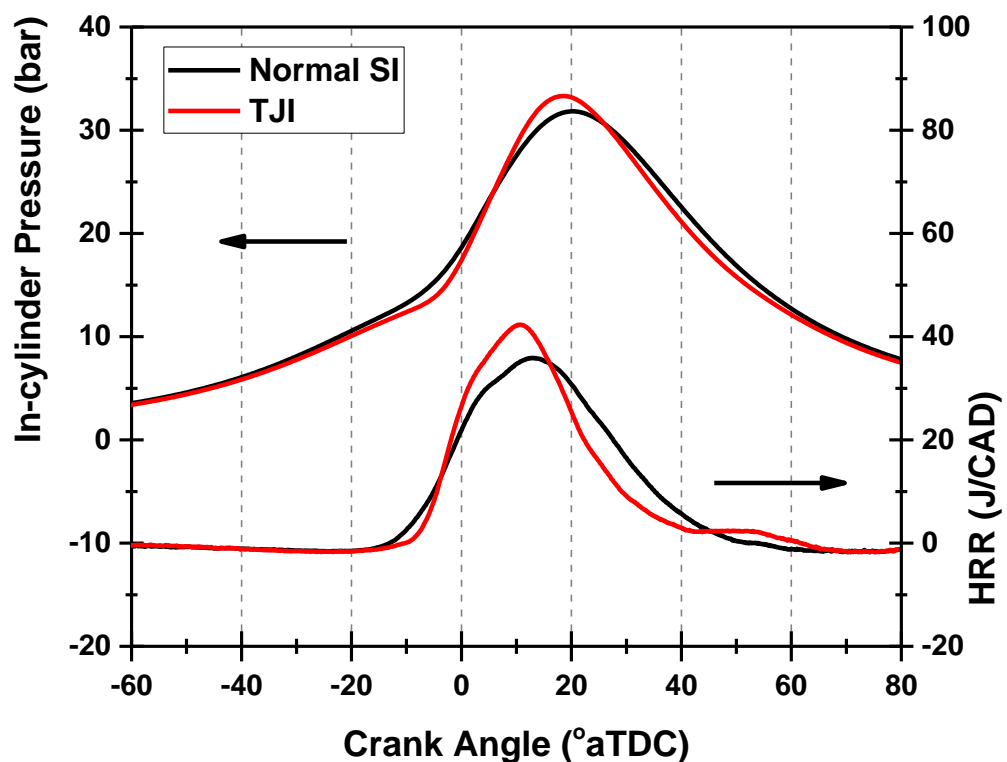


Figure 5.8 In-cylinder pressure and HRR of the normal SI and TJI

MFB was calculated, and the key combustion parameters are presented in Figure 5.9, including the crank angles of MFB 0%–10% (CA0–CA10), MFB 10%–90% (CA10–CA90)

and MFB 50% (CA50). In comparison, the TJI combustion had longer initial combustion duration of CA0–CA10, earlier CA50 and a shorter main combustion duration of CA10–CA90 than the main chamber SI operation. A 25% reduction in the combustion duration could be achieved under this condition.

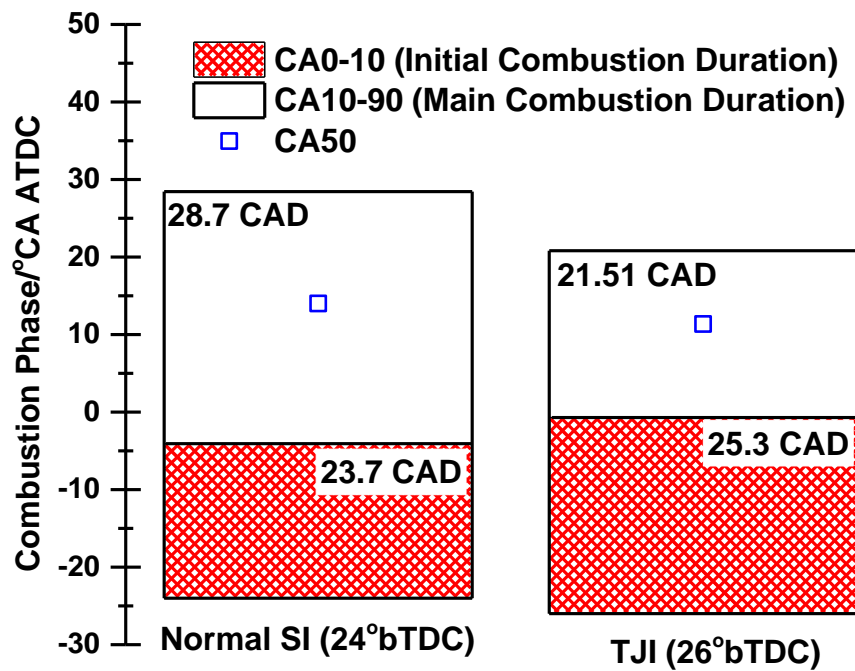


Figure 5.9 Combustion phase of normal SI and TJI

High-speed images of the combustion are displayed in Figure 5.10 from -8.2° CA aTDC to 6.2° CA aTDC. For TJI, two separated visible flame tips were firstly observed at -8.2° CA aTDC, which were assumed to be the flame fronts ignited by the turbulent jets. At -4.6° CA aTDC, another flame front became visible, and all three flame fronts started to merge with each other. By 2.6° CA aTDC, the three flames had completely merged into a single flame, with no evident distinction between them. Subsequently, the remaining unburned gas was rapidly consumed by the propagating flame and almost the entire window was fulfilled with a bright luminescence at 6.2° CA aTDC. Compared with TJI, the image sequence of the normal SI presented a typical flame front formed by SI and propagated towards the cylinder walls. Moreover, in the normal SI operation, the pre-

mixed air–fuel mixture was ignited at one site and then expanded gradually from the top right region of the main chamber, where the spark plug was installed. The jet development and the flame initialisation could not be observed from the top window due to the presence of the TJI unit. However, the flame development in the main chamber for TJI revealed that the flame front reached the cylinder earlier than with normal SI. The results demonstrate the relatively fast flame propagation of TJI, which is consistent with the results for cylinder pressure and HRR.

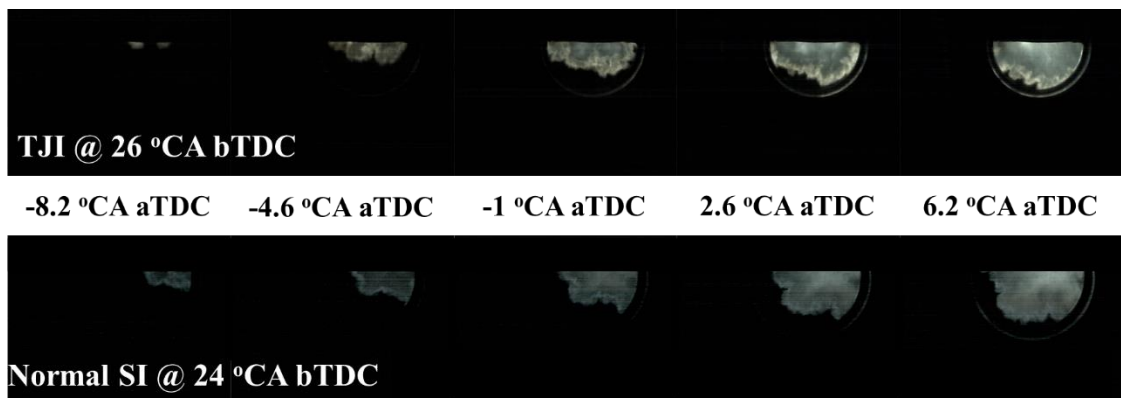


Figure 5.10 Image sequence of normal SI and TJI at 1200 rpm, 1 bar, MBT spark timing

5.3 Effect of Pre-chamber Ignition on the Lean-burn Limit at WOT

Lean-burn techniques reduce engine emissions, whilst simultaneously increasing engine efficiency. The combustion of the lean mixtures can reduce the engine emissions below the given legal limitations [137]. Moreover, the combustion temperature is significantly reduced, thereby reducing NO_x. However, the increasing amount of excess air affects the mixture's ignitability and decreases the laminar flame speed, which causes misfire and incomplete combustion. One of the solutions is to increase the ignition energy and enhance the level of turbulence. The main advantage of using the pre-chamber ignition system is that it allows running the combustion engine under the lean condition. To verify the potential of TJI, this condition was conducted for the normal SI and TJI. During the lean limit exploration, the engine was fired with the stoichiometric air–fuel ratio until the cylinder head metal temperature reached 95 °C and then was operated with the appropriate air–fuel ratio. The tests were carried out at 1200 rpm at WOT with 1.0 bar intake pressure. Experimental data were recorded when the cylinder head temperature reached 90 °C.

To determine the lean-burn limit by the normal SI in the main chamber, the SI was varied and set to the MBT timing at each air–fuel ratio as the air–fuel ratio was increased. The cyclic variation started to rise as the amount of fuel was reduced with increasing air–fuel ratio. The lean-burn limit was reached when the coefficient of variation in IMEP (COV_{IMEP}) exceeded 5%. In the case of the normal SI combustion, the lean-burn limit was 1.12 at this engine operating condition.

Following, the experiment was carried out to determine the effect of an unfuelled pre-chamber ignition on the lean limit. Only the main chamber was fuelled by gasoline via a PFI injector. Some of the main chamber charge returned to the pre-chamber volume during the compression stroke via the pre-chamber nozzle, as shown in Figure 5.11. Then, the pre-chamber charge was ignited by the pre-chamber spark plug. To ignite the main chamber mixture, the pre-chamber injected very reactive radicals. Compared with the normal spark plug ignition, the unfuelled pre-chamber could ignite a more diluted mixture and extend the lean limit to $\lambda = 1.23$. This finding can be explained by faster combustion due to the multiple ignition and flames by the high-temperature turbulent jets produced from the pre-chamber.

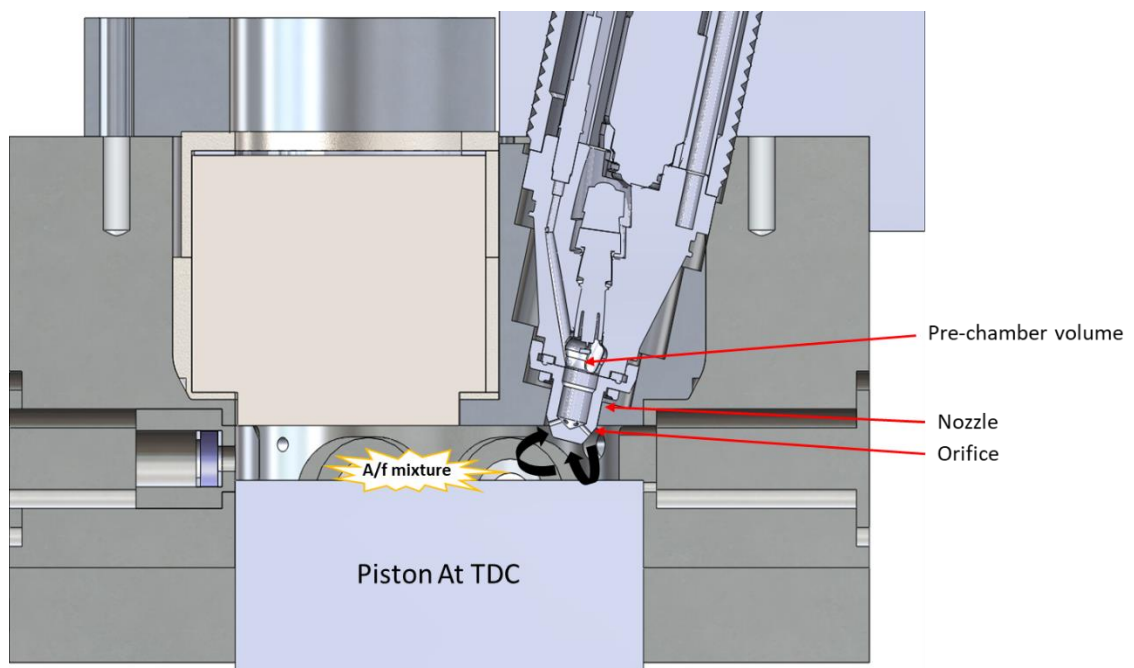


Figure 5.11 Sectioned view showing the interaction between the main chamber and the pre-chamber.

Finally, engine tests were carried out with actively fuelled pre-chamber ignition combustion. The fuel was injected into the pre-chamber by using a Delphi DI injector as

described in Chapter 3. The pre-chamber fuelling event was timed to end at 50° CA before spark. This time was selected to ensure a well-mixed fuel–air mixture could be formed in the pre-chamber prior to the spark discharge. The pre-chamber injection fuel was set at 0.3 mg/pulse. The lambda value of the pre-chamber air–fuel mixture was approximately 0.78, with the pre-chamber air mass calculated based on the mean gas temperature, and the pre-chamber injection pressure was set to 70 bar. Following the same procedure as the unfuelled pre-chamber ignition experiments, the air–fuel ratio was increased and spark timing was adjusted to the MBT at each air–fuel ratio until the lean-burn limit of $COV_{IMEP} \leq 5\%$ was reached. The fuelled pre-chamber proved to be capable of burning a leaner mixture, with the lean limit reaching 1.71. This finding can be explained by the higher thermal energy and more active radicals contained in the multiple jets of partially burned fuel-rich mixture in the pre-chamber. These high-temperature radicals provided higher ignition energy as well as multiple ignition sites compared with the unfuelled pre-chamber and normal single point SI process. These parameters caused a rapid combustion rate. Figure 5.12 compares the lean limit for all the combustion modes. The spark timing was 27°, 26° and 22° CA bTDC for normal SI, pre-chamber without auxiliary fuel and pre-chamber with auxiliary fuel, respectively.

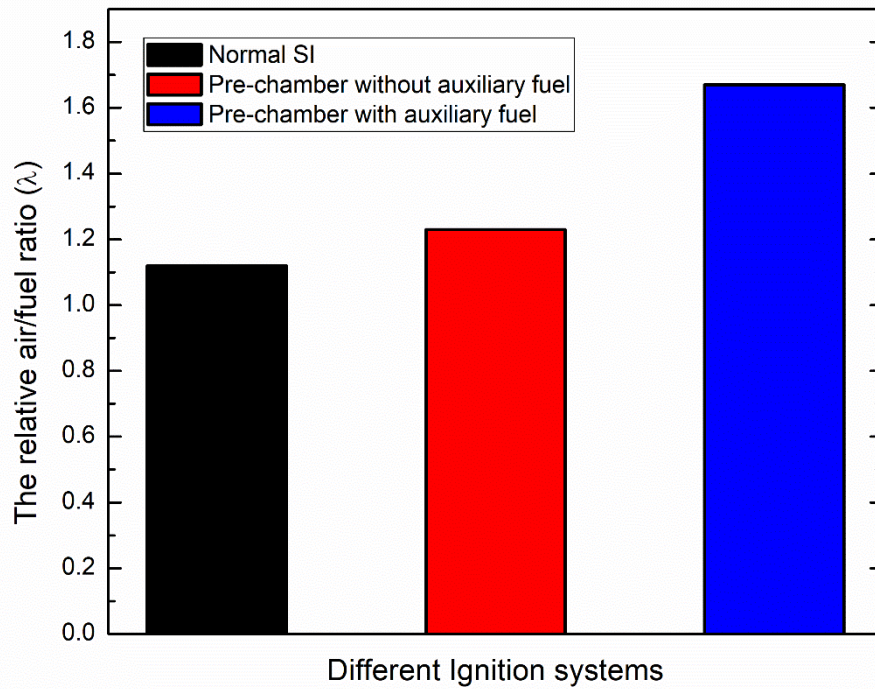


Figure 5.12 Maximum lean-burn limit of pre-chamber ignition (with and without auxiliary fuel) and normal SI

The variation in IMEP with the different ignition systems at the lean-burn limit is presented in Figure 5.13. The IMEP result shows that the values are correlated with the air–fuel ratio, which decreased with increasing lambda. At the same air–fuel ratio, the IMEP value is higher by using the pre-chamber ignition system than by the normal SI because of the faster heat release of the pre-chamber ignition combustion operation.

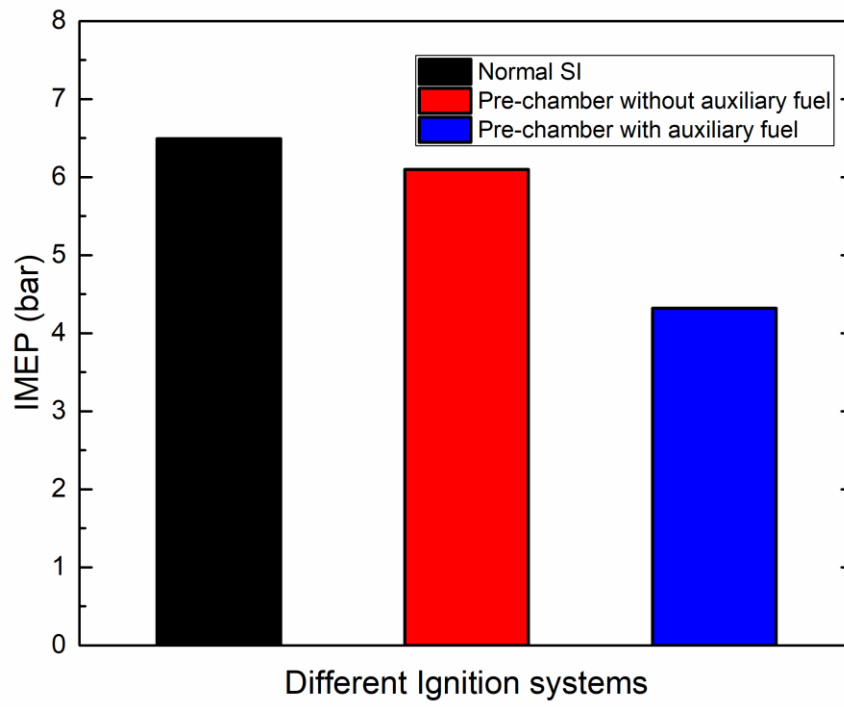


Figure 5.13 IMEP results at MBT for pre-chamber (with and without auxiliary fuel) and normal SI

5.4 TJI at Different Intake Pressures

Table 5.2 Test condition

Speed	1200 rpm
Fuel	Gasoline
Spark timing	MBT
End of pre-chamber injection	50° CA bTDC
Compression ratio	8.4
Inlet pressure	0.7, 0.8, 0.9 and 1 bar
Lambda (λ)	1 to lean limit λ (until $COV_{IMEP} > 5\%$)
Pre-chamber injected fuel	0.3–0.5 (mg/pulse)

A different engine load was used to further evaluate the TJI performance and explore the maximum lean lambda by adjusting the inlet pressure from 0.7 to 1.0 bar. At each operation condition, the main chamber fuel quantity was decreased to reach the lean-burn limit defined by 5% COV_{IMEP} . Then, the pre-chamber fuelling quantity was adjusted to achieve increments of 0.1 lambda until the new lean limit was reached. Spark timing was adjusted to obtain the optimum combustion phasing during the test. Figure 5.14 indicates the maximum lambda reached by TJI and the corresponding IMEP at different inlet pressures. The maximum lambda achieved by TJI was 1.71, which was reached at 1.0 bar inlet pressure. As the inlet pressure decreased to 0.7 bar, the lean-burn limit was reduced to lambda 1.1 due to the reduced flame speed at lower pressure and temperature. The corresponding IMEP was reduced from 4.6 to 3.2 bar when the inlet pressure was decreased from 1 to 0.7 bar because less fuel was burned.

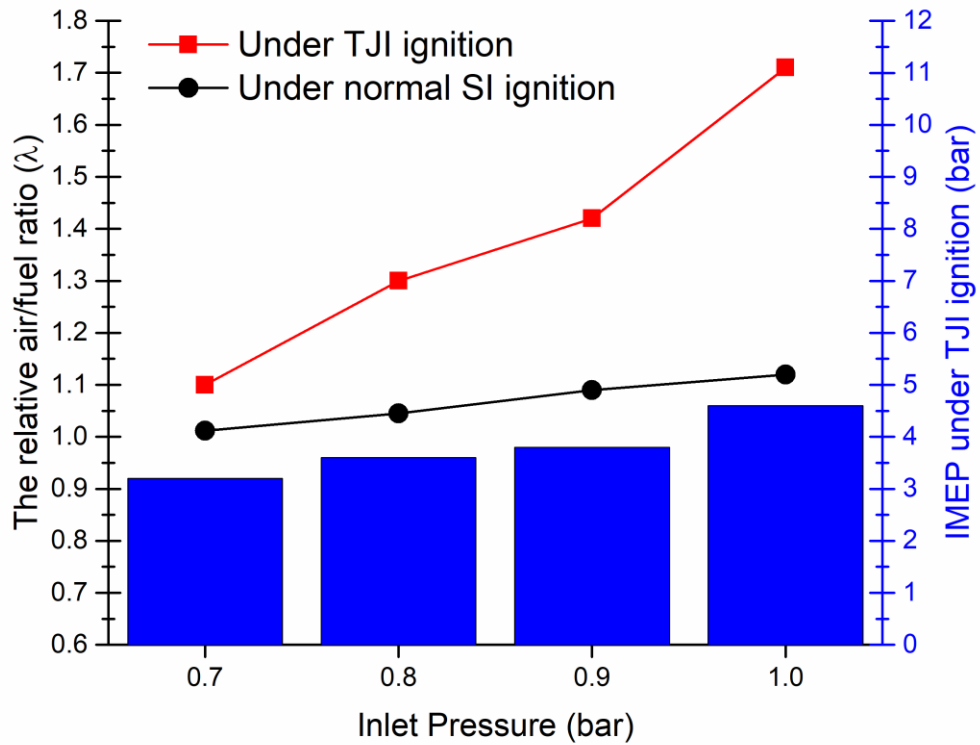


Figure 5.14 Lean-burn limit with TJI under different inlet pressures

Figure 5.15 compares the engine output IMEP under stoichiometric and maximum lean condition at different inlet pressures. Substantial decrease in engine load could be observed under higher inlet pressure given that leaner lambda was used at higher inlet pressure. When lean combustion was utilised at the mid-load, wider throttle opening with higher inlet pressure was required to maintain the engine load similar to the stoichiometric condition. The IMEP with stoichiometric air–fuel mixture at 0.7 bar could be restored by increasing the inlet pressure to 0.9 or 1.0 bar with lean combustion mode.

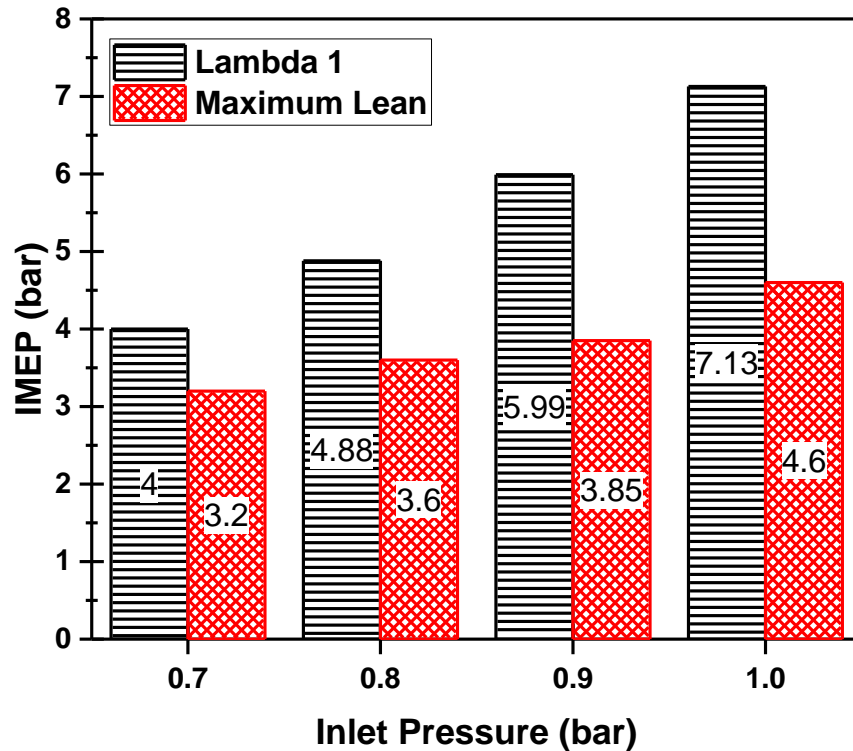


Figure 5.15 IMEP under stoichiometric ratio and lean-burn limit at different inlet pressures under TJI ignition

Figure 5.16 illustrates the effects of the pre-chamber on NO_x emissions. Running the combustion under lean condition reduces the NO_x emissions. The low NO_x emissions were due to the reduction in peak combustion temperature and in the residence time at high temperatures. With very lean-burn combustion ($\lambda = 1.71-1.8$), the NO_x emissions become negligible. During this test, the fuel consumption rate and the intake air mass flow rate were not measured. Therefore, the total exhaust flow mass rate was unknown, and the specific emission could not be calculated. However, the volumetric emissions measured in ppm were adequate to qualitatively indicate the differences of different inlet pressures under different lambda values.

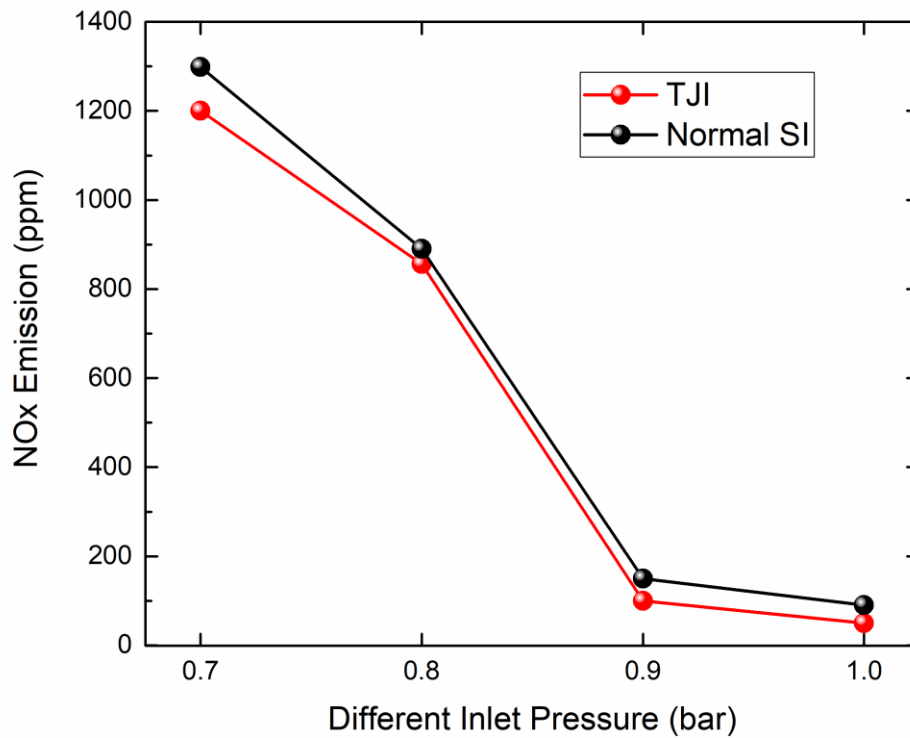


Figure 5.16 NOx emission at the lean-burn limit of different intake pressures (1200 rev/min, maximum lean and MBT spark timing)

Figure 5.17 shows that the HC emissions increased as the inlet pressure or lean-burn limits increased because of the lower combustion and exhaust temperatures of the lean-burn mixtures. The mechanisms of HC changes are correlated to the in-cylinder combustion temperature and the combustion efficiency. However, further lean combustion leads to unstable combustion and generates more HC emissions. For similar reasons, the CO emission were higher at the WOT, as indicated in Figure 5.18.

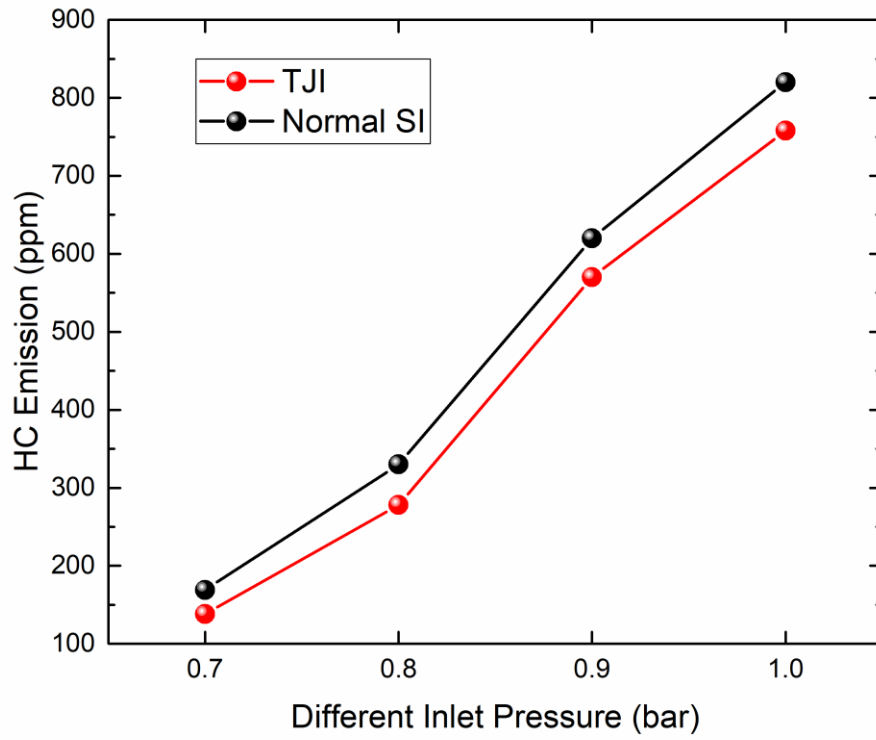


Figure 5.17 HC emission at the lean-burn limit at different loads (1200 rev/min, maximum lean and MBT spark timing)

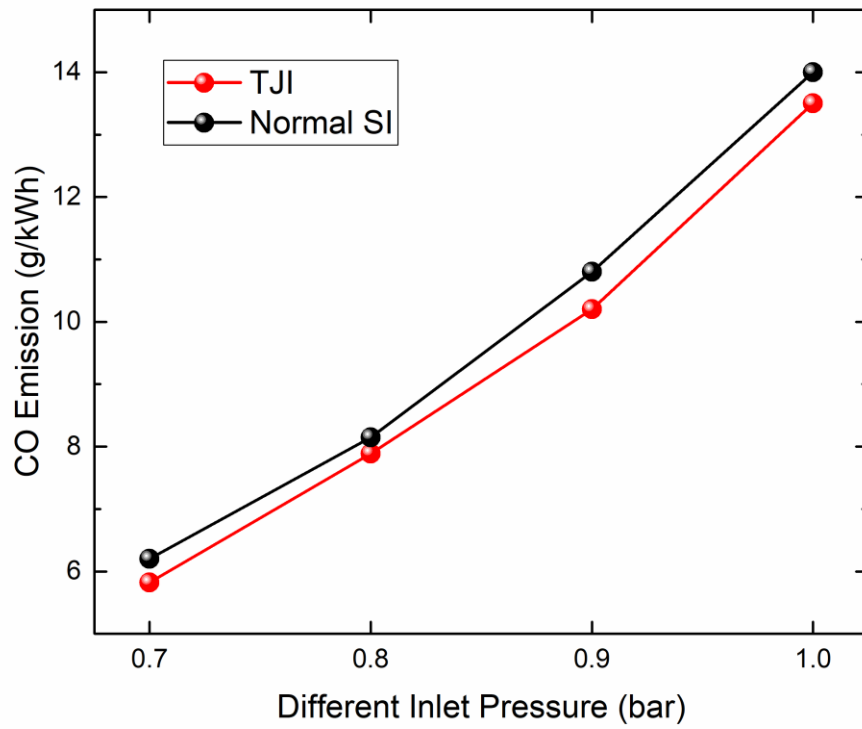


Figure 5.18 CO emission at the lean-burn limit at different inlet pressures (1200 rev/min, maximum lean and MBT spark timing)

5.5 Jet Ignition at Different Engine Speeds

This section presents the results for different speeds of 800, 1000 and 1200 rpm using the pre-chamber ignition system. The inlet air pressure was fixed at 1 bar. Table 5.3 summarises the experimental test conditions. The engine experiment was conducted in two stages. Firstly, the MBT spark timing at lambda 1 was determined. Secondly, the main chamber fuel was reduced to find the lean-burn limit. In the meantime, the amount of pre-chamber fuel and injection timing was varied to reach the lean-burn limit at the MBT spark timing. The end of injection in the pre-chamber was fixed at 50° CA Btdc, whereas the injection duration was varied between and 0.3–0.5 mg/ pulse. The results show that more fuel injection was required inside the pre-chamber to extend the lean-burn limit given that a slightly rich pre-chamber mixture produces more radical species in the TJI entering the main chamber. The lean-burn limit was defined to be $COV_{IMEP} \leq 5$. However, some results are presented at $COV_{IMEP} > 5$ to show the effect of unstable combustion on exhaust emissions and combustion parameter, which is discussed in the following section.

Table 5.3 Test condition

Speed	800, 1000 and 1200 rpm
Fuel	Gasoline
Spark timing	MBT
End of pre-chamber injection	50–70° CA bTDC
Compression ratio	8.4
Inlet pressure	1 bar
Lambda (λ)	1 to lean limit λ (until $COV_{IMEP} > 5$).

The effects of engine speeds on the lean-burn limit are shown in Figure 5.19 for both ignition systems. In general, the pre-chamber ignition system improves the combustion stability and extends the lean-burn limits for all speeds compared with the normal SI because of the increased ignition energy and ignition sites of the multiple turbulent jets. The lean-burn limit λ increases with increasing engine speed. At the highest speed of 1200 rpm, the leanest mixtures occur at $\lambda = 1.71$ with $COV_{IMEP} = 4.57\%$. However, at the lowest speed of 800 rpm, the leanest mixtures occur at $\lambda = 1.51$, followed by the speed of 1000 rpm at $\lambda = 1.69$. The primary reason for the increased lean-burn limit is the increased turbulence and the flame speed with the engine speed. Interestingly, COV_{IMEP}

decreases as the engine speed is increased, especially at high λ values (Figure 5.21). Therefore, the level of dilution is increased as the engine speed increases, which in turn increases flame speed and stability, especially in the early stages of flame development. One of the main advantages of jet ignition is its ability to be used successfully at high engine speeds due to the extremely high speed jet. All jet ignition technologies contribute to ignition enhancement through a combination of increased combustion stability by improving kernel growth as well as accelerated ignition and combustion of the main chamber air–fuel mixture.

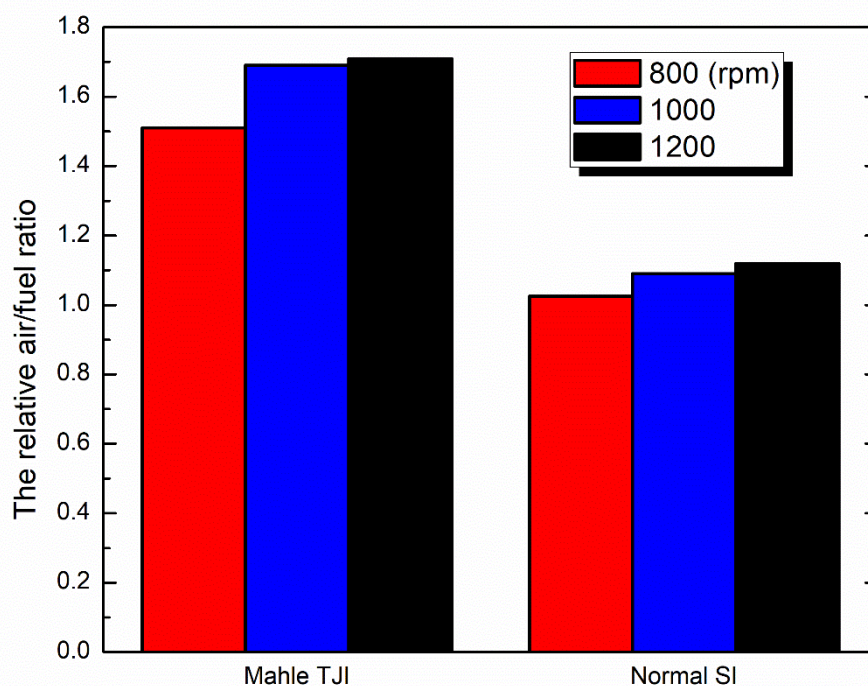


Figure 5.19 Comparison of lean-burn limits between pre-chamber and normal SI systems at different speeds (800, 1000 and 1200 rpm)

Figure 5.20 shows the variation in IMEP_{net} with different lambdas and speeds. At a lower engine speed, the volumetric efficiency increased, and more fuel was injected into the main chamber at the same air–fuel ratio, resulting in a higher IMEP. As expected, the IMEP decreased with lambda as less fuel was burned. For example, at the speed of 800 rpm, a drop in IMEP = 5.614 bar at lambda 1.4 compared with IMEP = 8.17 bar at lambda = 1.2 was observed.

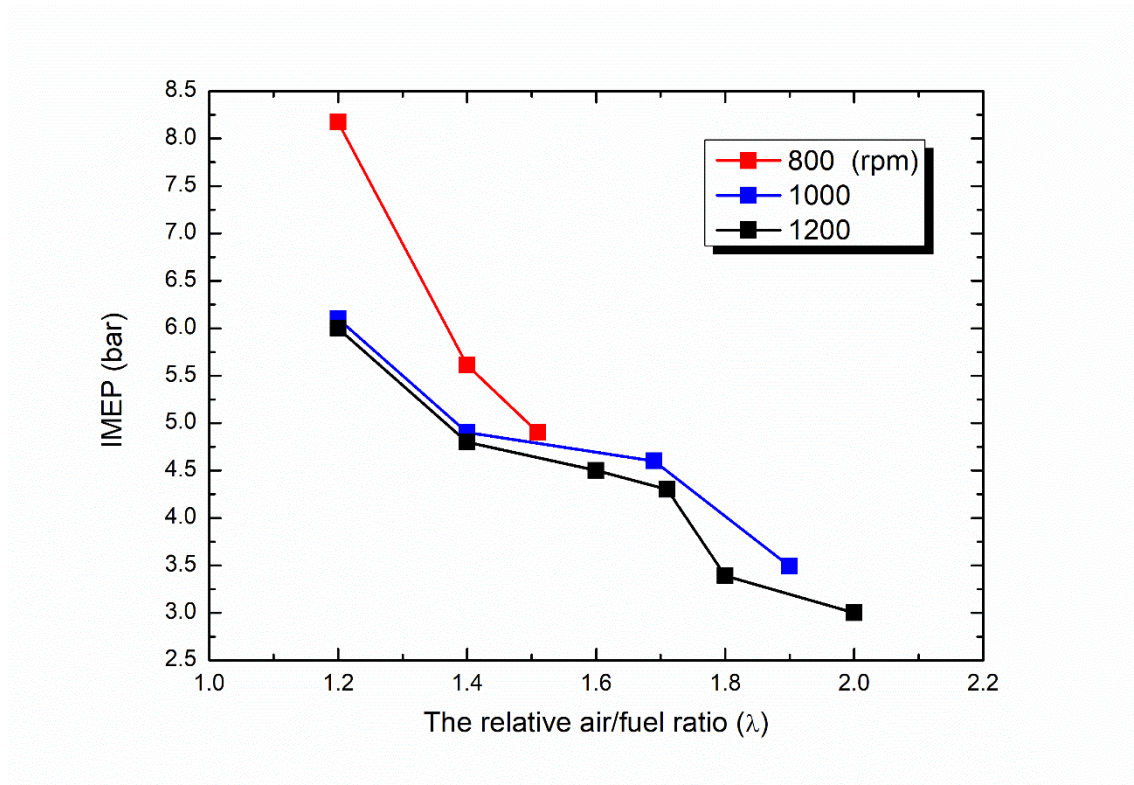


Figure 5.20 Effect of engine speed on IMEP by using pre-chamber ignition and gasoline fuel at inlet pressure 1 bar and MBT spark timing

The lean limit was defined as $COV_{IMEP} \leq 5\%$. As shown in Figure 5.21, COV_{IMEP} increased with the lambda as the HRR decreased. The pre-chamber ignition led to lower cyclic variation due to faster combustion of multiple flames that originated from the TJI.

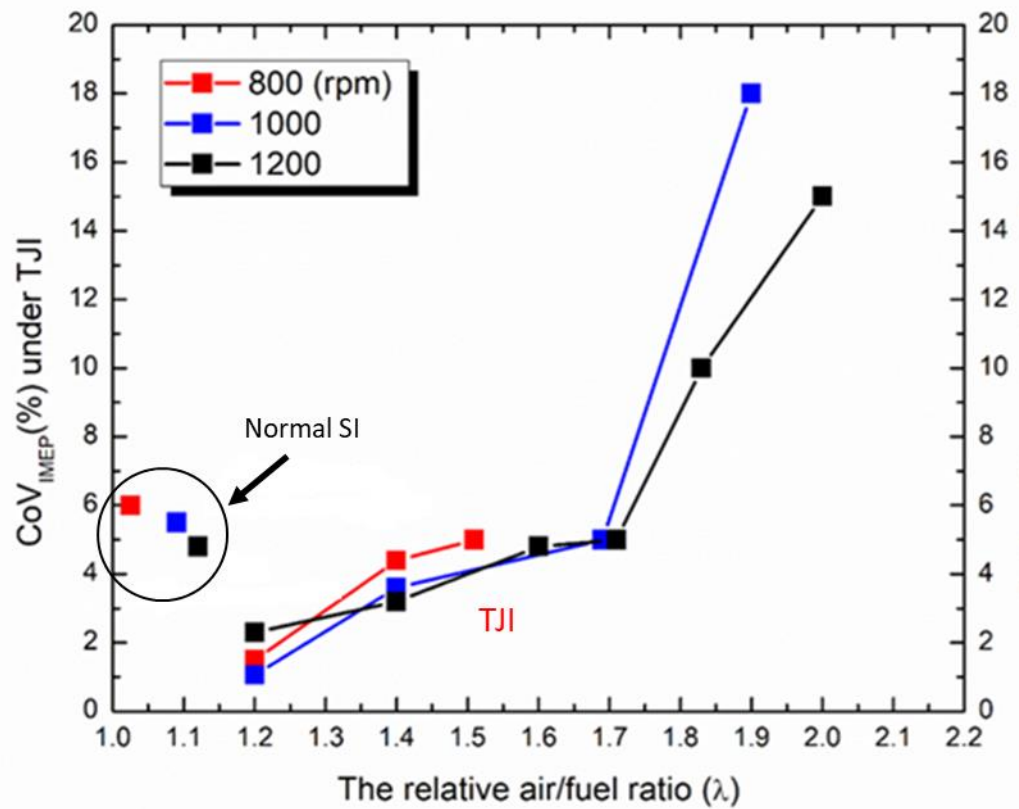


Figure 5.21 Effect of engine speed on COV_{IMEP} by using pre-chamber and normal SI system and gasoline fuel

Figures 5.22 and 5.23 present the effect of different speeds on MFB 0%–10% (CA_0 – CA_{10}) and crank angle 10%–90% (CA_{10} – CA_{90}) at different lambdas, respectively. The smaller values of CA_0 – CA_{10} and CA_{10} – CA_{90} were mainly attributed to the reduced time per crank angle at the higher engine speed. For the same reason, the spark timing in the pre-chamber was more advanced at higher engine speed, as shown in Figure 5.24. For instance, at lambda 1.2, the spark timing in the pre-chamber was 16 and 22 for speeds 800 and 1200 rpm, respectively.

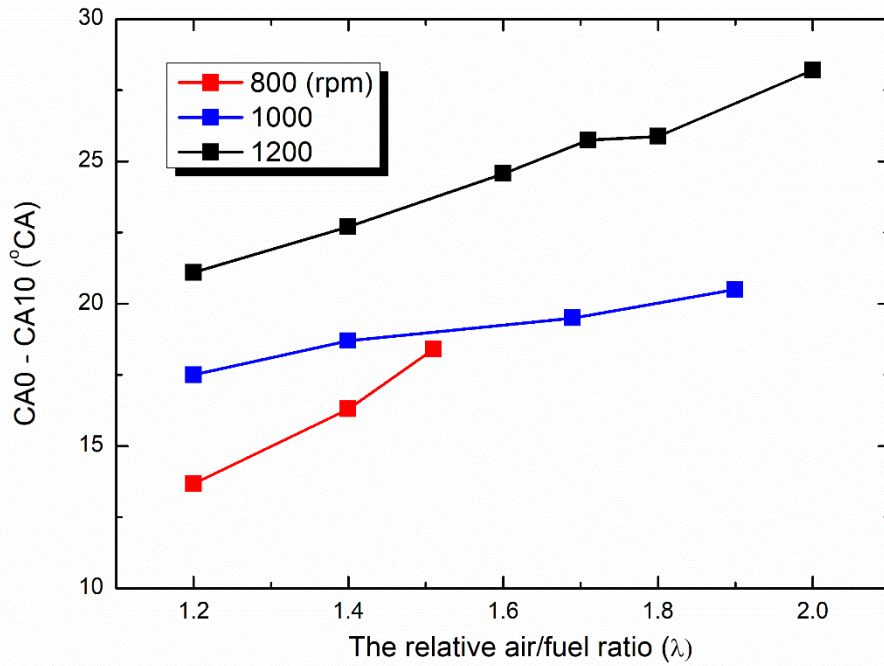


Figure 5.22 Effect of engine speed on 0%–10% MFB by using pre-chamber ignition and gasoline fuel at inlet pressure 1 bar and MBT spark timing

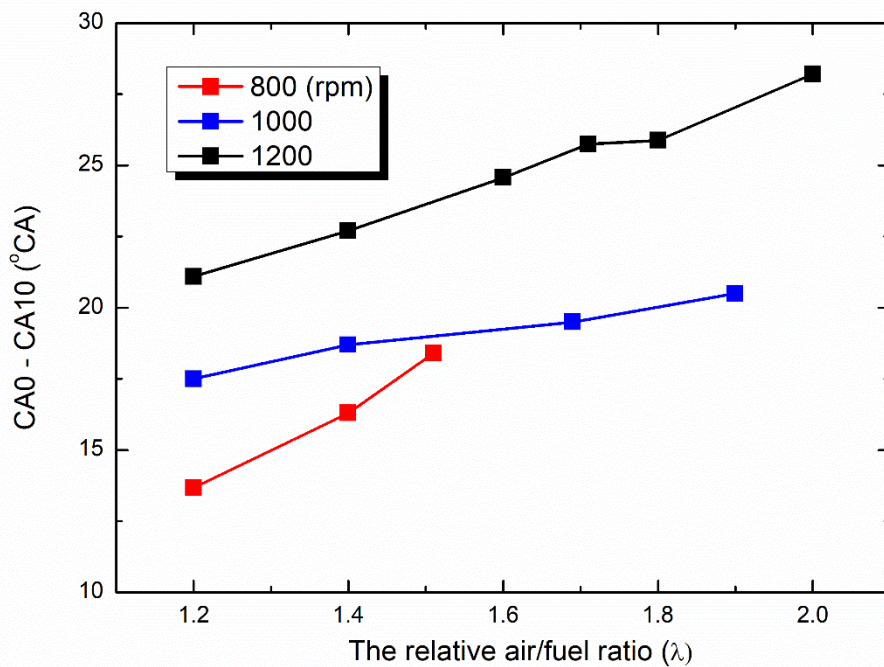


Figure 5.23 Effect of engine speed on 10%–90% MFB by using pre-chamber ignition and gasoline fuel at inlet pressure 1 bar and MBT spark timing

Figure 5.24 shows that the engine speed affects the pre-chamber MBT spark timing. At lower speed, the spark timing was retarded, whereas at higher speed, the spark timing was more advanced. The spark timing was also retarded with lambda. In some cases, the spark timing was limited by knock limit, COV_{IMEP} and misfire. The knock limit extension at MBT (optimal combustion phasing) and at maximum spark retard (5% CoV $IMEP_g$) was quantified by utilising the normal SI and TJI systems.

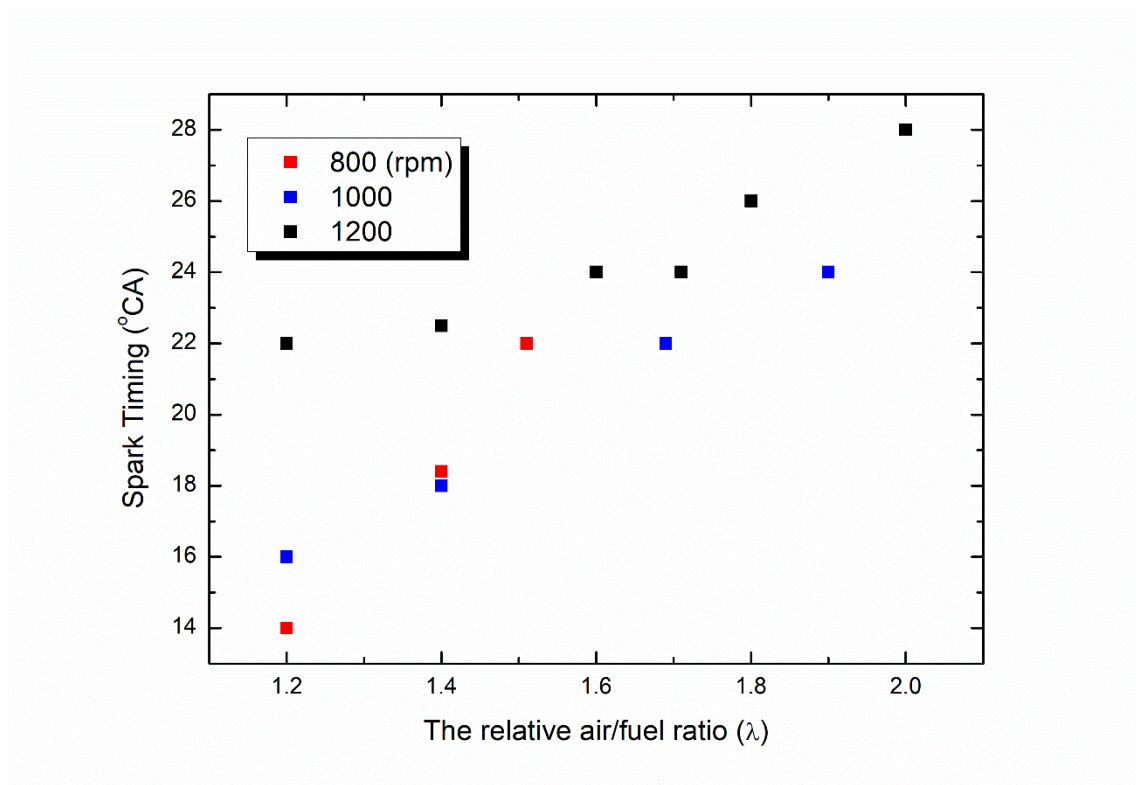


Figure 5.24 Effect of engine speed on MBT spark timing by using pre-chamber ignition and gasoline fuel

Figure 5.25 shows the reduction of NO_x emission with increasing lambda. The NO_x emission was reduced with increased lambda due to lower combustion temperature. Lower speed combustion engine produced the highest NO_x emission due to lower lambda at the lean-burn limit.

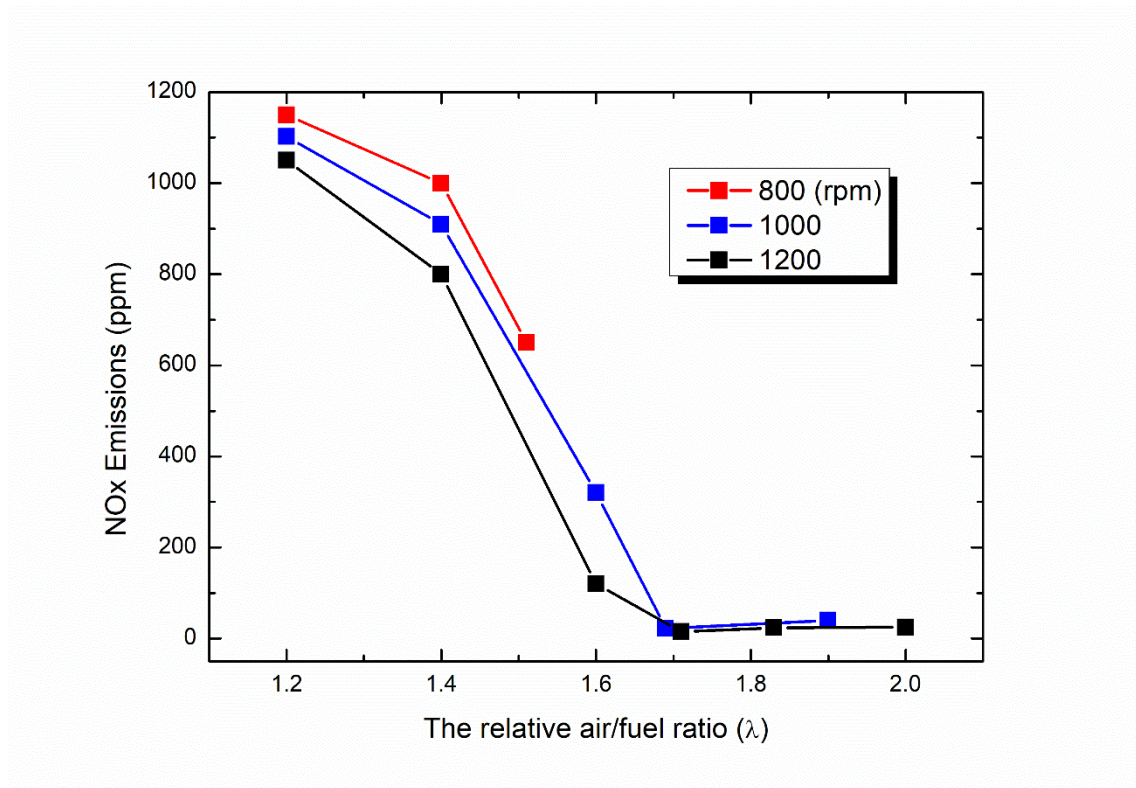


Figure 5.25 Effect of engine speed on NOx emissions by using pre-chamber ignition and gasoline fuel

As shown in Figure 2.26, the HC emissions generally increased with lambda for all speeds due to the reduced combustion temperature and increased cyclic variation. Beyond the lean-burn limit, the HC emissions increased more rapidly due to poor combustion stability and partial burning. Moreover, low combustion temperature increased the probability of wall quenching, thereby leading to more unburned HC emissions. In addition, the pre-chamber crevice volume increased the HC emissions. Therefore, Mahle designed a small pre-chamber (small pre-chamber volume, ~2% of the clearance volume) to reduce the crevice volume and combustion surface area to minimise the HC emissions.

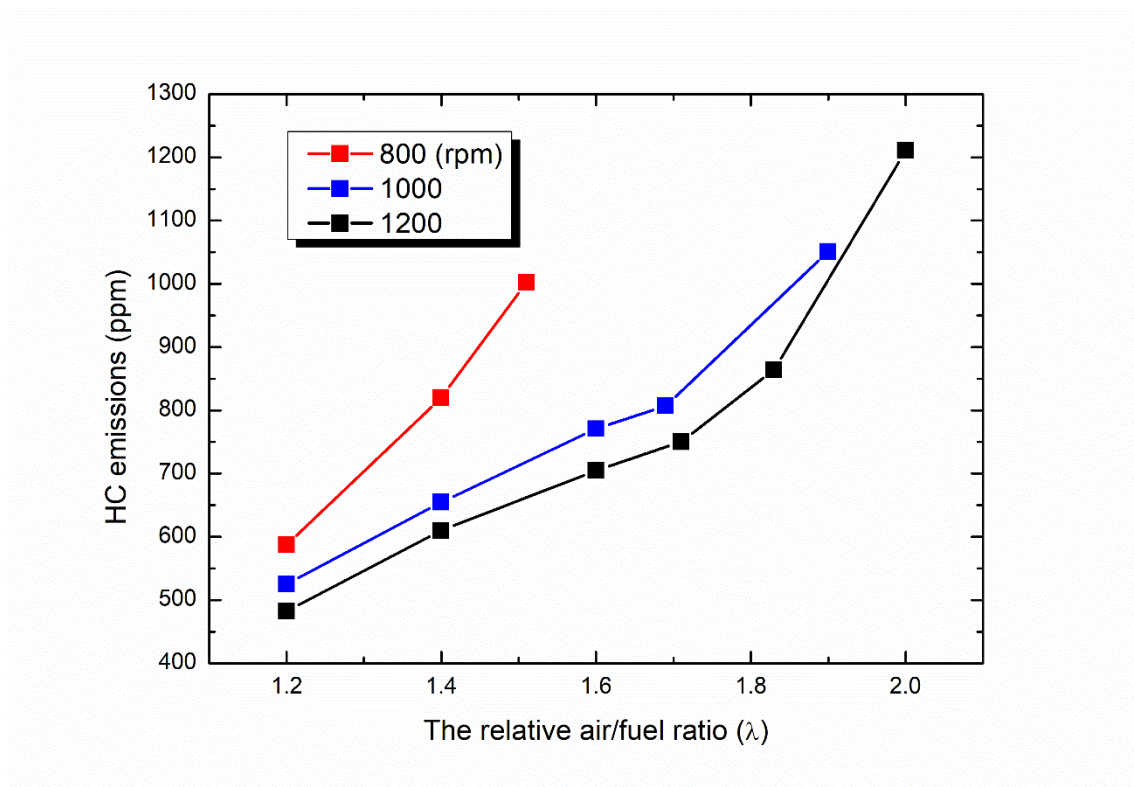


Figure 5.26 Effect of engine speed on HC emissions by using pre-chamber ignition and gasoline fuel at inlet pressure 1 bar and MBT spark timing

As shown in Figure 2.27, the CO emissions increased with lambda in a similar trend to the unburned hydrocarbons because of the incomplete combustion present in the leaner mixtures.

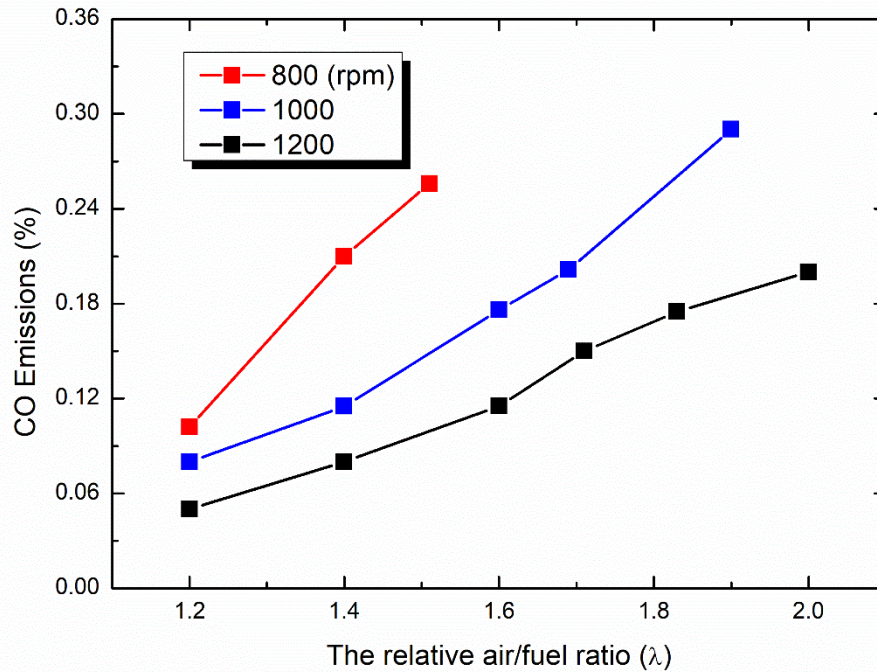


Figure 5.27 Effect of engine speed on CO emissions by using pre-chamber ignition and gasoline fuel at inlet pressure 1 bar and MBT spark timing

5.6 Summary

The modified single-cylinder engine with the Mahle TJI unit was shown to operate according to the design. It is well suited for the in-cylinder combustion studies and engine performance analysis of the conventional SI in the main chamber and the pre-chamber ignition with and without additional fuelling. Experiments were carried out to study the combustion characteristics of TJI, and the results were compared with those of normal SI in the single-cylinder optical engine. The thermodynamic and optical results reveal that TJI could lead to faster burn rates than the normal SI and its ability to extend significantly the lean-burn limit. Together with the in-cylinder heat release analysis, high-speed combustion imaging was used to compare the flame propagation features of TJI and normal SI. The following conclusions have been drawn from the experimental results:

(1) Under the stoichiometric condition, TJI exhibited a slightly retarded start to combustion due to the ignition delay caused by the pre-chamber jet formation. After ignition by multiple-jets, the main chamber pressure rose more rapidly than the normal SI, and the main combustion duration of TJI was greatly reduced.

- (2) With pre-chamber ignition, multiple jet flames were observed in the main chamber and subsequently merged as one propagating flame. Compared with the single flame originating from the spark plug in the main chamber, the multiple-jet ignited flames and the subsequently merged flame propagated significantly faster.
- (3) When the inlet pressure was fixed at 1.0 bar with WOT, the lean-burn limit was extended from $\lambda = 1.1$ in the SI mode to $\lambda = 1.2$ in the unfuelled pre-chamber operation and $\lambda = 1.7$ in the fuelled pre-chamber operation because of the multiple ignition sites and higher thermal energy and radicals of turbulent jets formed from the pre-chamber ignition combustion.
- (4) The maximum lean lambda reached by TJI was correlated with the inlet pressure. The decrease in inlet pressure caused a decrease in engine IMEP and narrowing of the lean limit.
- (5) The concentration and specific NO_x emissions decreased with the increased lean-burn limit at higher intake pressure.
- (6) The concentration of HC and CO emissions became higher with extended lean-burn limit because of the lower combustion and exhaust temperatures.
- (7) The lean-burn limit of the pre-chamber ignition operation increased with the engine speed between 800 rpm to 1200 rpm at WOT because of the faster flame speed.
- (8) When the lambda was less than 1.7, NO, CO and HC emissions were found to be lower at higher engine speed at the same lambda. Beyond lambda 1.7, the NO emission was virtually zero.

**Chapter 6 TJI Combustion and Emissions
of Gasoline, Anhydrous Ethanol and Wet-
Ethanol in an Optical Engine**

6.1 Introduction

This chapter presents the results and discussion on the effectiveness of the TJI system on combustion stability, lean limit and emissions in a single-cylinder optical engine fuelled with gasoline, anhydrous and wet-ethanol.

Table 6.1 summarises the properties of the fuels tested. The differences in fuel properties affect the fuel burning and combustion process. For instance, anhydrous ethanol and wet-ethanol are less prone to knocking combustion than gasoline because of their higher research octane number. In addition, their higher latent heat of vaporisation reduces the charge temperature, especially in DI engines. However, the lower calorific value of ethanol in volume is only approximately 72% compared with gasoline. Under fixed engine speed and load condition, approximately 1.61 times more volumetric ethanol is required due to its relative low stoichiometric ratio. Combining the two aspects, a total of 1.16 times greater volumetric energy is contained when the stoichiometric ethanol/air mixture is utilised. To produce a stable combustion in the pre-chamber for the subsequent jet ignition of lean or diluted mixture in the main chamber, a slightly rich or stoichiometric mixture is prepared in the pre-chamber.

Table 6.1 Physical–chemical characteristics for gasoline, ethanol and hydrous ethanol [107][138]

Properties	Gasoline	Anhydrous Ethanol	Wet-Ethanol
Chemical formula	$C_nH_{1.87n}$	C_2H_5OH	10% water in ethanol (E90W10)
Density (1 bar, 21 °C)	0.74 kg/litre	0.79 kg/litre	0.816 kg/litre
Lower heating value	41.087 MJ/kg	28.865 MJ/kg	25.318 MJ/kg
Latent heat of vaporisation (kJ/kg).	305	840	-
Reid vapour pressure	1.03 bar	0.18 bar	-
Volumetric energy	31.6 MJ/litre	22.8 MJ/litre	21.18 MJ/litre
Stoichiometric AFR	14.421	8.953	7.853
Oxygen content	0	34.8	36.42
RON	97	109	106

6.2 Experimental Test Conditions

All experiments were carried out at 1200 rpm and WOT with gasoline, hydrous and wet-ethanol. Table 6.2 shows the test conditions for all experiments. For each fuel, the following three combustion modes were studied: (1) conventional SI combustion without the pre-chamber, (2) SI in the pre-chamber without additional fuel injection in the pre-chamber and (3) SI in the pre-chamber with additional fuel injection. For each combustion mode, after warming up the engine, the spark timing was adjusted to find the MBT at lambda 1. The fuel amount was then reduced, and the MBT spark timing was found until the maximum lean-burn limit, which was defined by $COV_{IMEP} \leq 5\%$. The fuel

injection in the pre-chamber was set at 50° CA before the spark discharge to allow the mixture formation.

The pre-chamber injection fuel was set to 0.3, 0.5 and 0.5 mg/pulse for gasoline, ethanol and wet-ethanol, respectively, to achieve stable combustion of the leanest air–fuel mixture in the main chamber as measured by the highest overall lambda. The pre-chamber air mass was calculated based on the mean gas temperature. The in-cylinder temperature, pressure and composition were effectively modelled as homogeneous at each instance. The gas medium was assumed to obey the perfect gas law. This information was added into the manuscript. Then, the lambda values of the pre-chamber mixture were approximately 0.78, 0.9 and 1 for gasoline, ethanol and wet-ethanol, respectively. The thermodynamic state within the pre-chamber at the time of injection was approximately 5 bar and 550 K. The pre-chamber volume is 1 cm³, which was only 1.27% of the main chamber volume at TDC.

Table 6.2 Test condition

	Ethanol	Wet-ethanol	Gasoline (baseline)
Speed (rpm)	1200	1200	1200
Spark timing (°CA)	MBT/Lean-burn Limited	MBT/Lean-burn Limited	MBT/Lean-burn Limited
End of pre-chamber injection (°CA bTDC)	50	60	50
Compression ratio	8.4	8.4	8.4
Inlet pressure (bar)	1	1	1
Lambda (λ)	1 to maximum λ (1.9) (until COVIMEP \geq 5%)	1 to maximum λ (1.77) (until COVIMEP \geq 5%)	1 to maximum λ (1.71) (until COVIMEP \geq 5%)
Pre-chamber injection fuel (mg/pulse)	0.5	0.5	0.3
Pre-chamber air/fuel ratio at lean limit	0.9	1	0.78

6.3 Results and Discussions

6.3.1 Effect of Fuel on IMEP and Lean-burn Limit

Figure 6.1 shows the maximum lean-burn limit for each of the combustion modes of gasoline, ethanol and wet-ethanol. The normal SI combustion mode started with lambda 1 and SI in the main chamber at the MBT spark timing. Then, the amount of fuel was decreased until the lean-burn limit was reached with SI in the main chamber. The engine was able to operate with the highest lambda with ethanol fuel using SI in the main chamber because of the relatively faster burning rates of ethanol [139].

As indicated in Figure 6.1, the maximum relative air–fuel ratio or lambda was extended slightly for all three fuels when the SI was in the pre-chamber without pre-chamber fuel injection. This finding can be explained by the piston motion and subsequent flow interaction between the combustion cavities when the pre-chamber was fed a pre-mixed air–fuel mixture from the main chamber. The multiple ignition and combustion sites caused by the turbulent high-temperature jets of high-temperature gas from the pre-chamber produce high energy products from this combustion event, and then transferred to the main chamber after the combustion has started in the pre-chamber. The most significant extension to the lean-burn limit was achieved by the addition of fuel injection in the pre-chamber. The heat release analysis and combustion images indicated that the ignition of the near stoichiometric mixture in the pre-chamber resulted in much faster combustion of the mixture in the main chamber as a result of multiple ignition sites by the highly active gas jets emanating from the pre-chamber nozzle holes. These jets of radicals enter the main chamber with high turbulence and temperature to ignite the main chamber charge at multiple sites and subsequent multiple flames in the chamber.

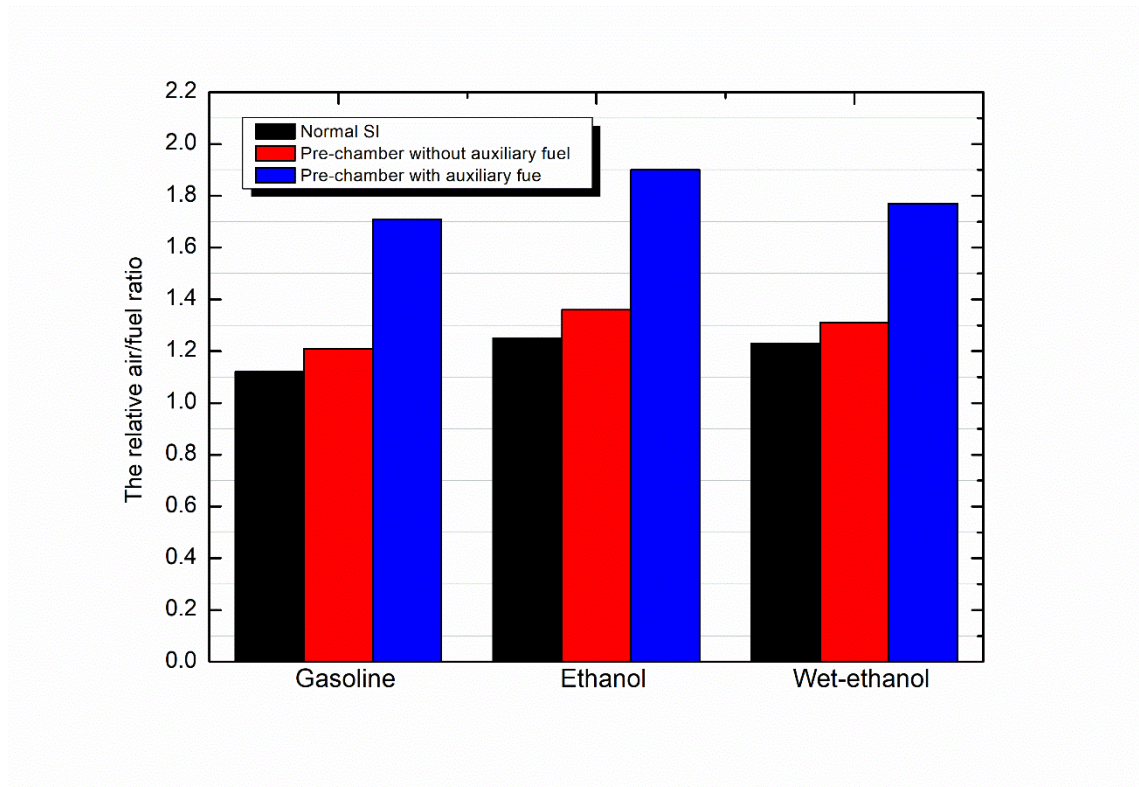


Figure 6.1 Comparison of lean-burn limits between normal SI and pre-chamber ignition (with and without auxiliary fuel) combustion systems for gasoline, ethanol and wet-ethanol

Figure 6.2 illustrates the variation in IMEP with different fuels and lambda at 1200 rpm and inlet pressure 1 bar with fuel injection in the pre-chamber. The IMEPnet values shown in the figure are related to the maximum lambda that the pre-chamber can achieve with stable combustion, where the corresponding net IMEP was recorded at the MBT spark timing of each fuel. The IMEP values decreased with increasing lambda as less fuel was injected. However, the IMEP values of all three fuels were similar, and the IMEP of ethanol was slightly higher, followed by wet-ethanol and gasoline. These results are based on the difference in the energy input of each fuel. In the case of constant volumetric air flow rate, the input energy contained in a stoichiometric mixture of one kilogram of intake air and fuel is 2.92, 3 and 3 kJ for gasoline, ethanol and wet-ethanol, respectively.

The gasoline engine operation was limited to lambda of 1.7. As the lambda exceeded the lean limit of 1.7, an increasing number of cycles was misfired and partially burned, as indicated by the high COV of IMEP of more than 5%, as shown in Figure 6.3. The figure

reveals that ethanol had more stable combustion, and the lean limit was extended to $\lambda = 1.9$ followed by wet-ethanol with lambda of 1.77.

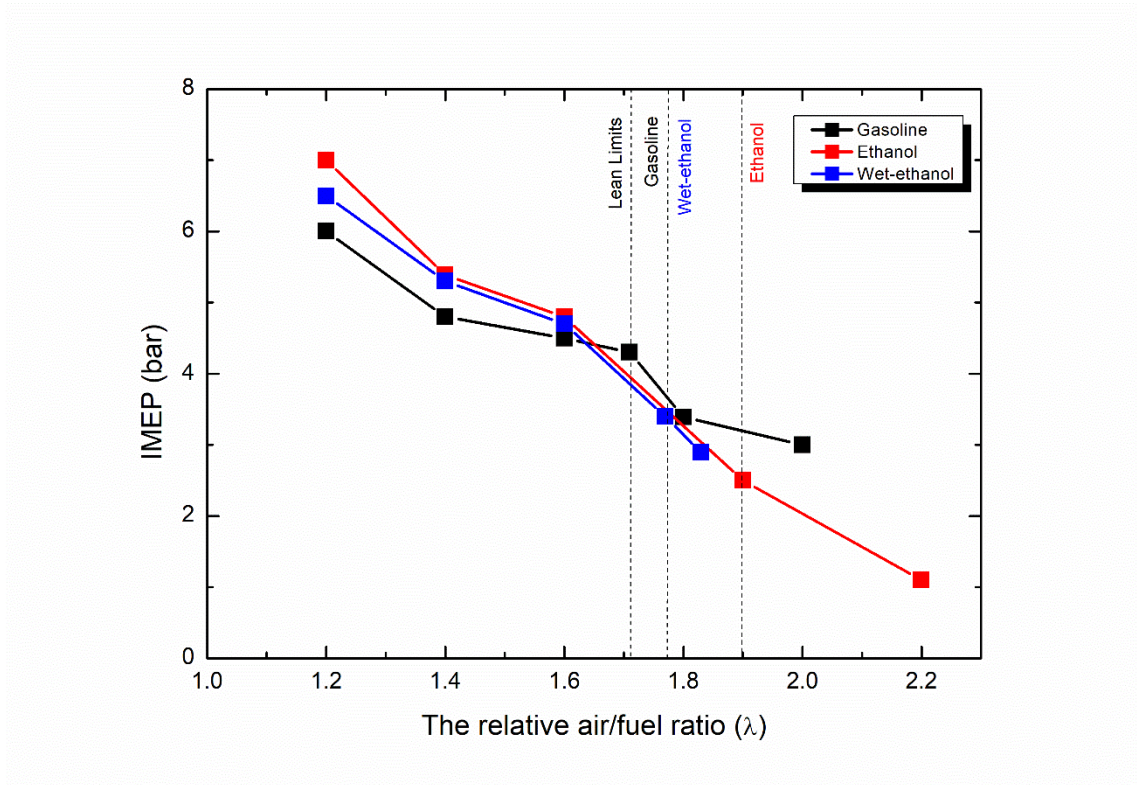


Figure 6.2 Effect of air–fuel ratio of each fuel on IMEP variation with pre-chamber fuel injection

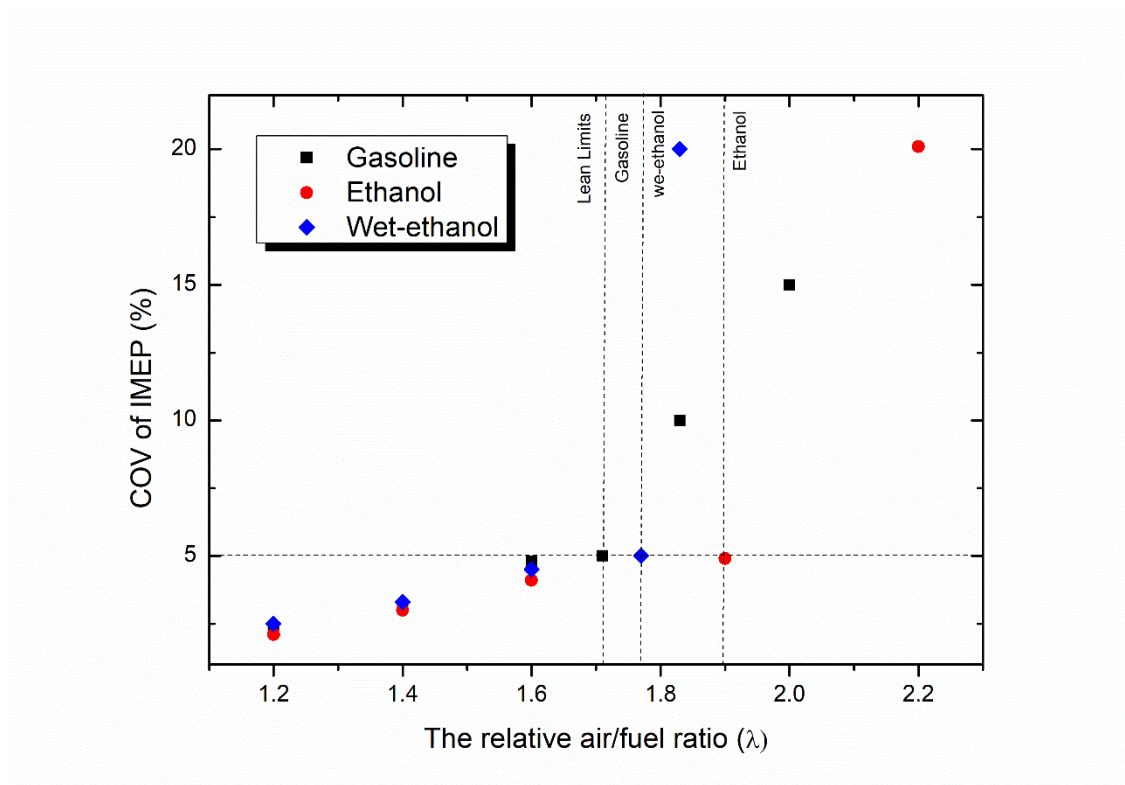


Figure 6.3 Effect of air–fuel ratio of each fuel on combustion stability at 1200 rpm, inlet pressure 1 bar

6.3.2 Effect of Fuel on Exhaust Emissions

Figure 6.4 shows that the NO_x emission was reduced with increased lambda due to lower combustion temperature. Gasoline combustion produced the highest NO_x emission, followed by the wet-ethanol and then ethanol. This finding can be explained by the advanced spark timing and higher peak cylinder pressure and temperature results shown in Figures 6.8 and 6.10. The latent heat of vaporisation of ethanol can also contribute to the lower NO_x emission. For ethanol, the NO_x emissions became extremely low at the lean limit lambda 1.9 as the maximum combustion temperature dropped below 1800 K. Temperature here refers to the in-cylinder mean gas temperature, which was calculated based on a standard single-zone model according to the measured pressure.

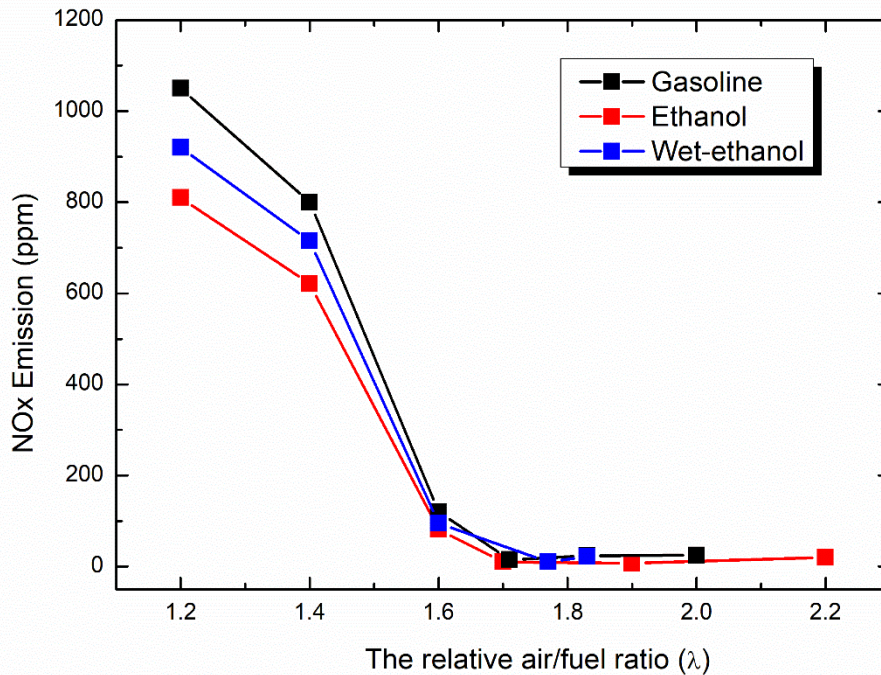


Figure 6.4 Effect of air–fuel ratio on NOx emissions at inlet pressures 1 bar, 1200 rpm maximum lean and MBT spark timing with fuel pre-chamber

Figure 6.5 shows the HC emissions result for gasoline, ethanol and wet-ethanol at MBT spark timing, inlet pressure 1 bar and 1200 rpm. The mechanisms of HC changes were correlated with the in-cylinder combustion temperature and the combustion efficiency. When lambda was increased, the lean combustion resulted in lower engine load and thereby lower in-cylinder temperature, thereby leading to an increase in HC emissions at lean condition. However, lean combustion caused unstable combustion and generated more HC emissions, which can be indicated by the COV of IMEP under lean condition. The IMEP and COV results are shown in Figures 6.2 and 6.3, respectively. Ethanol showed lower level of HC emissions due to its faster flame speed and shorter combustion duration, as shown in Figures 6.7 and 6.8. Combustion was faster, thereby reducing HC emissions. The CO emissions were extremely low because the lean combustion was running with excess air. The CO emission results follow a similar trend to the HC emissions for the same reasons, as shown in Figure 6.6.

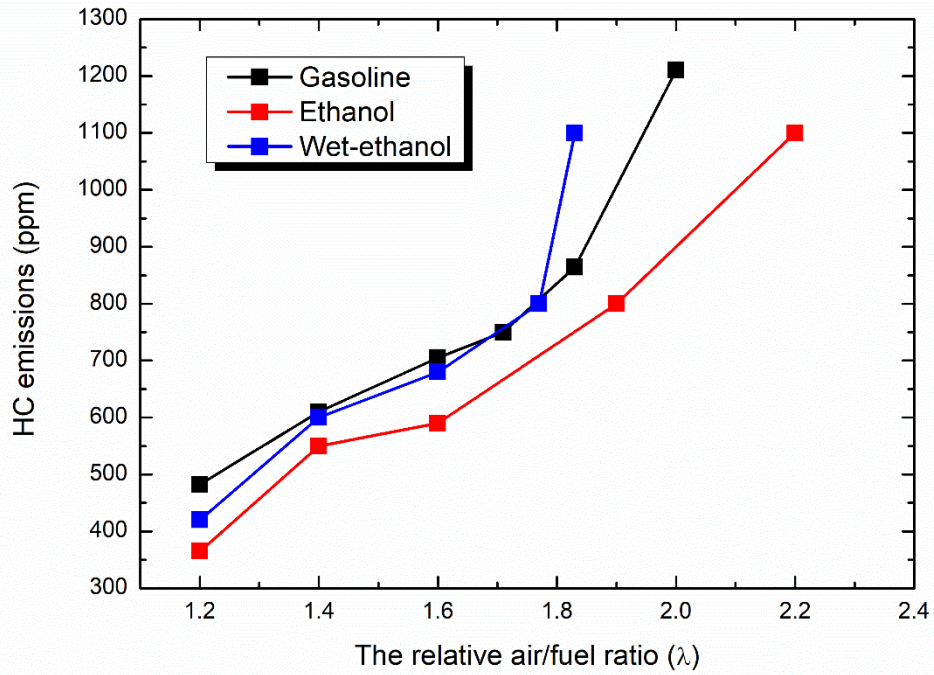


Figure 6.5 Effect of air–fuel ratio of each fuel on HC emissions at inlet pressures 1 bar, 1200 rpm maximum lean and MBT spark timing with fuel pre-chamber

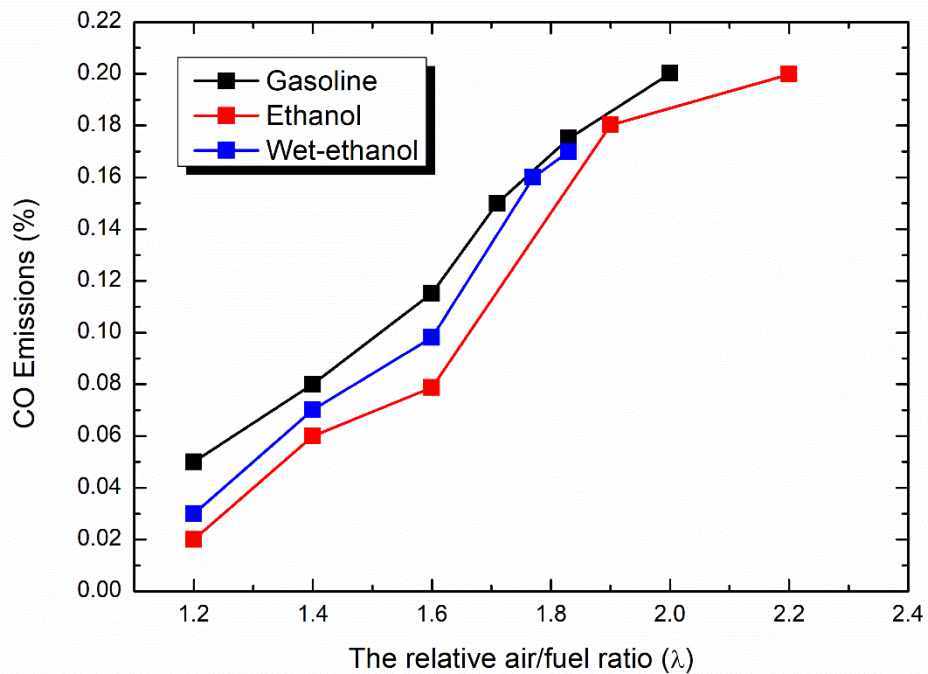


Figure 6.6 Effect of air–fuel ratio of each fuel on CO emissions at inlet pressures 1 bar, 1200 rpm maximum lean and MBT spark timing with fuel pre-chamber

6.3.3 Comparison of the Combustion and Heat Release Processes

Figures 6.7 and 6.8 show the initial heat release and main combustion duration expressed as the MFB 0%–10% (CA 0–10) and crank angle 10%–90% (CA 10–90), respectively. The figures show that the initial heat release and the main combustion duration increased with leaner mixture, and the ethanol burned at a faster rate with retarded MBT timings. The difference in the MBT timing became greater with increased lambda.

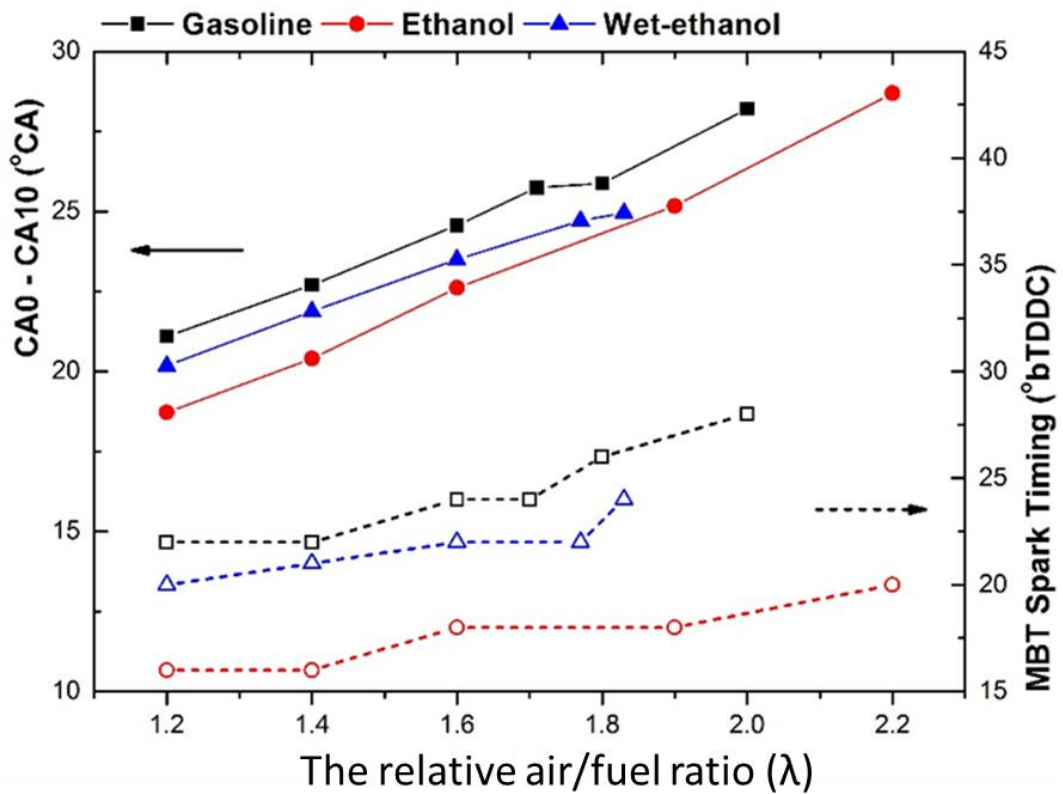


Figure 6.7 Effect of fuel on 0%–10% MFB at inlet pressure 1 bar, 1200 rpm and MBT spark timing

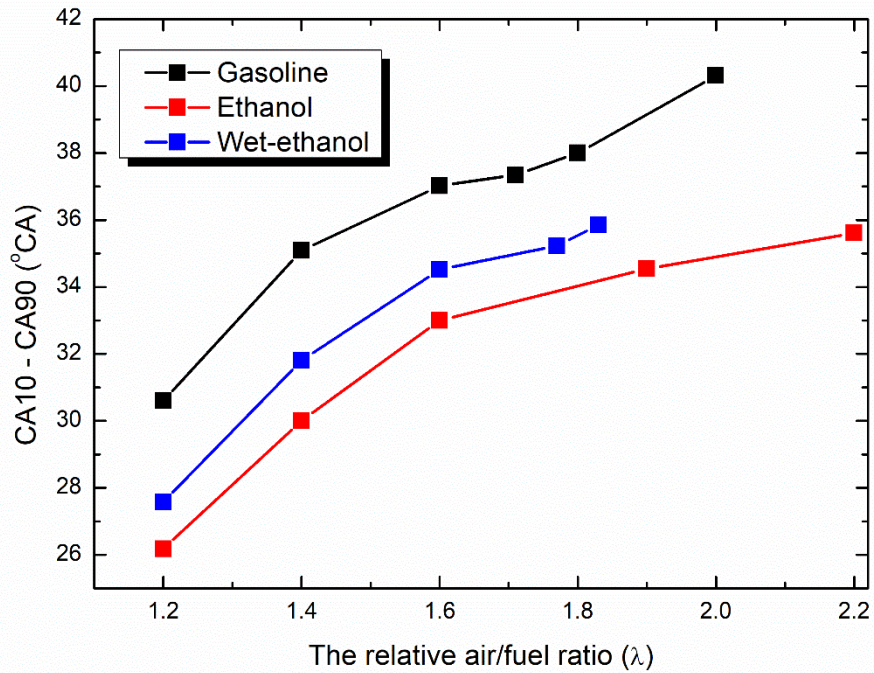
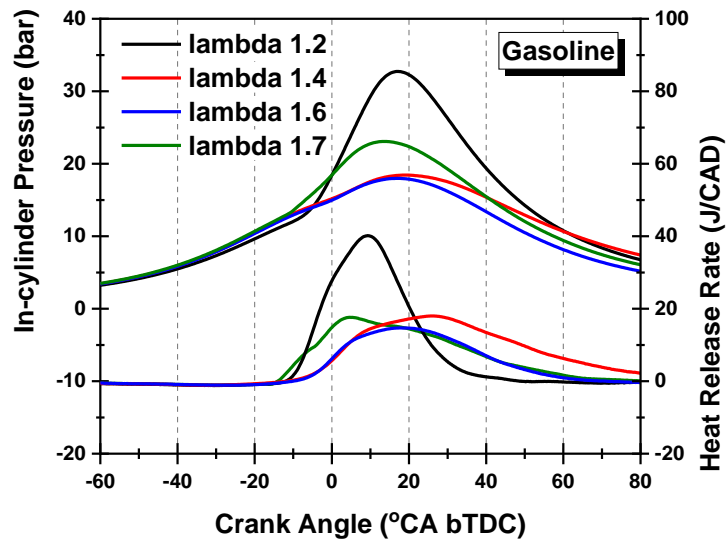


Figure 6.8 Effect of pre-chamber fuel on 10%–90% MFB at inlet pressure 1 bar, 1200 rpm and MBT spark timing

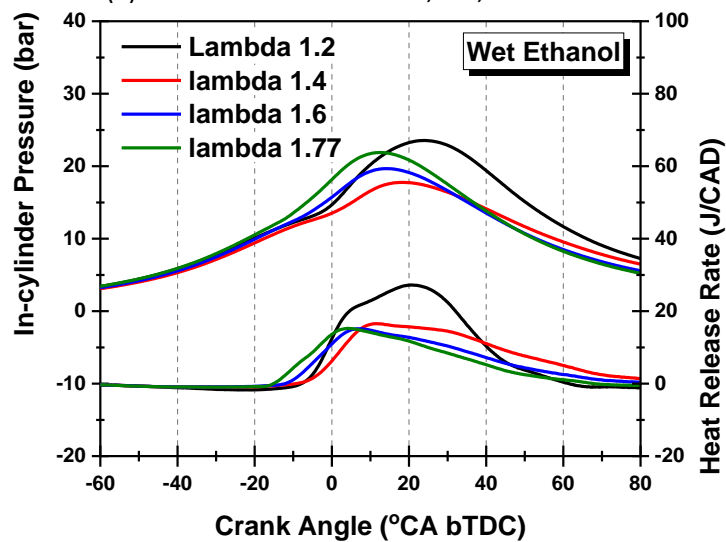
Figure 6.9 plotted the in-cylinder pressure traces and the corresponding HRRs of each fuel operating at different air–fuel ratios. Without auxiliary fuel injection into the pre-chamber, the peak cylinder pressure of the main chamber consistently declined when lambda increased from 1.2 to 1.6. When the auxiliary fuel was injected into the pre-chamber to reach the maximum lean condition, the cylinder pressure slightly increased despite the leaner mixture used in the main chamber. As indicated by the HRR curves, the start of combustion was advanced and the initial development was promoted when auxiliary fuel was provided into the pre-chamber (Table 6.3).

Table 6.3 Test condition

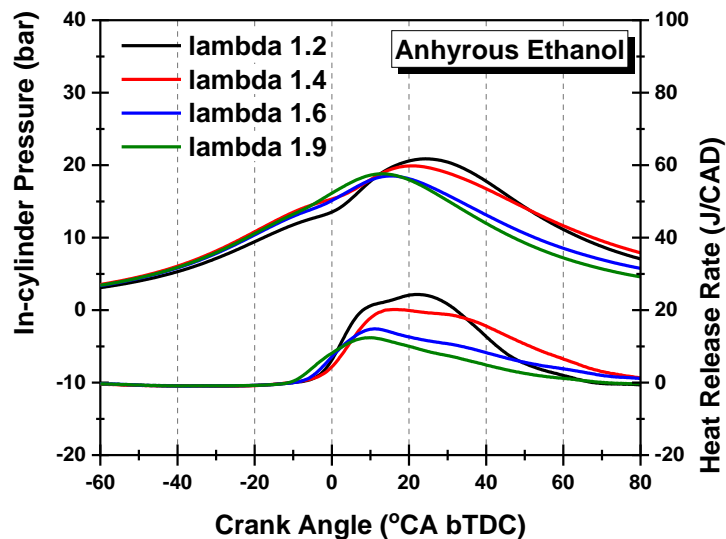
	Gasoline	Ethanol	Wet-Ethanol
Normal SI	Lambda 1-1.2	Lambda 1-1.2	Lambda 1-1.2
Using unfuelled pre-chamber ignition system	Lambda 1.1-1.3	Lambda 1.1-1.3	Lambda 1.1-1.3
Using fuelled pre-chamber ignition system	Lambda 1.4 – lean limit (1.71)	Lambda 1.4 – lean limit (1.9)	Lambda 1.4 – lean limit (1.77)



(a) Gasoline at lambda 1.2, 1.4, 1.6 and 1.7.



(b) Wet-ethanol at lambda 1.2, 1.4, 1.6 and 1.77.



(c) Anhydrous ethanol at lambda 1.2, 1.4, 1.6 and 1.9.

Figure 6.9 In-cylinder pressure and HRR at different lambdas: (a) gasoline, (b) wet-ethanol, (c) anhydrous ethanol

6.3.4 Imaging Results

A high-speed video camera was used to capture the flame propagation through the half circle window at 6000 fps, producing a temporal resolution of 1.2° CA between the adjacent frames. All the images were captured with lambda fixed at 1.3 and spark timing at 22° CA bTDC. Figure 6.10 shows typical flame propagation images at different crank angles of gasoline, ethanol and wet-ethanol. The inflamed area for ethanol is greater than wet-ethanol and gasoline at the same crank angle timing.

The flame images were then converted into binary images to calculate the flame radius, flame speed and shape factor, as shown in Figure 6.11. The mean flame radius and flame speed of each fuel are depicted in Figures 6.12 and 6.13, respectively. The flame radius is calculated based on the measured flame area of the binary flame images averaged over 30 cycles. The ethanol flame expands at the highest speed followed by wet-ethanol and gasoline, consistent with the heat release results. For instance, at 10.8° CA aTDC, the speed of flame was 57.28, 52.20 and 35.98 m/s for ethanol, wet-ethanol and gasoline, respectively. Half of the optical window has to be blocked to mount the pre-chamber ignition system. Therefore, the ignition near the pre-chamber tip and the initial flame development could not be visualised. In this case, the image sequences started at the middle of the flame propagation, and the flame speed continuously decreased at the end of combustion.

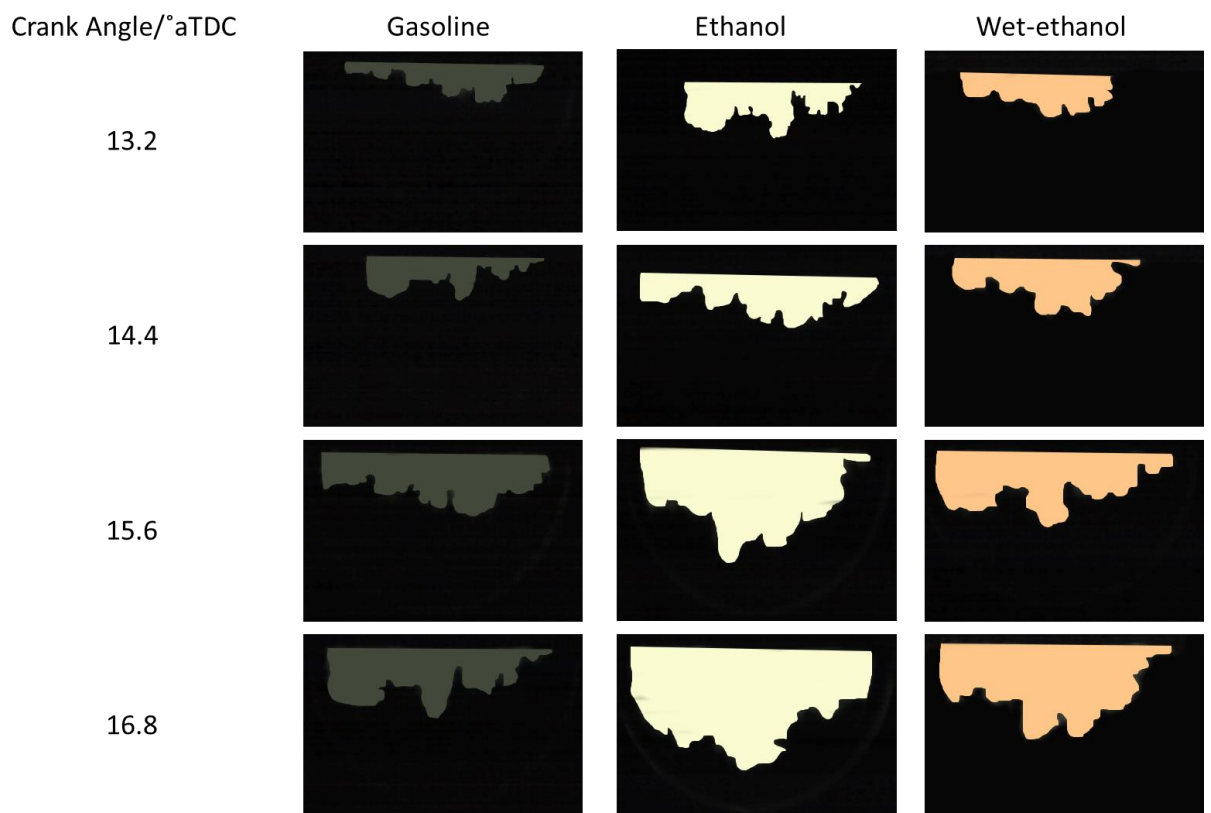


Figure 6.10 Images of the flame propagation of different fuels at lambda 1.3 and spark timing 22° CA bTDC

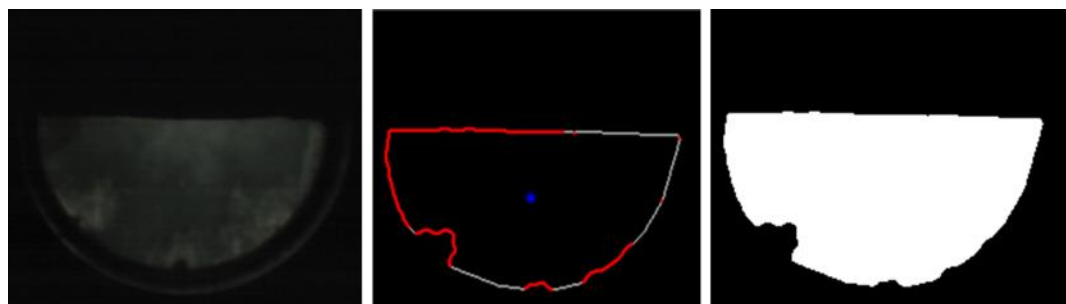


Figure 6.11 Stages of image processing (from left to right, the original natural light image, the selected parameter and binarised image)

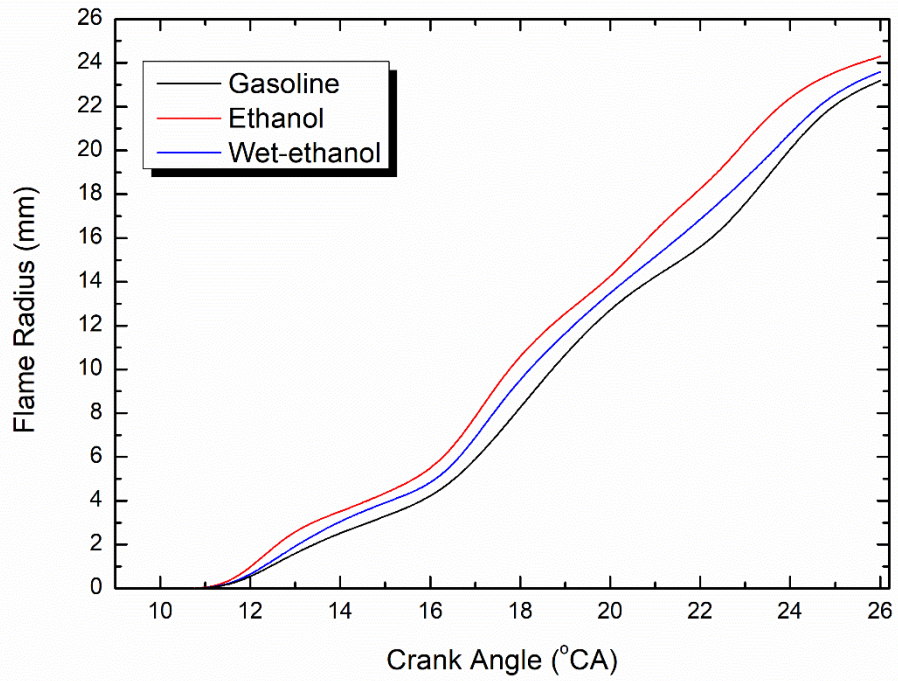


Figure 6.12 Effect of fuel on mean flame radius development

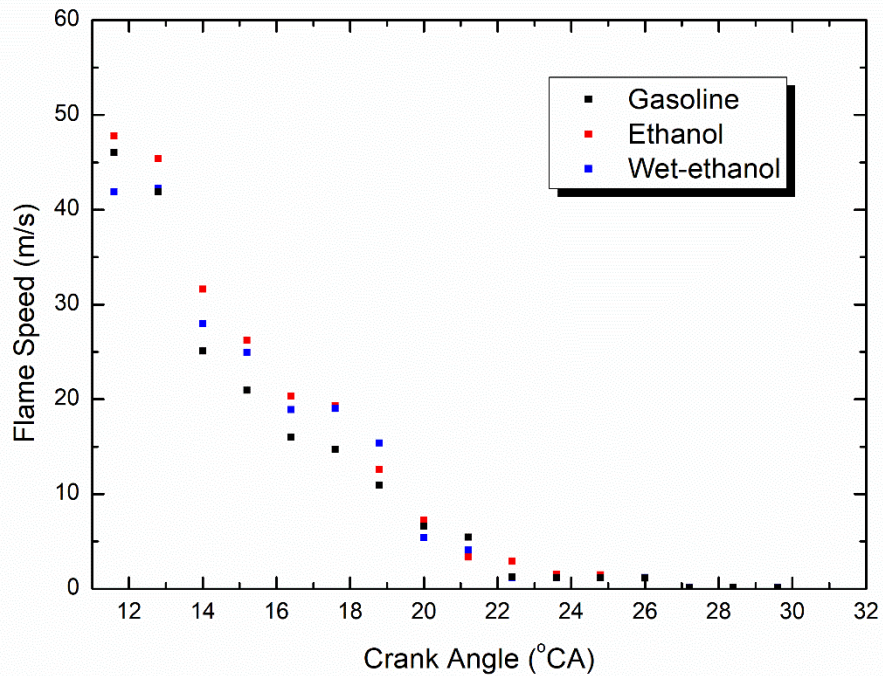


Figure 6.13 Effect of fuel on the flame speed

6.4 Summary

Engine experiments were carried out to study the effect of TJI from a small pre-chamber in a single-cylinder optical engine fuelled with gasoline, anhydrous ethanol and wet-ethanol. The presence of multiple high-temperature turbulent gas jets significantly extended the lean-burn limits of all three fuels as well as shortened the combustion duration with retarded MBT spark timing. The most extended lean-burn operation was achieved with ethanol at a lambda of 1.9. In addition, ethanol and wet-ethanol produced higher IMEP because of their faster combustion and heat release, as indicated by the initial heat release and main combustion duration, CA0–CA10 and CA10–CA90 results. Even with 10% water, the wet-ethanol could still burn faster and produce better engine performance than gasoline.

The extended lean-burn limits by the TJI also led to significant reduction in NO emissions. When operated at lambda 1.9, little NO_x emission was produced from the ethanol fuel. In general, anhydrous and wet-ethanol fuels produced lower NO, HC and CO emissions than gasoline as the combustion temperature was lowered and combustion became more stable and more complete than those of gasoline combustion.

The high-speed combustion chemiluminescence imaging provided direct evidence of the multiple combustion sites in the main chamber as a result of the high-temperature TJI. The technique also illustrated that ethanol had the fastest flame speed followed by wet-ethanol and gasoline.

**Chapter 7 Spectroscopic Studies on
Ignition and Combustion by SI and Jet
Ignition**

7.1 Introduction

To enhance the understanding of the effect of TJI on the ignition and combustion in the main combustion chamber with different fuels, Spectroscopic measurements were carried out to follow the evolution of chemical species (OH, HCO and CH radicals) that marked the ignition and flame front initial growth as well as the high-speed imaging of the TJI sites through endoscopic detection.

7.2 Experimental Test Conditions

All experiments were carried out at 1200 rpm and WOT with gasoline or ethanol. The spark timing was fixed at 22° CA bTDC for the main chamber ignition and 10° CA bTDC for the pre-chamber ignition, producing similar pressure traces at baseline engine operation at different air–fuel ratios. To increase λ (the relative air–fuel ratio), the fuel amount was reduced whilst the inlet air pressure was fixed at 1 bar. The upper limit of the COV_{IMEP} is defined as $\leq 5\%$. The fuel injection duration in the pre-chamber was fixed at 50° CA prior to the spark discharge to allow the mixture formation to take place. The pre-chamber injection fuel was set to 0.3 mg/pulse for both fuels. The pre-chamber air mass was calculated based on the calculated mean gas temperature, and then the lambda values of the pre-chamber mixture were 0.78, and 1.1 for gasoline and ethanol, respectively. The thermodynamic state within the pre-chamber at the time of injection was approximately 5 bar and 550 K. The pre-chamber volume was 1000 mm³, which is 1.27 % of the main chamber volume at TDC.

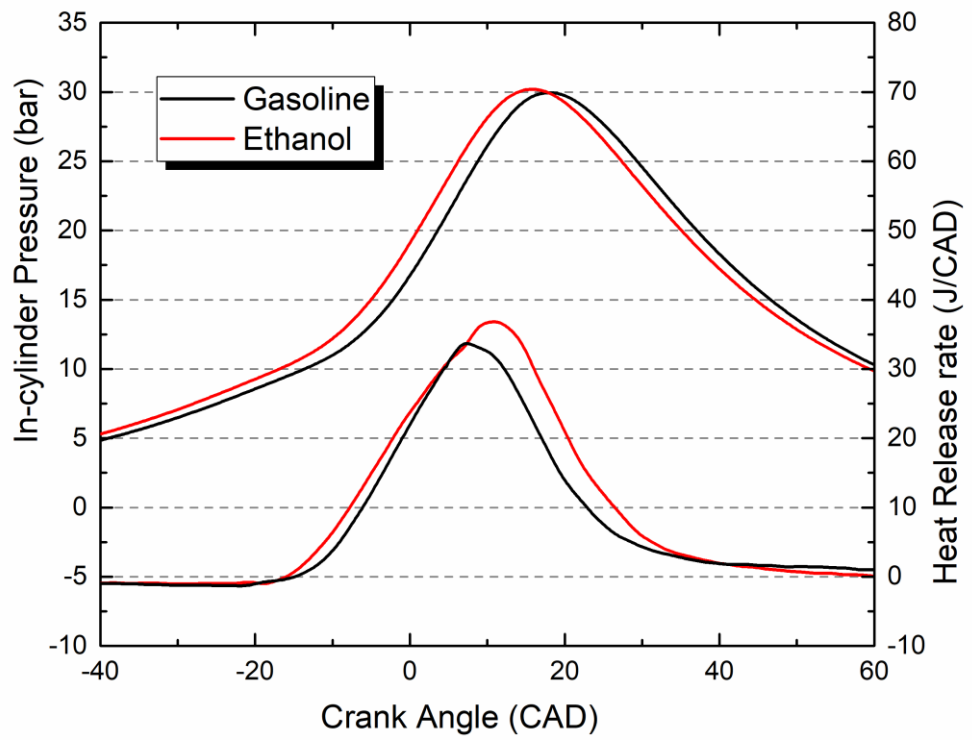
As discussed in Chapter 4, the spectroscopic measurement was carried out by a SpectraPro HRS 500 imaging spectrograph via a single-leg fibre optic bundle (Figure 4.11). The fibre optics was connected to the spectrograph's input slit at one end. The other end of the fibre was placed behind a small sapphire window inside the side window slot, as shown in Figure 4.12. The combustion light emission was collected and focused on the entrance slit of the SpectraPro HRS-500 spectrometer. The spectral image formed on the spectrograph exit plane was recorded with a gated PI-MAX4 ICCD camera. Data were detected with the spectrograph placed at three central wavelengths, 310, 330 and 430 nm, to investigate a wider spectral range using a 600 l/mm grating

with a blaze wavelength of 150 nm. The intensifier-gate delay was set at 31 ns, and width of 0.81 μ s at 1200 rpm for the imaging and spectroscopy measurements.

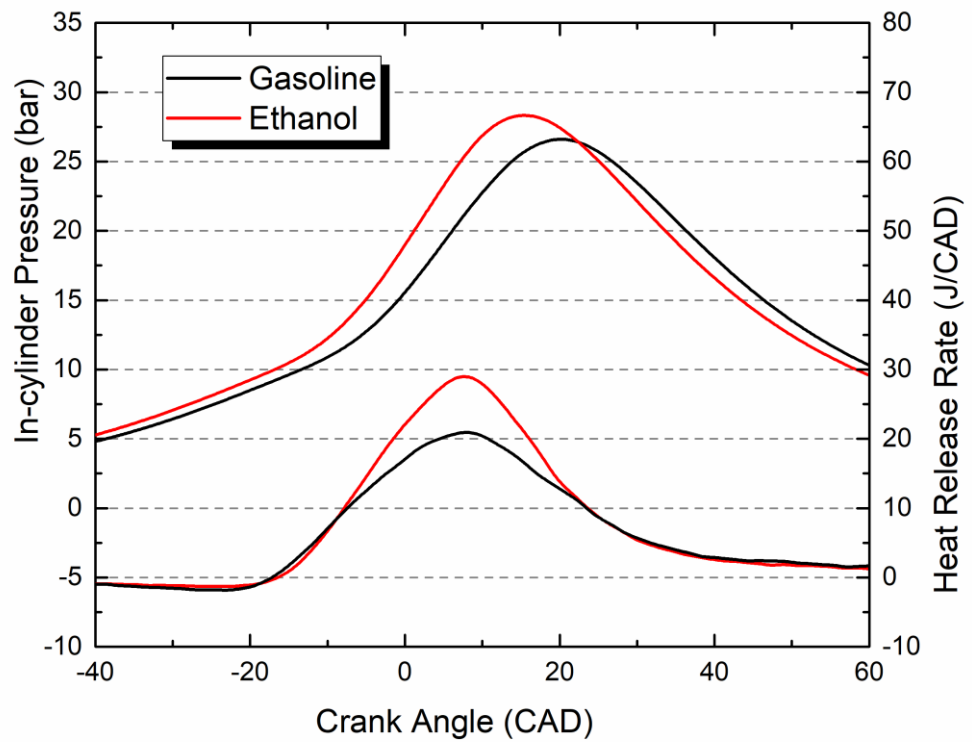
7.3 Results and Discussion

7.3.1 Spectroscopic Investigation of Initial Combustion Fuelled by Ethanol and Gasoline with Normal SI System

Figure 7.1 shows the in-cylinder pressure traces and HRR for gasoline and ethanol under stoichiometric and lean conditions ($\lambda = 1.1$) with SI in the main chamber at a fixed spark timing of 22° CA bTDC. Ethanol produces higher peak cylinder pressure at an earlier crank angles at the same spark timing in both cases. The largest difference in the maximum cylinder pressure between ethanol and gasoline occurs under stoichiometric condition with 31.4 bar for ethanol and 29.1 bar for gasoline. This finding is caused by the relatively faster burning rate of ethanol [140], as well as the higher energy input of ethanol in the cylinder. The lower heating values and the stoichiometric AFR of gasoline and ethanol are 41.087 and 28.865 MJ/kg and 14.421 and 8.953. Under constant throttle (constant volumetric air flow rate), the input energy contained in a stoichiometric mixture of one kilogram of intake air and fuel is 2.92 and 3 MJ for gasoline and ethanol, respectively. As expected, the cylinder pressures and HRRs drop slightly with leaner mixtures.



(a) Lambda 1.0



(b) Lambda 1.1

Figure 7.1 In-cylinder pressure and HRR curves for the main chamber spark ignition at 22° CA bTDC

The corresponding net IMEP of both fuels under different relative air–fuel ratios are shown in Figure 7.2. During the test, different air–fuel ratios were achieved by adjusting the fuel injection duration under constant throttle opening. Therefore, the highest IMEPs were obtained at lambda 1.0 with ethanol.

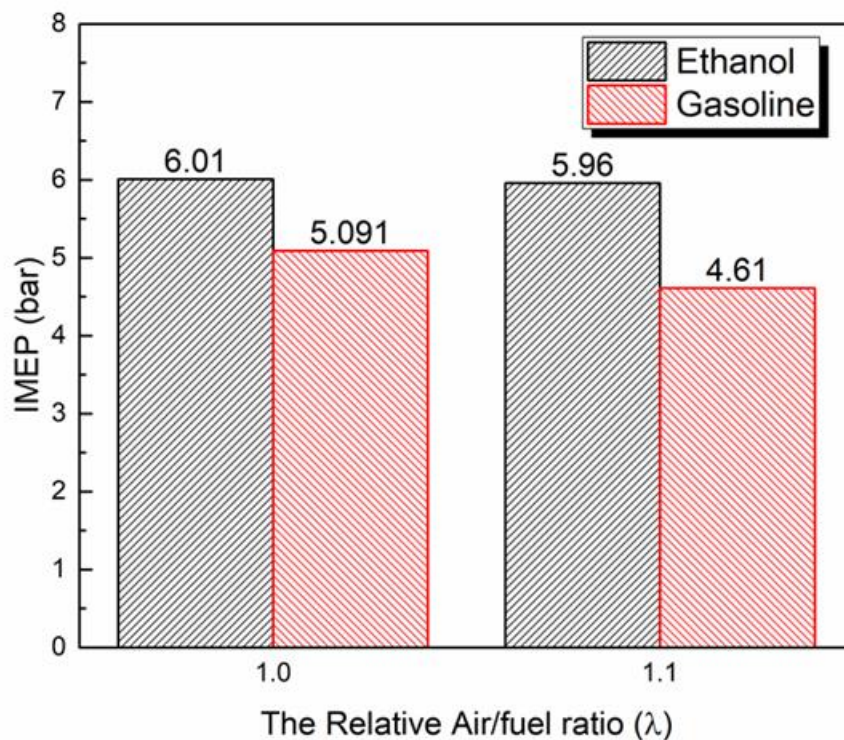


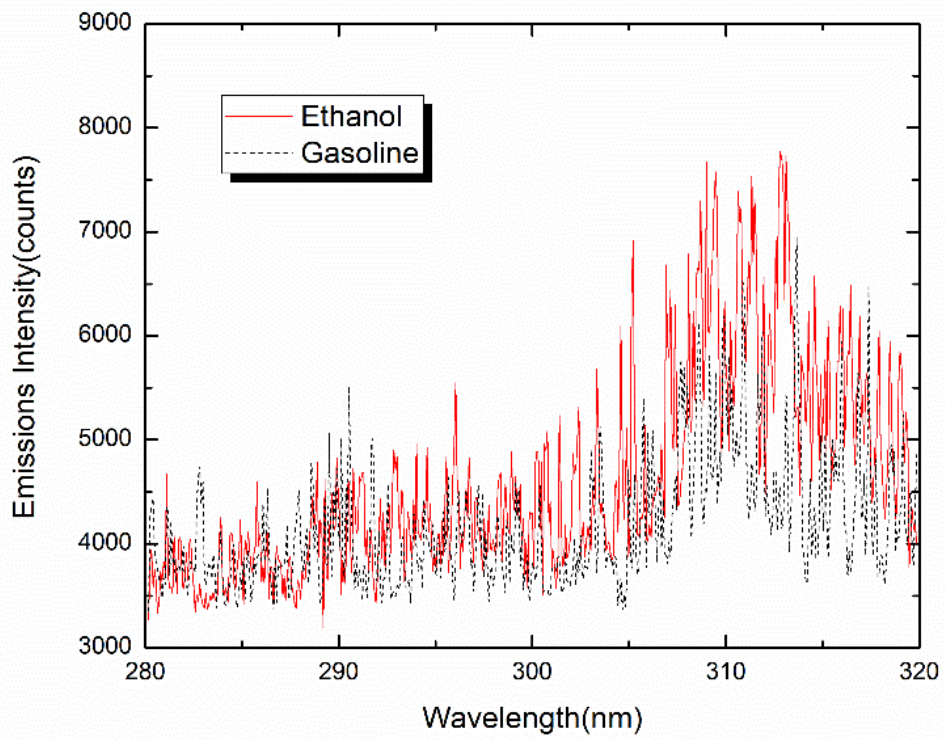
Figure 7.2 IMEP at different relative air–fuel ratios (λ)

The spectroscopic measurements focused on OH, CHO and CH, which are the major radicals produced during high-temperature combustion reactions in the spark ignition combustion [141]. CH* formed inside the flame reaction zone of the initial flame kernel, and OH* was present in the hot burned gas region and the flame front. The strongest peak emission of OH was centred at 310 nm and CH and HCO at 430 and 330 nm, respectively. SI can be broken down into three stages, namely, pre-breakdown, breakdown and arc and glow phase. In the first two phases, highly energised electrons were produced to ionise and heat up the molecules. Ignition started during the arc and

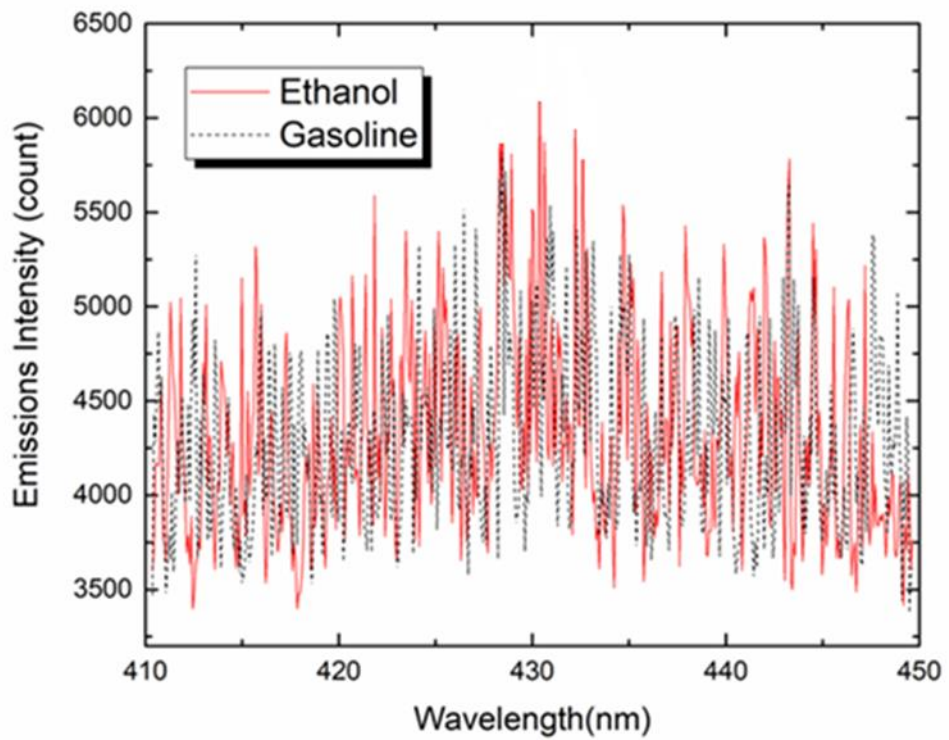
glow phases when the combustion charge was heated up to the adiabatic flame temperature, and high-temperature heat release reactions began.

The UV-visible emission spectra at the time of SI of 22° CA bTDC are shown in Figure 7.3. Figure 7.4 presents the relative intensities of OH, CH and CHO, which are obtained by integration of spectral peak at 310± nm for OH, 430± nm for CH and 330±nm for CHO. Both fuels produced higher OH and CH emissions intensity than HCO because the OH and CH radicals were produced by high-temperature exothermic reactions [141]. OH emission was higher than CH because CH radicals were reduced by the reaction with O₂ at the kernel flame phase of combustion, and OH radicals were present in the flame front and hot burned gas regions [142][143]. OH emissions increased at approximately 300 wavelength, where this spectrum is the CO–O recombination band spectrum from the burned gas zone [144]. HCO radicals were produced in the heat release reactions at the start of combustion, but the HCO emission was lower compared with the other radicals probably due to the replacement of HCO by CH and formaldehyde at increasing carbon content in the fuel [144].

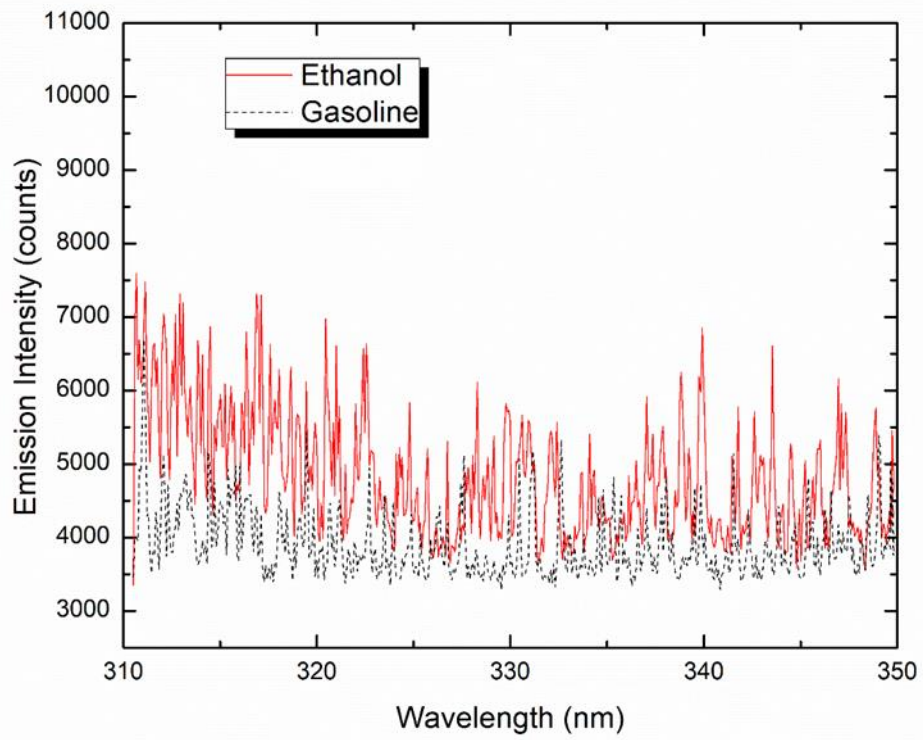
In the case of gasoline combustion, the emission intensities of these radicals decreased with a leaner mixture. However, ethanol exhibited a different behaviour; CH emissions increased as lambda increased. A higher CH intensity indicated that more O radicals were produced because the reaction, $C_2H + O = CH^* + CO$, is the primary source of flame CH*. Figure 7.5 compares the temporal changes in the emission intensity of OH, CHO and CH versus crank angle for ethanol (left) and gasoline (right). Ethanol illustrated higher emissions of OH, CHO and CH compared with gasoline given its higher cylinder pressure and temperature, resulting from the faster burn and higher energy input [142]. When compared with the HRR profiles (Figure 7.1), the peaks of the light emission occur before the maximum HRR.



(a) Emission intensity around 310 nm



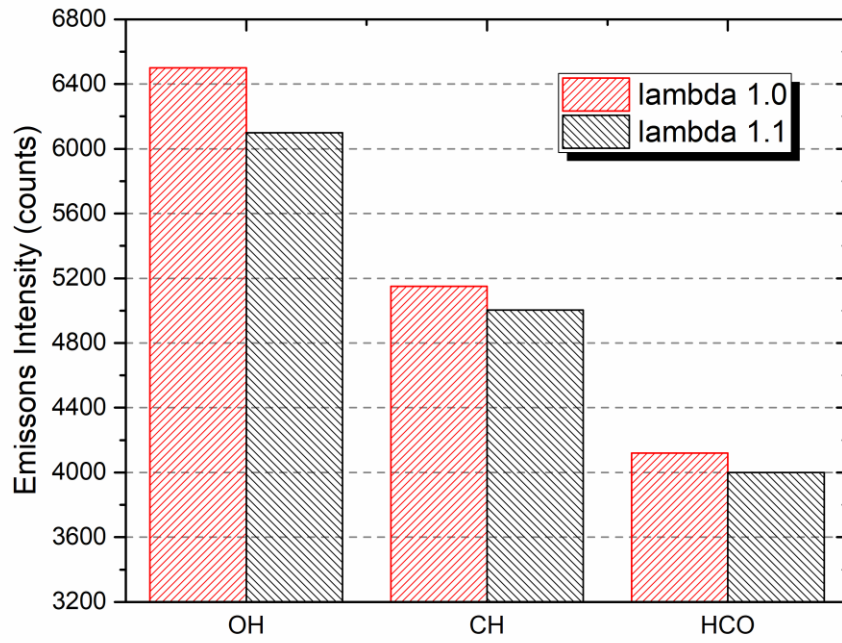
(b) Emission intensity around 430 nm



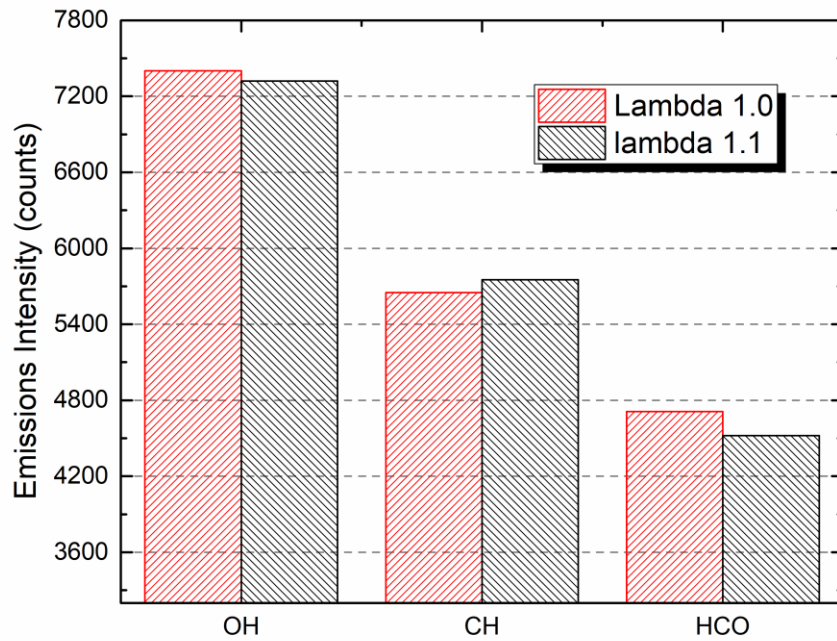
(c) Emission intensity around 330 nm

Figure 7.3 UV-visible emission spectrum of combustion of ethanol and gasoline at 22°

CA bTDC



(a) All emission intensity for gasoline



(b) All emission intensity for ethanol

Figure 7.4 Light emission intensities for gasoline and ethanol at different air–fuel ratios

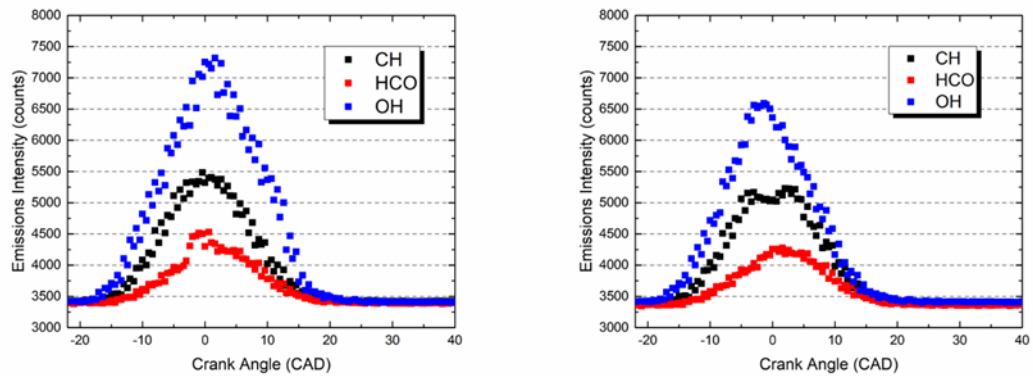
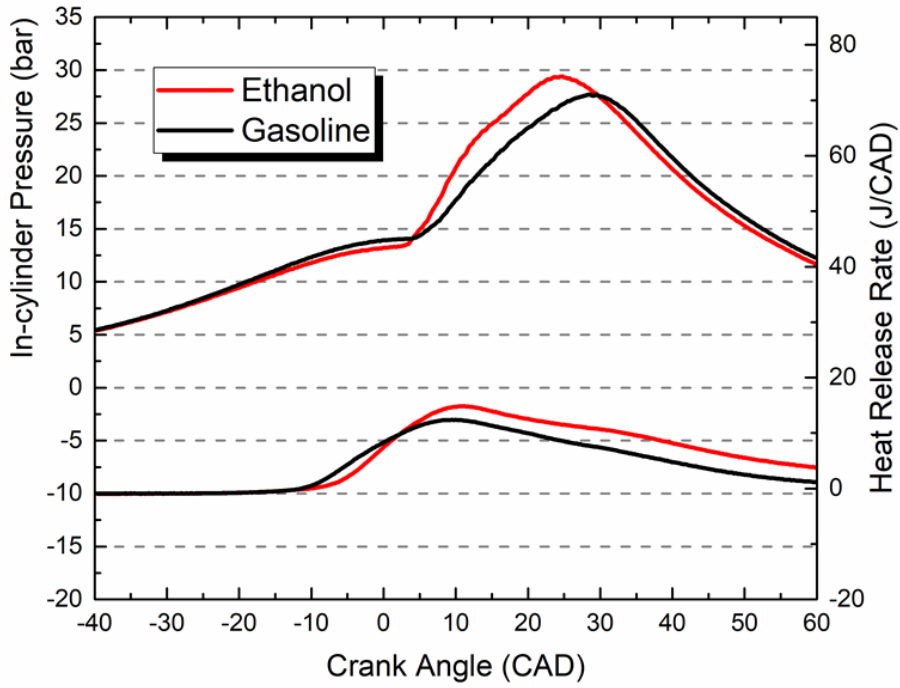


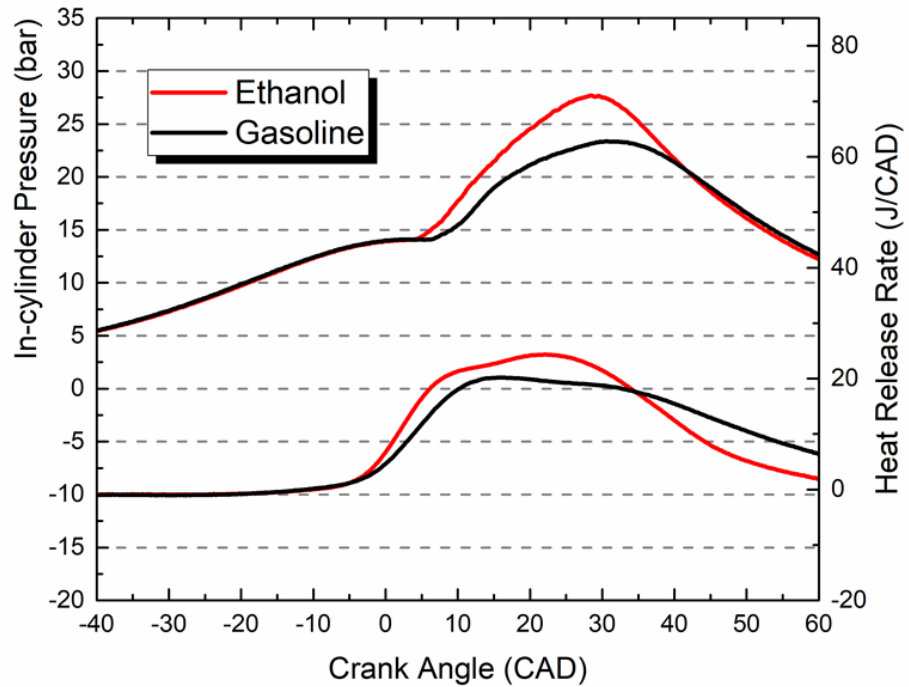
Figure 7.5 Emission intensity OH around 309 nm, HCO around 330 nm and CH around 430 nm vs crank angle for ethanol (left) and gasoline (right)

7.3.2 Spectroscopic Investigation of Initial Combustion Fuelled by Ethanol and Gasoline with Unfuelled Pre-Chamber Ignition System

Figure 7.6 depicts the in-cylinder pressure and HRR with gasoline and ethanol under fixed spark timing 10° CA bTDC in the unfuelled pre-chamber. Figure 7.7 illustrates the variation in IMEP between both fuels with two lambda values. The IMEP values of ethanol was slightly higher than those of gasoline. These results are based on the difference in the energy input of each fuel.



(a) Under lambda 1.0



(b) Under lambda 1.2

Figure 7.6 In-cylinder pressure and HRR at fixed spark timing 10° CA bTDC

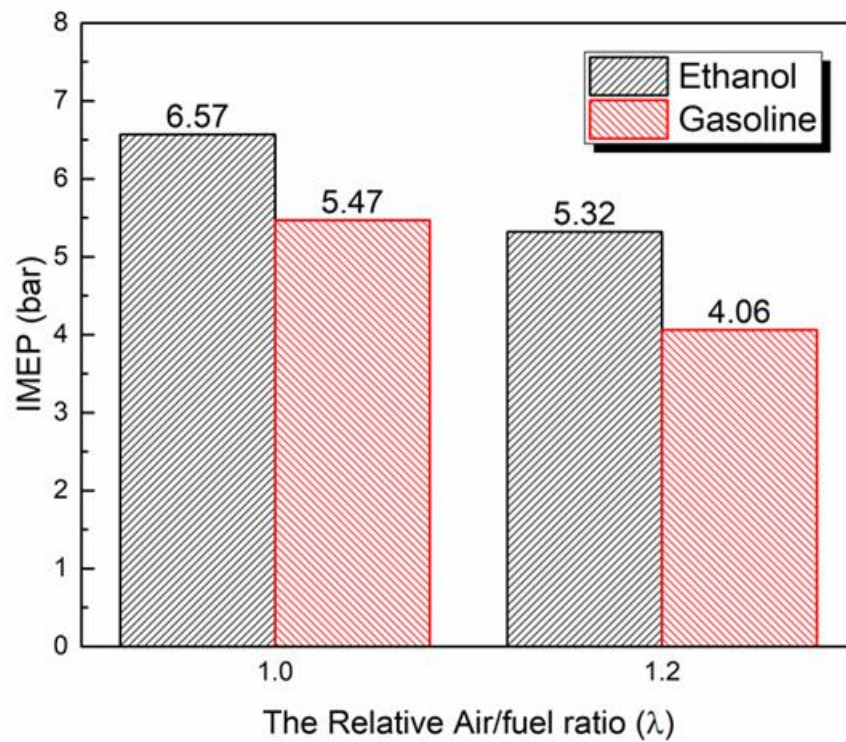
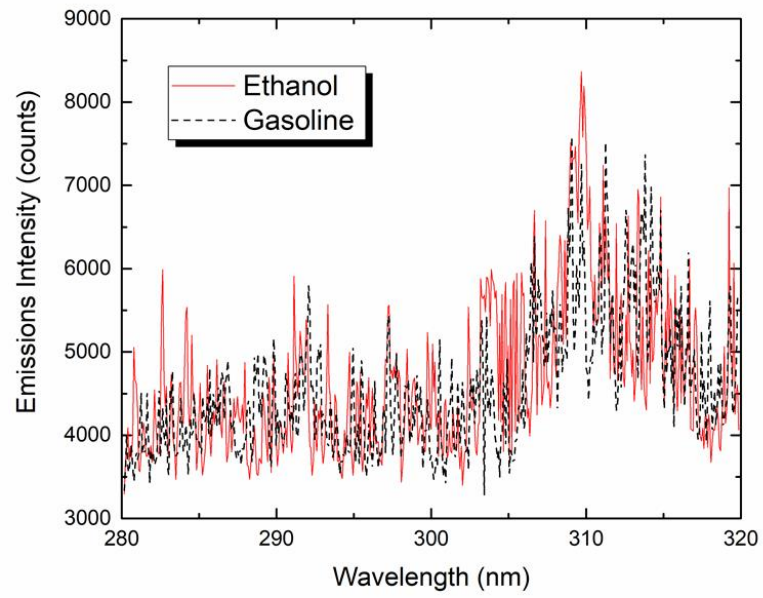
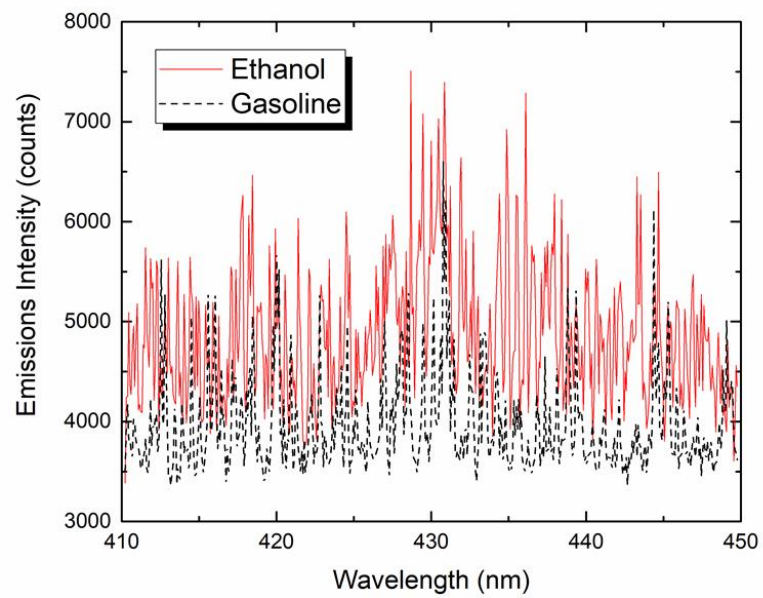


Figure 7.7 Effect of fuel on IMEP variation with lambda with unfuelled pre-chamber

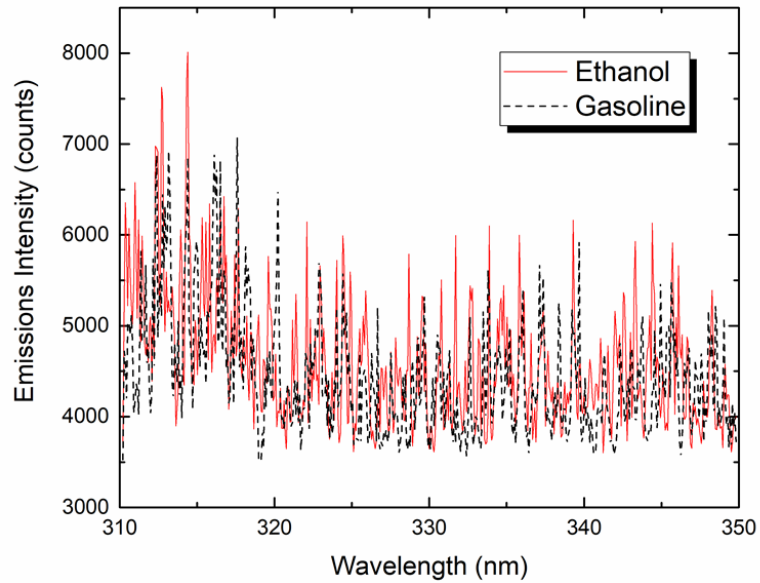
The spectroscopic measurements of the pre-chamber ignition show similar results to the SI in the main chamber for both fuels (Figure 7.8). For both fuels, OH emission was higher than CH, followed by HCO. On the contrary with normal SI, all emissions, including CH spectra emission, decreased with air–fuel ratio because of the high temperature produced from pre-chamber ignition.



(a) Emission intensity around 310 nm



(b) Emission intensity around 430 nm



(c) Emission intensity around 330 nm

Figure 7.8 UV-visible emission spectrum of ethanol and gasoline combustion at 10° CA bTDC

The temporal changes in the chemiluminescence intensities in Figure 7.9 indicate that jet ignition combustion was characterised with higher chemiluminescent emissions from all three radicals than the SI in the main chamber. This finding can be explained by the multiple ignition regions associated with the hot jet of partially burned mixtures emanating from the pre-chamber. In the normal SI in the pre-chamber, ethanol combustion produced higher spectra emissions than gasoline when ignited in the pre-chamber.

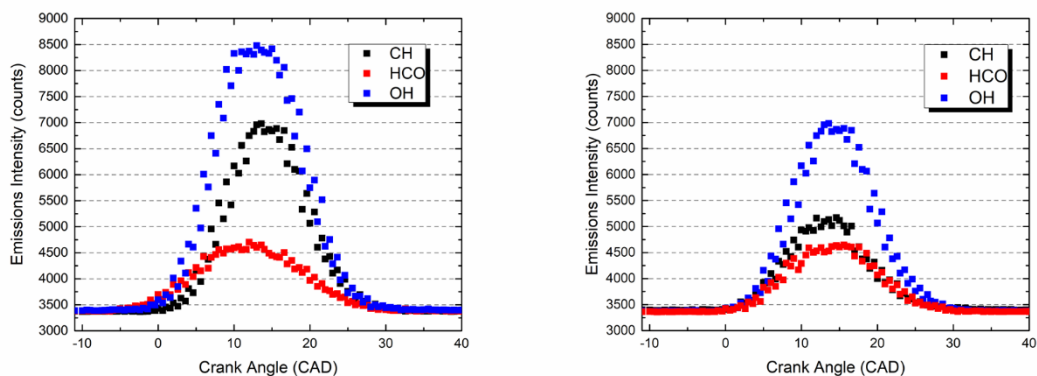


Figure 7.9 Emission intensity OH around 309 nm, HCO around 330 nm and CH around 430 nm vs crank angle for ethanol (left) and gasoline (right)

The differences between the two ignition systems are further illustrated in Figure 7.10 by the high-speed images of the ignition and flame propagation in the main chamber. The first visible site of combustion was located near the spark plug with ignition in the main chamber, whereas the initial combustion appeared in more regions with greater intensity by TJI from the pre-chamber.

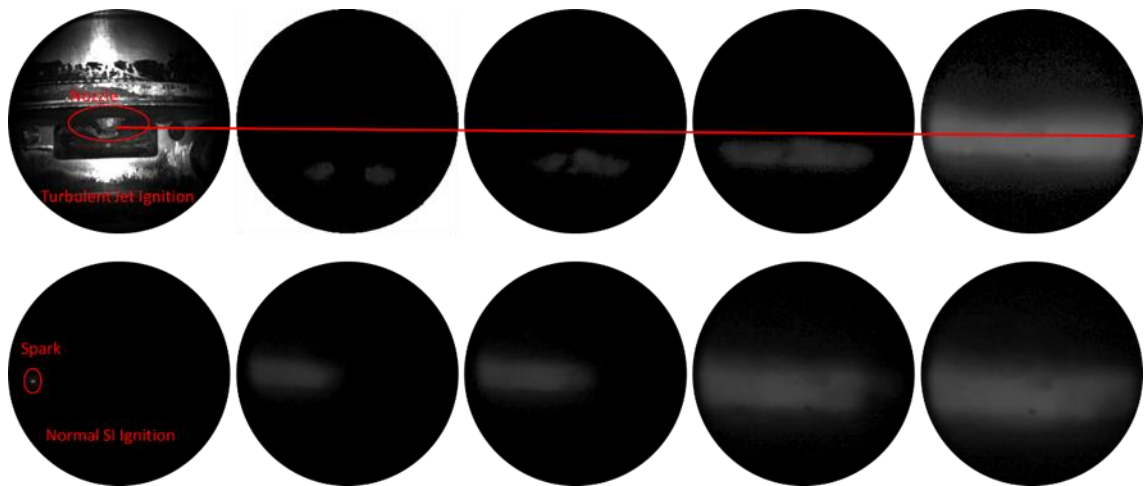


Figure 7.10 Comparison between normal SI and jet ignition system

7.3.3 Spectroscopic Investigation of Initial Combustion Fuelled by Ethanol and Gasoline with Ignition in the Fuelled Pre-Chamber

In this section, the combustion in the main chamber is presented with SI in the pre-chamber fuelled with gasoline or ethanol. The spark timing was fixed at 10° CA bTDC, start of injection at 50° CA bTDC and injection fuel of 0.3 mg/pulse for both fuels. To obtain a more reliable comparison, the lambda of 1.4 was selected to ensure stable and, repeatable combustion in the optical engine [3]. The results imply that all spectra emissions increased with fuelled pre-chamber compared with unfuelled pre-chamber and normal spark combustion even after increasing lambda up to 1.4, as shown in Figure 7.11. This is because more radicals were formed and injected from the fuelled pre-chamber into the main chamber.

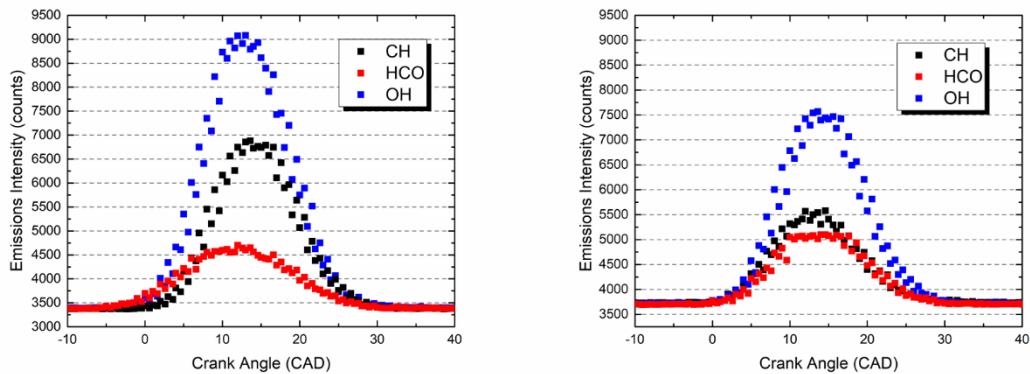


Figure 7.11 Emission intensity OH around 309 nm, HCO around 330 nm and CH around 430 nm vs crank angle for ethanol (left) and gasoline (right).

Figure 7.12 presents the crank angle of MFB 0%–10% (CA0–CA10), MFB 10%–90% (CA10–CA90) and crank angle MFB 50% (CA50) of two ignition system (normal SI versus TJI) under different lambda values and fuel conditions. In the comparison of CA0–CA10 between TJI and normal SI at lambda 1, TJI showed longer time in this stage because of the pre-chamber jet formation. In the comparison of CA50 between the two combustion modes, TJI had relatively early combustion phasing. The main combustion duration of CA10–CA90 was evidently shortened by applying TJI because the pre-chamber injected very reactive radicals. These radicals were highly reactive and readily ignited the main chamber air–fuel mixture. The comparison of the initial combustion duration of CA0–CA10 between fuelled pre-chamber and unfuelled pre-chamber, the fuelled pre-chamber exhibited shorter time in this stage due to the effect of auxiliary fuel in the pre-chamber, thereby increasing the pre-chamber pressure and injecting the pre-chamber products rapidly. Moreover, the initial heat release and main combustion duration prolonged with leaner mixture under both ignition systems. Compared with gasoline, ethanol exhibited slightly shortened combustion duration and relatively early combustion phasing throughout different test conditions due to its faster burning rate.

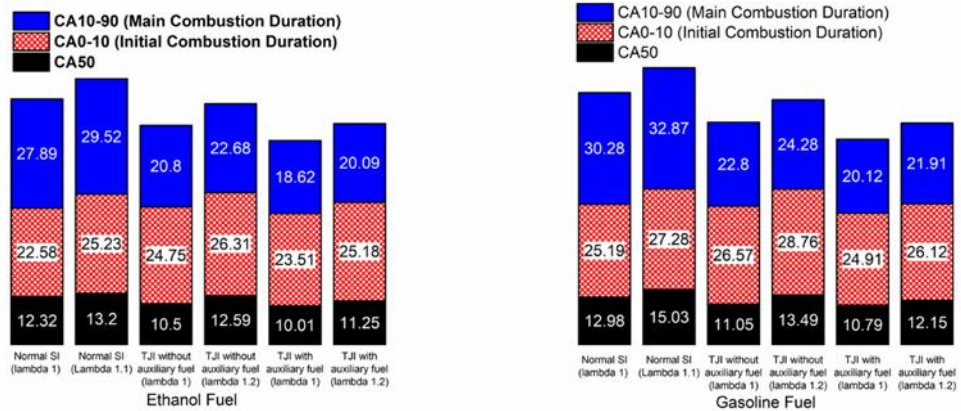
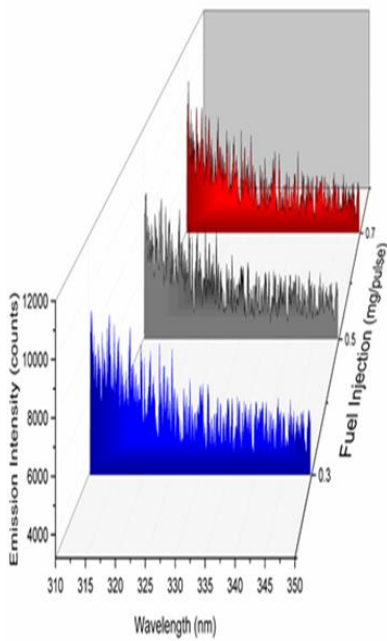
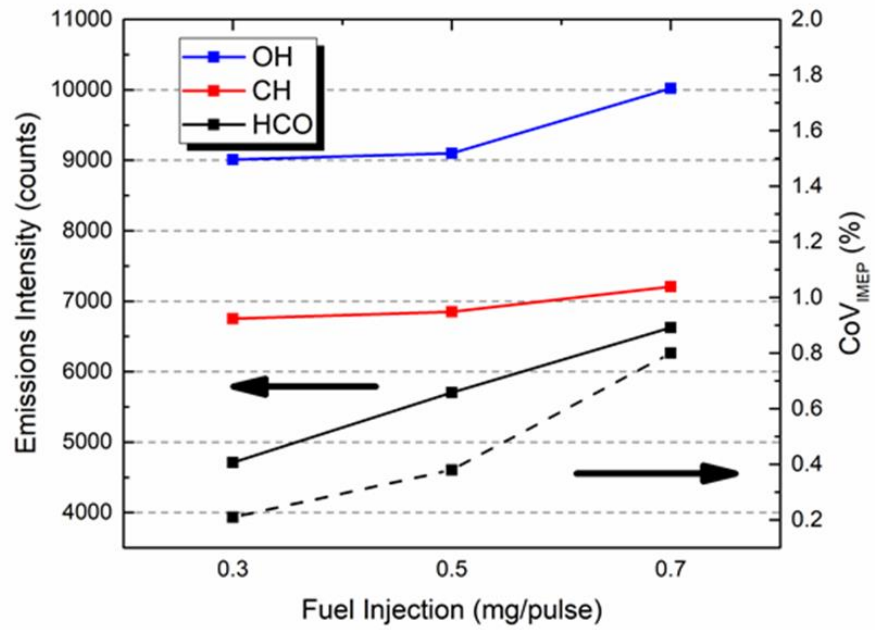


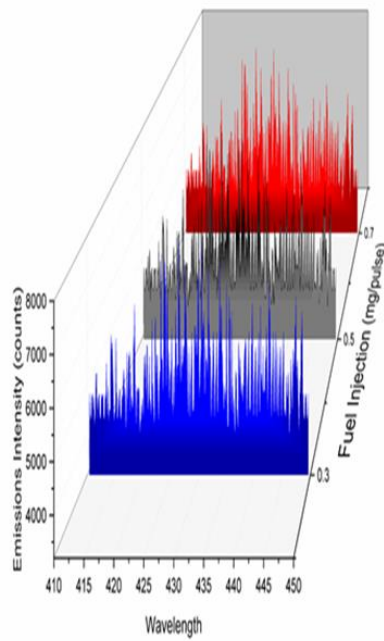
Figure 7.12 Effect of fuel on 0%–10%, 10%–90% MFB and CA50 at inlet pressure 1 bar and 1200 rpm under different ignition systems

To investigate the effect of mixture strength in the pre-chamber, the fuel amount injected was increased to 0.5 and 0.7 mg/pulse whilst the other parameters were fixed. As shown in Figures 7.13 and 7.14, as the amount of fuel and fuel–air ratio in the pre-chamber increased, the light emission intensities increased from the combustion of ethanol and gasoline fuel in the main chamber due to the increased quantity of radicals in the pre-chamber. However, the chemiluminescence intensities of the radicals during the ethanol combustion (Figure 7.13) were less affected than those gasoline. In particular, the CH emission during the gasoline combustion was much more sensitive to the pre-chamber gas mixture than that during ethanol combustion. The shape of the emission spectra of each radical remained the same as the pre-chamber mixture strength was changed.

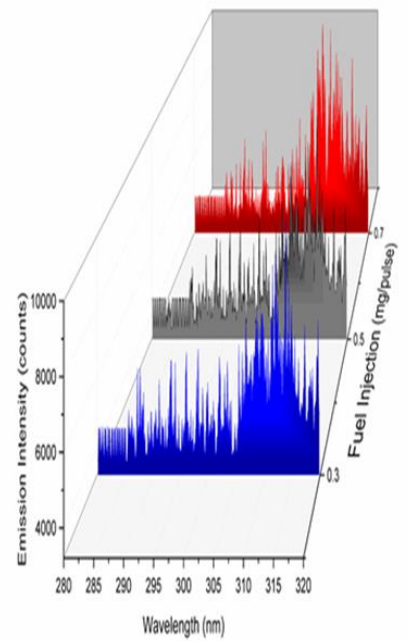
The top graph of Figures 7.13 and 7.14 reveals that the combustion stability is also presented as a function of the pre-chamber fuelling, together with the chemiluminescence intensities. At the fuel injection of 0.7 mg/pulse, the combustion became less stable for both fuels though an extremely strong emission spectra for OH and CH exist. However, as the mixture inside the pre-chamber becomes rich in fuel, the injected products from the pre-chamber can contain more partial combustion products and radicals and become more reactive. In addition, due to faster pressure rise in the pre-chamber with more fuel, the greater pressure drop between the pre and main chamber can cause the hot TJI to penetrate deeply in the main chamber and quench near the cylinder wall or piston top.



emission intensity @ 330 nm



emission intensity @ 430 nm



emission intensity @ 310 nm

Figure 7.13 Spectra emissions of ethanol at lambda 1.4, spark timing 10° CA bTDC and injection timing 50° CA bTDC with different injection durations (0.3, 0.5 and 0.7 mg/pulse)

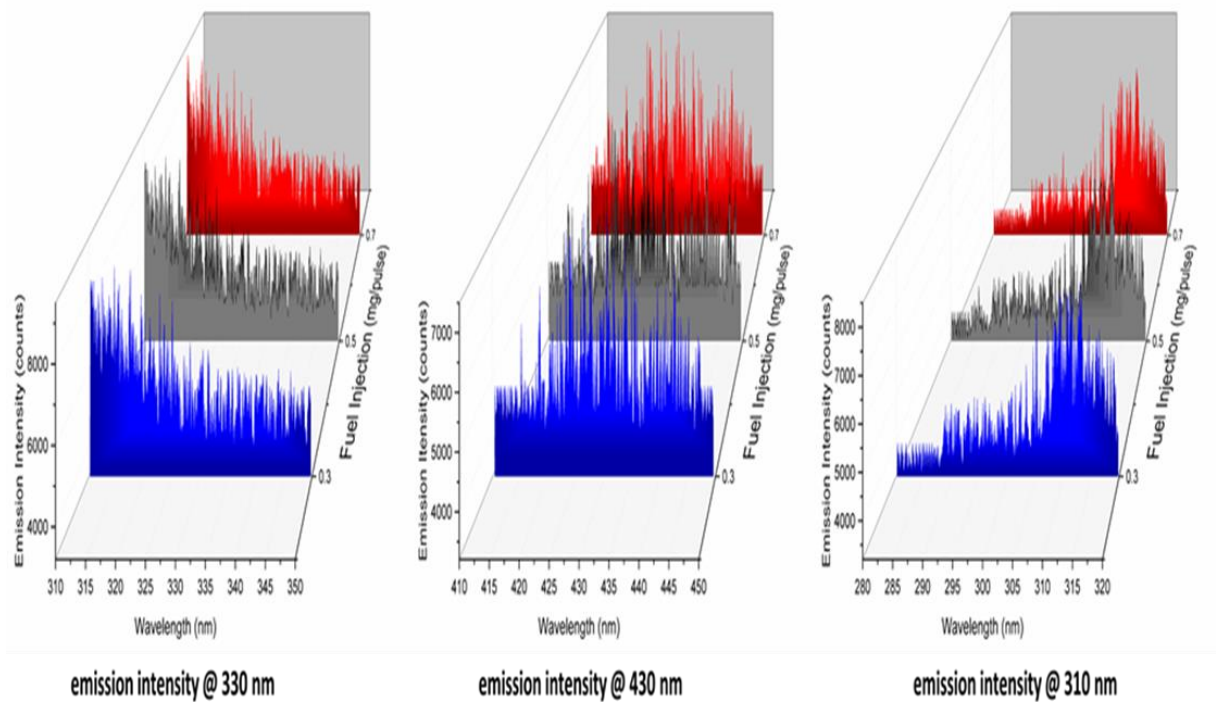
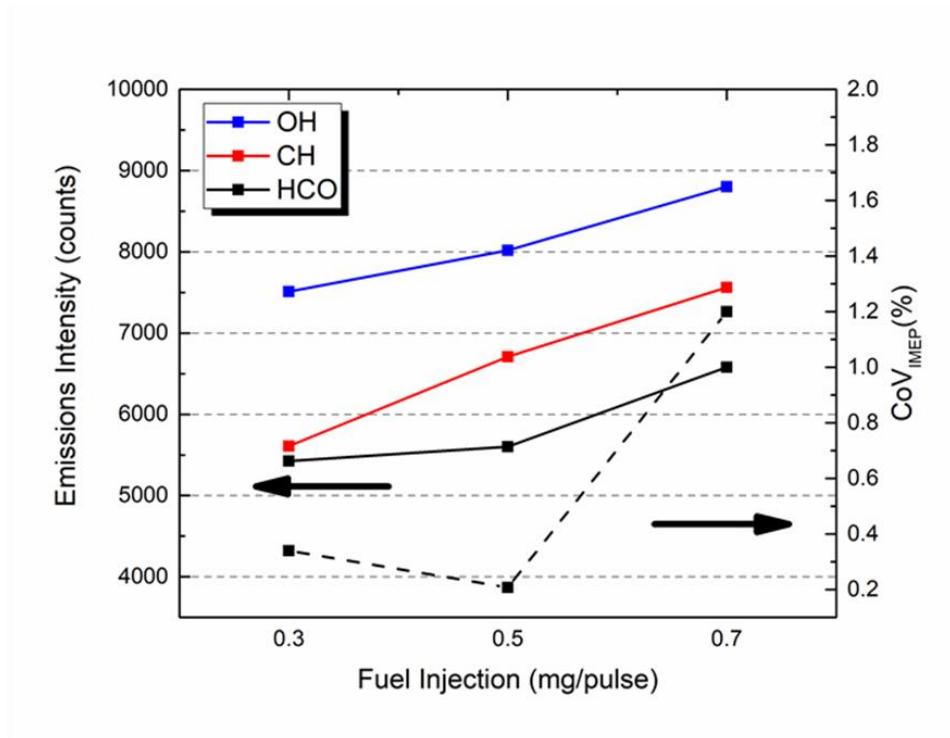


Figure 7.14 Spectra emissions of gasoline at lambda 1.4, spark timing 10° CA bTDC and injection timing 50° CA bTDC with different injection durations (0.3, 0.5 and 0.7 mg/pulse)

Next, the effect of injection timing in the pre-chamber was studied. The fuel injection was fixed at 0.3 mg/pulse and the spark timing at 10° CA bTDC, whereas the start of the pre-chamber injection was changed to 30°, 50° and 70° CA bTDC. The results reveal that

the injection timing has less effect on spectral emission intensity, as shown in Figure 7.15. However, as the injection timing was advanced to 70° CA bTDC, OH and CH emission intensities became lower, the combustion became unstable and the HCO increased, indicating incomplete combustion. The injection at 50° CA bTDC is optimal for both fuels based on the emission spectra and combustion stability. The results indicate that the actual mixture strength at the time of the pre-chamber SI varied with the pre-chamber injection probably caused by the interaction of the air flow into the pre-chamber. The fuel when injected early in the pre-chamber was likely to become more diluted at the time of SI by the incoming air. However, delayed injection in the pre-chamber may be unable to produce a near stoichiometric mixture at the point of spark discharge. A detailed and accurate CFD analysis is required to fully understand the results.

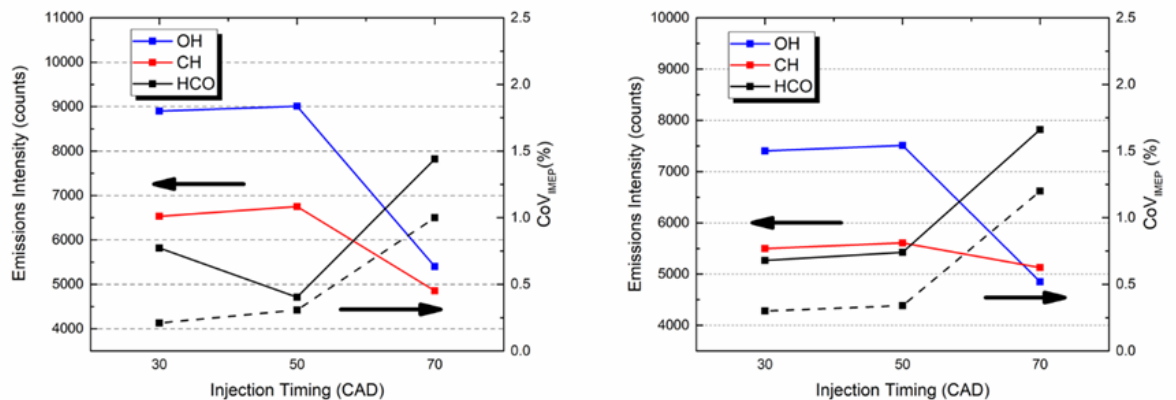


Figure 7.15 Effect of pre-chamber fuel injection timing for ethanol (left) and gasoline (right)

Finally, the effect of spark timing in the fuelled pre-chamber was investigated by fixing the injection at 50° CA bTDC, fuel injection 0.3 mg/pulse. Figure 7.16 shows the emission intensities measured at 10° CA bTDC. The spark timing advanced and the emission intensities became stronger as more combustion occurred at the time of measurement. Ethanol exhibited stronger emission particularly OH and CH spectra compared with gasoline because ethanol had the fastest flame speed and exhibited less cyclic variation.

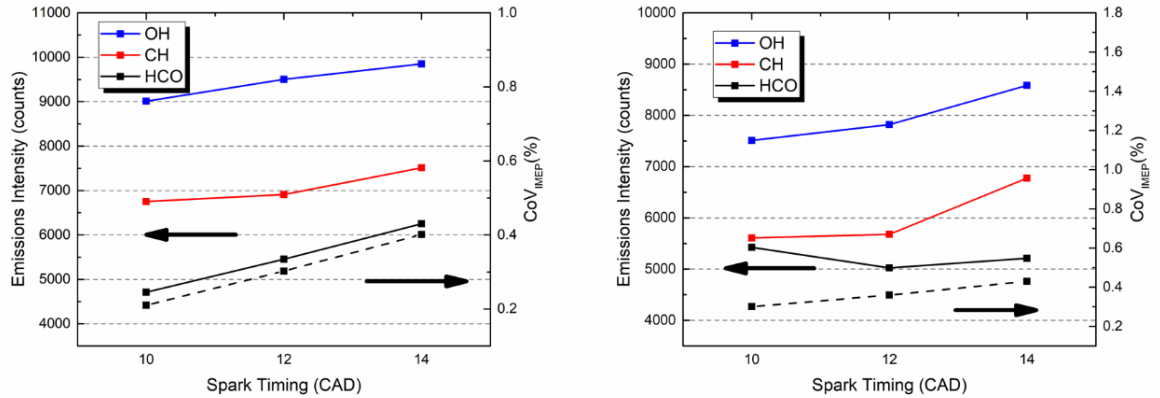


Figure 7.16 Spectral emission intensity at injection timing 30°, 50° and 70° CA bTDC for ethanol (left) and gasoline fuel (right)

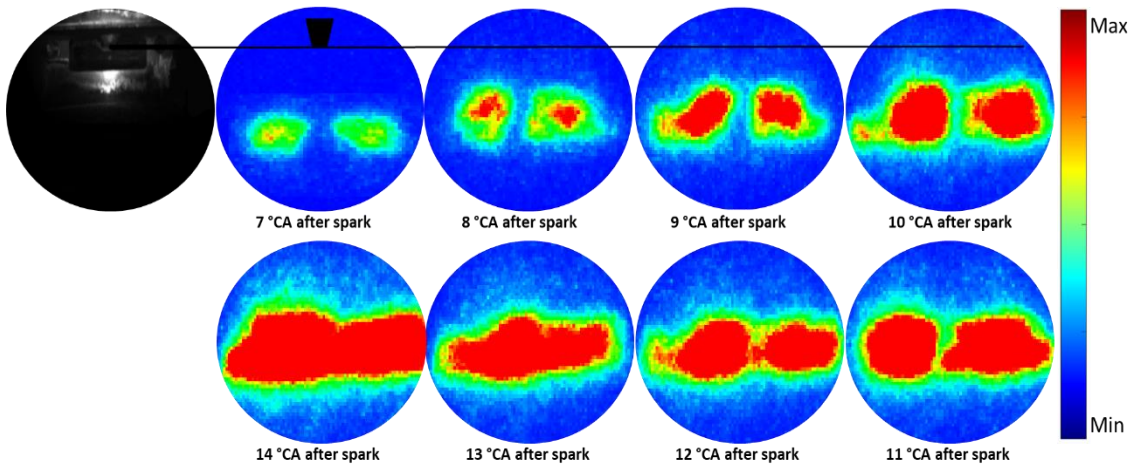
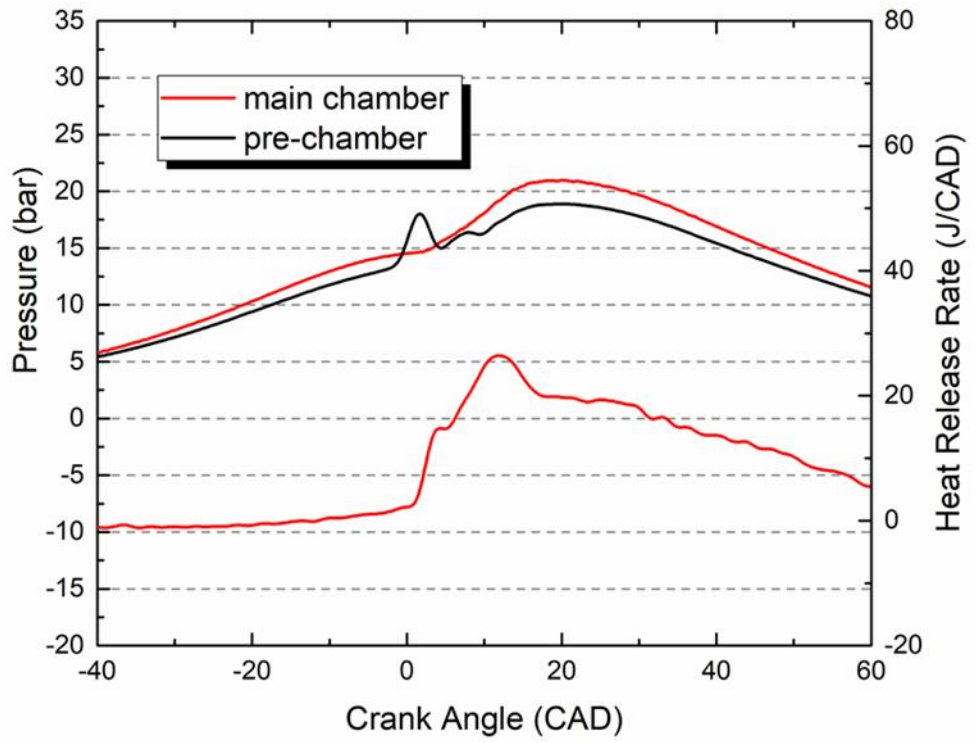
7.3.4 Ignition and Combustion Studies by ICCD Imaging

The high-speed video imaging was useful to visualise the ignition and combustion processes in the same cycle, but it is limited by the low light emission of lean-burn combustion. To explain the ignition process and understand flame propagation characteristics during combustion, an ICCD camera (*Pimax4*, Princeton) coupled with endoscope was used in place of the high-speed video camera. The engine was obtained at the spark timing of 10° CA bTDC in the pre-chamber and injection timing at 50° CA bTDC at an overall lambda 1.4. The images were obtained for different fuel quantities of 0.3, 0.5 to 0.7 mg/pulse in the pre-chamber.

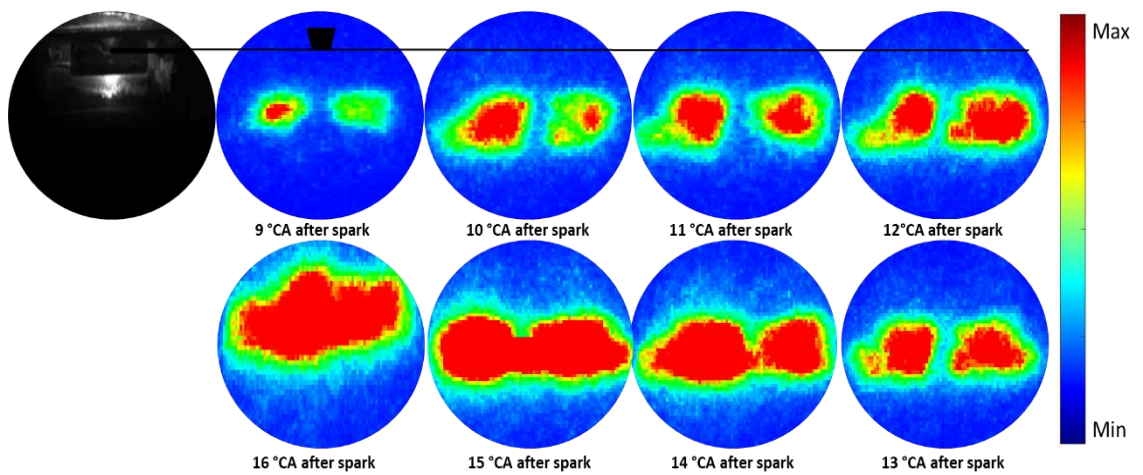
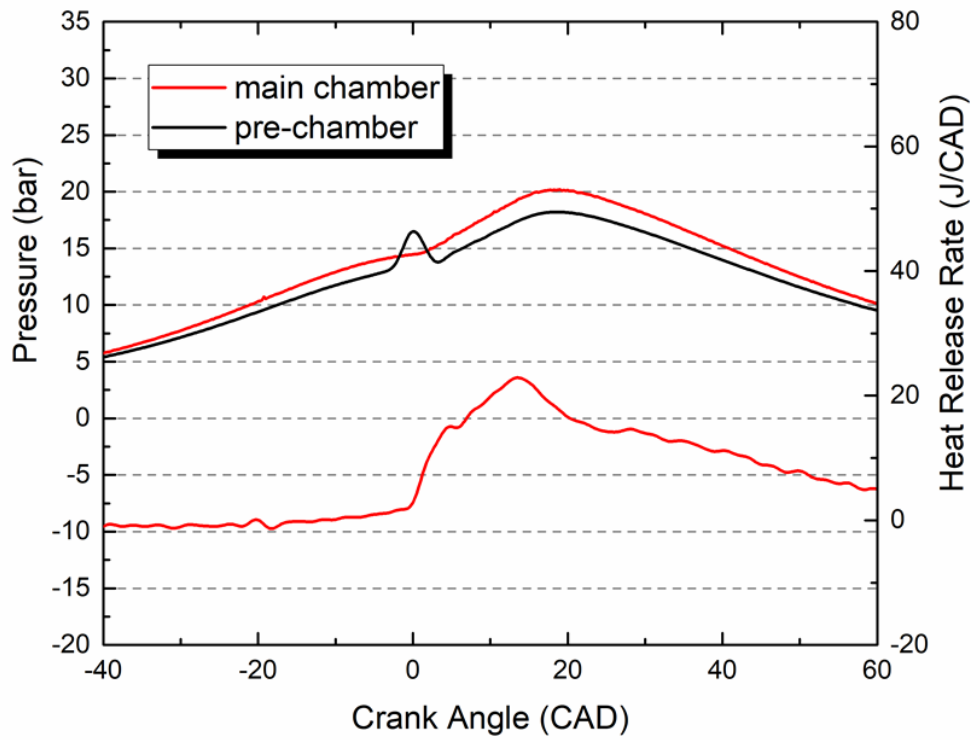
Figure 7.17 depicts the in-cylinder pressure traces of the main chamber and pre-chamber and the corresponding combustion images of ethanol. The pre-chamber pressure becomes higher than the main chamber pressure when the spark plug at the pre-chamber ignites the air–fuel mixture then combustion continues across the pre-chamber. The pre-chamber products were injected to the main chamber through the nozzle orifices and then captured by the ICCD camera because of the increased pre-chamber pressure. At fuel injection of 0.7 mg/pulse, the visible chemiluminescence sites in the main chamber initially appeared at 7° CA after SI and they were delayed to 9° CA and 11° CA after SI as the injection duration of ethanol in the pre-chamber was reduced to 0.5 and 0.3 mg/pulse, respectively, which are approximately two CAD after the pre-chamber pressure increased. The delayed and detached appearance of the light emission sites away from the nozzle clearly demonstrated that these jets were

quenched when leaving the orifices. The light emission sites in the first image were coloured green based on the light intensity and were produced by the hot partially burned jets. The jets initially occurred approximately at the point of peak of the pre-chamber pressure. In the next few frames, the light intensity in the middle region transformed into red as the higher temperature combustion occurred, and the high-temperature region in red expanded as the flame fronts moved outward from the jet ignition sites. In addition to the delayed appearance in the main chamber, the location of the first light emission sites became closer to the exit of the pre-chamber when the fuel injected in the pre-chamber was reduced. The distance from the nozzle orifice outlet was measured, the first light emission sites was reduced from 22.34 mm to 16.56 and 14.6 mm as the fuel injection in the pre-chamber was reduced from 0.7 mg/pulse to 0.5 and 0.3 mg/pulse. The jet formation size also decreased. These results can be explained by the greater pressure rise in the pre-chamber, which was caused by more heat released with increasing fuel in the pre-chamber. The larger pressure differential between the pre-chamber and the main chamber (with more fuel in the pre-chamber) results in the jets emanating the nozzle orifices at higher speed and travelled more distance before they are reignited in the main chamber. However, the higher temperature of the jets produced by the burning of more fuel in the pre-chamber reduces the ignition delay of the jets in the main chamber.

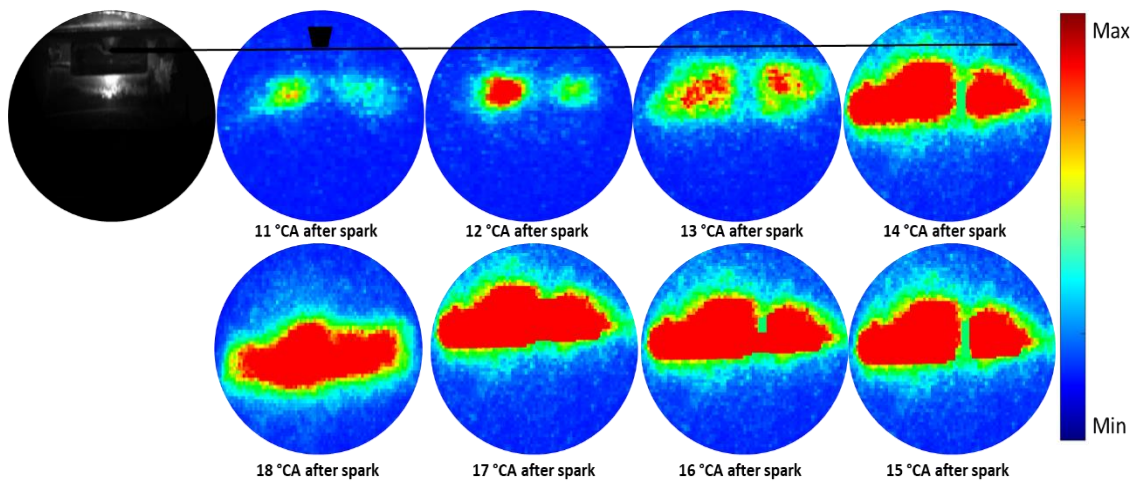
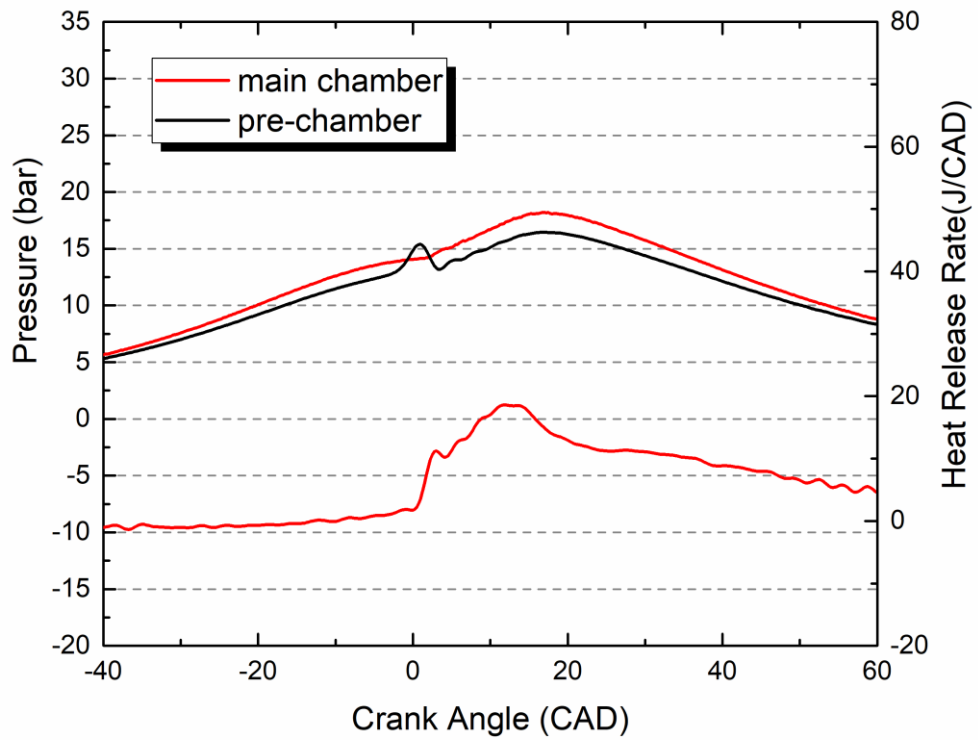
For the same reason, similar results are obtained with pre-chamber fuelled with gasoline. The visible jets first appear at 9° CA after spark with the fuel injection of 0.7 mg/pulse and is delayed to 11° and 12° CA after spark for fuel injection of 0.5 and 0.3 mg/pulse, as shown in Figure 7.18, approximately 2° CA delayed compared with those of the ethanol operation. The locations of the first visible jets are 20.05, 15.51 and 14.31 for fuel injection of 0.7, 0.5 and 0.3 mg/pulse, respectively. They are slightly shorter than those of the ethanol because the pre-chamber pressure is lower than that of ethanol by 2 bar.



(a) Fuel injection 0.7 mg/pulse

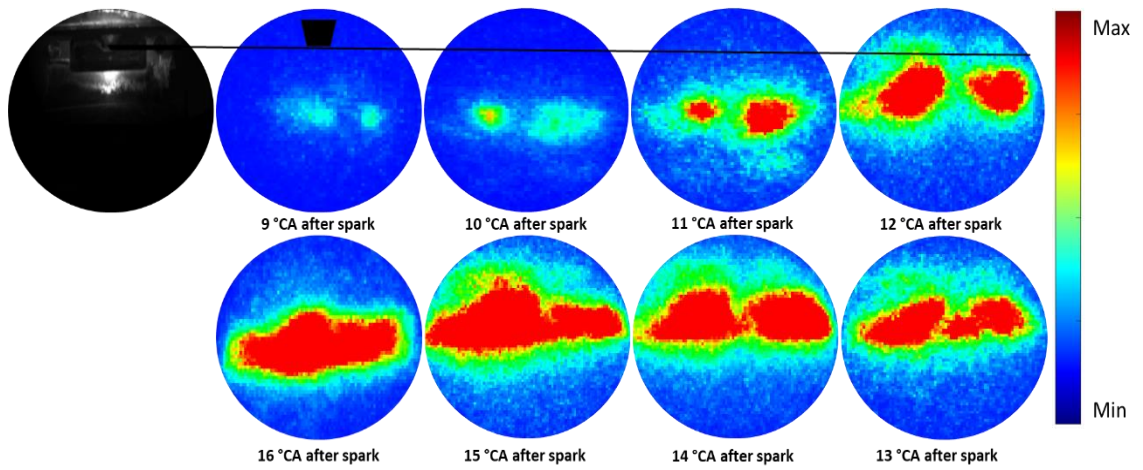
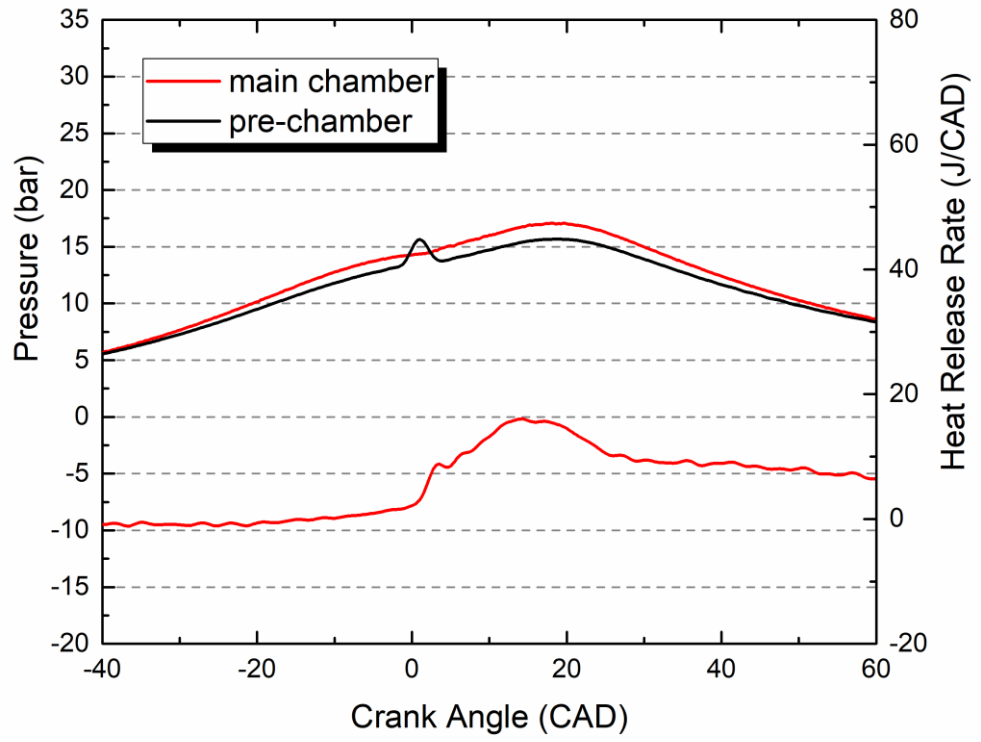


(b) Fuel injection 0.5 mg/pulse

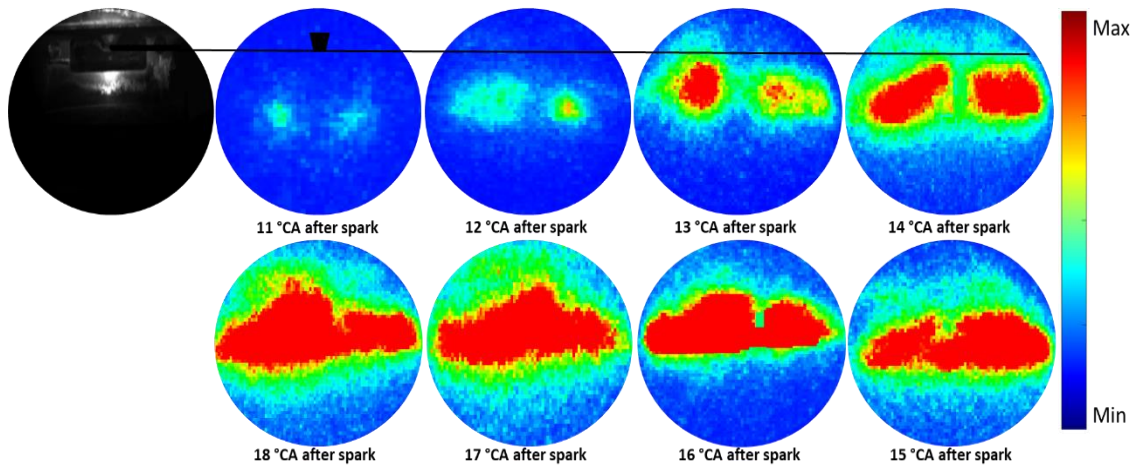
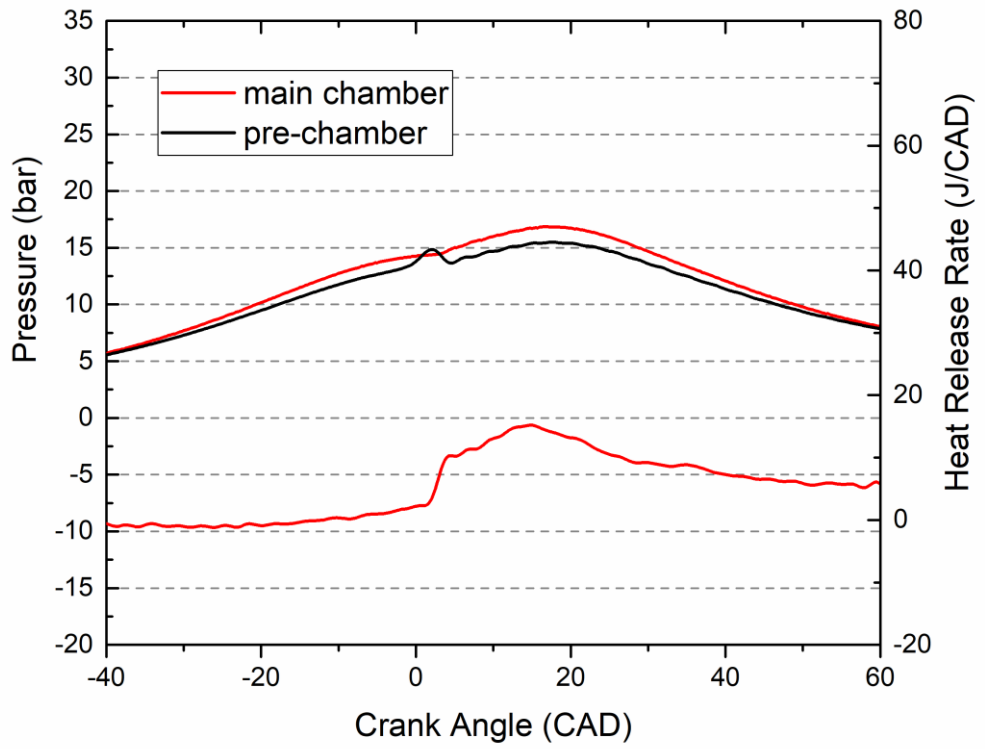


(c) Fuel injection 0.3 mg/pulse

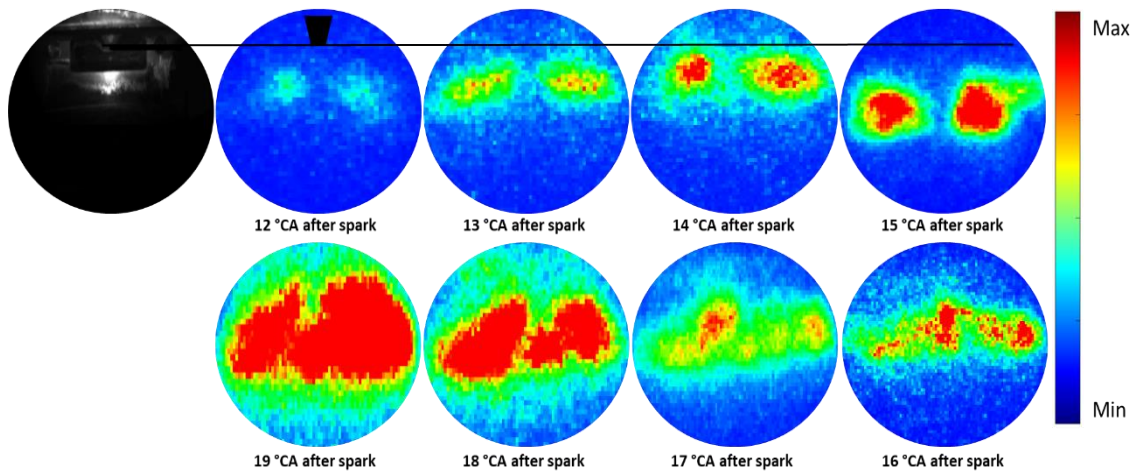
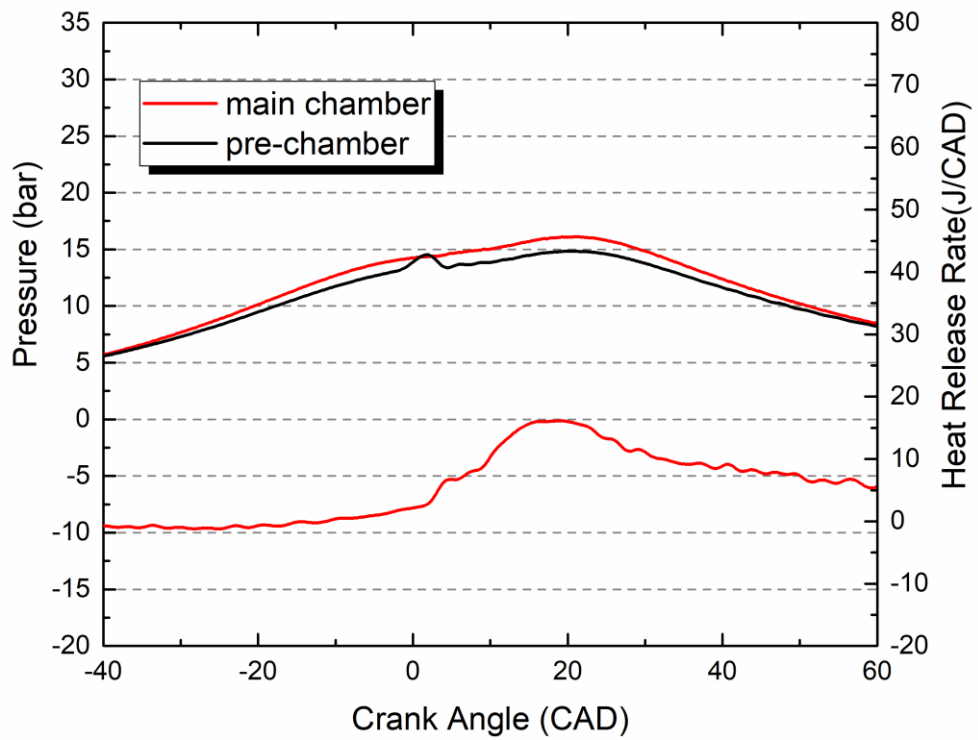
Figure 7.17 Pre-chamber and main chamber pressure and ICCD images of ignition sites in the main chamber at fixed injection timing of 50° CA bTDC and spark timing of 10° CA bTDC fuelled by ethanol under fuel injection duration of 0.3, 0.5 and 0.7 mg/pulse



(a) Fuel injection of 0.7 mg/pulse



(b) Fuel injection of 0.5 mg/pulse



(c) Fuel injection of 0.3 mg/pulse

Figure 7.18 Pre-chamber and main chamber pressures and ICCD images of ignition sites in the main chamber at fixed injection timing of 50° CA bTDC and spark timing of 10° CA bTDC fuelled by gasoline under fuel injection duration of 0.3, 0.5 and 0.7 mg/pulse

Figure 7.19 presents the jet travel distance and injection delay for both fuels at fixed injection timing of 50° CA bTDC and spark timing of 10° CA bTDC under different fuel injection durations of 0.3, 0.5 and 0.7 mg/pulse. The Figure illustrates the effect of fuel type and fuel injection on the injected pre-chamber products. Under different fuel

injection duration, ethanol greatly affected the injected products compared with gasoline. Moreover, at fuel injection duration of 0.7 mg/pulse, the injected radicals travelled deeper, and the jet flame appeared faster.

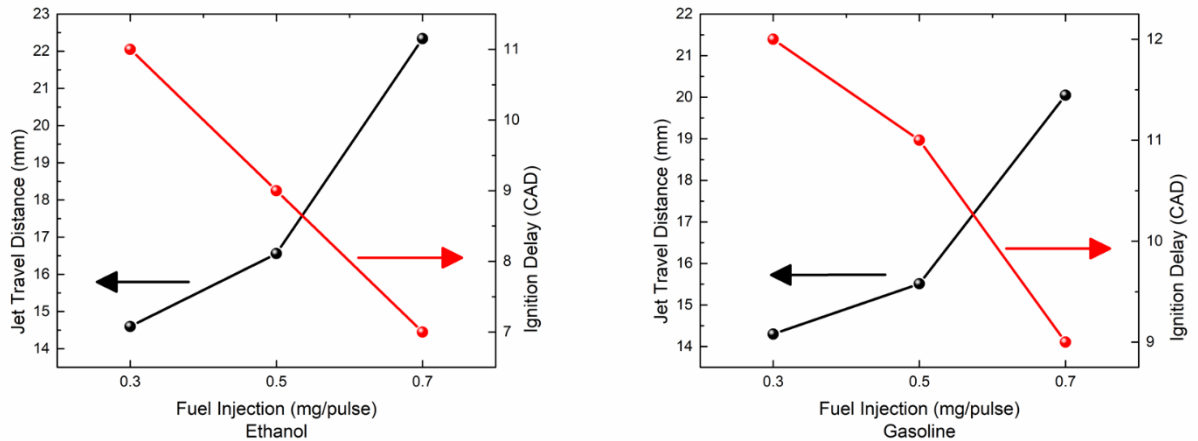
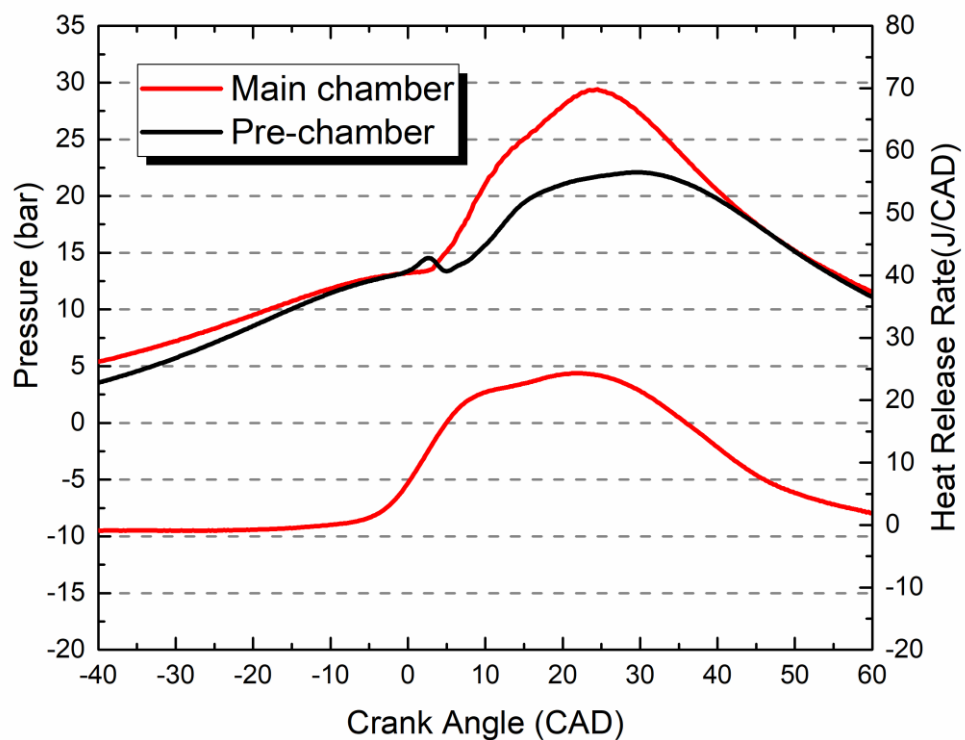


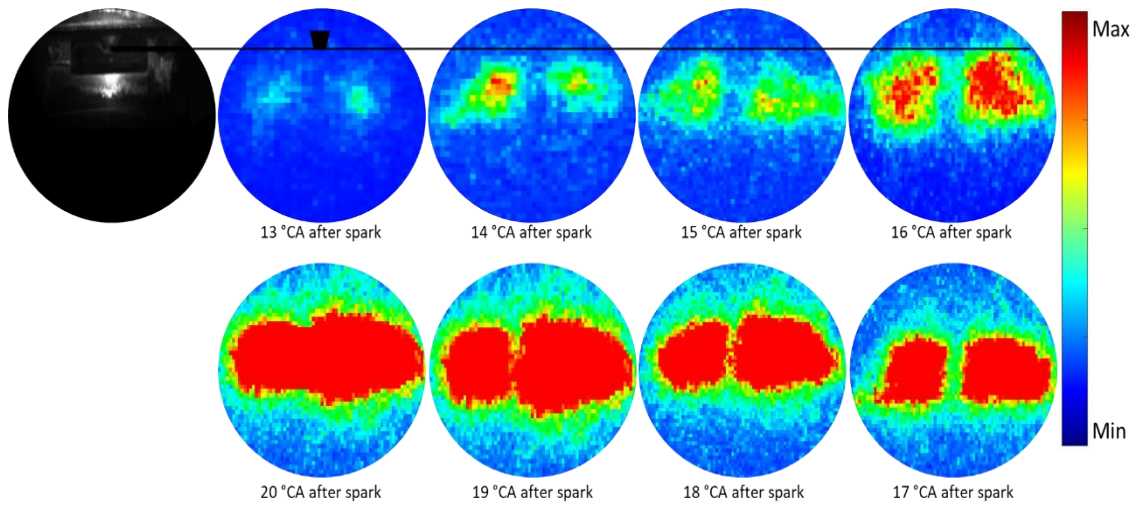
Figure 7.19 Jet travel distance and ignition delay for both fuels at different fuel injections (0.3, 0.5 and 0.7 mg/pulse).

Figures 7.20 and 7.21 present the pre-chamber and main chamber pressure and the corresponding combustion images of ethanol and gasoline at fixed spark timing of 10° CA bTDC in the pre-chamber at lambda 1.0 and 1.2. In this case, the main chamber charge was fired with unfuelled pre-chamber because it reached lambda 1.2 without using auxiliary fuel. The in-cylinder pressure traces of the main chamber and pre-chamber and the corresponding combustion images of lambda 1 for both fuels are shown in Figure 7.20. Interestingly, the pre-chamber pressure became slightly higher than the main chamber pressure when the spark plug at the pre-chamber ignited the air–fuel mixture, where it returned from the main chamber to the pre-chamber volume during combustion stroke. The combustion then continued across the pre-chamber and increased the pre-chamber pressure. The ICCD camera recorded the injected products from the pre-chamber through the nozzle orifices. These products initially appeared at 13° CA and 14° CA for ethanol and gasoline, respectively. The initial appearance of the injected products was delayed compared with the fuelled pre-chamber probably due to the effect of pre-chamber fuel to increase the pre-chamber pressure, thereby accelerating the injected radicals to leave the pre-chamber volume faster. After measuring the jet travel distance from the nozzle orifice outlet to main chamber, the

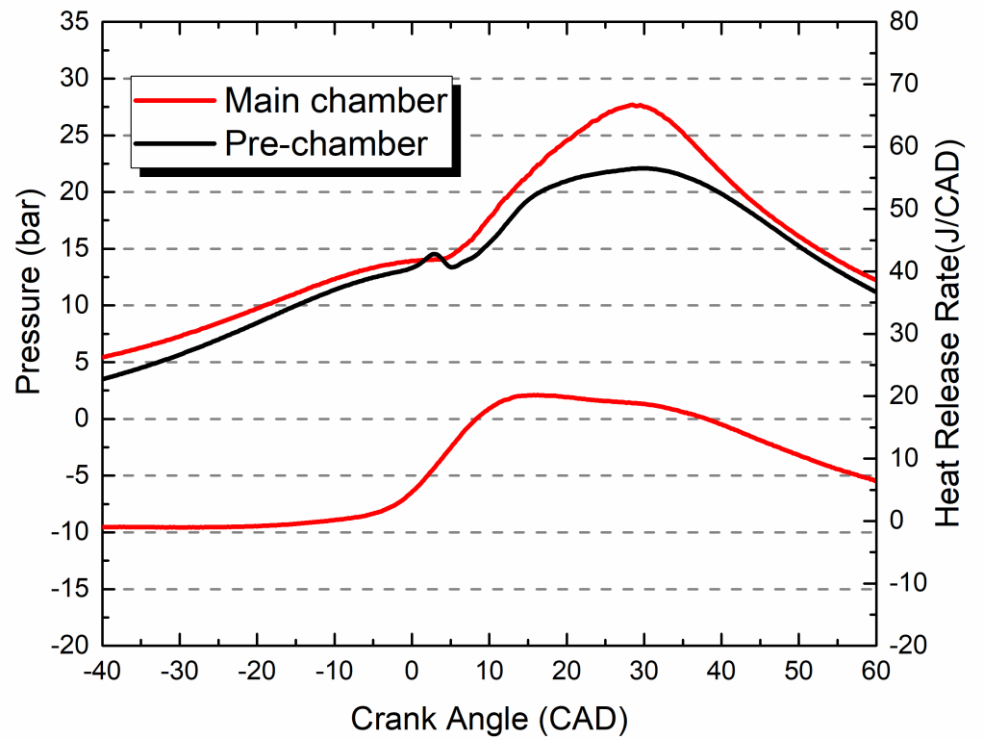
light emissions appeared at the distance of 14.4 mm for ethanol fuel, whereas it appeared at the distance of 14.21 for gasoline fuel.

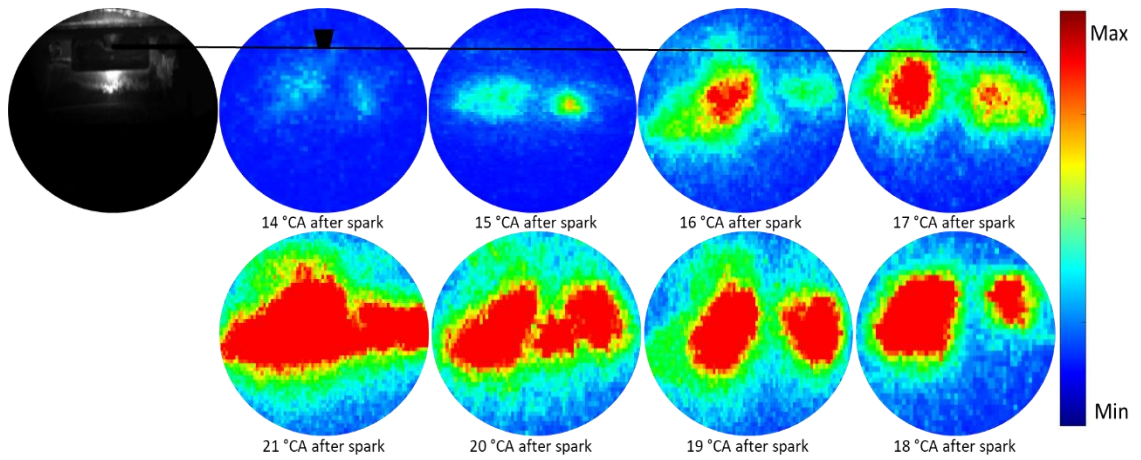
Figure 7.21 presents the in-cylinder pressure traces of the main chamber and pre-chamber and the corresponding combustion images of lambda 1.2 for ethanol and gasoline. Evidently, the combustion became slower for both fuels. The pre-chamber combustion became slower due to the effect of the main combustion, thereby delaying the first appearance of the visible chemiluminescence sites in the main chamber to 14° CA and 16° CA for ethanol and gasoline, respectively. Moreover, the injected jet travelled shorter than lambda 1.0, where the jet travel distance reduced to 13.85 and 13.23 for ethanol and gasoline, respectively.





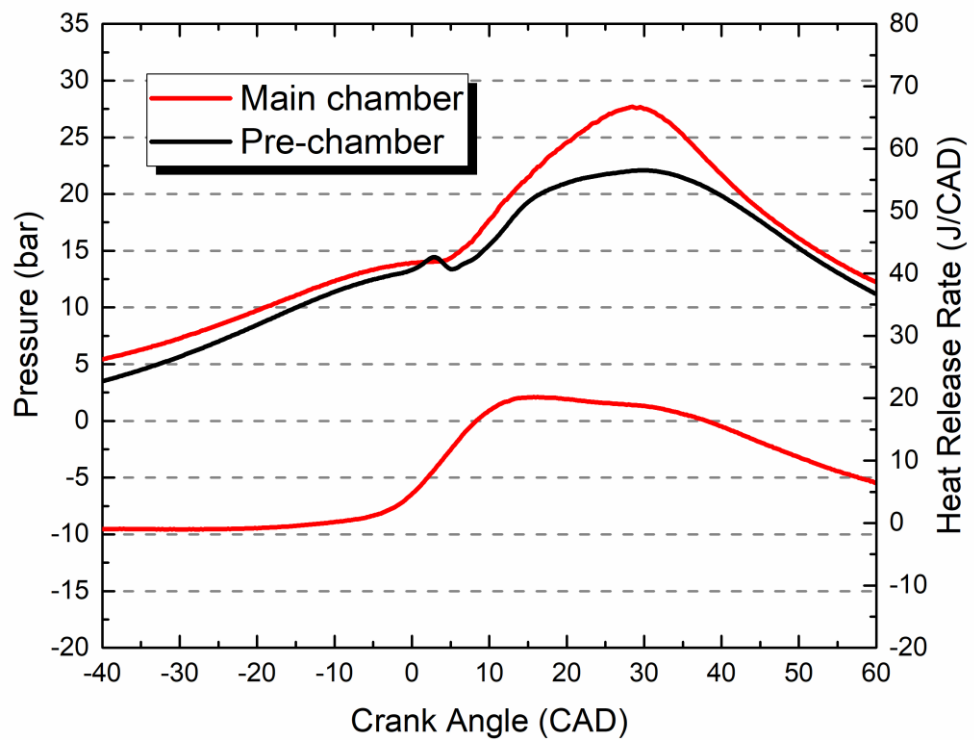
(a) Ethanol Fuel

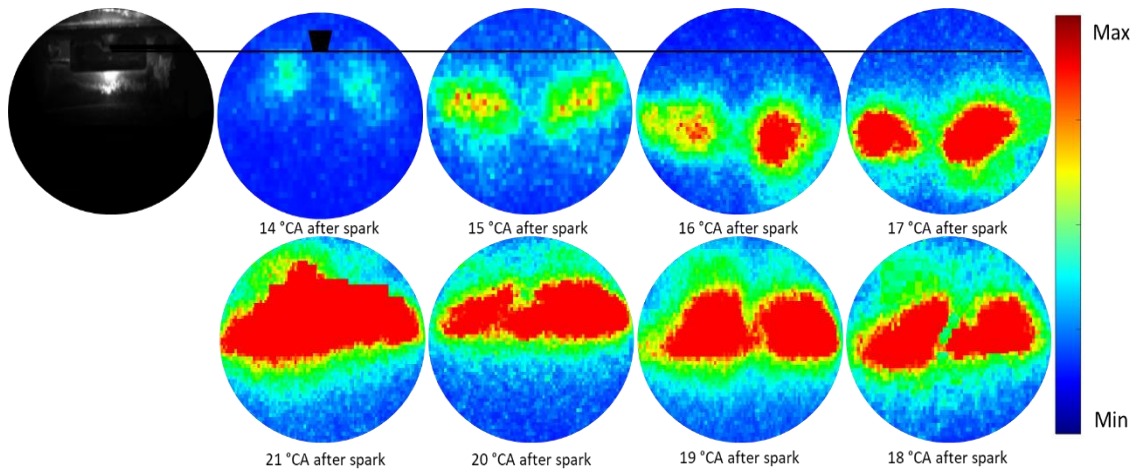




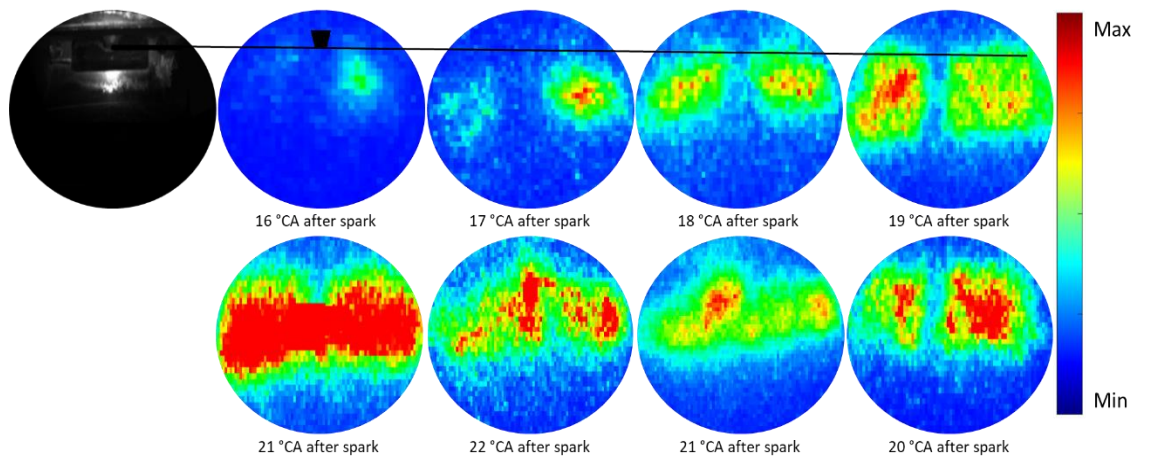
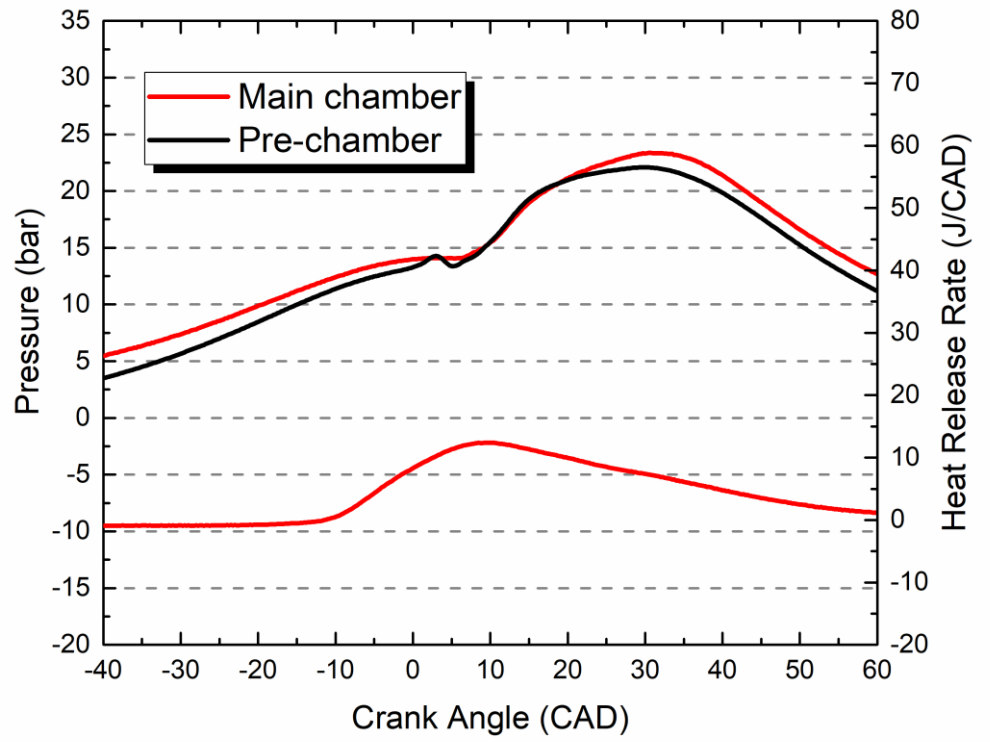
(b) Gasoline Fuel

Figure 7.20 Pre-chamber and main chamber pressures and ICCD images of ignition sites in the main chamber at fixed spark timing of 10° CA bTDC and $\lambda = 1.0$





(a) Ethanol Fuel

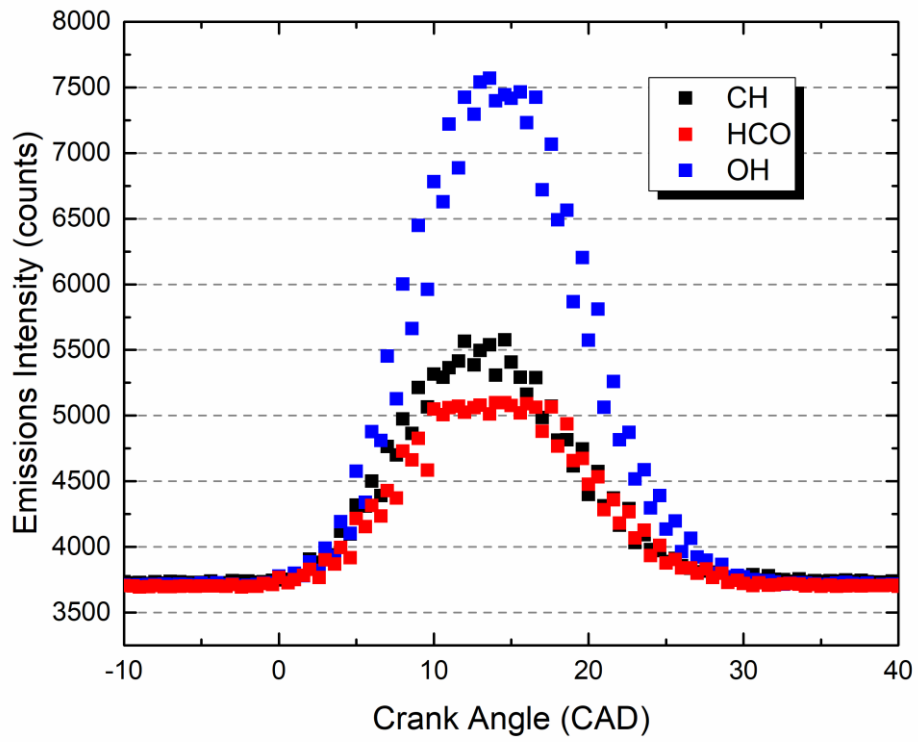


(b) Gasoline Fuel

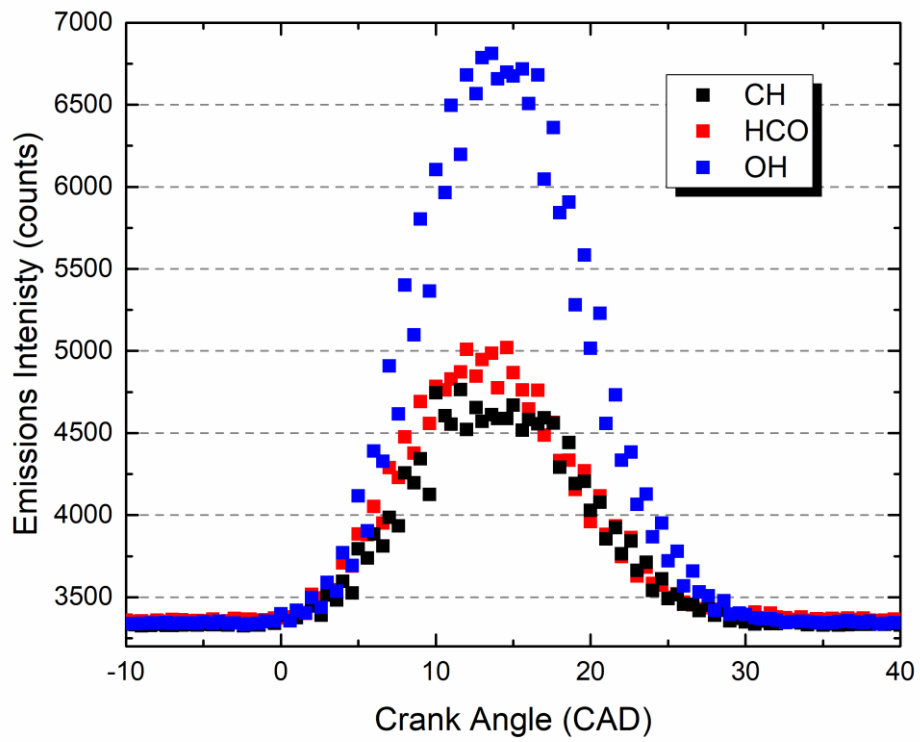
Figure 7.21 Pre-chamber and main chamber pressures and ICCD images of ignition sites in the main chamber at fixed spark timing of 10° CA bTDC and $\lambda = 1.2$

7.3.5 Spectroscopic Investigation of Initial Combustion Fuelled by Ethanol and Gasoline at Different Lambdas with Fuelled Pre-Chamber Ignition System

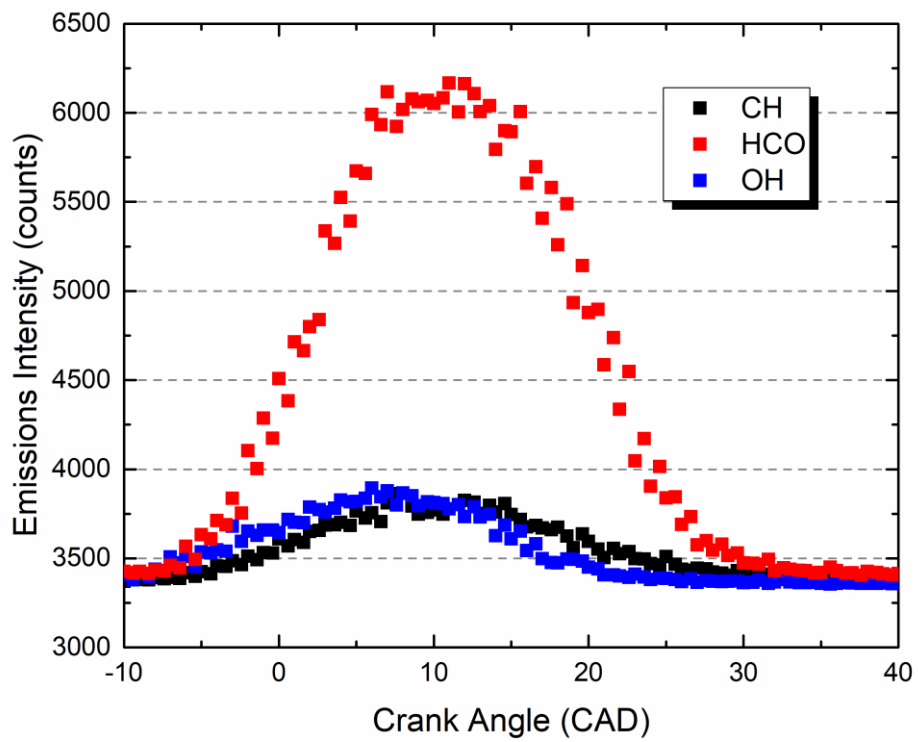
To compare the spectra emissions for OH, CH and HCO under different A-F ratios for each fuel. The pre-chamber spark timing was fixed at 10° CA bTDC, with 0.3 mg/pulse of fuel at the injection timing of 50° CA bTDC. Then, the main chamber fuel was reduced until the lean-burn limit of $CoV_{IMEP} \leq 5$ was reached. Figures 7.22 and 7.23 show the temporal emission intensity variation with crank angles ensemble-averaged over 15 cycles at different lambdas for gasoline and ethanol, respectively. The results reveal similar trends in the variation of emission intensity during combustion to those of the unfuelled pre-chamber. For both fuels, the peaks of OH, CH and HCO emissions decrease as the mixture in the main chamber becomes leaner because of the lower combustion temperature. Ethanol fuel combustion produces higher emission intensity due to the higher energy input and faster flame propagation. At the lean-burn limit of lambda 1.8 for gasoline, the HCO emission become greater than the CH due to incomplete combustion, and the combustion becomes unstable. The variation in the spectra emission represents cyclic variation that cannot be detected from the pressure trace [104]. The above results also indicate a correlation between spectra emissions and air-fuel ratios, which had previously been explored by Ohyama et al. [145] to infer the air-fuel ratio in a normal SI combustion and by Yamazaki et al. [146] in a burner combustion using spectra analysis.



(a) $\Lambda = 1.4$

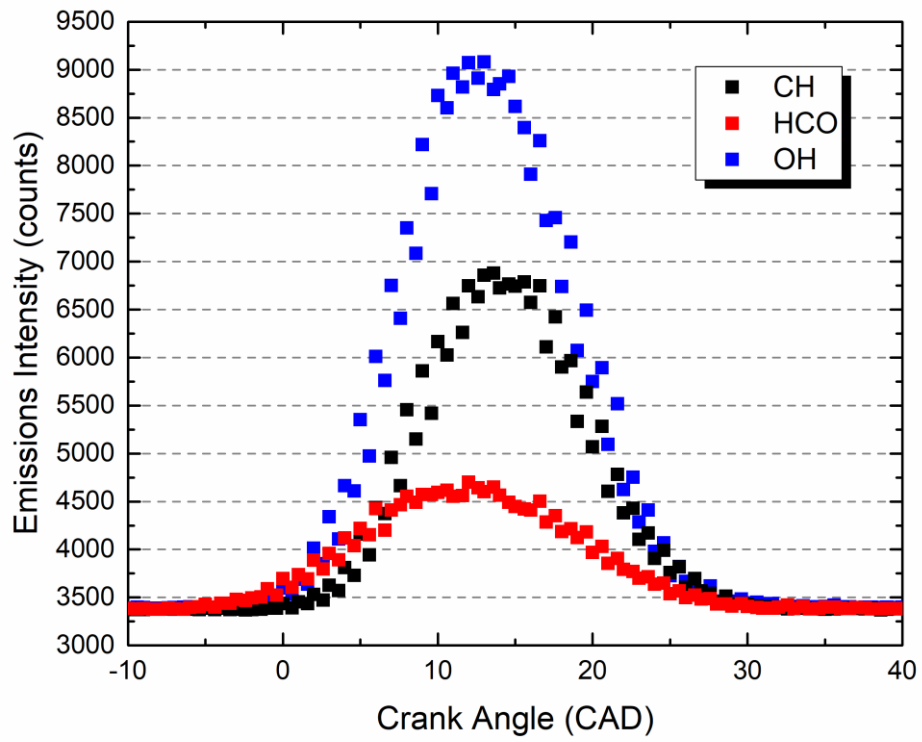


(b) $\Lambda = 1.6$

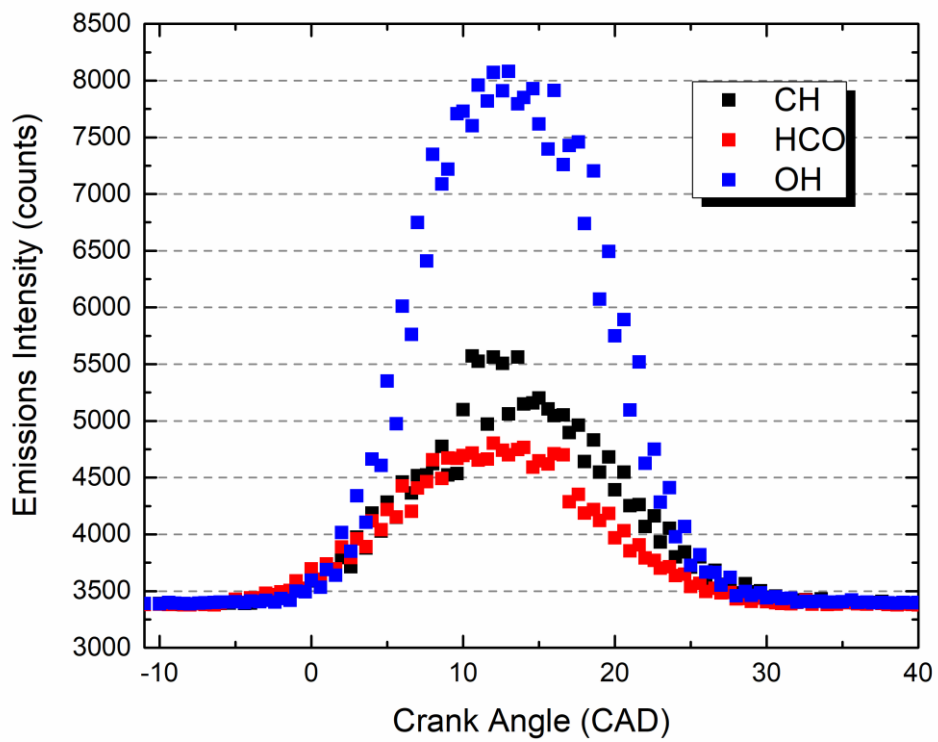


(c) Lambda = 1.8

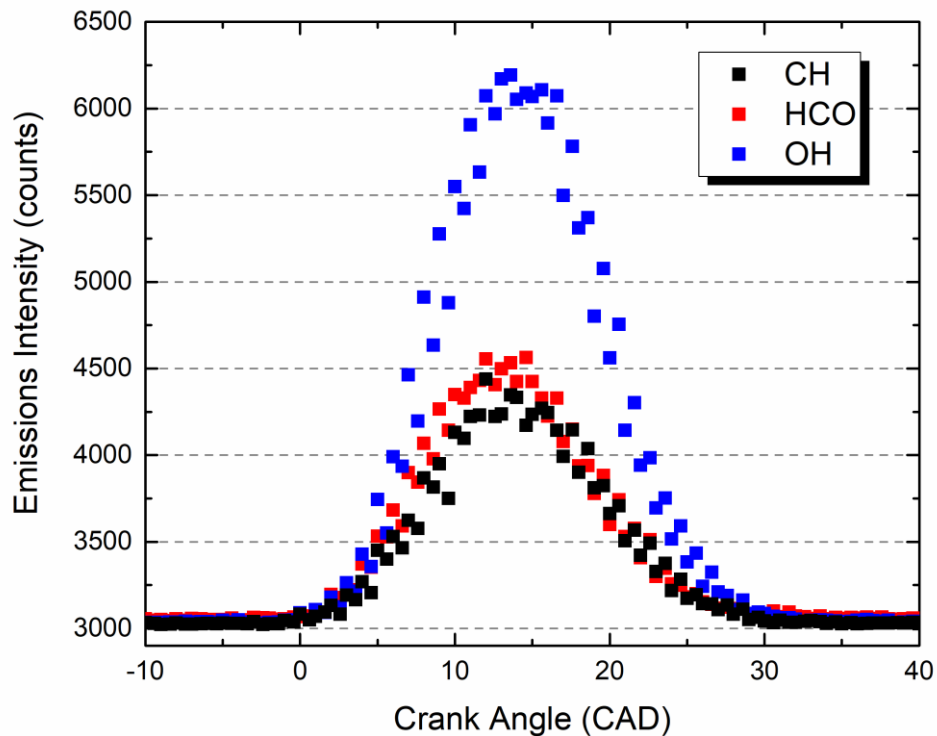
Figure 7.22 Temporal profiles of radical emission intensities at different relative gasoline to air ratios with a constant spark timing of 10° CA bTDC and 0.3 mg/pulse fuel injection at 50° CA bTDC



(a) $\Lambda = 1.4$



(b) Lambda = 1.6



(c) Lambda = 1.8

Figure 7.23 Temporal profiles of the radical emission intensities at different relative ethanol to air ratios with a constant spark timing of 10° CA bTDC and 0.3 mg/pulse fuel injection at 50° CA bTDC

Figure 7.24 summarises the emission spectra intensities for various ignition systems under different air–fuel ratios. The spark timing was fixed at 22° CA bTDC for the normal SI in the main chamber whereas fixed at 10° CA bTDC for the pre-chamber ignition. In the case of the fuelled pre-chamber ignition system, the injection duration was 50° CA bTDC, and the injected fuel was 0.3 mg/pulse. For all ignition systems, the combustion of ethanol produced higher emission intensities of all three radicals. The strongest chemiluminescent emission was produced by the jet ignition from the pre-chamber fuelled with ethanol. Furthermore, the HCO emission exhibits a monotonic increase with the air–fuel ratio as the combustion takes place at lower temperature and becomes less complete.

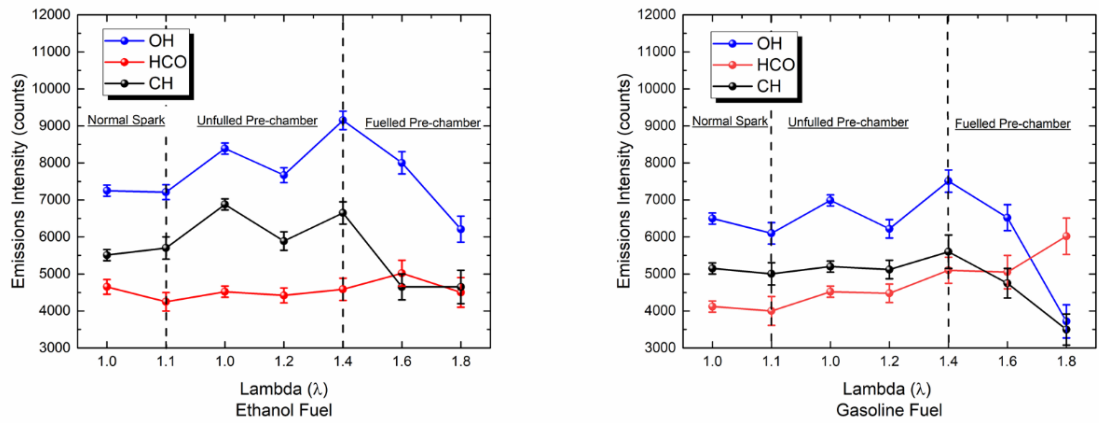


Figure 7.24 Variation of emission spectrum intensity for different ignition systems under different air–fuel conditions

7.4 Conclusions

In this chapter, the effects of pre-chamber ignition with or without gasoline or ethanol were investigated through in-cylinder pressure and high-speed optical and spectroscopic measurements at a constant engine speed of 1200 rpm and WOT. The spectral emissions of OH, CH and HCO radicals were analysed. High-speed and ICCD cameras were used to capture the ignition and combustion sparks in the combustion chamber.

The results indicate that ethanol combustion produced higher chemiluminescent emissions than gasoline. The OH spectral peak at 310 nm was the highest throughout the ignition and combustion processes, followed by CH emission at 430 nm and HCO at 330 nm. Their intensities increased to maxima before the maximum HRRs measured by the in-cylinder pressure. Stronger emission spectra were produced by the pre-chamber ignition compared with the normal SI in the main chamber. The highest emission intensities were observed with the fuelled pre-chamber ignition even with leaner air–fuel mixture in the main chamber.

At the fixed spark timing of 10° CA bTDC and injection at 50° CA bTDC in the pre-chamber, when increasing the fuel injected in the pre-chamber from 0.3, to 0.5 and 0.7 mg/pulse, the pre-chamber pressure increased rapidly to a higher peak value, thereby producing greater pressure differential between the pre-chamber and main chamber and faster turbulent jets of partially burned products at higher temperature. As the pre-chamber fuel increased, the emission spectra became stronger for both fuels. The

increase in the pre-chamber pressure caused the jets to travel deeper into the main chamber, and the ignition sites became large. However, the ignition delay of the main chamber combustion became shorter as the temperature of jets increased. The TJI of ethanol was characterised with greater momentum than gasoline due to the faster combustion speed of ethanol and higher energy input. When the pre-chamber spark timing was advanced, the OH and CH emission intensities increased due to higher pressure and temperature in the pre-chamber, thereby causing the pre-chamber products to travel deeper to ignite most of the main chamber charge. In comparison, the pre-chamber fuel injection timing has less effect. However, at the injection timing of 70° CA bTDC, the combustion becomes unstable.

Finally, the spectroscopic investigation at different air–fuel ratios with fuelled pre-chamber ignition reveals that the peaks of OH, CH and HCO dropped towards the lean-burn limits for both fuels. The intensity of the emission spectra depends on the ignition type, fuel properties and air–fuel ratios. In the case of gasoline, a monotonic increase in CHO emission was observed with increasing air–fuel ratios as the combustion temperature and combustion efficiencies decreased.

Chapter 8 Conclusions and Suggestions for Future Work

8.1 Conclusions of Research

The main goal of this research is to study the application of Mahle TJI in a specially modified full bore optical engine. The study involves thermodynamic and optical investigations of combustion under stoichiometric and lean-burn conditions and focuses on the effect of TJI on the combustion, emission and performance of the engine with different fuels. The main conclusions are summarised in the following sections.

8.1.1 Effect of TJI on Gasoline Combustion and Emissions at Different Loads

- Under stoichiometric condition, TJI exhibited slightly retarded start of combustion at the same spark timing as the SI was in the main chamber due to the ignition delay caused by pre-chamber jet formation. After being ignited by the multiple jets, the main chamber pressure rose more rapidly than by the normal SI, and the main combustion duration of TJI was largely reduced.
- Multiple jet flames were observed in the main chamber and subsequently merged as one propagating flame. Compared with the single-point ignition of the normal SI, multiple jet-ignited flames propagated at a much higher speed. As a result, the TJI could be applied to ignite leaner mixture and shorten combustion as confirmed by the in-cylinder high-speed imaging results.
- The maximum lambda at the lean-burn limit ($COV_{IMEP} < 5\%$) reached by TJI was correlated with the inlet pressure. The decrease in the inlet pressure reduced the engine IMEP and narrowed the lean limit.
- The NO_x emission decreased with the inlet pressure because of the extended lean-burn limit with increasing inlet pressure. However, HC and CO increased with inlet pressure due to the mainly unstable combustion and lower combustion temperature.

8.1.2 Effect of TJI on Gasoline Combustion and Emissions at Different Speeds

- The lean-burn limit of gasoline was extended from 800 rpm to 1200 rpm at WOT
- The IMEP values were slightly higher at low speed than at high speed for all different lambdas. However, the CA₀–CA₁₀ and 10%–90% MFB shows that the combustion was faster at low speed based on the crank angle, but it still cannot extend the lean limit compared with high speed.

- The MBT spark timing was more advanced with the engine speed for the conventional SI and pre-chamber ignition.
- The extended lean-burn limit produced much less NO_x emissions at 1200 rpm than at 800 and 1000 rpm. At low speed, the CO and HC emissions were higher due to poor combustion at lean condition.

8.1.3 Effect of TJI on Combustion and Emissions of Gasoline, Ethanol and Wet-ethanol Engine Operations

The most extended lean-burn operation was achieved with ethanol at a lambda of 1.9 at WOT of 1200 rpm. In addition, ethanol and wet-ethanol produced higher IMEP because of their faster combustion and heat release.

The extended lean-burn limits by the TJI also led to a significant reduction in NO emissions. In general, anhydrous and wet-ethanol fuels produced lower NO, HC and CO emissions than gasoline given that the combustion temperature was reduced and the combustion became more stable and complete than that of gasoline combustion.

The high-speed combustion chemiluminescence imaging provided direct evidence of the multiple combustion sites in the main chamber as a result of the high-temperature TJI. It also illustrated that ethanol had the fastest flame speed followed by wet-ethanol and gasoline.

8.1.4 Spectroscopic Analysis of In-cylinder Combustion Between Normal SI and Jet Ignition System in an Optical Engine Fuelled with Gasoline and Ethanol

- Ethanol combustion produced higher chemiluminescent emissions than gasoline combustion. The OH spectral peak at 310 nm was the highest throughout the ignition and combustion processes, followed by CH emission at 430 nm and HCO at 330 nm.
- Their intensities increased to maxima before the maximum HRRs measured by the in-cylinder pressure.
- Stronger emission spectra were produced by the pre-chamber ignition than the normal SI in the main chamber. The highest emission intensities were observed with the fuelled pre-chamber ignition even with leaner air–fuel mixture in the main chamber.

- The pre-chamber pressure increased faster to a higher peak value by increasing the fuel injected in the pre-chamber, producing greater pressure differential between the pre- and main chamber and faster turbulent jets of partially burned products at higher temperature.
- As the pre-chamber fuel increased, the emission spectra became stronger for both fuels. The increase in the pre-chamber pressure caused the turbulent high-temperature jets to travel deeper into the main chamber, and the ignition sites enlarged. However, the ignition delay of the main chamber combustion became shorter as the temperature of the jets increased.
- The OH and CH emission intensities increased due to higher pressure and temperature in the pre-chamber, causing the pre-chamber products to travel deeper to ignite most of the main chamber charge.
- The spectroscopic investigation at different air–fuel ratios with fuelled pre-chamber ignition revealed that the peaks of OH, CH and HCO dropped towards the lean-burn limits for both fuels.

8.2 Recommendations for Future Work

This research provide valuable insights to understand lean combustion and ignition enhancement by using a pre-chamber ignition system in an optical engine. To enhance understanding of these issues and improve the quality of the results, further works can be carried out.

In future work, the cylinder head can be redesigned to overcome problems associated with sealing and overheating. Using the external EGR system to understand the interaction of EGR on lean combustion with the pre-chamber ignition system is also recommended. In addition, the intake air heating automation and control must be improved to avoid inlet air temperature fluctuations whilst using the heater.

Further spectroscopic investigation is recommended for future work at different locations, exhaust and inlet valve to study the presence of different species to understand combustion. The rapid emissions of HC during heavy knock on the chemistry of pre-chamber ignition must be evaluated.

The effect of ethanol on lean combustion was investigated and reported in this work. Using other fuels, such as natural gas and methanol, is recommended for future work.

XI. References

- [1] G. Andrews, "Environmental impact and health concerns of SI emissions," Short course on SI engines emissions, University of Leeds.
- [2] J. Godoy, "Auto Emissions Killing Thousands," 2004.
- [3] M. Bunce, H. Blaxill, W. Kulatilaka, and N. Jiang, "The effects of turbulent jet characteristics on engine performance using a pre-chamber combustor," *SAE Tech. Pap. 2014-01-1195*, 2014.
- [4] Q. Liu, A. Cairns, H. Zhao, M. Anbari Attar, L. Cruff, and H. Blaxill, "The Effects of Charge Homogeneity and Repeatability on Particulates Using the PLIF Technique in an Optical DISI Engine," *SAE Int. J. Engines 7(1)500-518*, pp. 500–518, 2014.
- [5] I. Council, "JANUARY 2014 EU CO 2 EMISSION STANDARDS FOR PASSENGER CARS AND LIGHT-COMMERCIAL VEHICLES," no. January, 2014.
- [6] R. A. Stein, J. E. Anderson, and T. J. Wallington, "An Overview of the Effects of Ethanol-Gasoline Blends on SI Engine Performance, Fuel Efficiency, and Emissions," *SAE Int. J. Engines 6(1)470-487*, 2013.
- [7] N. Ozdor, M. Dulger, and E. Sher, "Cyclic variability in spark ignition engines: a literature survey," *SAE Pap.*, no. 940987, 1994.
- [8] G. I. E. P. S. A. Renault, W. K. Cheng, and J. B. Heywood, "The Effects of Initial Flame Kernel Conditions on Flame Development in SI Engine," 2018.
- [9] D. L. Lord, R. W. Anderson, D. D. Brehob, and Y. Kim, "The Effects of Charge Motion on Early Flame Kernel Development," *SAE Tech. Pap.*, no. 930463, 1993.
- [10] P. G. Aleiferis, A. M. K. P. Taylor, K. Ishii, and Y. Urata, "The nature of early flame development in a lean-burn stratified-charge spark-ignition engine," *Combust. Flame*, vol. 136, no. 3, pp. 283–302, 2004.
- [11] G. P. Blair, *The basic design of two-stroke engines*. Society of Automotive Engineers, Inc. 400 Commonwealth Drive Warrendale, PA 15096-0001, 1990.
- [12] K. Lee, C. Bae, and K. Kang, "The effects of tumble and swirl flows on flame propagation in a four-valve S.I. engine," *Appl. Therm. Eng.*, vol. 27, no. 11–12, pp. 2122–2130, 2007.
- [13] Y. Li, H. Zhao, Z. Peng, and N. Ladommatos, "Analysis of tumble and swirl motions in a four-valve SI engine.," *SAE Tech. Pap. 2001-01-3555*, no. 724, 2001.
- [14] A. N. Lipatnikov and J. Chomiak, "Modeling of Pressure and Non-Stationary

Effects in Spark Ignition Engine Combustion : A Comparison of Different Approaches," *SAE Tech. Pap.*, no. 2000-01-2034, 2000.

- [15] R. K. Rajput, *Internal Combustion Engines*. Laxmi Publications, 2005.
- [16] M. D. Checkel and D. S.-K. Ting, "Turbulence Effects on Developing Turbulent Flames in a Constant Volume Combustion Chamber," *SAE Pap. No. 930867*, no. 412, 1993.
- [17] K. Olsson and B. Johansson, "Combustion Chambers for Natural Gas SI Engines Part 2: Combustion and Emissions," *SAE Tech. Pap. 950517*, no. 412, 1995.
- [18] C. M. H.-T. P. State, University, and D. A. S.-T. P. S. University, "Turbulence Effects on Early Flame Kernel Growth," *SAE Tech. Pap. 872100*, 1987.
- [19] T. Inoue, S. Matsushita, K. Nakanishi, and H. Okano, "Toyota Lean Combustion System -," *SAE 930873*, no. 412, 1993.
- [20] J. Justus, "Kinetic Energy Recovery Boosting System for Future Passenger Cars," 2016.
- [21] R. J. Farrauto and R. M. Heck, "Catalytic converters: State of the art and perspectives," *Catal. Today*, vol. 51, no. 3-4, pp. 351-360, 1999.
- [22] N. Fraser, H. Blaxill, G. Lumsden, and M. Bassett, "Challenges for Increased Efficiency through Gasoline Engine Downsizing," *SAE Int. J. Engines*, vol. 2, no. 1, pp. 991-1008, 2009.
- [23] J. W. G. Turner *et al.*, "Ultra Boost for Economy: Extending the Limits of Extreme Engine Downsizing," *SAE Int.*, vol. 7, no. 1, pp. 387-417, 2014.
- [24] R. Egnell, "The influence of EGR on heat release rate and NO formation in a DI diesel engine," *SAE Tech. Pap. 2000-01-1807*, no. 724, 2000.
- [25] W. W. Pulkrabek, *Engineering fundamentals of the internal combustion engine*. New Jersey 07458: Prentice Hall, 2004.
- [26] G. R. Neame, D. P. Gardiner, and R. W. Mallory, "Improving the Fuel Economy of Stoichiometrically Fuelled SI Engines by Means of EGR and Enhanced Ignition - A Comparison of Gasoline, Methanol and Natural Gas," *SAE Int.*, no. 412, 1995.
- [27] S. Birch, "Diesel vs. gasoline: the fight goes on," *Automotive engineering international online: Tech briefs*. .
- [28] H. Zhao, *Advanced Direct Injection Combustion Engine Technologies and Development*, 1st ed. Woodhead Publishing.
- [29] S. Hatakeyama, Y. Sekiya, T. Murayama, and H. Tsunemoto, "A Study of Lean

- Burn of a 4 Stroke Gasoline Engine by the Aid of Low Pressure Air Assisted In-Cylinder Injection - Part II," *SAE Tech. Pap. Ser.*, 1999.
- [30] W. P. Attard, H. Blaxill, E. K. Anderson, and P. Litke, "Knock Limit Extension with a Gasoline Fueled Pre-Chamber Jet Igniter in a Modern Vehicle Powertrain," *SAE Int. J. Engines*, vol. 5, no. 3, pp. 2012-01-1143, 2012.
- [31] A. Cairns, H. Blaxill, and G. Irlam, "Exhaust Gas Recirculation for Improved Part and Full Load Fuel Economy in a Turbocharged Gasoline Engine," *SAE Tech. Pap. 2006-01-0047*, 2006.
- [32] T. Lake, J. Stokes, R. Murphy, R. Osborne, and A. Schamel, "Turbocharging Concepts for Downsized DI Gasoline Engines," *SAE Tech. Pap. 2004-01-0036*, 2004.
- [33] E. J. Tully and J. B. Heywood, "Lean-Burn Characteristics of a Gasoline Engine Enriched with Hydrogen Plasmatron Fuel Reformer," *SAE Tech. Pap. 2003-01-0630*, no. 724, 2003.
- [34] E. Toulson, H. C. Watson, and W. P. Attard, "The Lean Limit and Emissions at Near-Idle for a Gasoline HAJI System with Alternative Pre-Chamber Fuels," *SAE Tech. Pap. 2007-24-0120*, 2007.
- [35] A. Cairns *et al.*, "A Study of Gasoline-Alcohol Blended Fuels in an Advanced Turbocharged DISI Engine," *SAE Int.*, vol. 2, no. 1, pp. 41-57, 2009.
- [36] T. Date, S. Yagi, A. Ishizuya, and I. Fujii, "Research and Development of the Honda CVCC Engine," *SAE Tech. Pap. 740605*, 1974.
- [37] A. Maiboom *et al.*, "Various effects of EGR on combustion and emissions on an automotive DI Diesel engine: numerical and experimental study," *SAE Tech. Pap. 2007-01-1834*, 2007.
- [38] J. D. Benson, "The Influence of Engine and Fuel Factors on After-Run," *Automot. Eng. Congr. Expo.*, 1972.
- [39] J. C. Ingamells, "Effect of Gasoline Octane Quality and Hydrocarbon Composition on Afterrun," *1979 SAE Int. Fall Fuels Lubr. Meet. Exhib.*, 1979.
- [40] A. Oakley, H. Zhao, N. Ladommatos, and T. Ma, "Experimental Studies on Controlled Auto-ignition (CAI) Combustion of Gasoline in a 4-Stroke Engine," *SAE Tech. Pap. 2001-01-1030*, no. 2001-01-1030, 2001.
- [41] A. G., "Homogenous Charge Compression Ignition (HCCI) Engines," *Adv. Intern. Combust. Engines Fuel Technol.*, 2013.

- [42] J. Dale, M. D. Checkel, and P. R. Smy, "Application of high energy ignition systems to engines," *Prog. Energy Combust. Sci.*, vol. 23, no. 5–6, pp. 379–398, 1997.
- [43] E. Toulson, H. Schock, and W. Attard, "A Review of Pre-Chamber Initiated Jet Ignition Combustion Systems," *Intern. Combust. Engines*, 2010.
- [44] M. C. Turkish, "3 - Valve Stratified Charge Engines: Evolvement, Analysis and Progression," *SAE Tech. Pap. 741163*, 1974.
- [45] J. Renato and C. Gomes, "Torch Ignition System Analysis in an Spark Ignition Engine," *SAE Tech. Pap. 2005-01-4149*, 2005.
- [46] T. Reduction, N. E. Using, and H. Charge, "Theoretical Reduction in NO_x Emissions Using a Torch Ignition System Operating with Homogeneous Charge," *SAE Tech. Pap. 2015-36-0476*, 2015.
- [47] A. A. Gussak, L & P. Karpov, V & G. Slutskii, V & I. Spasskii, "Burning rate and stability in forechamber flame ignition in an internal-combustion engine," *Combust. Explos. Shock Waves* 19(5)628-630, 1983.
- [48] L. A. Gussak, "The Role of Chemical Activity and Turbulence Intensity in Prechamber-Torch Organization of Combustion of a Stationary Flow of a Fuel-Air Mixture," *SAE Tech. Pap. 830592*, 1983.
- [49] L. A. Gussak - The Institute of Chemical Physics of the Academy of Sciences of the USSR, "Effect of Adding Individual Combustion Products on Combustion of Methane Air Mixture," Russian, 1973.
- [50] J. A. Maxson, D. M. Hensinger, K. Hom, and A. K. Oppenheim, "Performance of Multiple Stream Pulsed Jet Combustion Systems," *SAE Tech. Pap. 910565*, 1991.
- [51] A. K. Oppenheim, J. Beltramo, D. W. Faris, J. A. Maxson, K. Hom, and H. E. Stewart, "Combustion by Pulsed Jet Plumes - Key to Controlled Combustion Engines," *SAE Tech. Pap. 890153*, 1989.
- [52] R. Latsch, "The Swirl-Chamber Spark Plug: A Means of Faster, More Uniform Energy Conversion in the Spark-Ignition Engine," *SAE Tech. Pap. 840455*, 1984.
- [53] G. Dober and H. Watson, "Modelling the Flame Enhancement of a HAJI Equipped Spark Ignition Engine," *SAE Tech. Pap. 1999-10-0051*, pp. 303–308, 1999.
- [54] E. Toulson, H. C. Watson, and W. P. Attard, "Gas Assisted Jet Ignition of Ultra-Lean LPG in a Spark Ignition Engine," *SAE Tech. Pap. 2009-01-0506*, 2009.

- [55] T. Lezanski, M. Kesler, T. Rychter, A. Teodorczyk, and P. Wolanski, "Performance of Pulsed Jet Combustion (PJC) System in a Research Engine," *SAE Tech. Pap. 932709*, 1993.
- [56] M. Kesler and T. J. Rychter, "A Jet Dispersed Combustion (JDC) Method to Stimulate Lean Burning in SI Piston Engines," *SAE Tech. Pap. 951006*, 1995.
- [57] S. Kito, K. Wakai, S. Takahashi, N. Fukaya, and Y. Takada, "Ignition limit of lean mixture by hydrogen flame jet ignition," *SAE Tech. Pap. 1999-08-0330*, 1999.
- [58] K. Wakai, S. Kito, and I. Sumida, "Effect of Small Hydrogen Jet Flame on Augmentation of Lean Combustion," *SAE Tech. Pap. 931943*, 1993.
- [59] S. Couet, P. Higelin, and B. Moreau, "APIR: A New Firing Concept for the Internal Combustion Engines - sensitivity to knock and in-cylinder aerodynamics," *SAE Tech. Pap. 2001-01-1954*, 2001.
- [60] J. Geiger, S. Pischinger, R. Böwing, H.-J. Koß, and J. Thiemann, "Ignition Systems for Highly Diluted Mixtures in SI-Engines," *SAE Tech. Pap. 1999-01-0799*, 1999.
- [61] M. Kettner, M. Rothe, A. Velji, U. Spicher, D. Kuhnert, and R. Latsch, "A New Flame Jet Concept to Improve the Inflammation of Lean Burn Mixtures in SI Engines," *SAE Tech. Pap. 2005-01-3688*, 2005.
- [62] V. Weng, J. Gindele, G. Töpfer, U. Spicher, R. Latsch, and D. Kuhnert, "Investigation of the Bowl-Prechamber-Ignition (BPI) Concept in a Direct Injection Gasoline Engine at Part Load," *SAE Tech. Pap. 1999-01-3658*, 1999.
- [63] Najt, P.M., Rask, R.B., and Reuss, D.L., "Dual Mode Engine Combustion Process," United States Patent No. 6595181., 2003.
- [64] J. Kojic, A., Hathout, J.-P., Cook, D., and Ahmed, "Control of Auto-Ignition Timing for Homogeneous Combustion Jet Ignition Engines," Patent No. PCT/US2004/029613., 2005.
- [65] J. Kojic, A., Hathout, J.-P., Cook, D., and Ahmed, "Control of Auto-Ignition Timing for Combustion in Piston Engines by Prechamber Compression Ignition," Patent No. PCT/US2004/029612, 2005.
- [66] J. Getzlaff, J. Pape, C. Gruenig, D. Kuhnert, and R. Latsch, "Investigations on Pre-Chamber Spark Plug with Pilot Injection," *SAE Tech. Pap. 2007-01-0479*, 2007.
- [67] M. Bunce and H. Blaxill, "Methodology for Combustion Analysis of a Spark Ignition Engine Incorporating a Pre-Chamber Combustor," *SAE Tech. Pap. 2014-01-2603*, 2014.

- [68] P. Chinnathambi, M. Bunce, and L. Cruff, "RANS Based Multidimensional Modeling of an Ultra-Lean Burn Pre-Chamber Combustion System with Auxiliary Liquid Gasoline Injection," *SAE Tech. Pap. 2015-01-0386*, 2015.
- [69] G. R. Gentz and E. Toulson, "Experimental Studies of a Liquid Propane Auxiliary Fueled Turbulent Jet Igniter in a Rapid Compression Machine," *SAE Int. J. Engines 9(2)777-785*, vol. 9, no. 2, pp. 2016-01-0708, 2016.
- [70] H. C. Watson, "Internal Combustion Engine Ignition Device," 5611307, 1997.
- [71] Z. Kyaw, "Chemical Control of S.I. Engine Combustion," The University of Melbourne, 1992.
- [72] H. C. Watson, "International Patent. Application PCT/ AU92/00552," PCT/AU92/00552, 1992.
- [73] J. Lawrence and H. C. Watson, "Hydrocarbon Emissions from a HAJI Equipped Ultra-lean Burn SI Engine," *SAE Tech. Pap. 980044*, no. 724, 1998.
- [74] E. Toulson, "Applying Alternative Fuels in Place of Hydrogen to the Jet Ignition Process," The University of Melbourne, 2008.
- [75] a K. Oppenheim, "Prospects for Combustion in Piston Engines," no. 724, 2002.
- [76] J. E. Dec, "Advanced compression-ignition engines - Understanding the in-cylinder processes," *Proc. Combust. Inst.*, vol. 32 II, no. 2, pp. 2727-2742, 2009.
- [77] W. Attard, N. Fraser, P. Parsons, and E. Toulson, "A Turbulent Jet Ignition Pre-Chamber Combustion System for Large Fuel Economy Improvements in a Modern Vehicle Powertrain," *SAE Int. J. Engines 3(2) 2010-01-1457*, vol. 3, no. 2, pp. 20-37, 2010.
- [78] T. Johansson, B. Johansson, P. Tunestål, and H. Aulin, "HCCI Operating Range in a Turbo-charged Multi Cylinder Engine with VVT and Spray-Guided DI," *SAE Tech. Pap. 2009-01-0494*, 2009.
- [79] W. P. Attard and P. Parsons, "A Normally Aspirated Spark Initiated Combustion System Capable of High Load , High Efficiency and Near Zero NOx Emissions in a Modern Vehicle Powertrain," *SAE Int. J. Engines 3(2) 2010-32-0088*, vol. 3, pp. 269-287, 2010.
- [80] R. P. Roethlisberger and D. Favrat, "Investigation of the prechamber geometrical configuration of a natural gas spark ignition engine for cogeneration: Part I. Experimentation," *Int. J. Therm. Sci.*, vol. 42, no. 3, pp. 239-253, 2003.
- [81] R. P. Roethlisberger and D. Favrat, "Investigation of the prechamber geometrical

- configuration of a natural gas spark ignition engine for cogeneration: Part II. Experimentation," *Int. J. Therm. Sci.*, vol. 42, no. 3, pp. 239–253, 2003.
- [82] A. Shah, P. Tunestal, and B. Johansson, "Scalability Aspects of Pre-Chamber Ignition in Heavy Duty Natural Gas Engines," *SAE Tech. Pap. 2016-01-0796*, no. group 1, 2016.
- [83] Y. Kawabata and D. Mori, "Combustion diagnostics & improvement of a prechamber lean-burn natural gas engine," *SAE Tech. Pap. 2004-01-0979*, vol. 113, no. 3, pp. 660–672, 2004.
- [84] L. S. Baumgartner, S. Karmann, F. Backes, A. Stadler, and G. Wachtmeister, "Experimental Investigation of Orifice Design Effects on a Methane Fuelled Prechamber Gas Engine for Automotive Applications," *SAE Tech. Pap. 2017-24-0096*, 2017.
- [85] G. Gentz, M. Gholamisheeri, and E. Toulson, "A study of a turbulent jet ignition system fueled with iso-octane: Pressure trace analysis and combustion visualization," *Appl. Energy*, vol. 189, pp. 385–394, 2017.
- [86] G. Gentz, B. Thelen, P. Litke, J. Hoke, and E. Toulson, "Combustion Visualization, Performance, and CFD Modeling of a Pre-Chamber Turbulent Jet Ignition System in a Rapid Compression Machine," *SAE Int. J. Engines*, vol. 8, no. 2, pp. 2015-01-0779, 2015.
- [87] W. P. Attard, E. Toulson, A. Huisjen, X. Chen, G. Zhu, and H. Schock, "Spark Ignition and Pre-Chamber Turbulent Jet Ignition Combustion Visualization," *SAE Tech. Pap. 2012-01-0823*, 2012.
- [88] A. Karvountzis-Kontakiotis, A. Dimaratos, L. Ntziachristos, and Z. Samaras, "Exploring the stochastic and deterministic aspects of cyclic emission variability on a high speed spark-ignition engine," *Energy*, vol. 118, pp. 68–76, 2017.
- [89] D. L. Flowers, S. M. Aceves, and J. M. Frias, "Improving Ethanol Life Cycle Energy Efficiency by Direct Utilization of Wet Ethanol in HCCI Engines," *SAE Tech. Pap. 2007-01-1867*, pp. 1070–1078, 2007.
- [90] X. Wu, R. Daniel, G. Tian, H. Xu, Z. Huang, and D. Richardson, "Dual-injection: The flexible, bi-fuel concept for spark-ignition engines fuelled with various gasoline and biofuel blends," *Appl. Energy*, vol. 88, no. 7, pp. 2305–2314, 2011.
- [91] U. S. D. of Energy, "Alternative Fuels Data Center," 2016. .
- [92] RFA, "Industry Statistics - World Fuel Ethanol Production," 2017. .

- [93] S. A. Duffield, James A.; Xiarchos, Irene M.; Halbrook, "Ethanol Policy: Past, Present, and Future," *SdL Rev*, vol. 53, p. 425, 2008.
- [94] J. D. Stephen, W. E. Mabee, and J. N. Saddler, "Will second-generation ethanol be able to compete with first-generation ethanol? Opportunities for cost reduction," *Biofuels, Bioprod. Biorefining*, vol. 6, no. 2, pp. 159–176 ref.90, 2012.
- [95] F. R.-C. and L. A. B. Cortez, "Towards ProAlcool II—a review of the Brazilian bioethanol programme," *Biomass and Bioenergy*, vol. 14, no. 2, pp. 115–124, 1998.
- [96] D. Ö. and B. İnan, "An Overview of Bioethanol Production From Algae," *Biofuels - Status Perspect. InTech*, 2015.
- [97] MICHAEL R. LADISCH¹ and KAREN DYCK, "Dehydration of Ethanol :," *Science (80-.)*, vol. 205, no. 4409, pp. 898–900, 1979.
- [98] H. J. Huang, S. Ramaswamy, U. W. Tschirner, and B. V. Ramarao, "A review of separation technologies in current and future biorefineries," *Sep. Purif. Technol.*, vol. 62, no. 1, pp. 1–21, 2008.
- [99] J. H. Mack, S. M. Aceves, and R. W. Dibble, "Demonstrating direct use of wet ethanol in a homogeneous charge compression ignition (HCCI) engine," *Energy*, vol. 34, no. 6, pp. 782–787, 2009.
- [100] R. Wiebe and J. C. Porter, *Alcohol-water injection for spark-ignition engines*. Peoria, Illinois, 1949.
- [101] S. Brewster, D. Railton, M. Maisey, and R. Frew, "The effect of E100 water content on high load performance of a spray guide direct injection boosted engine," *SAE Tech. Pap. 2007-01-2648*, no. 2007-01–2648, 2007.
- [102] R. Stone, *Introduction to Internal Combustion Engines*, 4th Editio. Macmillan Education UK., 2012.
- [103] B. G. Moxey, "A STUDY OF FLAME DEVELOPMENT WITH ISOCTANEALCOHOL BLENDED FUELS IN AN OPTICAL SPARK IGNITION ENGINE," Brunel University London, 2014.
- [104] N. Kawahara, E. Tomita, A. Takeuchi, S. Arimoto, Y. Ikeda, and A. Nishiyama, "Measurement of flame propagation characteristics in an SI engine using micro-local chemiluminescence technique," *SAE Tech. Pap. 2005-01-0645*, no. 724, 2005.
- [105] G. M. Rassweiler and L. Withrow, "Motion Pictures of Engine Flames Correlated

- with Pressure Cards,” *SAE Tech. Pap. 380139*, 1938.
- [106] A. Augoye and P. Aleiferis, “Characterization of Flame Development with Hydrous and Anhydrous Ethanol Fuels in a Spark-Ignition Engine with Direct Injection and Port Injection Systems,” *SAE Tech. Pap. 2014-01-2623*, vol. 01, no. 2623, 2015.
- [107] B. G. Moxey, A. Cairns, and H. Zhao, “A Study of Turbulent Flame Development with Ethanol Fuels in an Optical Spark Ignition Engine,” *SAE Tech. Pap. 2014-01-2622*, no. 2014-01–2622, 2014.
- [108] M. Fields, J. Zheng, S. Qian, P. J. Kindlmann, J. C. Swindal, and W. P. Acker, “Single-Shot Temporally and Spatially Resolved Chemiluminescence Spectra from an Optically Accessible SI Engine,” *SAE Tech. Pap. 950105*, no. 412, 1995.
- [109] R. Augusta, D. E. F. Madison, J. B. Ghandhi, J. Eng, and P. M. Najt, “Chemiluminescence Measurements of Homogeneous Charge Compression Ignition (HCCI) Combustion,” *SAE Tech. Pap. 2006-01-1520*, no. 724, 2010.
- [110] U. Fissenewert and V. Sick, “Characterization of Combustion and NO Formation in a Spray- Guided Gasoline Direct-Injection Engine using Chemiluminescence Imaging , NO-PLIF , and Fast NO Exhaust Gas Analysis,” *Sae Pap. 2005-01-2089*, 2005.
- [111] M. Tongroon, “COMBUSTION CHARACTERISTICS AND IN- CYLINDER PROCESS OF CAI COMBUSTION WITH ALCOHOL FUELS A thesis submitted for the degree of Doctor of Philosophy By Manida Tongroon School of Engineering and Design,” Brunel University London, 2010.
- [112] C. A. Srinivasan and C. G. Saravanan, “Emission Reduction on Ethanol – Gasoline Blends using 1 , 4 Dioxan,” *Proc. World Congr. Eng.*, vol. II, pp. 2–5, 2010.
- [113] T. Tanaka, M. Fujimoto, and M. Tabata, “Planar Measurements of NO in an S . I . Engine Based on Laser Induced Fluorescence,” no. 412, 1997.
- [114] P.-H. Lu, X. Xie, and M.-C. Lai, “Spectral Analysis and Chemiluminescence Imaging of Hydrogen Addition to HSDI Diesel Combustion Under Conventional and Low-Temperature Conditions,” in *SAE Technical Paper 2004-01-2919*, 2004.
- [115] H. Anders, M. Christensen, B. Johansson, A. Franke, M. Richter, and M. Aldén, “A Study of the Homogeneous Charge Compression Ignition Combustion Process by Chemiluminescence Imaging,” *SAE Tech. Pap. 1999-01-3680*, no. 724, 1999.
- [116] C. Antoni and N. Peters, “Cycle Resolved Emission Spectroscopy for IC Engines,”

- SAE Tech. Pap. 972917*, no. 412, 1997.
- [117] H. Shoji, Y. Tosaka, K. Yoshida, and A. Saima, "Radical Behavior in Pre-flame Reactions Under Knocking Operation in a Spark Ignition Engine," *SAE Tech. Pap. 942061*, no. 412, 1994.
- [118] L. M. Pickett, S. Kook, and T. C. Williams, "Visualization of Diesel Spray Penetration, Cool-Flame, Ignition, High-Temperature Combustion, and Soot Formation Using High-Speed Imaging," *SAE Int. J. Engines*, vol. 2, no. 1, pp. 2009-01-0658, 2009.
- [119] J. E. Dec and R. E. Canaan, "PLIF Imaging of NO Formation in a DI Diesel Engine," no. 724, 1998.
- [120] H. Liu, M. Yao, Z. Zheng, and Y. Wang, "An Investigation of Different Ported Fuel Injection Strategies and Thermal Stratification in HCCI Engines Using Chemiluminescence Imaging," *SAE Tech. Pap.*, pp. 163-2010, 2010.
- [121] S. F. Dingle, "LUBRICANT INDUCED PRE-IGNITION IN AN OPTICAL SPARK-IGNITION ENGINE," Brunel University London, 2013.
- [122] H. Vafamehr, A. Cairns, and M. M. Koupaie, "The Competing Chemical and Physical Effects of Transient Fuel Enrichment During Heavy Knock in an Optical SI Engine Using Ethanol Blends," *SAE Tech. Pap. 2017-01-0665*, 2017.
- [123] S. C. Johnston, C. W. Robinson, W. S. Rorke, J. R. Smith, and P. O. Witze, "Application of Laser Diagnostics to an Injected Engine," *SAE Tech. Pap. 790092*, 1979.
- [124] R. A. Hicks, M. Lawes, C. G. W. Sheppard, and B. J. Whitaker, "Multiple Laser Sheet Imaging Investigation of Turbulent Flame Structure in a Spark Ignition Engine," no. 412, 1994.
- [125] M. F. J. Brunt and A. L. Emtage, "Evaluation of Burn Rate Routines and Analysis Errors," *SAE Tech. Pap. 960609*, no. 412, 1996.
- [126] D. R. Lancaster, R. B. Krieger, and J. H. Lienesch, "Measurement and Analysis of Engine Pressure Data," *SAE Tech. Pap. 750026*, 1975.
- [127] A. Cairns and C. G. W. Sheppard, "Cyclically Resolved Simultaneous Flame and Flow Imaging in a SI Engine," no. 724, 2000.
- [128] M. S. Krzysztof Z. Mendera, Andrzej Spyra, "Mass fraction burned analysis," *J. KONES Intern. Combust. Engines*, no. 3, pp. 193-201, 2002.
- [129] J. Heywood, *Internal Combustion Engine Fundamentals*. Singapore: McGraw-Hill,

1988.

- [130] M. L. Sztenderowicz and J. B. Heywood, "Cycle-to-Cycle IMEP Fluctuations in a Stoichiometrically-Fueled S.I. Engine at Low Speed and Load," *SAE Tech. Pap. 902143*, 2009.
- [131] L. Gillespie, M. Lawes, C. G. W. Sheppard, and R. Woolley, "Aspects of Laminar and Turbulent Burning Velocity Relevant to SI Engines," *SAE Tech. Pap. 2000-01-0192*, no. 724, 2000.
- [132] G. P. Beretta, M. Rashidi, and J. C. Keck, "Turbulent flame propagation and combustion in spark ignition engines," *Combust. Flame*, vol. 52, no. C, pp. 217–245, 1983.
- [133] W. Gander, G. H. Golub, and R. Strebel, "Fitting of circles and ellipses-least squares solution," *SVD Signal Process. III*, 1994.
- [134] D Buran, "Turbulent flame propagation in a methane fuelled spark ignition engine," University of Leeds, 1998.
- [135] L Gillespie, "Imaging and Analysis of Turbulent Flame Development in Spark Ignition Engines," University of Leeds, 1998.
- [136] A. Cairns, "Turbulent Flame Development in a Spark Ignition Engine," University of Leeds, 2001.
- [137] L. S. Baumgartner, S. Wohlgemuth, S. Zirngibl, and G. Wachtmeister, "Investigation of a Methane Scavenged Prechamber for Increased Efficiency of a Lean-Burn Natural Gas Engine for Automotive Applications," *SAE Int. J. Engines*, vol. 8, no. 2, pp. 2015-01–0866, 2015.
- [138] R. A. Stein *et al.*, "Effect of Heat of Vaporization, Chemical Octane, and Sensitivity on Knock Limit for Ethanol - Gasoline Blends," *SAE Int. J. Fuels Lubr.*, vol. 5, no. 2, pp. 2012-01–1277, 2012.
- [139] K. Nakata, S. Utsumi, A. Ota, K. Kawatake, T. Kawai, and T. Tsunooka, "The Effect of Ethanol Fuel on a Spark Ignition Engine," *SAE Tech. Pap. 2006-01-3380*, no. 724, 2006.
- [140] S. Russ, "A Review of the Effect of Engine Operating Conditions on Borderline Knock," *SAE Tech. Pap. 960497*, no. 412, 1996.
- [141] S. S. Merola, P. Sementa, C. Tornatore, and B. M. Vaglieco, "Spectroscopic Investigations and High Resolution Visualization of the Combustion Phenomena in a Boosted PFI SI Engine," *SAE Int. J. Engines*, vol. 2, no. 1, pp. 2009-01–1814,

2009.

- [142] S. Di Iorio, A. Irimescu, S. S. Merola, P. Sementa, and B. M. Vaglieco, "Spectroscopic Investigation of Initial Combustion Stages in a SI Engine Fuelled with Ethanol and Gasoline," *SAE Tech. Pap. 2017-32-0092*, 2017.
- [143] K.T.Walsh, M.B.Long, M.A.Tanoff, and M.D.Smooke, "Experimental and computational study of CH, CH*, and OH* in an axisymmetric laminar diffusion flame," *Proc. Combust. Inst.*, vol. 27, no. 1, pp. 615–623, 1998.
- [144] A. G. Gaydon, *The Spectroscopy of Flames*. Chapman and Hall Ltd, 1957.
- [145] Y. Ohyama, M. Ohsuga, and H. Kuroiwa, "INTERNATIONAL ^ Study on Mixture Formation and Ignition Process in Spark Ignition Engine Using Optical Combustion Sensor," *SAE Tech. Pap. 901712*, 1990.
- [146] M. Yamazaki, M. Ohya, and K. Tsuchiya, "Int. Chem.," *Int. Chem. Eng*, vol. 30, no. 160, 1990.

XII. Appendix

List of appendices

- (A) Cylinder Head Design
- (B) Belt and Pulley Arrangement
- (c) Cross-sectional View of Cylinder Head
- (D) Pre-chamber Dimension
- (E) Top Window
- (F) Side Window
- (G) Modified Side Window
- (H) Required Waveform

Schematic of Experimental Engine

Imaging techniques

- (1) High-speed Camera with Intensifier
- (2) High-speed Camera without Intensifier
- (3) High-speed Camera with Full Top View Window
- (4) **FastCam** Mini with Telescope
- (5) **FastCam** Mini with Lambert Intensifier

(A) Cylinder Head Design

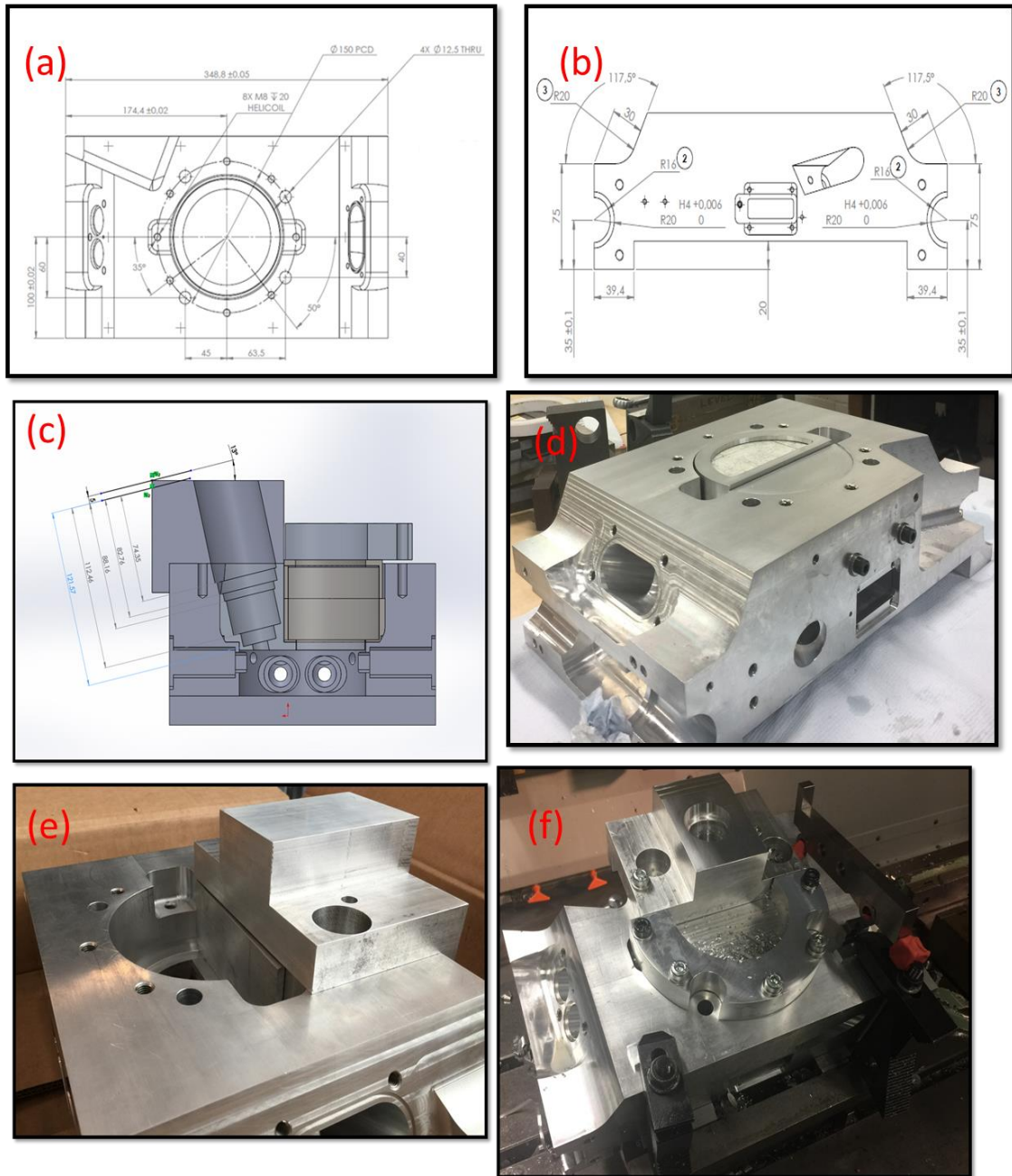


Figure 8.1 Cylinder head design: (a, b) cylinder head drawing, (c) multi-hole dimensions, (d) cylinder head, (e) cylinder head and adapter, (f) cylinder head during machining

(B) Belt and Pulley Arrangement

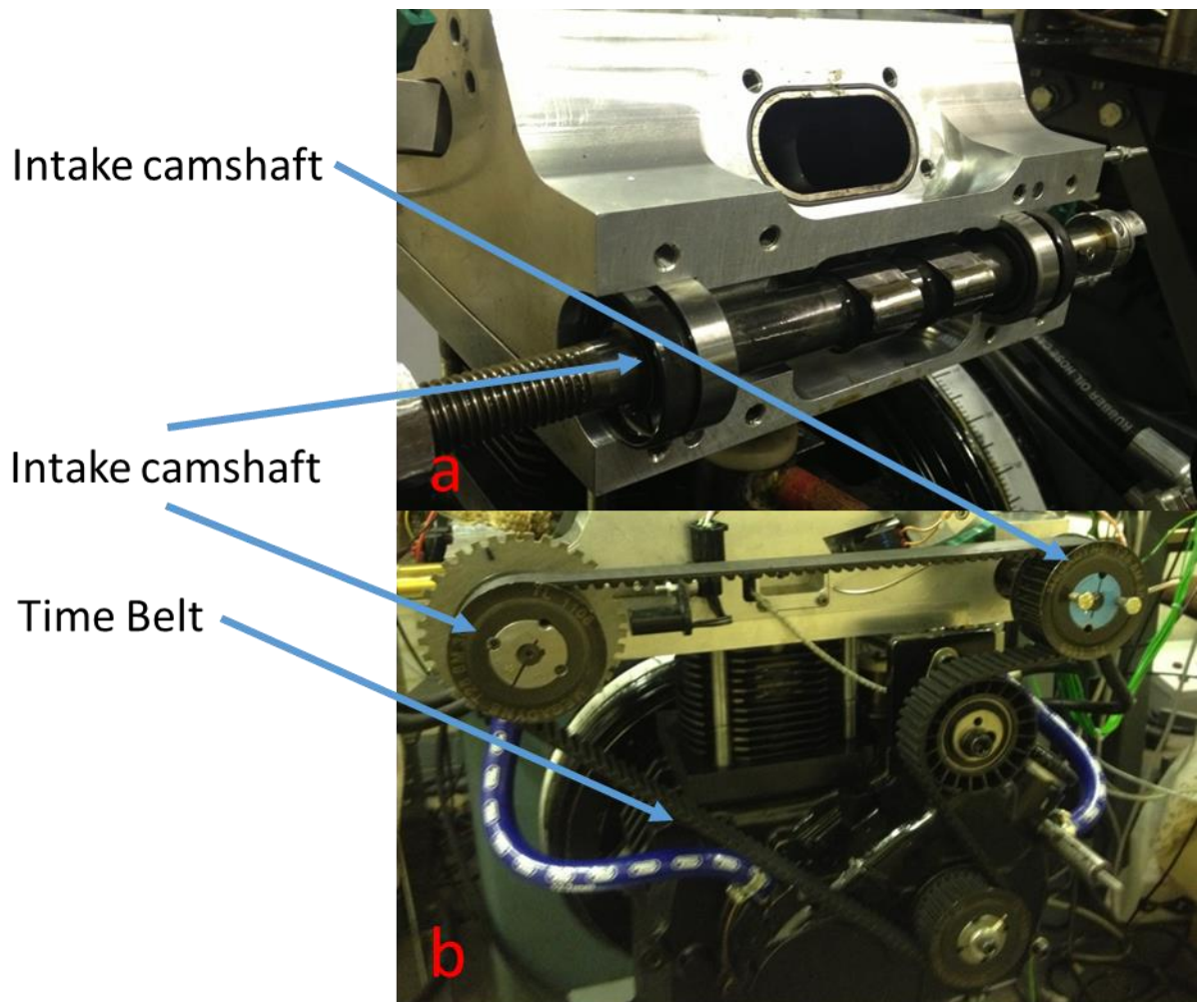


Figure 8.2 Image of the engine showing the belt and pulley arrangement with the intake cam (a), belt is driven off a pulley connected to the crankshaft via a toothed gear (b)

(C) Cross-sectional View of Cylinder Head

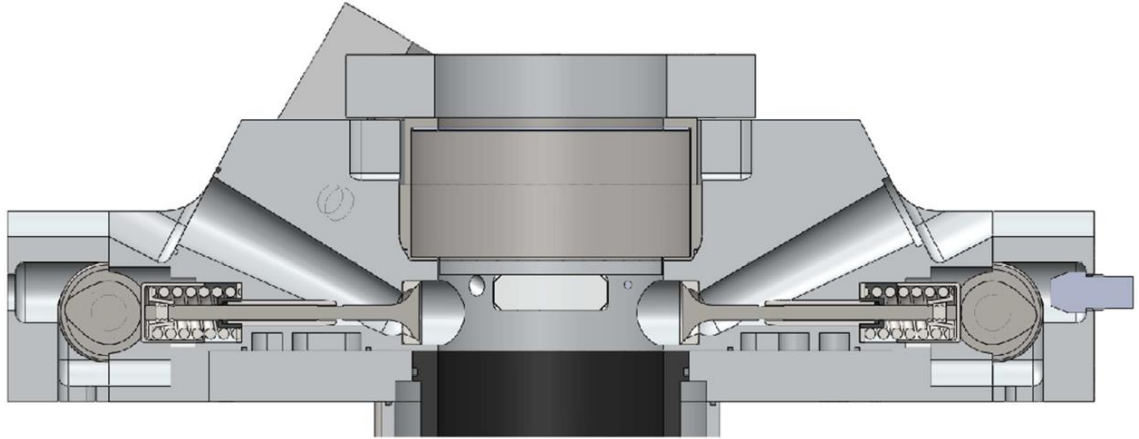


Figure 8.3 Cross-sectional view of the engine showing the inlet and exhaust port geometry

(D) Pre-chamber Dimension

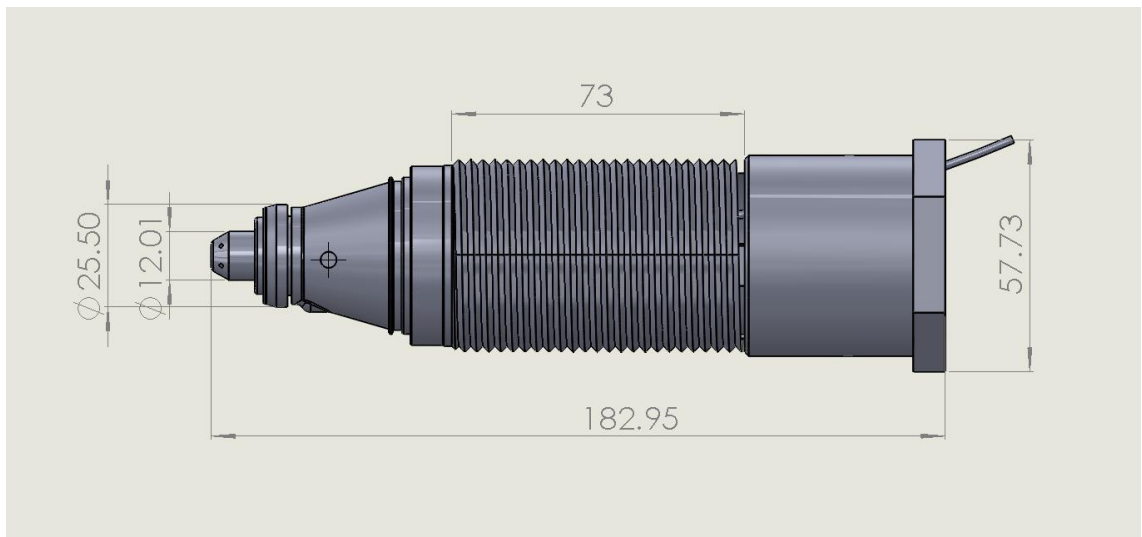
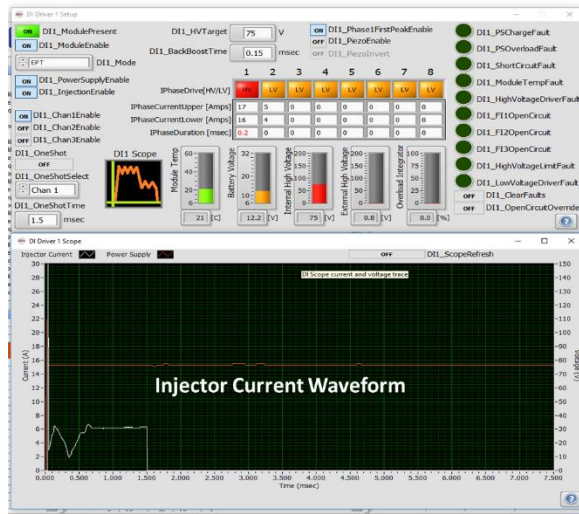
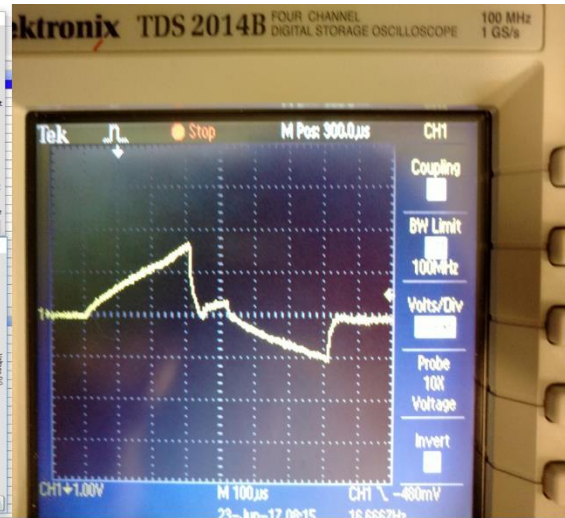


Figure 8.4 Pre-chamber dimension

(H) Required Waveform



NI Driver: Injector controlled waveform



Delphi Driver: Injector controlled waveform

Figure 8.8 Comparison between the required and existing waveform

(I) Schematic of Experimental Engine

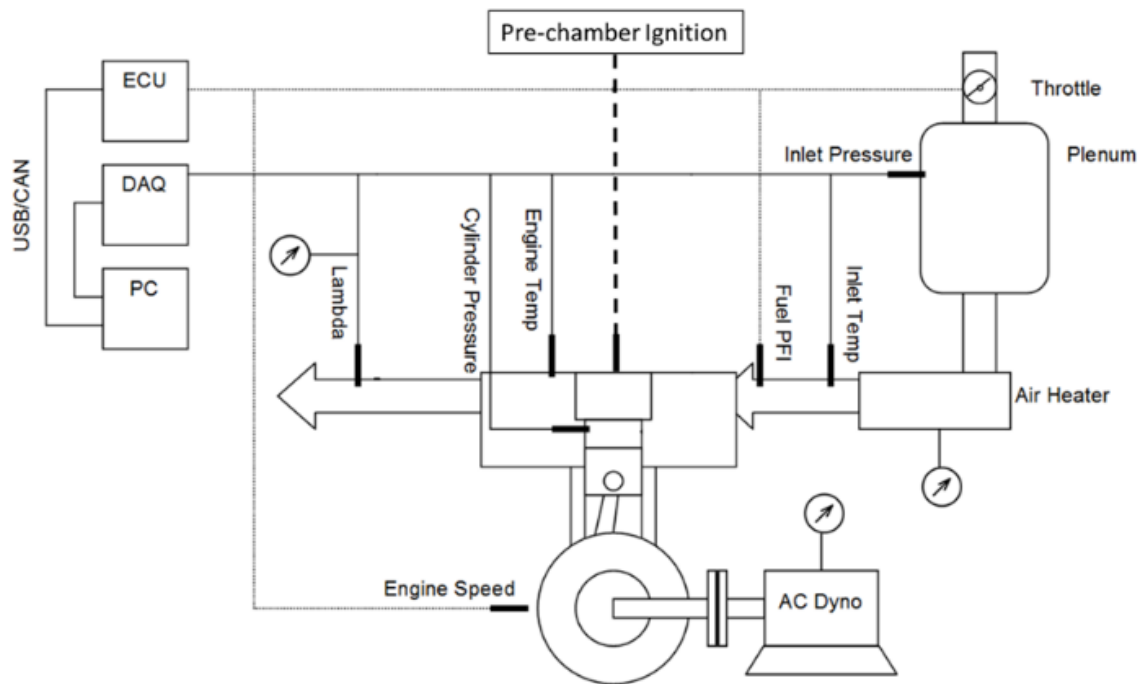


Figure 8.9 Schematic of the experimental engine control and data acquisition systems

(J) Imaging Techniques

(1) High-speed Camera with Intensifier

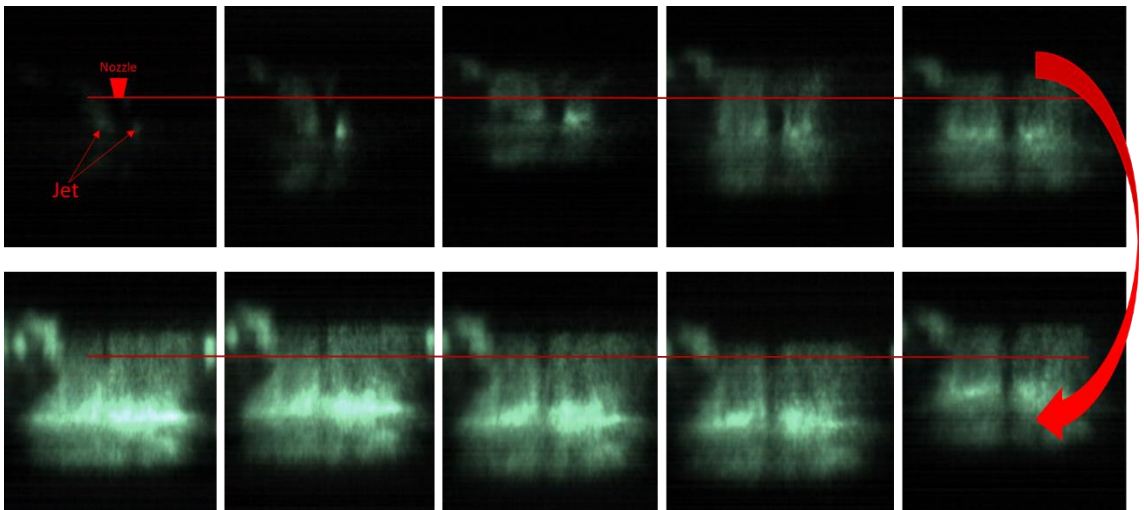


Figure 8.10 High-speed images with intensifier

(2) High-Speed Camera without Intensifier

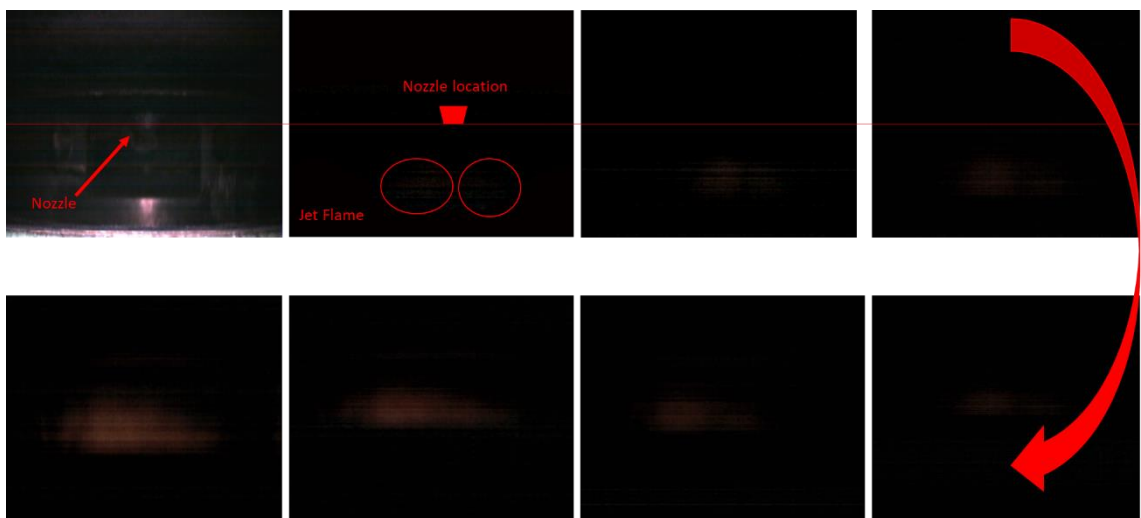
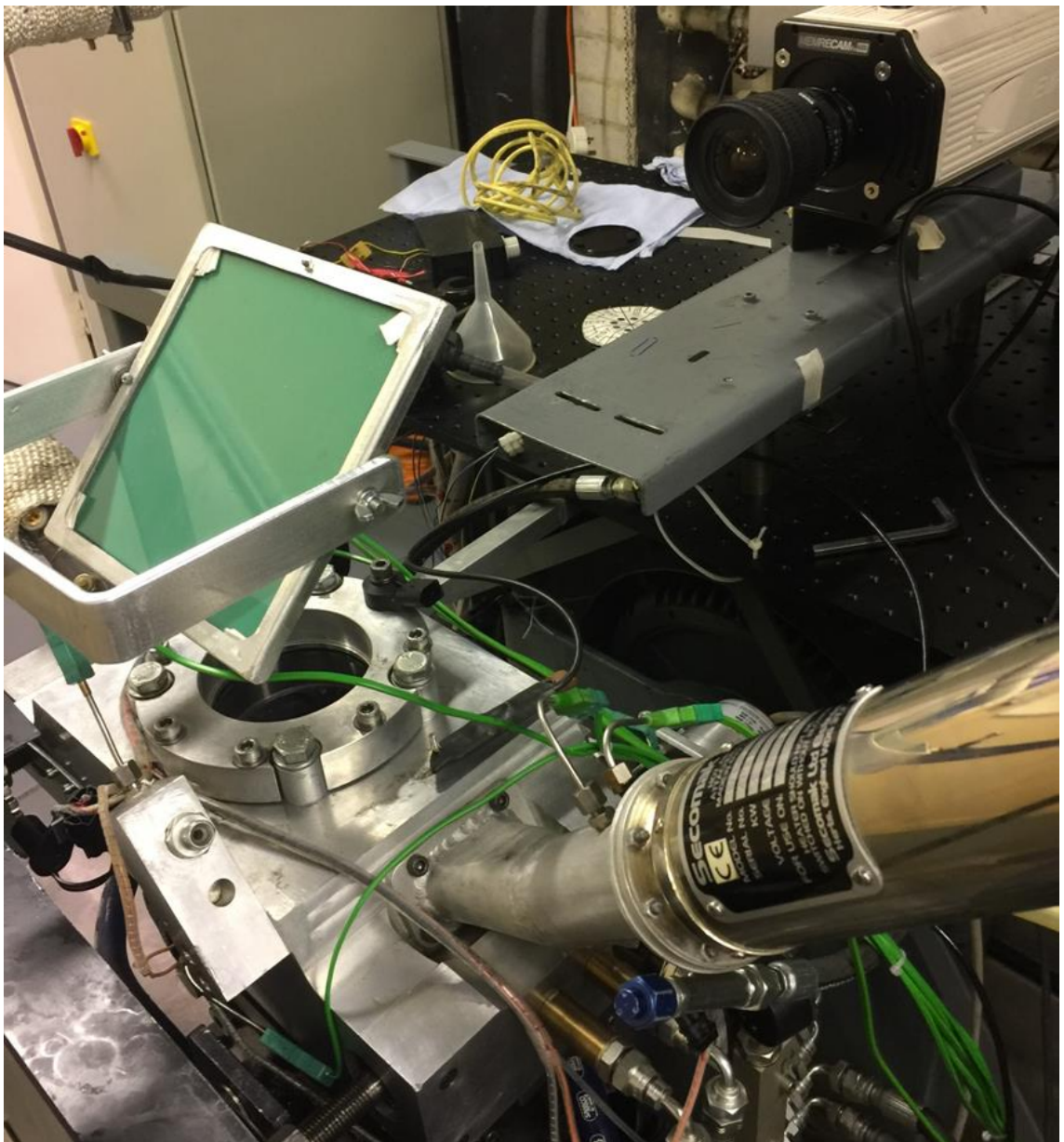


Figure 8.11 High-speed images without intensifier

(3) High-speed Camera with Full View



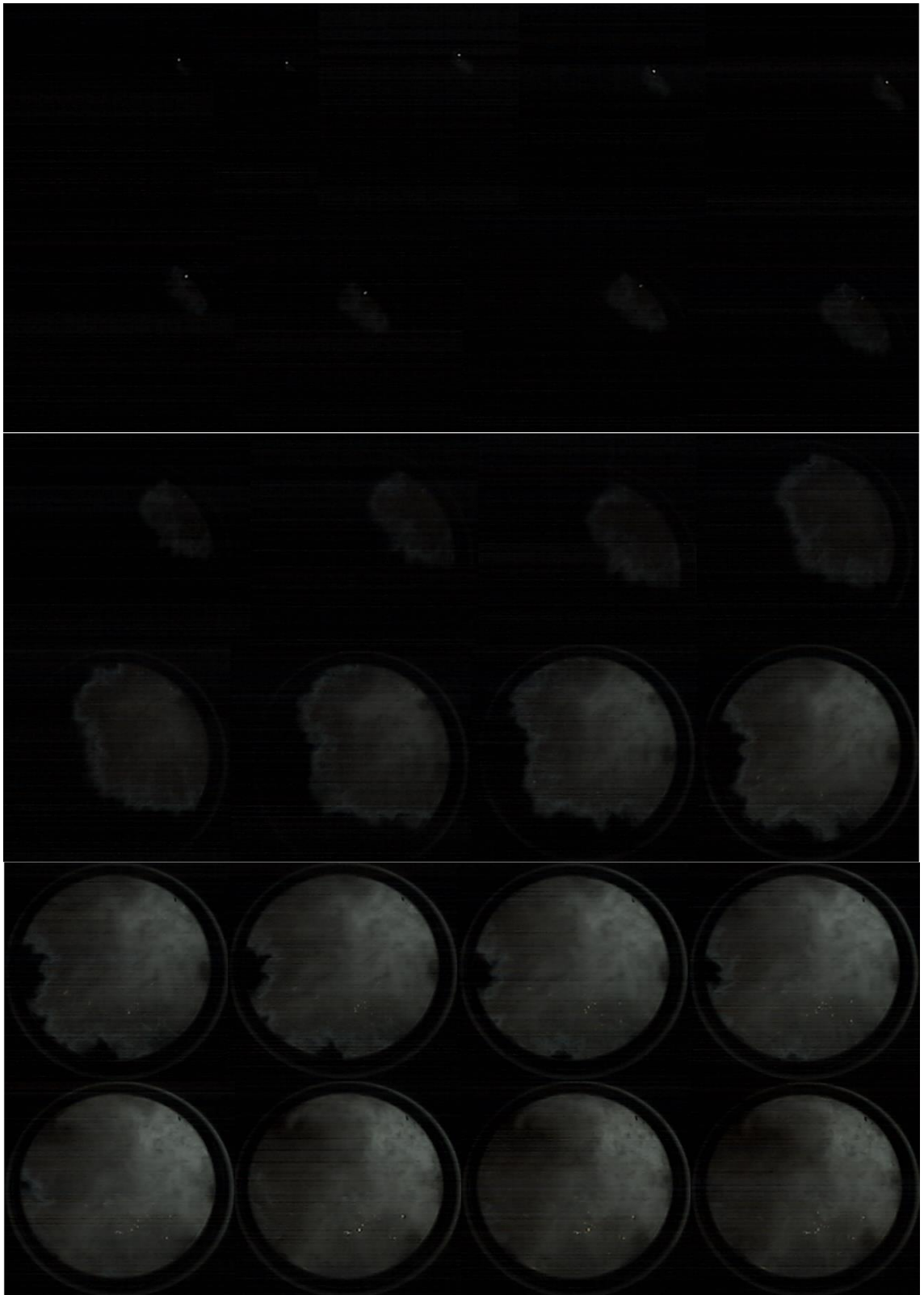


Figure 8.12 Top view images with full circle window

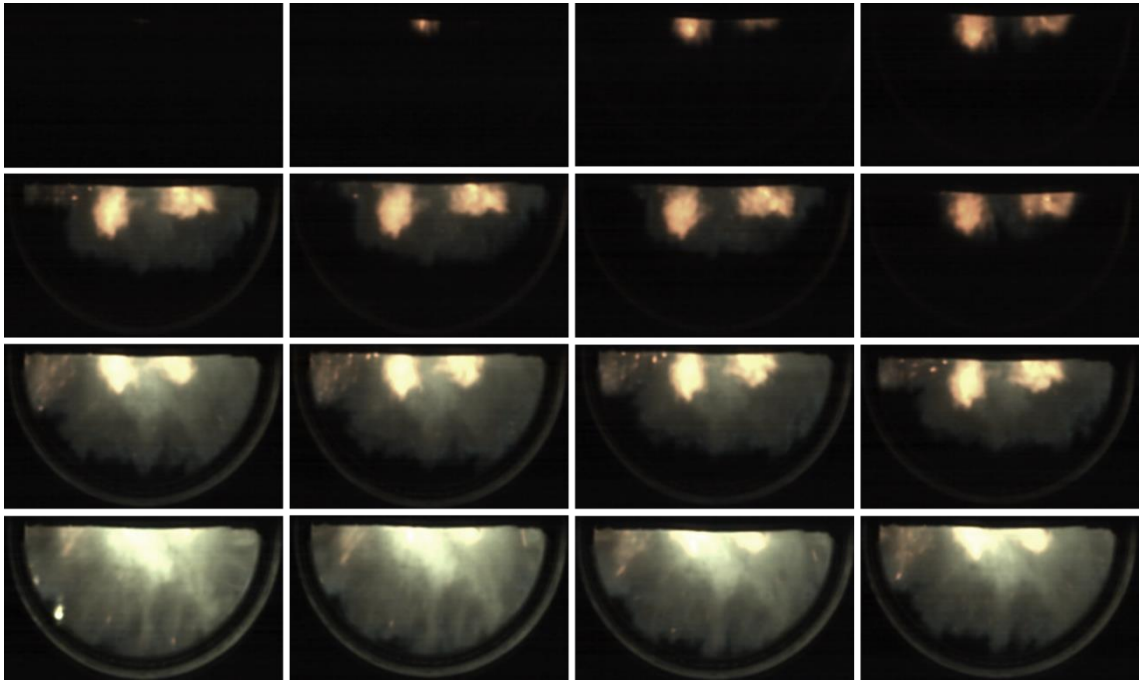


Figure 8.13 Top view images with modified half window

(4) *FastCam* Mini with Telescope



Figure 8.14 *FastCam* mini with telescope

(5) *FastCam* Mini with Lambert Intensifier

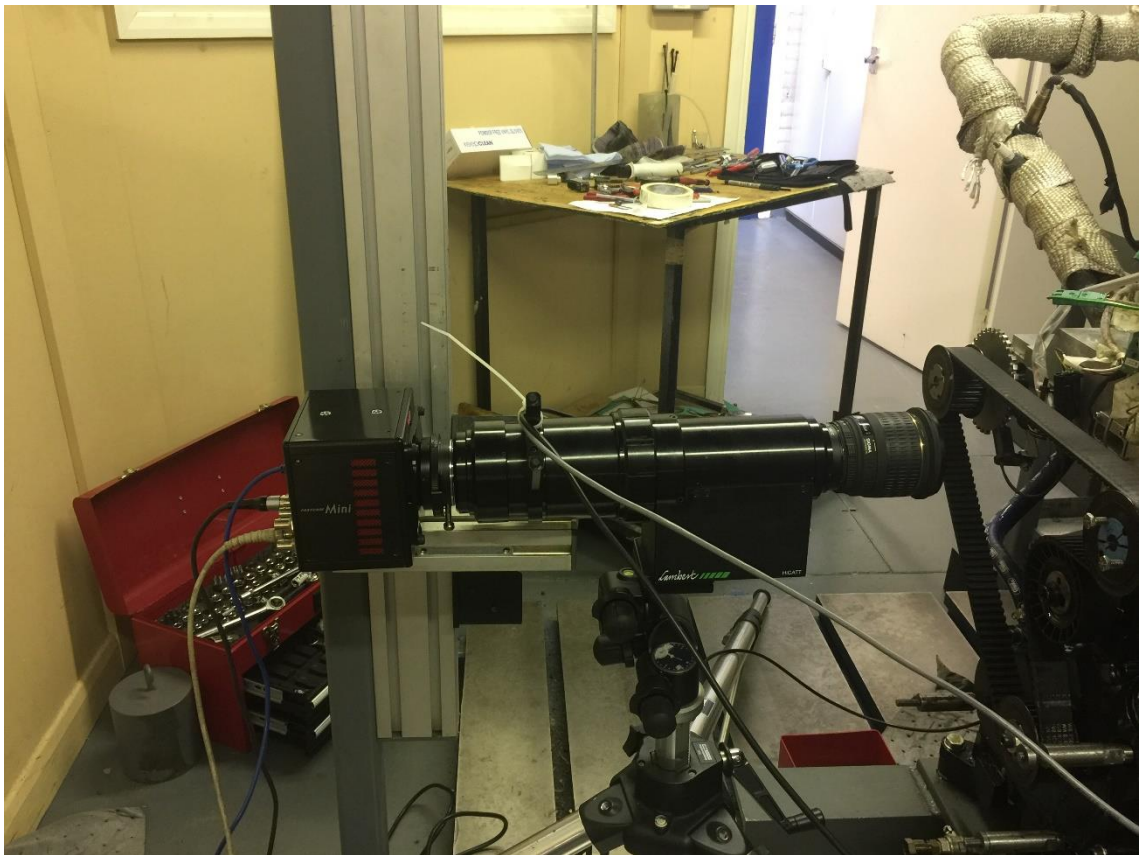


Figure 8.15 *FastCam* mini with Lambert intensifier